

# **Axial Transport Behavior and Thermal Treatment of Polydisperse Materials in Direct Heated Rotary Kilns**

Dissertation

Zur Erlangung des akademischen Grades

**Doktor-Ingenieur**

**(Dr.-Ing.)**

von: M. Sc. Haozhi Jie  
geb am: 13.08.1990 in Nanjing, China

Genehmigt durch die Fakultät für Verfahrens- und Systemtechnik  
der Otto-von-Guericke-Universität Magdeburg

Gutachter: Prof. Dr.-Ing. Fabian Herz  
Prof. Dr.-Ing. Eckehard Specht  
Dr.-Ing. Jochen Mellmann

eingereicht am: 28.04.2020

Promotionskolloquium am 07.10.2020

# Acknowledgement

I do very appreciate the guidance and support of my supervisor Prof. Dr.-Ing. Fabian Herz. Since 2014, he has provided me with many professional insights, constructive advice and helpful comments. His kind encouragement also motivates me to make continuous effort during my Ph.D. career, especially when I was frustrated and had self-doubt. In addition, he has a very efficient time management, high working intensity and strong research enthusiasm. I have no excuse to slacken off when working with him. It is my great honor to be his Ph.D. student and he will always be a role model for my career and life.

I am incredibly grateful to Prof. Dr.-Ing. Eckehard Specht, who has totally changed my life. Though an hour late for the first meeting with him, I successfully became a Hiwi at his Chair in 2013. Many thanks for offering me the opportunity, which opens the door to research for me. My confidence and research interest are gradually growing through increasingly more communication and discussions with him. Not only does he support me a lot about research, he also provides me invaluable assistance in dealing with the troubleshooting of my life. Besides, I especially thank the financial support from him.

I thank sincerely my parents for their mental and financial support as well. Finally, I would like to thank my wife, Mengjie Shi. If I were a bird, the research enthusiasm would be one wing and she would be another helping me fly to the success. If someone asks me what achievements I have received in my Ph.D. career, I will reply without any hesitation, firstly, I made some progress in rotary kiln and secondly, I found my wife!

## Abstract

Rotary kilns are industrial reactors which are widely used in the chemical, metallurgy, food and pharmaceutical industry for the thermal process of granular materials. Due to the high process temperatures and limited access of measuring technology, the industrial operation of the system is characterized by empiricism. As a result, the potential for optimizing process in terms of energy efficiency, product quality and safety is in a limited extent. Therefore, mathematical process models could be implemented to counteract this.

In the present work, an existing process model is further developed with a discrete description of the axial particle transport. In particular, the transport behavior of polydisperse particle system in the rotary kiln is analyzed numerically and experimentally. On the one hand, the transient behavior on an industrial scale is experimentally investigated on a pilot rotary kiln with a length of 5 m and a diameter of 400 mm. For this purpose, a new video analysis method is implemented, with which bulk bed profiles can be continuously recorded for the first time. A mathematical model to describe the transient flow of the bulk material is validated with the help of the results obtained with varying operating and bulk material parameters.

On the other hand, a new mathematical model based on the ring-core structure is developed to describe the steady state axial transport and the residence time of each particle size in the polydisperse system. This model is also validated on the pilot rotary kiln mentioned above, whereby the influence of the bulk material and operating parameters on the particle-discrete residence time distributions is determined.

This stationary model will be implemented in an existing thermal process model for directly fired rotary kilns. The influence of particle dispersity and size on product

quality is demonstrated using the reference process of quartz sand calcination. The axial temperature profiles, as well as the local heat transfer coefficients and heat flows are presented and compared.

# Zusammenfassung

Drehrohröfen sind Industriereaktoren, die in der Chemie-, Metallurgie-, Nahrungsmittel- und Pharmaindustrie zur thermischen Aufbereitung von granularen Stoffen breite Anwendung findet. Aufgrund der meist hohen Prozesstemperaturen und nur bedingt messtechnischen Zugänglichkeit ist der industrielle Betrieb solcher Anlagen von Empirie geprägt. Das Potential zur Optimierung der Prozesse hinsichtlich Energieeffizienz, Produktqualität und Sicherheit ist somit nur bedingt möglich. Dem entgegenzuwirken können mathematische Prozessmodelle genutzt werden.

Im Rahmen der vorliegenden Arbeit wird ein bereits bestehendes Prozessmodell um eine diskrete Beschreibung des axialen Partikeltransportes weiterentwickelt. Insbesondere das Transportverhalten polydispenser partikulärer Systeme im Drehrohr wird hierfür numerisch und experimentell analysiert. Zum einen wird das transiente Verhalten im technischen Maßstab an einem Pilotdrehrohr mit einer Länge von 5 m und einem Durchmesser von 400 mm experimentell untersucht. Hierfür wird eine neuartige Videoanalysemethode implementiert, mit der erstmalig die Dynamik der Schüttgutprofile kontinuierlich erfasst werden kann. Mit Hilfe der bei variierenden Betriebs- und Schüttgutparametern ermittelten Ergebnisse wird ein mathematisches Modell zur Beschreibung des transienten Schüttgutverlaufes validiert.

Andererseits wird ein neues mathematisches Modell entwickelt, das auf der Ring-Kern-Struktur basiert, um den stationären axialen Transport und die Verweilzeit jeder Partikelgröße im polydispersen System zu beschreiben. Dieses Modell wird ebenfalls an dem zuvor erwähnten Pilotdrehrohr validiert, wobei der Einfluss der Schüttgut- und Betriebsparameter auf die partikeldiskreten Verweilzeitverteilungen bestimmt wird.

Dieses stationäre Modell wird in ein bestehendes Thermoprozessmodell für direkt

befeuerte Drehrohröfen implementiert. An dem Referenzprozess der Quarzsandkalzination wird der Einfluss der Partikeldispersität und des Größenanteils auf die Produktqualität aufgezeigt. Die axialen Verweilzeit-Temperaturverläufe, sowie die lokalen Wärmeübergangskoeffizienten und Wärmeströme werden hierfür gegenübergestellt.

# Table of Contents

<b>Acknowledgement</b>	II
<b>Abstract</b>	III
<b>Zusammenfassung</b>	V
<b>Table of Contents</b>	VII
<b>List of Abbreviations</b>	X
<b>1 Introduction</b>	1
1.1 Research background	1
1.2 Objective of the thesis	3
<b>2 Transient axial transport</b>	4
2.1 Literature review of axial solid transport	4
2.1.1 Steady state flow	4
2.1.2 Transient behavior	6
2.2 Modeling of axial solid transport	8
2.2.1 Mathematical model of steady state	8
2.2.2 Mathematical model of transient behavior	14
2.3 Experimental analysis of axial solid transport	19
2.3.1 Experimental apparatus and materials	19
2.3.2 Experimental details and measuring method	21
2.3.3 Data analysis method	22
2.4 Results and discussions	26
2.4.1 Stationary time	26
2.4.2 Influence of rotational speed	29
2.4.3 Influence of feed mass flow rate	33
2.4.4 Influence of axial inclination	36
2.5 Conclusion	39
<b>3 Residence time distribution</b>	41
3.1 Literature review	41
3.1.1 Residence time behavior of monodisperse system	41

VII

3.1.2 Transverse segregation	43
3.2 Mathematical model of transverse segregation and RTD	46
3.2.1 Modeling of transverse segregation in a bidisperse bulk bed	46
3.2.2 Modeling of transverse segregation in a polydisperse bulk bed	52
3.2.3 Assumptions for modeling the transverse segregation in a bi- and polydisperse bulk bed	55
3.3 Experiment of residence time distribution	56
3.3.1 Experimental apparatus and materials	56
3.3.2 Experimental details and measuring method	58
3.3.3 Data analysis method	62
3.4 Results and discussion	75
3.4.1 Influence of rotational speed	75
3.4.2 Influence of inclination angle	81
3.4.3 Influence of feed mass flow rate	86
3.4.4 Influence of particle size	90
3.5 Conclusion	95
<b>4 Process modeling of bi- and polydisperse system</b>	<b>97</b>
4.1 Process model	97
4.1.1 Basic structure of the process model	97
4.1.2 Heat transfer between the covered wall and bulk bed	99
4.2 Influence of RTD on thermal process	104
4.2.1 Improvement of transverse segregation model in bidisperse system and application in process model	104
4.2.2 Improvement of transverse segregation model in polydisperse system and application in process model	112
4.2.3 Assumptions of particle bed in process model	118
4.3 Results and Discussion	120
4.3.1 Simulation results with monodisperse particle system	120
4.3.2 Influence of particle diameters in monodisperse systems	124
4.3.3 Simulation results with bidisperse particle system	131
4.3.4 Influence of particle mass ratios in bidisperse particle system	137
4.3.5 Influence of particle diameters in bidisperse particle system	142



4.3.6 Simulation results with polydisperse particle system	145
4.3.7 Influence of particle mass ratios in polydisperse system	148
4.4 Conclusion	151
<b>5 Conclusion and recommendation</b>	<b>153</b>
5.1 Conclusion	153
5.2 Future Work	155
<b>References</b>	<b>156</b>
<b>Appendix</b>	<b>162</b>

# List of Abbreviations

## Latin letter symbols

A	Particle bed cross section area	$m^2$
$A_0$	Total transverse particle bed area	$m^2$
$A_1$	Transverse area of largest size particle I in polydisperse system	$m^2$
$A_2$	Transverse area of second largest size particle II in polydisperse system	$m^2$
$A_i$	Transverse area of No. i particle bed	$m^2$
C	Tracer concentration	-
c	The length of chord at surface of bed (cross section view)	m
$c_p$	Specific heat capacity	J/kg/K
E(t)	Residence time distribution function	$\text{min}^{-1}$
D	Inner diameter of rotary kiln	m
$D_z$	Axial dispersion coefficient	$m^2s^{-1}$
dA	Increment of area	$m^2$
$d_p$	Particle diameter	mm
$d_0$	Sauter mean diameter of mixing particles	mm
dv	Increment of volume	$m^3$
dz	Axial component of rotary kiln	m
F	Filling degree	-
Fr	Froude number	-
g	Gravitational acceleration	$m/s^2$
$H_i$	Real particle bed depth from video analysis	m
$H_{mr}$	Real height of each measuring rod	m
$\dot{H}$	Enthalpy	W
h	Particle bed depth	m
$h_0$	Digital height of each measuring rod in the photo of empty kiln	mm

$h_i$	Digital height of the free measuring rod in the photo	mm
$h(t_i)$	Particle bed depth at time in transient process	m
L	Length of rotary kiln	m
$l_2$	Half chord of area II	m
$\dot{M}$	Feed mass flow rate of solid	kg/h
$\dot{M}_{S,out}$	Discharge mass flow rate of solid	kg/h
$m_{s,i}$	Weight of tracers in each collected box	kg
N	Number of cascades per circulation (chapter 2)	-
N	Number of different size particles (chapter 3 and 4)	-
$N_s$	Total number of samples	-
n	Rotational speed of rotary kiln	rpm
$n_c$	Critical rotational speed	rpm
O	Center of circle (transverse view of rotary kiln)	-
P	Test points in video analysis	-
Pe	Peclet number	-
$\dot{Q}$	Heat flow	W
R	Inner radius of rotary kiln	m
$R_1$	Radius of largest size particle bed I in polydisperse system	m
$R_2$	Radius of second largest particle bed II in polydisperse system	m
$R_i$	Radius of No. i particle bed	m
$R_{fuel}$	Reaction energy term for fuel conversion	W
$R_1'$	Radius of largest size particle bed I in adjusted model	m
$R_2'$	Radius of second largest particle bed II in adjusted model	m
$R_i'$	Radius of No. i particle bed in adjusted model	m
RT	Residence time above the selected reference temperature	min
r	Radius of particle path in bed	m
$r_0$	Minimum distance between O and particle bed surface	m
S	Surface	$m^2$
T	Temperature	$^{\circ}C$

$t_i$	Time points in the experiments	min
$\bar{t}$	Mean residence time	min
$u$	Average axial transport velocity of a single particle	m/s
$u_1$	Local axial velocity of largest size of particles	m/s
$u_2$	Local axial velocity of second largest size of particles	m/s
$u_i$	Local axial velocity of No. i size particles	
$\bar{u}_1$	Mean particle velocity of largest size of particle	m/s
$\bar{u}_2$	Mean particle velocity of second largest size of particle	m/s
$\bar{u}_i$	Mean particle velocity of No. i size of particle	m/s
$\dot{V}$	Average volumetric transport rate	m <sup>3</sup> /s
$\dot{V}_1$	Volume flow rate of biggest particles	m <sup>3</sup> /s
$\dot{V}_2$	Volume flow rate of second biggest particles	m <sup>3</sup> /s
$\dot{V}_i$	Volume flow rate of No. i particle bed	m <sup>3</sup> /s
$\bar{v}_w$	Mean particle velocity in the active layer at the vortex point	m
$X_i$	The initial mass flow fraction of No. i size particles	-
$Z$	Total number of finite axial elements	-
$z_0$	The axial transport distance of particle per cascade	m
$z$	Axial length / Position	m

**Greek letter symbols**

$\alpha$	Heat transfer coefficient	W/m <sup>2</sup> /K
$\beta$	Inclination angle of the kiln	°/rad
$\Theta$	Dynamic angle of repose	°
$\Delta$	Dimensionless thickness of the active layer	-
$\Delta t$	Measuring time interval	min
$\delta_i$	Active layer thickness of each particle size bed	m
$\delta_{max}$	Maximal active layer thickness	m
$\delta V$	Volume element of particle bed	m <sup>3</sup>
$\varepsilon$	Half filling angle	°/rad

$\varepsilon_1$	Half filling angle of biggest size particle bed	$^{\circ}/\text{rad}$
$\varepsilon_2$	Half filling angle of second large size particle bed	$^{\circ}/\text{rad}$
$\varepsilon_i$	Half filling angle of No. i particle bed	$^{\circ}/\text{rad}$
$\theta$	Dimensionless time	-
$\Lambda$	Ratio between $\delta$ and maximum active layer thickness	-
$\lambda_s$	Thermal conduction coefficient of solid bed	W/m/K
$\xi$	Dimensionless x-coordinate,	-
$\xi_0$	Initial condition	-
$\rho_b$	Bulk density	kg/m <sup>3</sup>
$\rho_{b0}$	Bulk density of mixing particles	kg/m <sup>3</sup>
$\rho_{bi}$	Bulk density of each size particles	kg/m <sup>3</sup>
$\nu_A$	Inclination angle of the boundary line to the bed surface	rad
$\chi$	Thickness of gas film	-
$\psi$	Angle between surface of material and kiln axis	$^{\circ}/\text{rad}$
$\omega$	Angular velocity	rad/s

**Subscript or superscript**

amb	Ambient
bo	Bottom
eff	Effective
in	Inlet
g	Gas gap
G	Gas phase
GS	Heat transfer between gas phase and solid bed
GW	Heat transfer between gas phase and inner wall
M	Steel shell
max	Maximum
mo	Monodisperse particle system
out	Outlet

ov	Overall
ref	Reference
reg	Regenerative
S	Solid bed
Shell	Shell surface
Steady	Steady state of particle bed
W	Inner wall
WS	Heat transfer between inner wall and solid bed
$\varepsilon$	Radiation heat transfer
$\alpha$	Convection heat transfer
$\lambda$	Contact heat transfer

# 1 Introduction

## 1.1 Research background

Rotary kilns are industrial reactors widely used in chemical and metallurgical processes for the thermal treatment of bulk materials like calcination of limestone, sintering of cement and pyrolysis of solid waste. Based on mode of heat transfer, the kilns are classified as direct and indirect heated systems. The basic component of a direct fired rotary kiln is a steel cylinder lined with refractory bricks. To reach the process temperature, a burner is installed at the upper or lower end of the kiln, so that the bulk is in direct contact with the flame and the hot gas. It could be up to 4 m inner diameter, around 150 - 180 m length, and operated up to 5 rpm rotational speed, as well as in the range of 5 ° inclination angle. The kiln is filled with granular materials with a typical filling degree from 10% to 30% of the total volume. Raw materials are fed to the upper end and travel along the axis to the lower end of the kiln with a velocity depending on the axial and circumferential motion caused by gravity and rotation. So, the contact time between bulk and hot gas strongly depends on the axial transport.

Although a large amount of studies has been done for axial transport, the transient motion behavior could still not be described. The transient axial transport is of importance for the total process because it defines the residence time of particles as well as the heat transfer surface of the bulk material along the kiln such as start-up, irregularities in feed rate and fluctuations in the physical properties of materials. In order to develop successful process models and effective control system, it is therefore of great significance to understand the unsteady motion resulting from sudden changes of operational factors which could be strongly coupled with heat and mass transfer, chemical reaction and dust entrainment inside of the kiln.

The axial transport behavior strongly depends on the bulk material properties,

especially the particle size. In industrial application, the bulk bed is often considered as a polydisperse particle system with wide particle size range. In these systems segregation effects could occur. A typical segregation is shown in Figure.1.1, where the

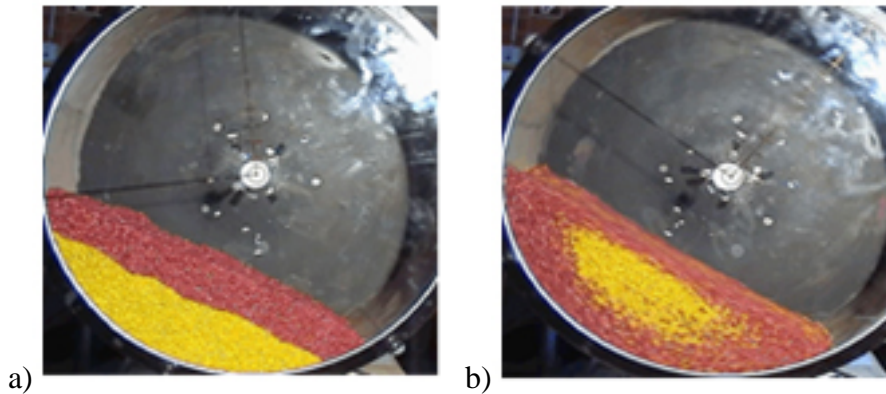


**Figure 1.1** Segregation process with 4 mm and 2mm glass beads with 1:1 weight

particle system consists of bidisperse glass beads in diameter of 2 mm (yellow) and 4 mm (red) and is presented in transverse section. In this figure, the part a) is the initial condition of mixing process, where the two size particles are not mixed and just accumulated in two layers. The Figure 1.1 (b) is the condition after kiln circulation. The small particles move through gaps of big particles and concentrated in the middle of particle bed which is always in the core. In the same time, big particles located outside of the bed as an outer ring. Hence, the typical ring-core structure is considered as basic structure of transverse segregation in rotary kilns.

By the application of this structure, different axial particle velocity profiles could be derived from the connections between constant mass flow rate and varied cross section areas. With the velocity profiles, the residence time of different location inside of kiln could also be calculated and it is quite important for thermal treatment. For example, during limestone calcination, the residence time of particle temperature above 850 °C should be known to make sure the enough reaction time. Furthermore, the new heat transfer model of the whole system will also be developed by considered the



segregation structure. The heat transfer of big particle consists of 1) contact between upper particle bed and hot gas or flame, 2) contact between inner wall surface and bottom particle bed, 3) radiation between upper particle bed and inner wall surface. However, for small particles, the heat transfer is only by penetration through the big particle layer. Hence, a model should be created to describe all the effects in total process.

## **1.2 Objective of the thesis**

Therefore, this thesis presents the following results:

- (1) In chapter 2, mathematical model is developed to describe the transient behavior of axial solid transport in rotary kiln. This model is validated by experiments in a pilot rotary kiln. New measuring method was implemented to points and time of the axial bed depth profiles, as well as of the mass flow behavior. Influence of rotational speed, inclination angle, feed mass flow rate and particle diameters are also included.
- (2) In chapter 3, a new model with segregation effect was developed to describe the transverse section area in bidisperse system. Total residence time distributions are calculated based on this model and validated by some experiments in the same pilot kiln as in chapter 2. Different size of mixing glass beads particles are used as test materials and rotational speed, feed mass flow and inclination angel are all considered as influence factors.
- (3) The residence time distribution method developed in chapter 3 is implemented into an overall process model. Numerical simulations were done for a reference process with different polydisperse systems. Based on that, the temperature profiles of different particle diameters were shown by varying the operational conditions. So, the superimposing behavior of axial transport and heat transfer can be clearly seen for polydisperse bulk systems in rotary kilns.

## 2 Transient axial transport

### 2.1 Literature review of axial solid transport

#### 2.1.1 Steady state flow

In the industrial field, most kiln processes are under constant operational conditions which are rotational speed, inclination angle, mass flow rate and energy input. The axial transport is in steady state behavior which means mass flow rate inlet equals to mass flow outlet of the kiln and no change of axial bed depth profile. A number of investigations have been done to observe the steady state flow of granular solid through an inclined cylinder which slowly rotates about its own axis.

Sullivan et al. (1927) published the first experiment about steady state flow. During his experiments, operational conditions, particle physical properties and size of kiln are all considered as variables to show their influence. Some simple equations are derived to predict the mean residence time. Saeman (1951) derived a mathematical model for the steady state transport of a granular solid through an inclined cylinder. This model was validated by many other researchers till now and was widely accepted as basic model of axial transport. Kramers and Croockewit (1952) used the experimental data from Sullivan et al. (1927) to validate the Saeman's model and had good agreements. Furthermore, they also finished other experiments to reveal the relationship between setup variables and mean residence time.

Vahl and Kingma (1952) discussed the solid transport by using dry sharp sand and rye in glass and steel cylinders with a diameter of 110 mm and a length of 650 mm. Equations had been developed to give the volume transport rate, the loading in the drum and the time of passage inside of a kiln. Hogg et al. (1974) extended the model from Vahl and Kingma (1952) and presented the relationship between particle hold up and mass flow rate in the horizontal laboratory scale drum which obtained empirical

expression. However, Karra and Fuerstenau (1978) validated the model from Hogg et al. (1974) and found that the constraint on the constant  $B$  in their model was not general. Chatterjee et al. (1983) used a pilot scale kiln to investigate the effect of kiln inclination and rotational speed on residence time and hold up. Meanwhile, the influence of dam constructions inserted at the axis were also presented with 6 types of dams.

Lebas et al. (1995) built a special device to measure the bed depth with 200 mm intervals and indicated that the particle motion was very close to the ideal plug flow regime and the equation from Kramers and Croockewit (1952) about mean residence time had best agreement with his experiments. Later on, another study conducted by Liu and Specht (2006) indicated that for MRT and hold-up, Saeman's model presented good predictions over the entire range of parameters. Therefore, in conclusion, the model from Saeman (1952) was chosen as basic model in this thesis.

This model is limited to low rotation speed, which leads to slumping or rolling motion in transverse cross-section. It estimates three parts: (i) the profile of axial bed depth, hold-up and axial velocity, (ii) total hold-up, (iii) the mean residence time of particles. The principle of the Saeman's model is that the granular solid moves through the cylinder which is made up of a simple average particle motion, as shown in Figure 2.1. The basic assumption of particle motion in a cross-section of granular bed can be classified as follows:

- (1) The main body of the granular bed is considered as a rigid body when rotating around the axis.
- (2) There is no slip between particle bed and kiln wall which means the rigid body rotates with the angular velocity of the kiln.
- (3) There is a thin layer so called active layer on the free surface for particles falling down under gravity. Particles fall from upper part of bed to lower part of bed then enter to the rigid body.
- (4) The trajectory of a particle in the falling layer is a 2-D motion. One part of path

vector is parallel to the cylinder axis (axial component  $dz$ ) and another perpendicular to axis (transverse component). This results in the effective particle path (red line).

- (5) The dynamic angle of repose  $\Theta$  of particle material is constant.
- (6) The value of bulk density is constant in any position.

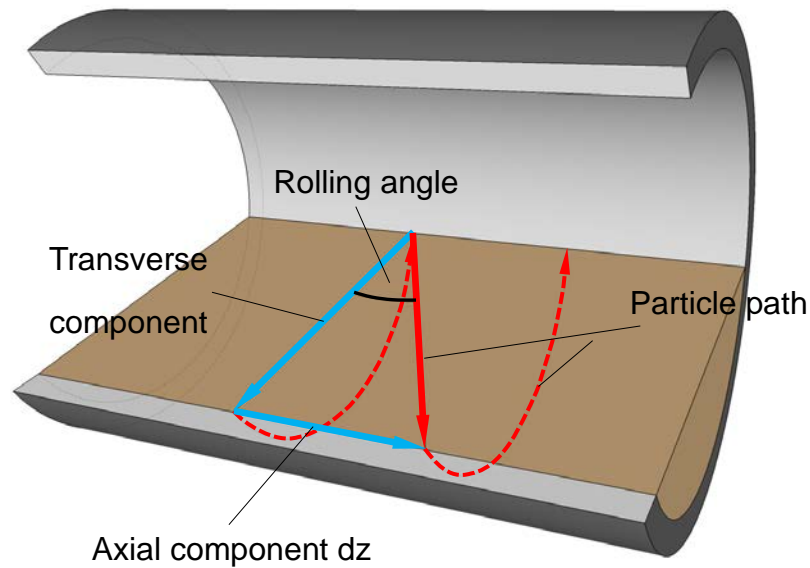


**Figure 2.1** Schematic graph of particle motion in granular bed

### 2.1.2 Transient behavior

If the operational conditions are varied, for example filling an empty kiln or changing rotational speed, inclination angle and feed mass flow rate during the production, the axial bed depth profile as well as the mass flow behavior are changed by time until getting steady state under the new process conditions. It is named as transient behavior and shown as basic description in Figure 2.2, which is the typical process from empty to steady state. In this case, the feed mass flow rate  $\dot{M}_{S,in}$  is constant, the particle bed profiles are represented as  $H$  and the time step is as  $t_i$ . In Figure 2.2, the bulk materials are transported from left to right and after some time come out from outlet which named as discharge flow  $\dot{M}_{S,out}$ . Within the period, the particle bed depth increases with increasing time and finally reaches steady state. After reaching steady state, the feed

mass flow rate equals to discharge mass flow rate and the particle bed depth profile will not be changed with time anymore.

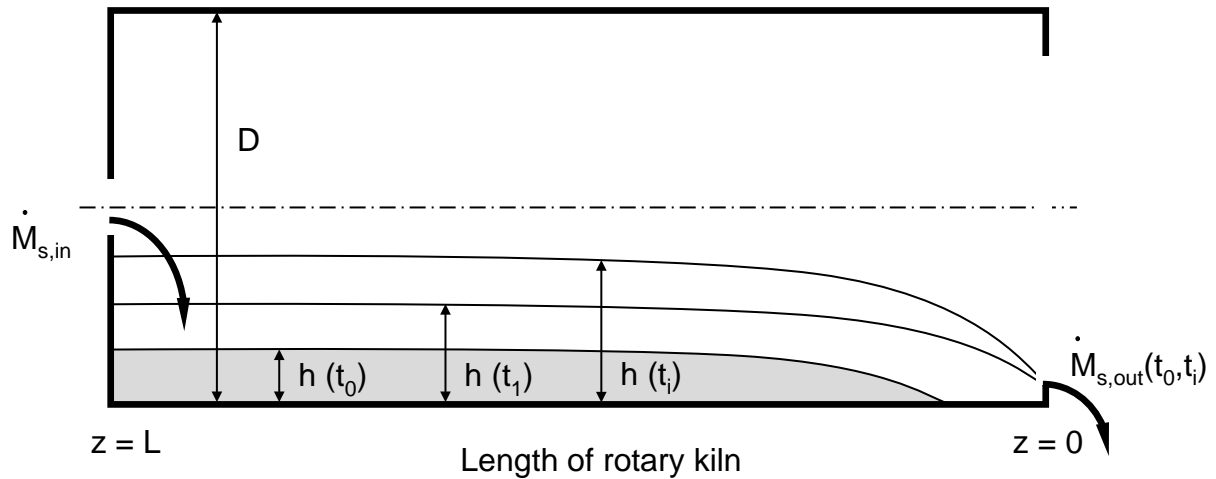


**Figure 2.2** Basic description of transient behavior within rotary kiln

Perron and Bui (1990) presented a semi-empirical model for the steady state flow within a drum with two fitted parameters. Based on it, a non-linear model by Perron and Bui (1992 and 1994) formulated as a multi-step algorithm to predict the outlet flow rate with step changed variables like feed mass flow rate, axial inclinations, rotational speed and discharge dam height.

Sai et al. (1992) reported experimental results of the mass flow rate at the discharge following a step change of the feed rate, the kiln rotational speed and the kiln inclination angle. To validate the model from Perron and Bui (1994), Sriram and Sai (1999) made the experiments by varying step changes not only in feed rate, but also in combining two or more operational variables simultaneously, such as the feed flow rate and rotational speed together, or inclination angle and rotational speed.

Spurling et al. (2000, 2001) did improvements of Saeman's model to describe the transient transport process and validated it with some small-scale experiments which

was a Perspex cylinder of length 1 m and internal radius 51.5 mm. The mechanism of particle transport of the transient process is the same as that in steady state conditions. The basic assumption is defined that the time scale of dynamic effect is large enough compared to the time of particle motion in the active layer. That means each short axial element of particle motion can be treated as in quasi-steady state condition.

In overall, after the study of Spurling, a relative trustable model of transient behavior was developed. However, there are still some parts that should be improved. At first, all the validated experiments from Spurling are in small scale. The size of kiln is in the range from 100 mm to 200 m diameter and 1 m to 2 m length. Moreover, the test materials are all below the diameter of 0.5 mm which are quite small and not contain big particle sizes conditions. Secondly, for the experiment, the bed depth was measured by the start-stop method. Although there were no differences between real values and measured values theoretically, starting and stopping the kiln will cause some errors by operators and the kiln itself which could not be eliminated and neglected especially in large kilns. Therefore, this time, a large-scale rotary kiln is used to validate the model from Spurling (2000 and 2001) and to study the influence of size scale. Meanwhile, a video analysis method will be described in chapter 2.3 to measure the particle bed depth profiles continuously.

## **2.2 Modeling of axial solid transport**

### **2.2.1 Mathematical model of steady state**

The structure of the particle bed with important geometrical parameters is shown in Figure 2.3. To make the model easily understood, the longitudinal section view and cross section view are shown in Figure 2.4 and 2.5.

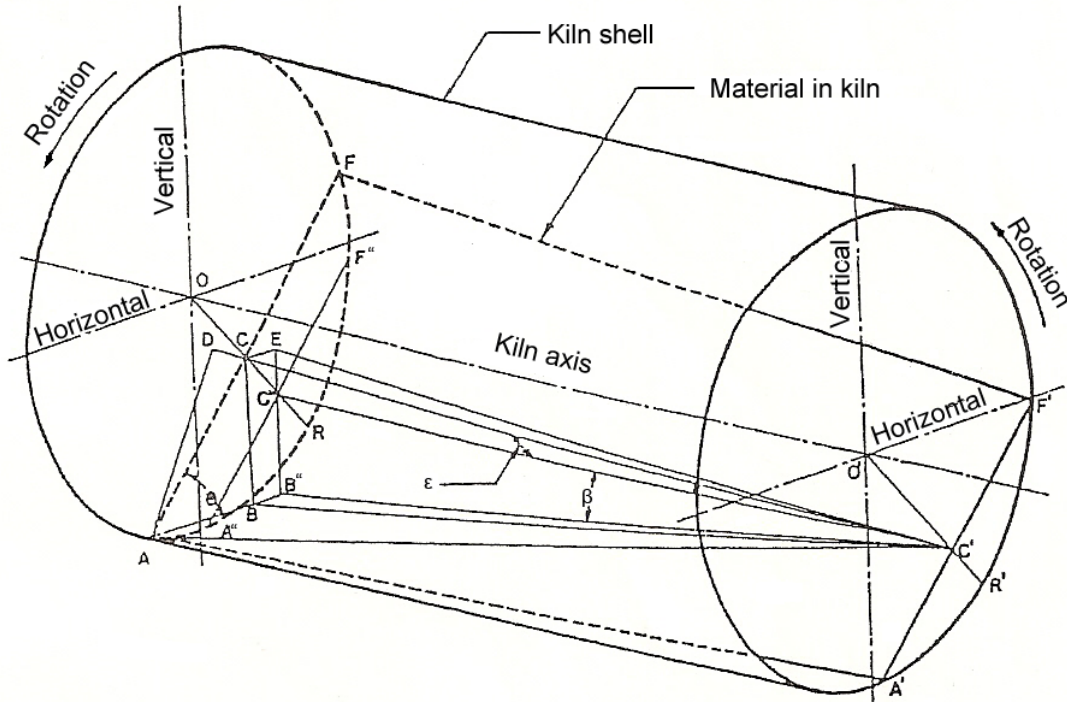


**Figure 2.3** Projection of a rotary kiln section showing geometry for derivation of axial transport followed by particles [Saeman (1951)]

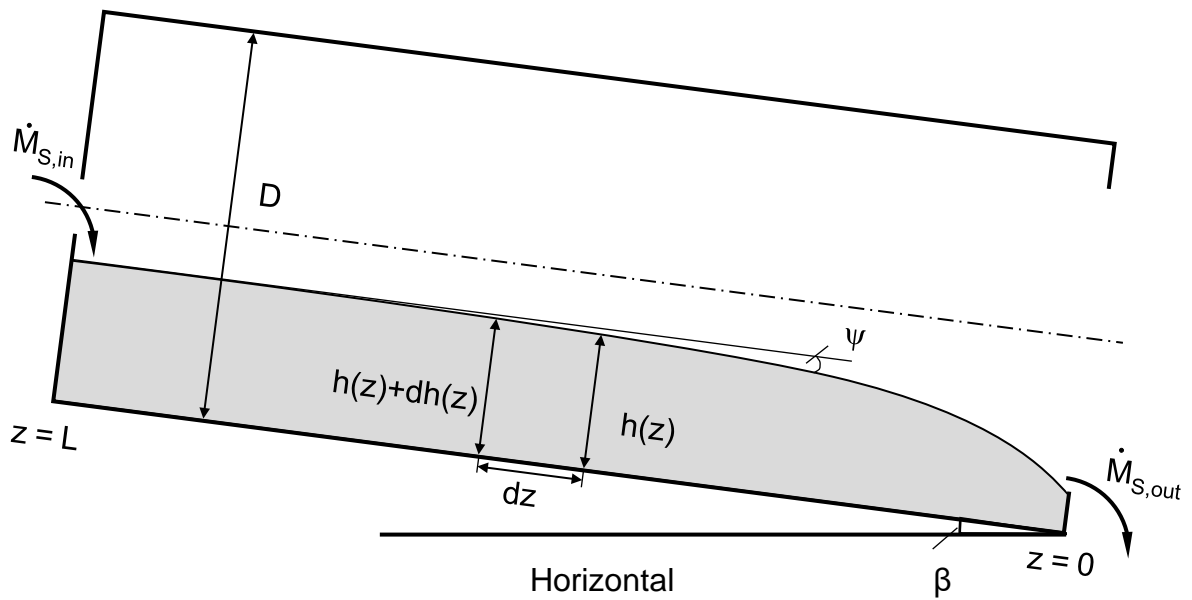


**Figure 2.4** Longitudinal section of the transport of granular solid through a rotated kiln

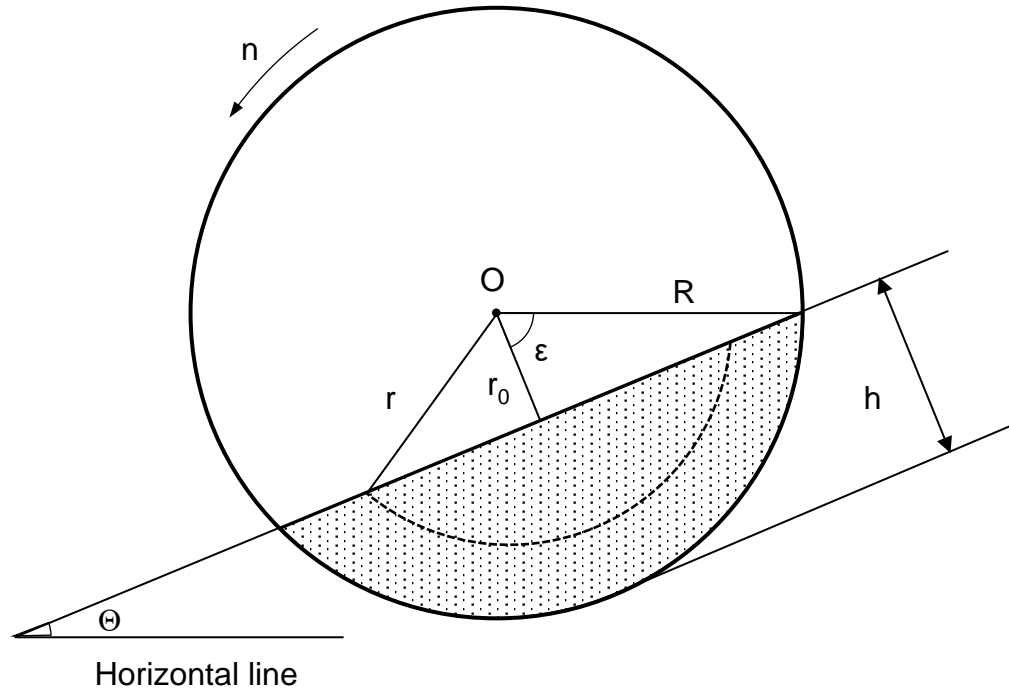


**Figure 2.5** Cross section of the transport of granular solid through a rotated kiln

The model begins from the geometric analysis of factors which is applied to develop transport velocity equation. The half of the axial transport distance of the particle per time is represented by

$$DC = \frac{AC^2}{CC'}, \quad (2.1)$$

$$CC' = CB \frac{\sin CBC'}{\sin CC'B} \text{ with } CB = AC \sin \theta, \quad (2.2)$$

where  $\Theta$  is the dynamic angle of repose and approximately equal to the angle  $CAB''$ . Also, angle  $CBC'$  is nearly  $90^\circ$ . So that  $\sin CBC' = 1$ . Since angle  $CC'B$  is the same order of magnitude as kiln slope and angle  $BC'B''$  is generally as small as angle  $CC'B$ . Thus,  $\sin CC'B = BC'B''$  and equation 2.2 can be written as

$$CC' = AC \frac{\sin \theta}{\text{angle } BC'B''}. \quad (2.3)$$



In Figure 2.2,  $CC''E = \Theta$ , thus,

$$\cos \theta = \cos CC''E = \frac{\tan EC'C''}{\tan CC'C''}. \quad (2.4)$$

Since angles  $EC'C''$  and  $CC'C''$  are quite small,  $\tan EC'C'' = EC'C''$  and  $\tan CC'C'' = CC'C''$ . At the same time, the angle  $CC'C''$  is the angle between surface of material and kiln axis which is named as  $\psi$ . Thus, equation 2.4 leads to

$$\text{angle } EC'C'' = \psi \cos \theta. \quad (2.5)$$

Because of  $EC'B'' = EC'C'' + C''C'B''$ , angle  $C''C'B''$  equals to the slope of kiln  $\beta$ , the equation 2.3 could be written as

$$CC' = \frac{AC \sin \theta}{\beta + \psi \cos \theta}. \quad (2.6)$$

Therefore, equation 2.1 could be derived into

$$DC = \frac{AC(\beta + \psi \cos \theta)}{\sin \theta}. \quad (2.7)$$

As we defined,  $z_0$  is the axial transport distance of particle per cascade ( $z_0 = 2DC$ ) and  $c$  the length of chord at surface of bed ( $c = 2AC$ ), equation (2.7) can be simplified as

$$z_0 = \frac{c(\beta + \psi \cos \theta)}{\sin \theta}. \quad (2.8)$$

The one particle average transport velocity for a specific path in the kiln is equal to the distance of single cascade and the number of cascades per unit time which is equal to the circulation speed per unit time and the number of cascades per circulation. The

number of cascades per circulation expressed as

$$N = \frac{\pi}{\arcsin \frac{c}{2r}}, \quad (2.9)$$

where

N = number of cascades per circulation

r = radius of particle path in bed

Thus, the average transport velocity is derived as:

$$u = nc \left( \frac{\beta + \psi \cos \theta}{\sin \theta} \right) \left( \frac{\pi}{\arcsin \frac{c}{2r}} \right), \quad (2.10)$$

where u is the average axial transport velocity of a single particle and n is rotational speed of kiln.

For a lightly loaded kiln

$$\arcsin \frac{c}{2r} = \frac{c}{2r}, \quad (2.11)$$

equation 2.9 will be simplified as

$$u = 2\pi rn \left( \frac{\beta + \psi \cos \theta}{\sin \theta} \right). \quad (2.12)$$

In generally, the feed mass flow rate is set as a given parameter. So, the velocity should connect the mass flow rate or volumetric rate. The increment of area from transverse view in Figure 2.3 is written as

$$dA = 2r \arcsin \frac{c}{2r} dr . \quad (2.13)$$

Multiplying equation 2.12 by equation 2.13 gives

$$dv = udA = 2\pi nr c \left( \frac{\beta + \varepsilon \cos \theta}{\sin \theta} \right) dr . \quad (2.14)$$

The length of the chord  $c$ , can be expressed as:

$$c = 2\sqrt{(r^2 - r_0^2)}, \quad (2.15)$$

where  $r_0$  is the vertical distance between the kiln axis and the free surface of particle bed and  $r_0 = R - h$ . The bed depth  $h$  is defined in Figure 2.4 as the radial distance between the inner wall of the kiln and the free surface of the granular bed.

Substituting equation 2.15 into 2.14 leads to

$$dv = 2\pi nr \left( \frac{\beta + \psi \cos \theta}{\sin \theta} \right) \left( \sqrt{(r^2 - r_0^2)} \right) dr . \quad (2.16)$$

The average volumetric transport rate  $\dot{V}$ , can be derived by directly integration of equation (2.16) from  $r = r_0$  to  $r = R$ , as

$$\dot{V} = \frac{4\pi n}{3} \left( \frac{\beta + \psi \cos \theta}{\sin \theta} \right) (R^2 - r_0^2)^{3/2} . \quad (2.17)$$

Substitution of  $dr_0/dz = \psi$  in equation (2.17) gives

$$\frac{dr_0}{dz} = \frac{3\dot{V} \tan \theta}{4\pi n (R^2 - r_0^2)^{3/2}} - \frac{\beta}{\cos \theta} , \quad (2.18)$$

which is the typical Seaman equation and the bed depth could be derived as

$$h = R - r_0. \quad (2.19)$$

Meanwhile, the mean residence time (MRT) is also an important parameter which indicate the transport time of the granular bed from inlet to outlet

$$MRT = \frac{\rho_s \cdot A \cdot \int_0^L F dz}{\dot{M}_s}, \quad (2.20)$$

where  $\rho_s$  is the bulk bed density of solid bed,  $\dot{M}_s$  is the feed mass flow rate, A is the inner cross-section area of the kiln which has strong correlation with half filling angle  $\varepsilon$  as

$$\varepsilon = \arccos\left(1 - \frac{h}{R}\right), \quad (2.21)$$

$$A = R^2(\varepsilon - \sin \varepsilon \cos \varepsilon). \quad (2.22)$$

And F is the filling degree of solid bed as

$$F = \frac{\varepsilon - \sin \varepsilon \cos \varepsilon}{\pi}. \quad (2.23)$$

### 2.2.2 Mathematical model of transient behavior

By extension of the steady state model to transient behavior, the mechanism of time dependent granular flow is the same. Each element can be treated as quasi-steady state within a short axial element of the bed. The steady state equation (2.17) is the starting point and could be rewritten as

$$\frac{dr_0}{dz} = C_A \dot{V} (R^2 - r_0^2)^{-3/2} - C_B, \quad (2.24)$$

where the coefficients  $C_A$  and  $C_B$  are

$$C_A = \frac{3 \tan \theta}{4\pi n}, \quad (2.25)$$

$$C_B = \frac{\tan \beta}{\cos \theta}. \quad (2.26)$$

In time dependent flow, the filling angle  $\varepsilon$  and the local volumetric flow rate  $\dot{V}$  are two dependent variables. And from the geometrical relationship in cross section view (Figure 2.4) the bed depth  $h$  can be expressed as

$$h = R(1 - \cos \varepsilon). \quad (2.27)$$

The equation (2.18) could be represented by  $\varepsilon$ ,  $z$ ,  $t$  and  $\dot{V}$  as a first order partial differential equation (PDE)

$$\left(\frac{\partial \varepsilon}{\partial z}\right)_t = \frac{C_A \dot{V}}{R^4 \sin^4 \varepsilon} - \frac{C_B}{R \sin \varepsilon}, \quad (2.28)$$

where  $z$  is the distance from the kiln discharge end.

A volume balance on solid bed is used to define the relationship between the variables and the whole system. From Figure 2.3, the differential axial control volume is defined from  $z$  to  $z + \delta z$  along the axis. Thus, a volume balance in transient duration is given by the assumption of  $V$  being a continuous function of  $z$  as

$$\left(\frac{\partial(\delta\dot{V})}{\partial t}\right) = \dot{V}_{z+\delta z} - \dot{V}_z = \left(\dot{V} + \left(\frac{\partial\dot{V}}{\partial z}\right)_t \delta z + O(\delta z^2)\right) - \dot{V}, \quad (2.29)$$

where  $\delta V$  is the volume of particle solid inside of the control volume,  $V_{z+\delta z}$  and  $V_z$  are the volumetric flow rate in and out of the control volume respectively. The bed cross section area  $A$  is a continuous function of  $x$ , the volume element  $\delta V$  can be expressed as

$$\delta\dot{V} = (A + O(\delta z))\delta z = A \delta z + O(\delta z^2), \quad (2.30)$$

and differentiates to time

$$\left(\frac{\partial(\delta\dot{V})}{\partial t}\right) = \left(\frac{\partial A}{\partial t}\right)_z \delta z + O(\delta z^2). \quad (2.31)$$

Due to the assumption, the  $\delta z \ll L$ , means  $O(\delta z^2) \rightarrow 0$ . A relationship is obtained between  $A$  and  $\dot{V}$  by combining (2.26) and (2.28)

$$\left(\frac{\partial A}{\partial t}\right)_z = \left(\frac{\partial\dot{V}}{\partial z}\right)_t. \quad (2.32)$$

With equation (2.22), partial derivative of  $A$  can be transferred to

$$\left(\frac{\partial A}{\partial t}\right)_z = 2R^2 \sin^2 \varepsilon \left(\frac{\partial \varepsilon}{\partial t}\right)_z, \quad (2.33)$$

and also, to  $\dot{V}$  as second first order PDE

$$\left(\frac{\partial \dot{V}}{\partial z}\right)_t = 2R^2 \sin^2 \varepsilon \left(\frac{\partial \varepsilon}{\partial t}\right)_z. \quad (2.34)$$

To eliminate the volumetric flow rate  $\dot{V}$  in (2.28), the non-linear second order PDE is created by differentiating with respect to  $z$  and combining (2.30) which obtains

$$2R^2 \sin^2 \varepsilon \left(\frac{\partial \varepsilon}{\partial t}\right)_z = \frac{\partial}{\partial z} \left\{ \frac{R^3 \sin^3 \varepsilon}{C_A} \left\{ R \sin \varepsilon \left(\frac{\partial \varepsilon}{\partial z}\right)_t + C_B \right\} \right\}_t, \quad (2.35)$$

where the  $C_A$  and  $C_B$  are defined as constant previously. Following the one-dimensional unsteady heat diffusion equation to simplify (2.35) provides

$$\rho c_\varepsilon \frac{\partial \varepsilon}{\partial t} = \frac{\partial}{\partial x} \left\{ k_\varepsilon \frac{\partial \varepsilon}{\partial z} \right\} + S_\varepsilon, \quad (2.36)$$

$$\rho c_\varepsilon = 2R^2 \sin^2 \varepsilon, \quad (2.37)$$

$$k_\varepsilon = \frac{R^4 \sin^4 \varepsilon}{C_A}, \quad (2.38)$$

$$S_\varepsilon = \frac{3C_B R^3}{C_A} \cos \varepsilon \sin^2 \varepsilon \left(\frac{\partial \varepsilon}{\partial z}\right)_t. \quad (2.39)$$

The characteristics of result are parallel to the  $z$  axis, which is  $t = \text{constant}$ , and therefore equation (2.35) is correct.

The PDE (2.35) is second order with respect to  $z$ . Thus, two boundary conditions of  $\varepsilon$  and an initial condition are required to solve this PDE:

- (i) At the  $z = 0$  position, where the kiln discharge end is the same boundary condition as steady state could be used and with the geometric relationship as

$$\varepsilon[0, t] = \arccos \left( 1 - \frac{h_{dam} + d_p}{R} \right). \quad (2.40)$$

- (ii) At the  $z = L$  position, where the kiln feed end is the volumetric feed rate  $\dot{V}_L$  is given as

$$\dot{V}_L[L, t] = \dot{V}_L[t] \text{ where } t \geq 0. \quad (2.41)$$

Substituting  $\dot{V} = \dot{V}_L$  in (2.28), a new boundary condition is set to be

$$\left(\frac{\partial \varepsilon}{\partial z}\right)_{t, z=L} = \frac{C_A \dot{V}_L[t]}{R^4 \sin^4 \varepsilon_L} - \frac{C_B}{R \sin \varepsilon_L}, \quad (2.42)$$

where,  $\varepsilon_L$  is the value of  $\varepsilon$  estimated at the kiln outlet.

- (iii) The initial condition is provided as

$$\varepsilon[x, t = 0] = \varepsilon_i[z] \text{ where } 0 < z < L. \quad (2.43)$$

For the transient behavior from one steady state to another steady state because of the change of mass flow rate or rotation speed, the axial profile  $\varepsilon_i[z]$  is given by solution of the initial steady state.

It should also be mentioned that a suitable condition indicating reaching steady state should be determined within the numerical solving process. Based on the definition of steady state, the bed depth profile is constant, and the discharge mass flow rate equals to feed mass flow rate. In this case, the discharge mass flow within transient process is derived as

$$\dot{M}_{S,out}(t_i) = \frac{M_{S,out}(t_i) - M_{S,out}(t_{i-1})}{\Delta t}, \quad (2.44)$$

where  $M_{S,out}$  is total weight of discharge particles which could be obtained as



$$M_{S,out}(t_i) = \dot{M}_{S,in} \cdot t_i - M_{hold\ up} . \quad (2.45)$$

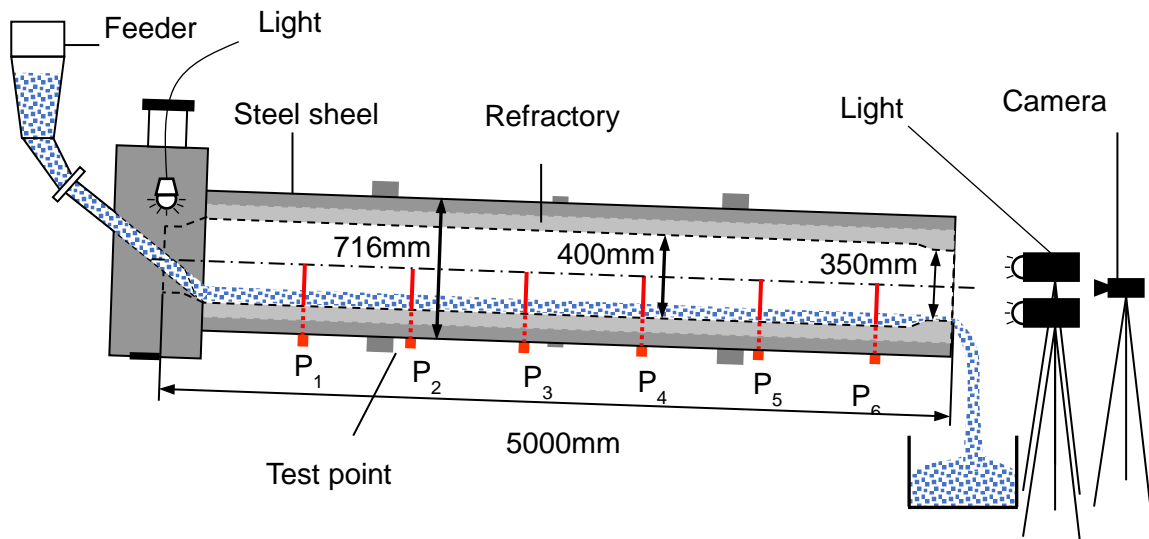
In transient process,  $M_{hold\ up}$  is the weight of the granular particle bed inside of the rotary kiln which is similar as steady state condition

$$M_{hold\ up} = \rho_S \cdot A_R \cdot \int_0^L F(t_i) dz . \quad (2.46)$$

## 2.3 Experimental analysis of axial solid transport

### 2.3.1 Experimental apparatus and materials




Figure 2.6 depicts the schematic diagram of the rotary kiln used in the experiments. The kiln consisted of a steel cylinder with 5 m length and 716 mm diameter, where the inner wall is made of refractory material resulting in an inner diameter of 400 mm. At both ends, there are conical changes in diameter up to 350 mm. The kiln can be operated at rotational speeds from 0.2 to 10 rpm and inclination angles from 0° to 5°. At the upper end of the kiln (material inlet), a differential mass balance feeder (K-TRON, type K2-ML-D5-S60) is installed to operate feeding rates up to 1 t/h. At the lower end of the kiln (material outlet), a natural gas burner is usually installed for the thermal treatment of the material. To realize the visibility of the bulk bed in the present study, the burner was removed and instead of that high intensity lights (Dedolight Dedocool, Max 500W) were installed. A 4K camera is positioned in the discharge end which is Panasonic DMC-G7 with objective H-PS45175 (45-175 mm, F4.0-5.6 ASPH) to record all the videos in 4K resolution. To analyze the change of bed height, at the refractory lining metal tubes with a radial length of 200 mm were installed at axial distances of 0.6 m (P1) 1.4 m (P2), 2.2 m (P3), 3.0 m (P4), 3.8 m (P5) and 4.6 m (P6) from the feeder.



**Figure 2.6** Schematic diagram of experimental apparatus

As test materials, quartz sand, glass beads and cement clinker are used which listed in Table 2.1. They can be approximately treated as spherical particles and as monodisperse systems.

**Table 2.1** Physical properties of test materials

	Quartz sand	Glass beads	Clinker
			
Particle diameter $d_p$ in mm	0.2	0.7 2.0 4.0	4.5
Bulk density $\rho_b$ in $\text{kg/m}^3$	1570	1560	1410
Dynamic angle of repose $\Theta$ in $^\circ$	32	32	31

### 2.3.2 Experimental details and measuring method

The operational conditions of test experiments are shown in Table 2.2.

**Table 2.2** Operational test conditions

Kiln inner diameter in m	0.4
Kiln length in m	5
Temperature in °C	20
Rotational speed $n$ in rpm	0.6; 1; 2; 3; 4
Feed mass flow rate $\dot{M}_S$ in kg/h	100; 300; 500
Inclination $\beta$ in °	1; 2; 5

As we have introduced in chapter 2.1, a new way which called video analysis method is used in our experiments to take the particle bed depth profiles continuously without stopping the kiln. The whole process of particle motion was recorded by the camera mentioned before. And the experiments were done by following steps:

- (1) After setting the appropriate position of the camera and light, the kiln was started under fixed operation condition without feeding test material.
- (2) The camera was turned on and a video of more than 1 round of rotation was recorded for the empty kiln.
- (3) The test materials were then fed into the kiln.
- (4) The videos of particle bed should be recorded in the same time intervals, such as every 5min and be numbered as  $t_1, t_2, \dots, t_i$ . During taking videos, the discharged particles were also collected and weighted in equal intervals (e.g. 30s) to get the discharge mass flow rate.
- (5) Finally, when the discharge mass flow rate was equal to the feed rate, the granular bed reached steady state and the transient process was finished.

The bed depth profiles of different time steps were digitally measured from the recorded

videos. Images were extracted by using screenshot software when the angle between measuring rod and horizontal line is  $58^\circ$  (Figure 2.7a). This value is based on the particle dynamic angle of repose and equals to  $(90^\circ - \Theta)$ . Image processing software “Gimp” was utilized to analyze the images obtained before and the bed depth was calculated with

$$H_i = H_{mr} \left(1 - \frac{h_i}{h_0}\right), \quad (2.47)$$

where  $h_i$  is the digital height of the free measuring rod in the picture at any time (Figure 2-7b),  $h_0$  is the digital height of each measuring rod in the picture of empty kiln (Figure 2-7a),  $H_{mr}$  is real height of each measuring rod and with 200 mm.

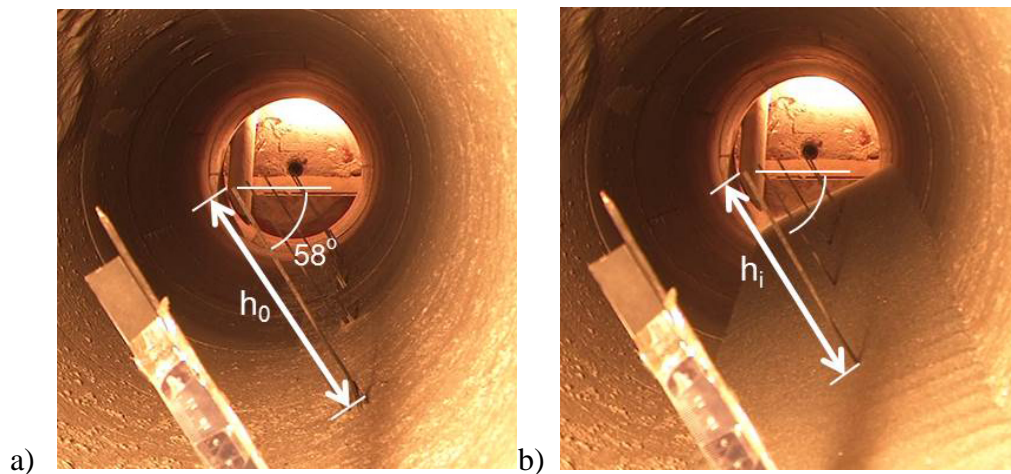


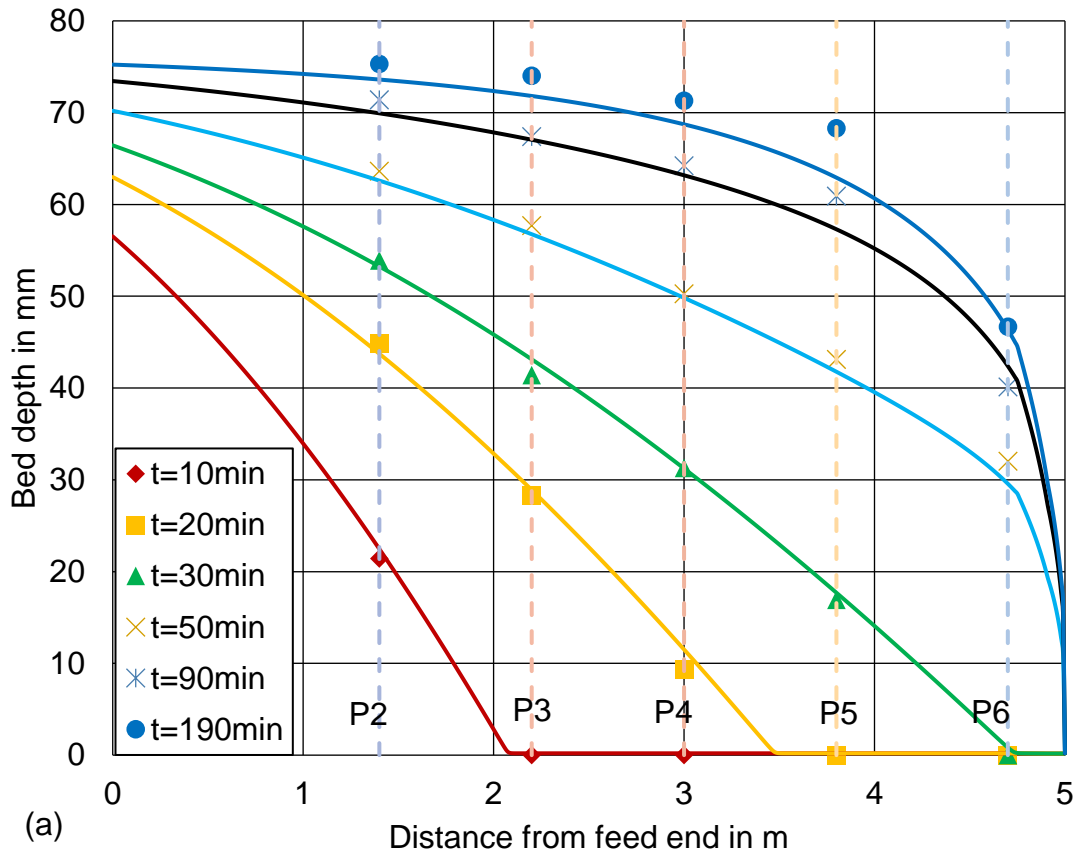
**Figure 2.7** Screenshot from experiment video in empty kiln and  $t=i$  condition

### 2.3.3 Data analysis method

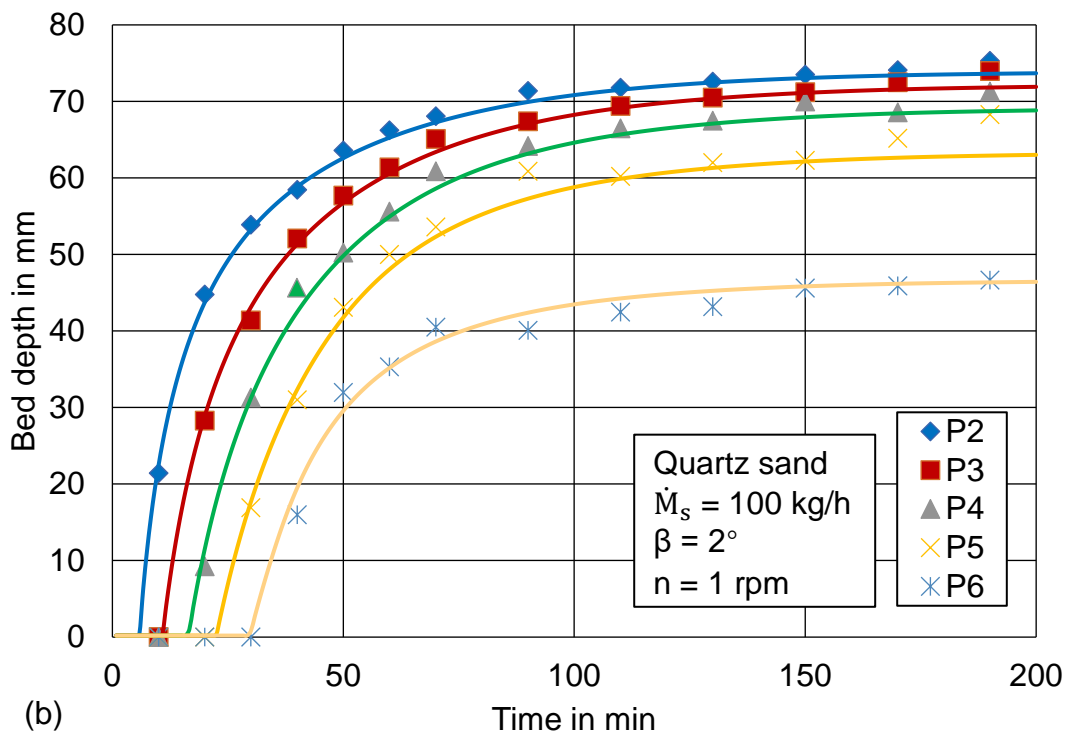
The analysis of experimental data is shown from Figure 2.8 to 2.10 for test materials of quartz sand. The representative graphs present the transient process under 100 kg/h feed mass flow rate,  $2^\circ$  inclination angle and 1 rpm rotational speed operational conditions. Solid lines are the simulation results based on equation 2.35 which could be solved with two boundary conditions (equation 2.40 and 2.42) and initial condition (equation 2.43). At the same time, the experimental values are shown as dots in the same figures. In

Figure 2.8, it is clear to see that within the first 10 min the bed depth has the highest increasing speed, but this speed will decrease with enlarged bed depth continuously. After reaching 100 min which is 50% of total time, the granular bed reaches 90% of steady state condition. In contrast, the bed depth will take another 100 min to finally reach steady state which is only 10% of total depth. By combining Figure 2.8 and 2.9, it shows that the discharge of particles appears when granular bed moves to the discharge end of kiln and owns the same changing pattern with bed depth which is very fast in the beginning and then decreasing continuously. It should be noticed that the discharge flow rate becomes 80% of feed flow rate at 50% of total time which is lower than the condition of bed depth (90%) at this time point. With the constant feed mass flow rate, it is clear to know that due to the characteristic of segment, the increment of bed depth and cross section area are not the same which means (i) in the range of second half time, the discharge rate will be changed by even a small increment of bed depth; (ii) the increasing rate of discharge flow is gentle and peace overall and much different from the rate of bed depth increasing.

Figure 2.10 shows the  $R^2$  value of bed depth between experiment and simulation. From the knowledge of statistic,  $R^2$  value equals to 0.995 means the possibility of simulation depth equaling to experiment depth is 99.5%. Therefore, Spurling model under this operation condition could be validated. After collecting all other data in different operational conditions, the  $R^2$  values are all around 0.99 (in appendix A) which means both data is accurate. That is to say, the continuous experimental method and dynamic model could be widely used in large scale kilns. It should be mentioned that for the test point P6, because of the influence of the conical dam in the outlet, there agreement between experimental and simulated results are not perfect as other 4 test points.



(a)



(b)

**Figure 2.8** Transient bed depth profiles with (a) different time steps, (b) with different test points

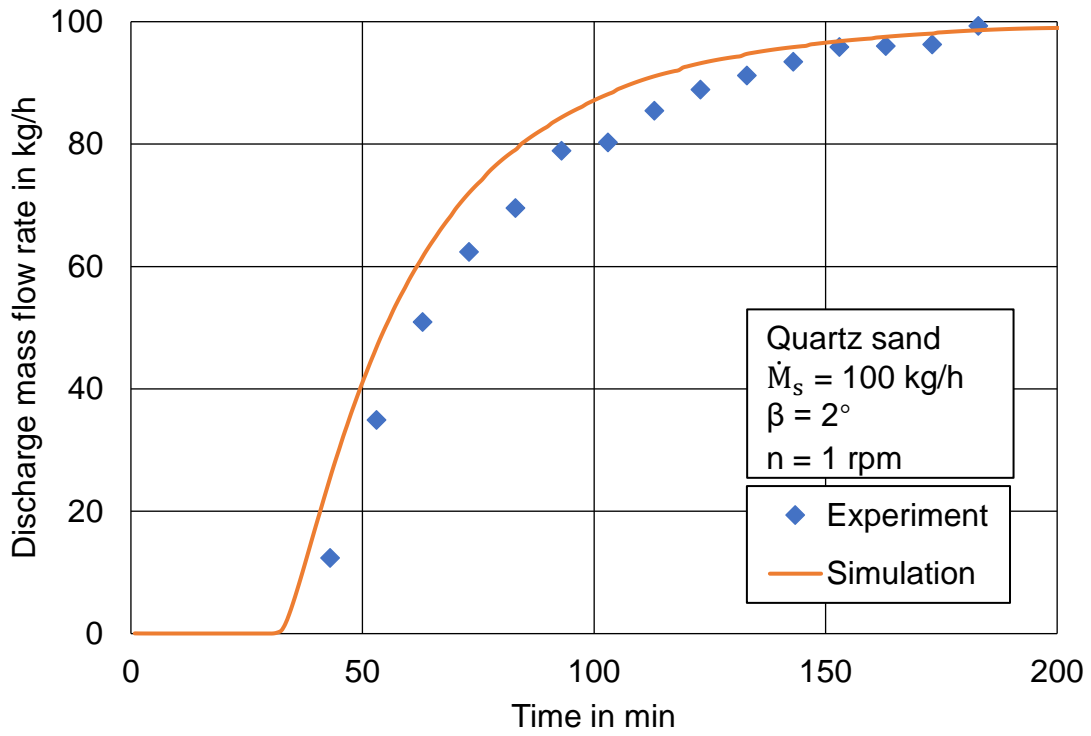


**Figure 2.9** Experimental and simulated discharge mass flow rate with time

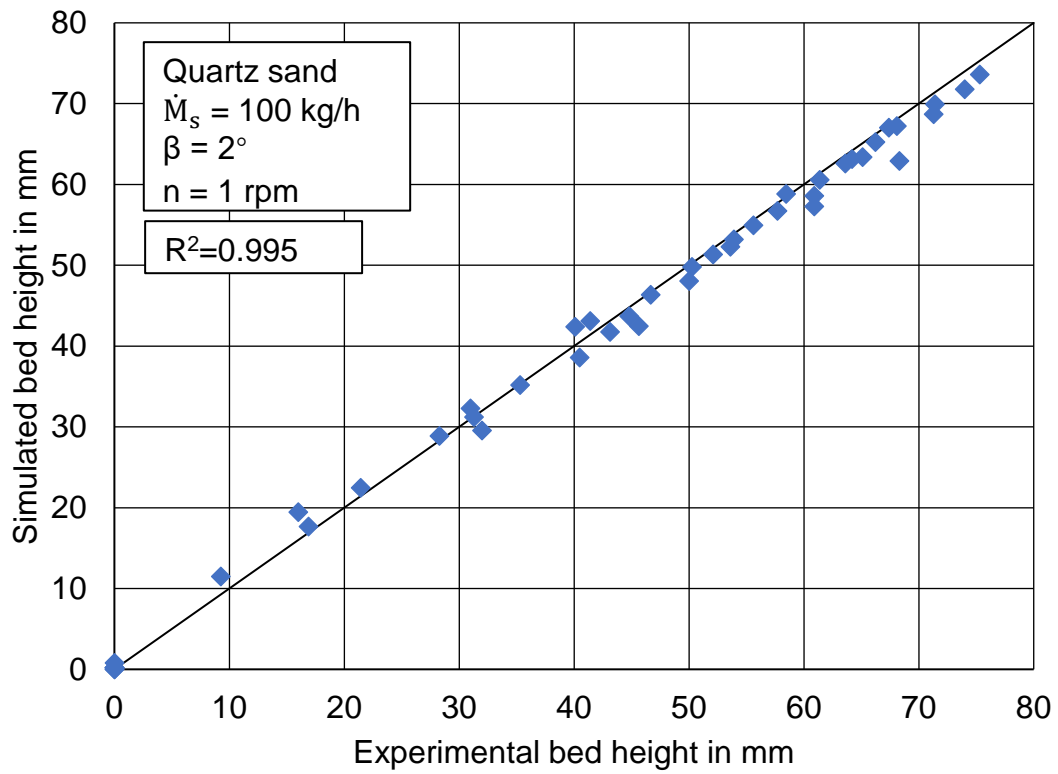


**Figure 2.10** The comparison between experimental and simulated results

## 2.4 Results and discussions

### 2.4.1 Stationary time

The stationary time is a time to describe how fast an empty kiln reaching steady state is and it is an essential parameter of the transient process. In chapter 2.1, the steady state is always determined from bed depth or discharge mass flow rate. So, there are two kinds of stationary time shown in the following figures which are measured from bed depth and discharge mass flow rate separately. Each operational condition has 6 stationary time which contains 5 bed depth points (P2 to P6) plus 1 discharge mass flow rate point named as “MS”. The values of time are all from experimental data which show good agreement with simulated results before.

The connections between stationary time and rotational speed, inclination angle or feed flow rate are shown from Figure 2.11 to Figure 2.13. Firstly, it is clear to see that with the raising of rotation speed or axis inclination angle, the stationary time decreases rapidly which is from about 300 min to 150 min. After that, the rate of descending becomes slower and slower and the minimum value is below 50 min. In contrast, increasing of feed mass flow rate only leads to a slightly increment of stationary time which shows less impact compared to rotational speed and inclination angle.

Secondly, the stationary time based on discharge mass flow rate are always larger than the time of bed depth and the difference between them will be reduced with decreasing stationary time which could be clear observed from Appendix A. By the analysis of Figure A.1, for one operational condition, the lower stationary time leads to larger time difference. That is to say, the position closed to the inlet where P2 and P3 located are always the first two reaching steady state. In contrast, P3 and P4 owns relatively large stationary time and lower time differences. It should be mentioned that, due to impact of conical dam in the end of the kiln, P5 could have relative higher stationary time compared to P3 and P4 and higher time difference especially under low rotational speed



or low inclination angle. In general, from Figure 2.11 to 2.13, the overall stationary time of bed depth are similar to the time of discharge mass flow rate. Therefore, in industrial field, the stationary time of discharge mass flow rate is considered as major stationary time which could be easily measured.

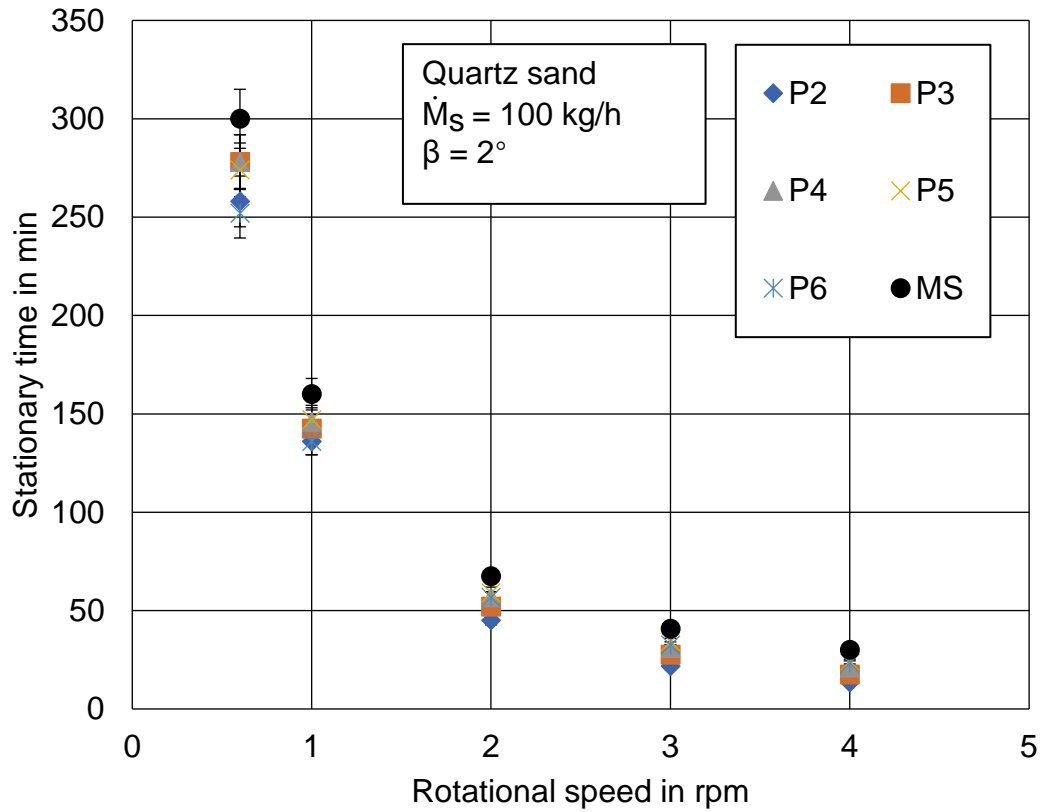


**Figure 2.11** Experimental stationary time dependence of rotational speed

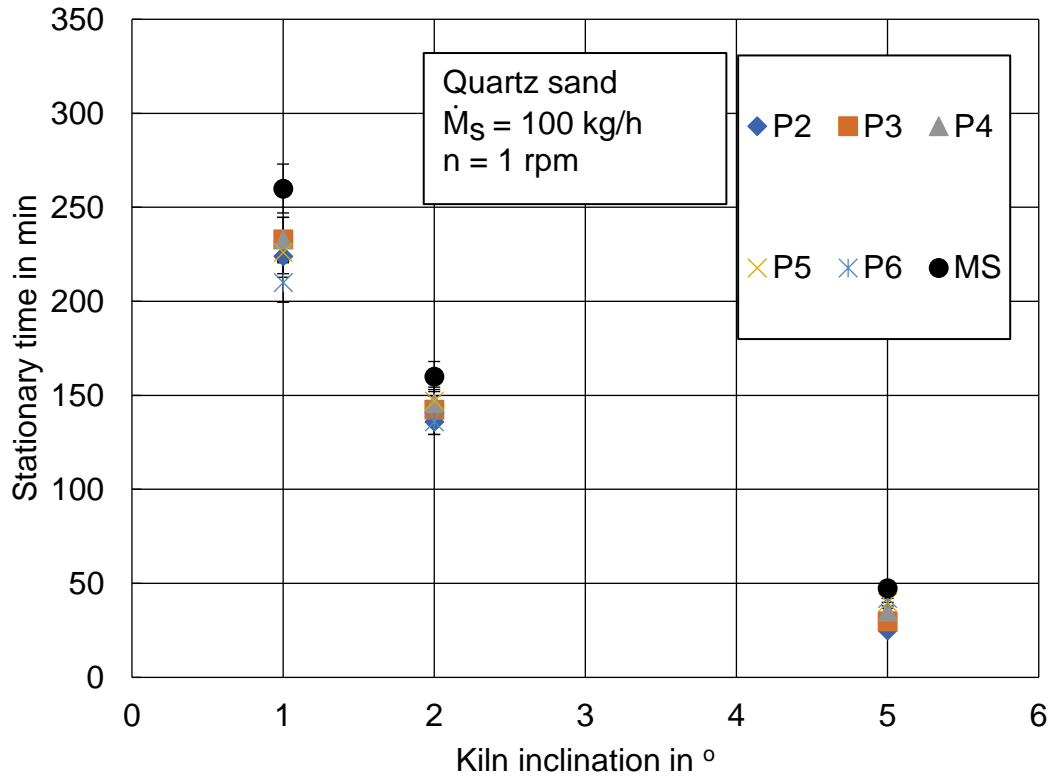


**Figure 2.12** Experimental stationary time dependence of inclination angle

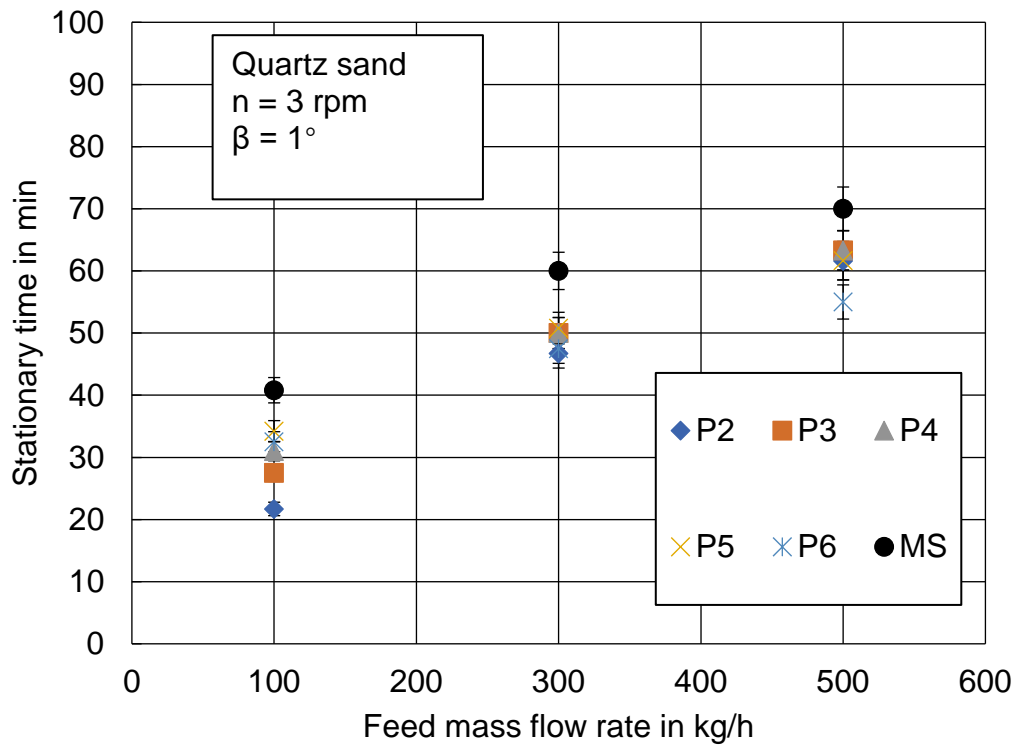


**Figure 13** Experimental stationary time dependence of feed mass flow rate

### 2.4.2 Influence of rotational speed

After the description of stationary time, the particle bed depth profiles of transient process should also be considered. The bed depth profiles with different rotation speed at fixed time proportion which is from 25% to 75% of total time are drawn in Figure 2.14. And the results in different test points are shown in Figure 2.15. In these two figures, the horizontal axis is the rotational speed and the vertical axis is the rate between real bed depth and steady state bed depth.

In Figure 2.14, the differences of rate in different positions are always enlarging with increasing cylinder rotational speed. In contrast, regardless of changing rotational speed, the rates near inlet positions are always larger than the rates near outlet. Moreover, in 25% of total time, the differences between each position are quite large. And in 75% of total time, these differences are extremely small and all over 0.9 which are nearly steady state conditions.

To observe Figure 2.14(a) in detail, in the beginning of transient behavior, the bed depth rates have high values and small differences in low rotational speed condition. This means in this case the particle bed depth is more closed to the steady state condition. However, these rates will have large difference with increasing rotational speed. That means, with high rotational speed condition, the axial position near inlet will have high bed depth but the position near outlet has extremely low bed depth, even zero.

There are two reasons to explain it. Firstly, with low rotation speed, it takes large quantities of time to reach steady state (in chapter 2.4.1). Hence the real time of 25% of the total time is much more than high-speed condition which leads to more particle material fed into the kiln. Secondly, the materials will be firstly accumulated near the inlet of kiln and the segment cross section determines that the particle bed depth will raise fast from an empty kiln. Therefore, these two reasons cause relatively high proportion and homogeneous bed depth profiles under low rotational speed conditions.

In contrast, with high rotation speed, little time leads to a small amount of materials be stored inside of kiln which leads to small particle bed depth and nonhomogeneous bed depth profile.

After 50% of total time, due to the constant feed mass flow rate, the rising of particle bed depth in P2 and P3 is quite slow where they have already been around 80% of the steady state. Furthermore, the segment cross section determines that with constant volume increment, the growth rate of bed depth is not uniform. For an empty kiln, in the beginning of transient process, the height of the bed depth is small but with extremely high increasing speed. In contrast, after 50% of stationary time, the whole bulk bed is over 80% of steady state with slow increasing speed. Therefore, after 50% of total time the particle bed will be quite close to steady state regardless of rotational speed. After 75% of total time, the granular beds are fully developed which come to above 90% of steady state and will have extraordinarily little increments until reaching steady state. By the way, the segment cross section not only leads to low bed depth increment in second half of total time, but also smaller stationary time of bed depth than of mass flow rate.

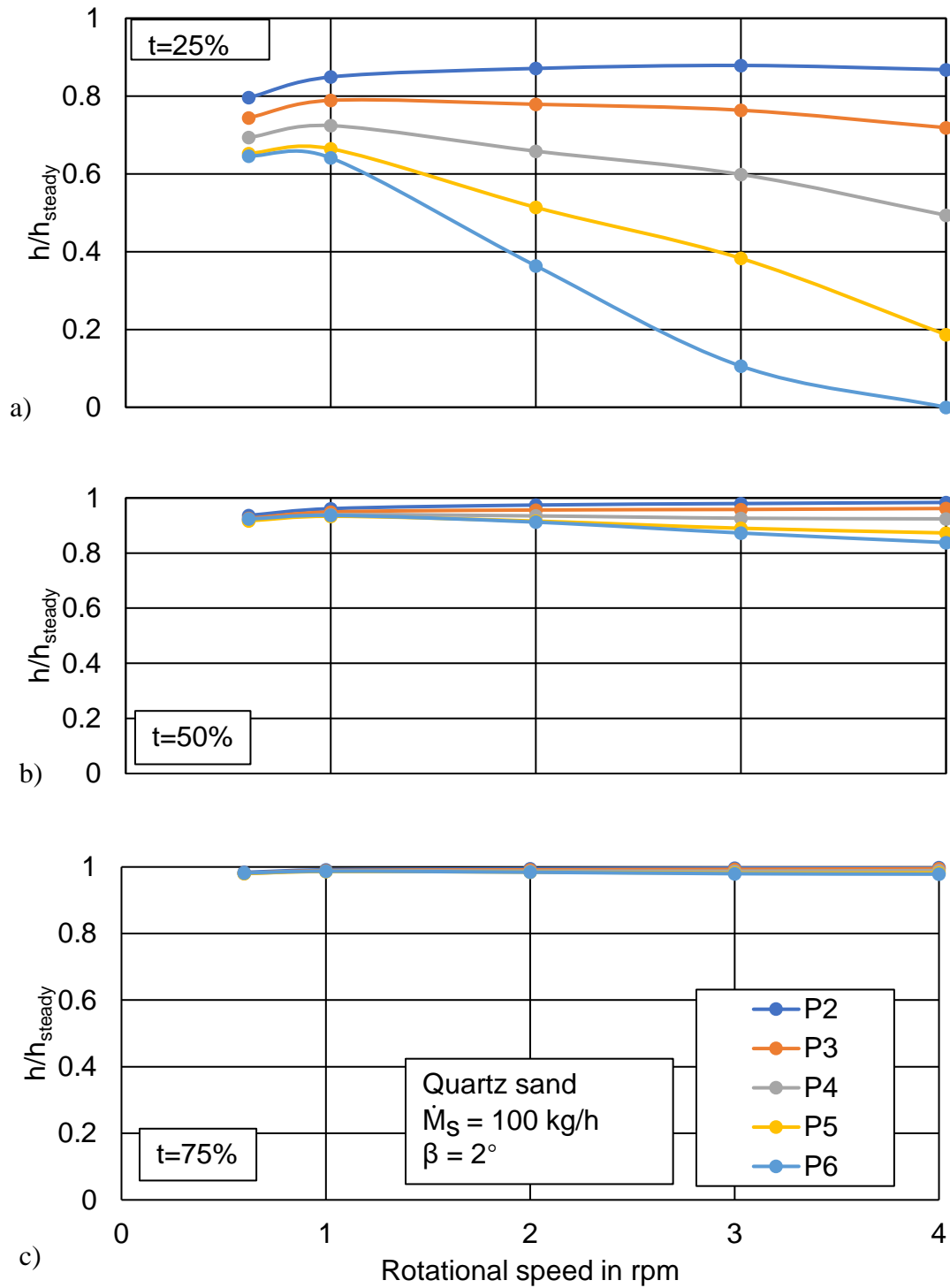


**Figure 2.14** The influence of rotational speed on the rate of particle bed depth in transient process with different time points (experimental results)

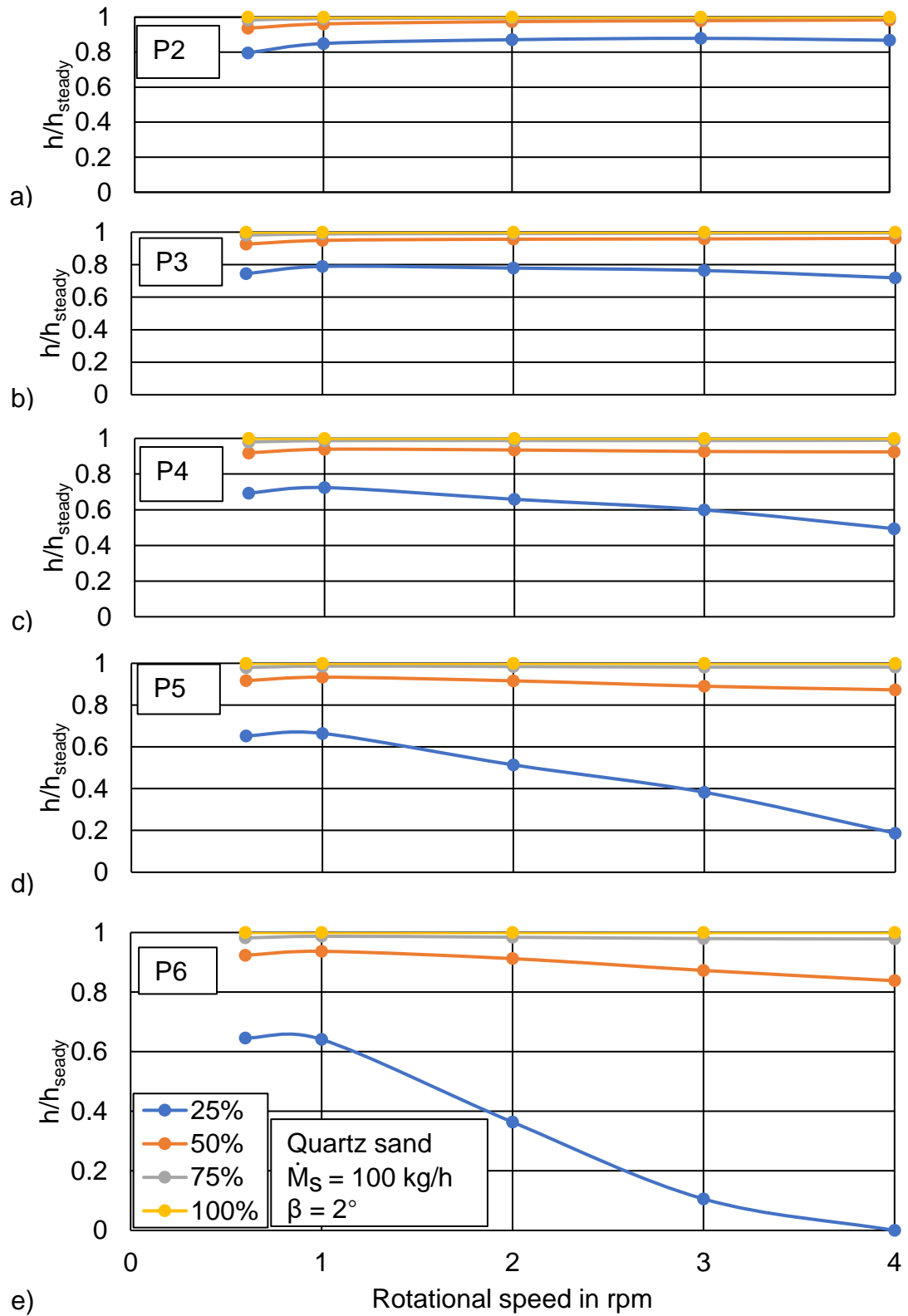


**Figure 2.15** The influence of rotational speed on the rate of particle bed depth in transient process with different test points (experimental results)

### **2.4.3 Influence of feed mass flow rate**

The influence of feed mass flow rate on granular bed transient behavior is shown in Figure 2.16 and 2.17. Because of fixed setting of axis inclination angle, rotational speed and other physical properties of the kiln, the particle motion performance inside of kiln will keep constant. Hence, for 25% of stationary time, with enlarged feed mass flow rate, the differences of bed depth rate between each test points will be reduced. That means the large feed mass flow rate leads to higher particle bed depth along the whole kiln and the bed depth also approaching steady state conditions. Conversely, low feed mass flow rate brings low bed depth and large difference of bed depth rate between each measuring point which is the also caused by the physical property of segment cross section. Combining the analysis about whole process from 25% to 100% of total time which shown in Figure 2.16 and 2.17 the overall tendency of granular bed transport is that, with large feed rate, the influence of the feed mass flow rate could be neglected. That is to say, the bed depth rate along the axis will firstly increase with enlarged feed mass flow rate but gradually approach a fixed value especially for the position far from the inlet of kiln. Therefore, changing of feed mass flow rate is not an effective method affecting the stationary time which could also be observed from Figure 2.13.

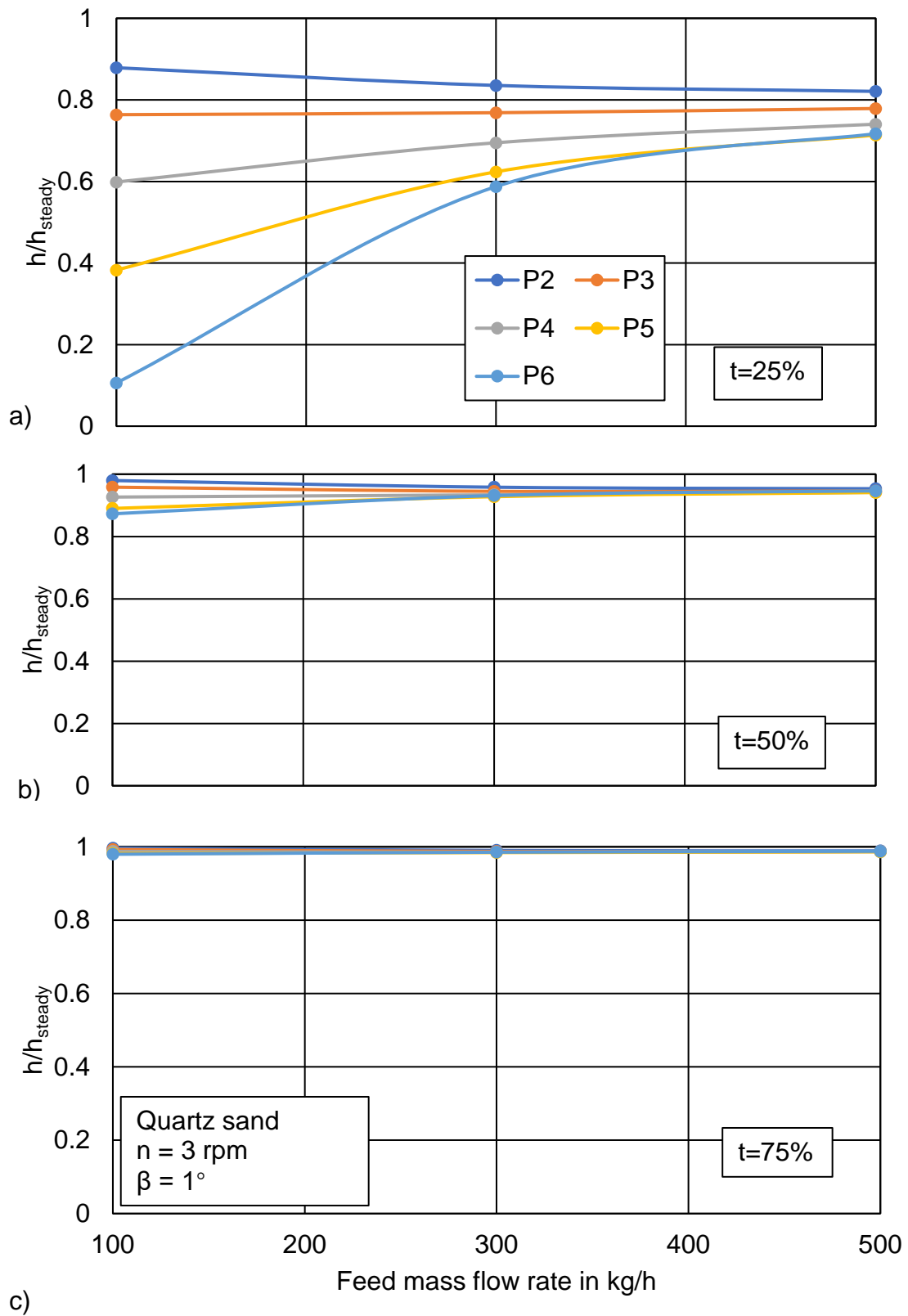


**Figure 2.16** The influence of feed mass flow rate on the rate of particle bed depth in transient process with different time points (experimental results)



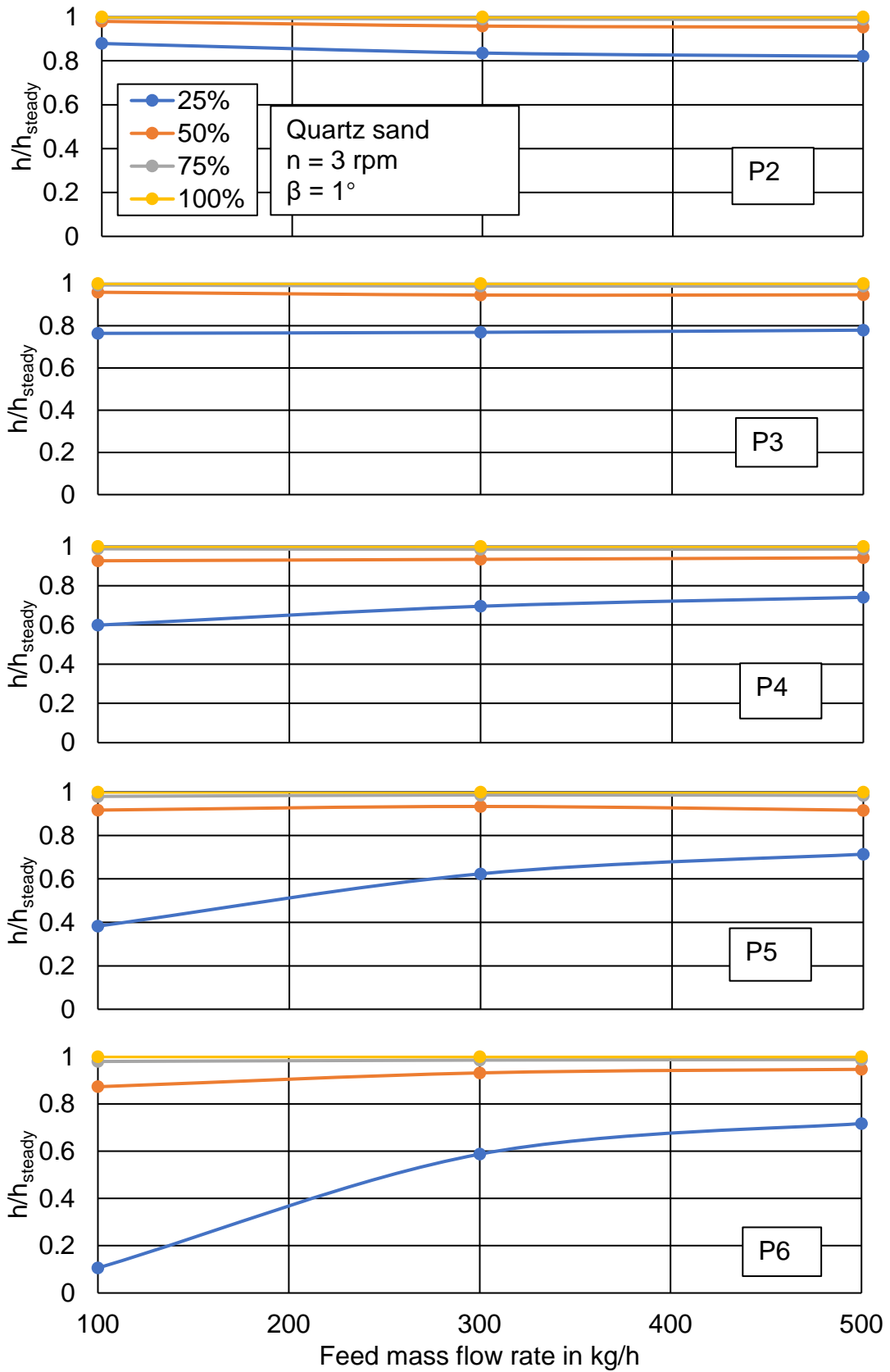


**Figure 2.17** The influence of feed mass flow rate on the rate of particle bed depth in transient process with different test points (experimental results)

#### 2.4.4 Influence of axial inclination

The relationships between axial inclination angle of rotary kiln and bed depth profile are also studied and shown in Figure 2.18 and 2.19 respectively. In Figure 2.18 it is clear to see that, in the beginning of transient process which is 25% of stationary time, the difference of particle bed rate between each test points will have significant increment with enlarged inclination angle. That means, the inclination angle has strong influence on the whole particle bed depth. However, the impact on each test points are not the same. for P3 to P6, the bed depth rate will always be reduced with increased inclination. By combining of Figure 2.19, it could be observed that the test points further from inlet is the higher decrement of bed depth rate will be. After that, with increasing of process time, especially after 50% of stationary time, the particle bed depth rate of each test points will become quite homogeneous which means the whole particle bed profile will close to steady state condition. Therefore, the influence of the inclination angle is not essential in the last 50% of stationary time which is quite similar with the impact of rotational speed.

In contrast, for test point P2 which is closed to the inlet, the rate of depth will have slightly increment with enlarged inclination angle. The rate of bed depth increases first which could reach the highest value around  $2^\circ$  angle and keeps constant with further increasing inclination angle. The reason of it seems to be that with increasing of inclination angle, the particle bed depth value decreases and could reach steady state faster. However, this influence will disappear if the inclination angle is large enough which is around  $2^\circ$  in our kiln. After 50% of total time, the rates of bed depth are all approximately the same around 96% of steady state which means the inclination angle will have little influence on the particle bed depth rate in the second half time region.

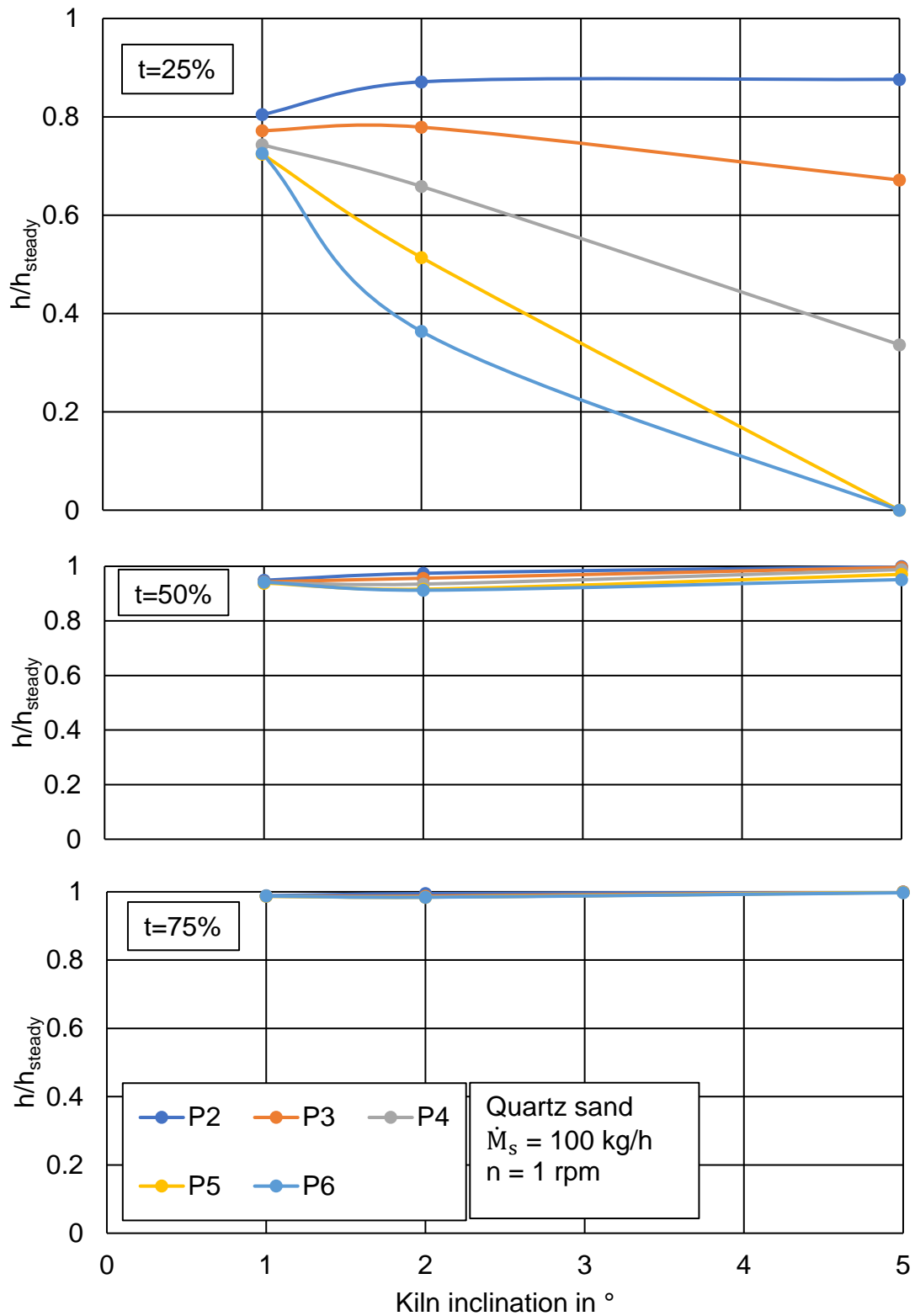


**Figure 2.18** The influence of inclination angle on the rate of particle bed depth in transient process with different time points (experimental results)

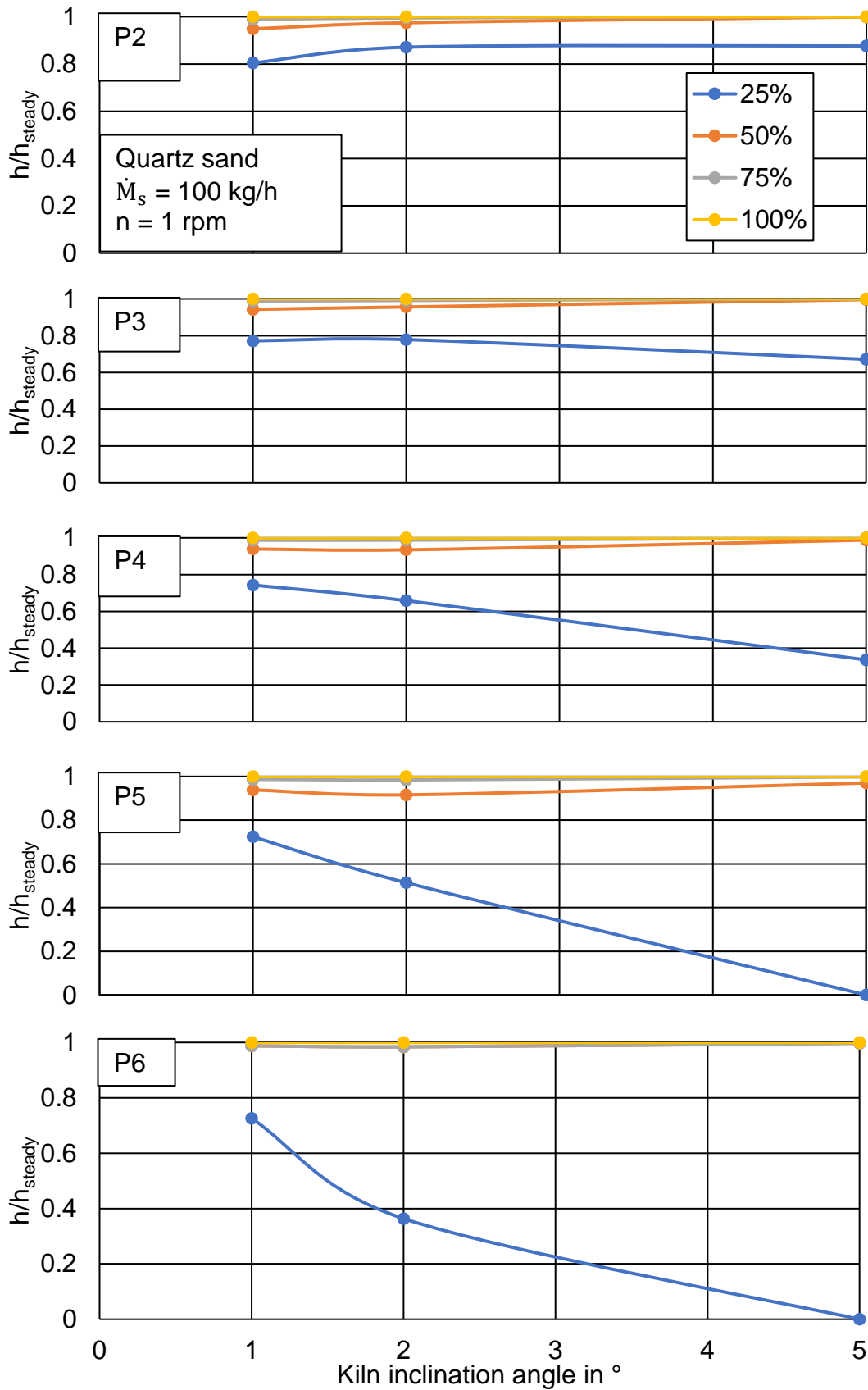


**Figure 2.19** The influence of inclination angle on the rate of particle bed depth in transient process with different test points (experimental results)

## 2.5 Conclusion

In this chapter, the model of transient transport in the rotary kiln was developed which was based on the mathematical model from Spurling (2000). The validation of the model was finished within a pilot-scale rotary kiln. A new measuring method was implemented to record the transient behavior and mass flow rate continuously. Quartz sand, glass beads and cement clinker were selected as test materials with monodisperse system. The rotational speed, inclination angle, feed mass flow rate and particle diameters are also considered as essential parameters to impact the transient process which obtain following results.

- 1) The new method called video analysis has been proved to have good performance getting accurate particle bed depth profiles continuously without stopping the kiln within operational process.
- 2) The mathematical model of transient process based on Spurling (2000) has been validated in large pilot scale kiln which shows good agreement with experimental results and could be implemented with different operational conditions.
- 3) For transient process, the dramatically increasing of particle bed depth is in the first half of stationary time. Generally, within this region, the particle bed depth in each test points will reach over 80% of steady state depth. In contrast, the rest 20% will be slightly arrived in the second half of stationary time.
- 4) The stationary time measured from bed depth is always smaller than from discharge mass flow rate and this difference will be reduced with increasing rotational speed or inclination angle. The stationary time from bed depth are also not the same along kiln axis. The positions close to the inlet have shorter stationary time and higher bed depth. Conversely, the position far from inlet has larger stationary time and lower bed depth.
- 5) The rotational speed or inclination angle has strong influence on stationary time. The enlarged rotational speed or inclination angle will all lead to significant reducing of stationary time especially when they are small values such as 1 or 2 rpm,

1 or 2 °. However, this impact will be smaller and smaller with increasing rotational speed and inclination angle which means after some critical operational conditions, the stationary time is not so large and will approach a fixed value.

- 6) In contrast, the feed mass flow rate has opposite pattern compared to rotational speed and inclination angle. The stationary time will slightly increase with enlarged feed mass flow rate and the time difference between each case is not huge. Therefore, the feed mass flow rate is not an essential parameter impacting stationary time.

## 3 Residence time distribution

### 3.1 Literature review

#### 3.1.1 Residence time behavior of monodisperse system

Studying the time of passage is an important way to acquire the solid transport inside the kiln. The residence time behavior can be described by the mean residence time (MRT) and the residence time distribution (RTD). MRT is a time which describe the mean time of particle transport from the feed end to discharge end. Due to the semi-fluidized mechanical means, the solid particles flowing through the kiln contain both axial and radial dispersion which leads to different residence time behavior of the particle fractions. Hence, MRT could inaccurately describe the particle transport and RTD is necessary for the design, improvement and scale up of industry.

Rutgers (1965) used long grain rice to study longitudinal mixing in rotary kilns. In his studies, the residence time distribution profile was measured and the Bodenstein number were chosen to describe the condition of dispersion and with low rotational speed, the longitudinal dispersion is smaller than radial mixing. Abouzeid et al. (1974) built a non-segregating transport system and used the axial dispersion model for the description of particle transport. And this axial dispersion model was always being used to describe the axial transport inside of rotary kiln till now which will be introduced in the following section (see Chapter 3.2). From his experiments, the mean residence time and variance of the residence time distribution could determine the two parameters, the axial convective velocity and the axial dispersion coefficient. Hehl et al. (1978) created the similar experiments with extremely fine soda powder inside a small-scale rotary kiln (250 mm diameter and 600 mm length). The axial dispersion model was implemented with varies of different operational conditions to analyze the residence time distribution. It could conclude that under low rotational speed condition, the soda

particle corresponds to nearly ideal mixing in the transverse direction, and practically no mixing in axial direction.

Mu, J. and Perlmutter, D. D. (1980) developed a new model to estimate the residence time distribution which was based on the model of transverse motion from Rutgers (1965). In this case, the transverse particle motion was divided into two parts which is cascade region and plug flow region. A block diagram for a single stage showing concentrations and flow quantities was first introduced to show how the particle flow move in one cascade. Although there was a function of residence time distribution derived, some parameters from empirical values still limited the further application.

Sai et al. (1990) created empirical equations of mean residence time and dispersion number separately from a series number of tracer experiments. However, the tracer did not have the same density as the working materials. Richard et al. (2003) reviewed critically the previous literature of both experiments and simulation models and proposed new design empirical equations for the axial dispersion coefficient which contained rotational speed, filling degree, diameter of kiln and particle properties. The shape of particle was also considered as validate parameters by Gao et al. (2013). Alumina particles with different shape (sphere, cylinder and quadrilobed), density, and geometry were used as bulk materials. The model proposed by Saeman (1952) were proved as accurate prediction of MRT and RTD. However, the axial dispersion was also determined from experimental data and the raw materials in the experiments were monodisperse particle system.

A novel particulate trajectory model was developed by Li (2002) to simulate the axial transport and dispersion of municipal solid waste inside of rotary kilns. The RTD could be predicted from simulation and validated by some experiments. Although the municipal solid waste consists of several kinds of materials, they were still treated as a monodisperse system and the axial segregation was not considered.



Abouzeid (2010) described the RTD in non-homogeneous particulates by some experiments. In this study, all particle systems suffered mutual separation and segregation among their constituents. The segregation would be occurred in axial direction which formed alternative bands of flowing components and radial direction which was a core of one component and a ring from the other component. Bensmann et al. (2010) used quartz sand as test materials with the particle size range of 0.5 to 1.6 mm. The bulk was theoretically classified as 6 different size ranges and each one was represented with a mean particle diameter. The residence time distributions were presented with different particle size fractions and the mean residence time was found to increase for particles with smaller diameters.

### **3.1.2 Transverse segregation**

From the study of Williams and Khan (1973), the main reasons of segregation were caused by particle size, shape, roughness, density and resilience. Based on it, the mechanisms of segregation could be classified as trajectory segregation and percolation. Pollard and Henein (1989) indicated that in most case of the rotary kiln operation, the segregation issues were caused by differences in particle size.

Bridgwater et al. (1985) indicated that trajectory segregation was the main cause of axial segregation or “banding” which means the different size of particles were selectively concentrated into bands over the kiln length. During the study, a mathematical model in the active layer of a free-flowing powder was built and could just get solution without axial diffusion.

In transverse plane, the segregation was mainly caused by percolation. It means when a bed of particles was disturbed so that rearrangement took place (rapid shearing, rotating), the small particles would have possibility to fall into voids which depended on the size of the particles (Savage, 1983). Therefore, the small particle would concentrate in the core of particle bed and the big particle moving surround it as an

outer ring which has already shown in Figure 1.1. Based on the principle of percolation, Boateng and Barr (1996) developed a model to predict the preferential movement of particles in active layer. In this model, an appropriate control volume in the active layer was selected to derive the PDE functions. The particle segregation profile in cross-section view was simulated and presented with the contour plots of jetsam concentration. This model was validated by the experiments of Henein (1980) and had good agreements with experimental results.

Alizadeh et al. (2013) reported a work by using radioactive particle tracking (RPT) to capture the flow of particles inside the rotating drum. In this case, both mono and polydisperse glass beads test materials were investigated inside a batch horizontal drum with 24 cm inner diameter and 36 cm length. From this study, it shows that there were no big differences of the velocity profiles and the active layer thickness between monodisperse and polydisperse system.

On the other hand, DEM simulation was also implemented in segregation section. He et al. (2007) performed a mathematical modelling by using Eulerian based continuum model and the simulation results of polydisperse system is shown in Figure 3.1. It could be clearly seen that there is a two-region bed structure in the cross-section view, active layer and passive layer. By using different size of particles, the ring-core structure could be clearly observed also, where fine particles concentrate in the core region and large particles occupy the outer ring region.

In overall, there are a large number of studies about residence time distributions in both monodisperse and polydisperse system till now. Most researches considered the axial dispersion and transverse segregation separately for the investigation of RTD. In axial view, axial dispersion model was implemented as basic model and the research relied on statistics method. Some empirical equations were developed within some lab-scale rotary kiln which could obtain the diffusion coefficients and the variance of RTD curves. On the other hand, there is no description of particle velocity profiles along the axis and

all the mathematical model could just predict the RTD in the discharge end. Therefore, these results could hardly be implemented in the currently known model of the heat transfer process in rotary kiln. The transverse location as well as the local axial velocity of each size particle bed must be known which are essential for the contact heat transfer within the polydisperse particle bed.

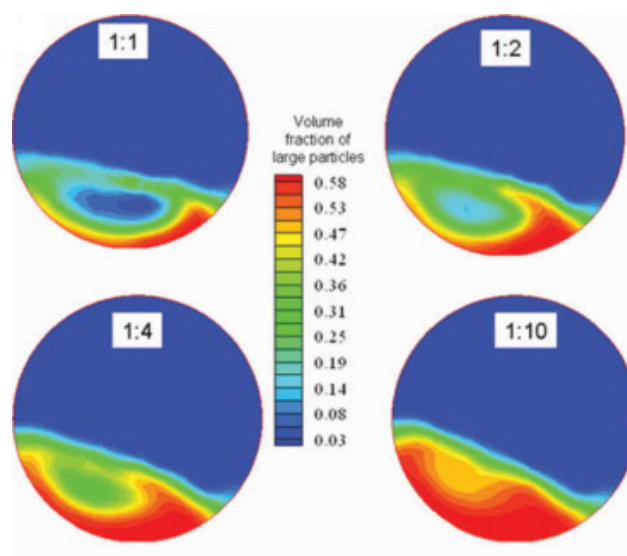


**Figure 3.1** Simulation results of polydisperse system from He et.al (2007)

On the other hand, although the DEM model is now widely applied in most particle system, it still needs high computer performance and too much calculation time (weeks or month). Moreover, for normal industrial scale condition, over million number of particles are contained inside of rotary kilns which means it is not possible to simulate the whole process of real condition. Therefore, a trustable PDE model about segregation inside of rotary kilns will be introduced in following chapters which could easily provide the transverse areas and location of each size particle bed. Furthermore, axial particle velocity profiles along the kiln axis and RTD will be derived from the model in polydisperse system and validated by with a pilot-scale rotary kiln.

## 3.2 Mathematical model of transverse segregation and RTD

### 3.2.1 Modeling of transverse segregation in a bidisperse bulk bed

The ring-core structure is chosen as major structure of transverse segregation and could be schematically described in Figure 3.2

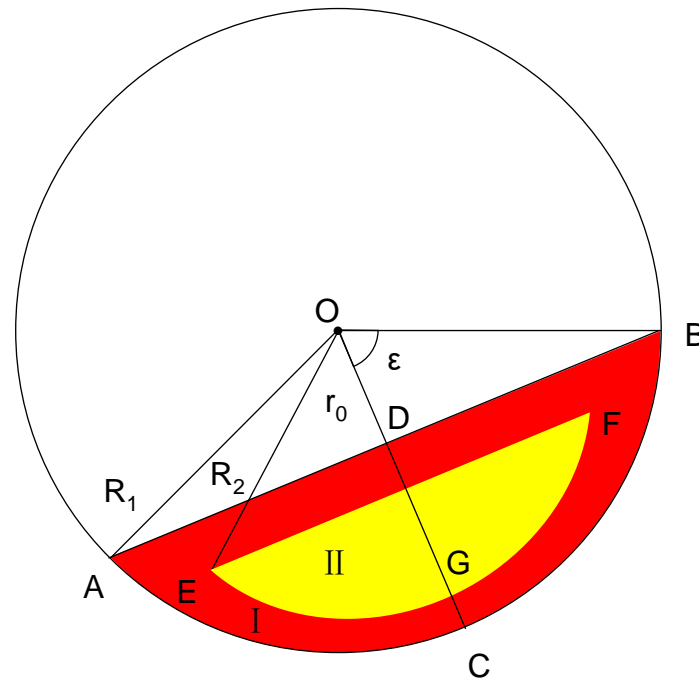


**Figure 3.2** Schematic of transverse segregation in bidisperse system

It is a typical bidisperse particle system where II represents the fine particle with area of  $A_2$  and I is the big particle with area of  $A_1$ . These two areas have the same center of circle O. Hence, OA is the radius of the segment ABC and OE is the radius of the small segment EFG which could be named as  $R_1$  and  $R_2$  separately.  $\varepsilon$  is the half filling angle of particle bed and  $r_0$  is the distance between center of circle to the upper surface of big particle bed.  $A_0$  is the total transverse particle bed area where

$$A_0 = A_1 + A_2 . \quad (3.1)$$

From the knowledge of geometry, Figure 3.2 could be changed to Figure 3.3, where the

area of big particle (I) and small particle (II) will not be changed with varied location of area II inside of particle bed. So,  $A_1 = A_1'$  and  $A_2 = A_2'$ .  $OE'$  is the new radius  $R_2'$  of segment  $E'F'G'$ .  $R_1, r_0, \varepsilon$  are the same as in Figure 3.2.

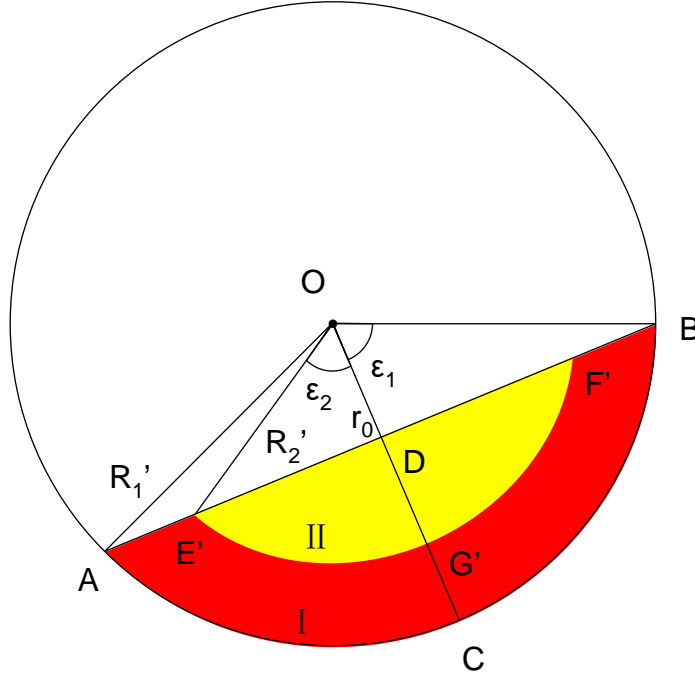


**Figure 3.3** Schematic of adjusted transverse segregation in a bidisperse bulk bed

It is clear to be observed that the adjusted structure also fits the model of Saeman. Hence, the equation 2.16 in chapter 2 could be directly implemented

$$dv = 2\pi nr \left( \frac{\beta + \psi \cos \theta}{\sin \theta} \right) \left( \sqrt{(r^2 - r_0^2)} \right) dr, \quad (3.2)$$

where  $n$  is the rotational speed of rotary kiln,  $\beta$  is the inclination angle of rotary kiln,  $\theta$  is the dynamic angle of repose,  $\psi$  is the angle between surface of material and kiln axis and  $r$  is the distance between  $O$  and any point of the upper surface. In the Saeman's model, the next step is directly integrating equation 3.2 from  $r = r_0$  to  $r = R$  and get

$$\dot{V} = \frac{4\pi n}{3} \left( \frac{\beta + \psi \cos \theta}{\sin \theta} \right) (R^2 - r_0^2)^{3/2}. \quad (3.3)$$

However, if the boundary conditions are changed to  $r = R_2'$  and  $r = R_1'$ , the equation 3.3 will be written as

$$\dot{V}_1 = \frac{4\pi n}{3} \left( \frac{\beta + \psi \cos \theta}{\sin \theta} \right) \left[ (R_1'^2 - r_0^2)^{3/2} - (R_2'^2 - r_0^2)^{3/2} \right], \quad (3.4)$$

where  $\dot{V}_1$  is the volume flow rate of big particles. And the volume flow rate  $\dot{V}_2$  of small particles could also be written as

$$\dot{V}_2 = \frac{4\pi n}{3} \left( \frac{\beta + \psi \cos \theta}{\sin \theta} \right) \left[ (R_2'^2 - r_0^2)^{3/2} \right], \quad (3.5)$$

with boundary conditions of  $r = R_2$  and  $r = r_0$ .

In most case, the initial mass flow fraction of each size of particle in the feeder is constant and could be named as  $X_i$ . This leads to

$$X_1 + X_2 = 1, \quad (3.6)$$

In a bidisperse system. Therefore, the volume flow rate could be derived as

$$\dot{V}_1 = \dot{M} X_1 / \rho_{b1}, \quad (3.7)$$

$$\dot{V}_2 = \dot{M} X_2 / \rho_{b2}, \quad (3.8)$$

where  $\dot{M}$  is the total feed mass flow rate,  $\rho_{b1}$  and  $\rho_{b2}$  are particle bulk density of big and small particles.

Furthermore, if  $\psi$  is known, the radius of  $R_1'$  and  $R_2'$  could be calculated from equation 3.4 and 3.5. Hence, by implementing the basic mathematical equation of Saeman's model in chapter 2

$$\frac{dr_0}{dx} = \frac{3\dot{V}_0 \sin \theta}{4\pi n \cos \theta (R^2 - r_0^2)^{3/2}} - \frac{\beta}{\cos \theta}, \quad (3.9)$$

and by adding the definition of  $\psi$

$$\psi = \frac{dr_0}{dx}, \quad (3.10)$$

equation 3.9 could be derived as

$$\psi = \frac{dr_0}{dx} = \frac{3\dot{V}_0 \sin \theta}{4\pi n \cos \theta (R^2 - r_0^2)^{3/2}} - \frac{\beta}{\cos \theta}, \quad (3.11)$$

where the axial profiles of  $r_0$  will be calculated from Saeman's model and the solving process has been introduced in chapter 2.  $\dot{V}_0$  is the total volume flow rate and calculated by

$$\dot{V}_0 = \frac{\dot{M}}{\rho_{b0}}. \quad (3.12)$$

In this case,  $\rho_{b0}$  is the particle mixing bulk density and will be measured by experiments.

Therefore,  $R_2'$  could be solved by either using the equation 3.4 with the condition of  $R_1' = R$ , which is the radius of inner surface and should be constant without considering the changing of inner diameter of the rotary kiln, or by equation 3.5 with known  $r_0$ . After getting the value of  $R_2'$ , the filling angle of area II could be derived as

$$\varepsilon_2 = \cos^{-1} \frac{r_0}{R_2'} . \quad (3.13)$$

The half chord of area II is

$$l_2 = \sqrt{R_2'^2 - r_0^2} . \quad (3.14)$$

So, the area of small particle could be derived as

$$A_2 = A_2' = \varepsilon_2 R_2'^2 - l_2 r_0 . \quad (3.15)$$

With equation 3.1, the area of big particle is

$$A_1 = A_0 - A_2 , \quad (3.16)$$

where

$$A_0 = F\pi R^2 , \quad (3.17)$$

and F is the filling degree which is described in chapter 2.

Therefore, the axial velocity of big and small particle could be derived as

$$u_1 = \frac{\dot{V}_1}{A_1} , \quad (3.18)$$

$$u_2 = \frac{\dot{V}_2}{A_2} . \quad (3.19)$$



According to the fundamental of numerical solving of Saeman's model, the length of rotary kiln is divided to finite element along axis by a fixed distance  $dz$  and

$$Z * dx = L, \quad (3.20)$$

where  $Z$  is the total number of finite elements.

The time of particle axial transport within any distance between point P and point Q along axis will be developed as

$$t_1 = \sum_{j=p}^q \frac{\delta x}{u_{1,j}}, \quad (3.21)$$

$$t_2 = \sum_{j=p}^q \frac{\delta x}{u_{2,j}}, \quad (3.22)$$

where  $p$  and  $q$  are the element number and  $p \in [1:Z]$ ,  $q \in [1:Z]$ .

Moreover, from the definition of MRT of the rotary kiln, the MRT of each size of particle is written as

$$MRT_1 = \sum_{j=1}^Z \frac{\delta x}{u_{1,j}}, \quad (3.23)$$

$$MRT_2 = \sum_{j=1}^Z \frac{\delta x}{u_{2,j}}. \quad (3.24)$$

And the mean particle axial velocity is derived as

$$\bar{u}_1 = \frac{L}{MRT_1}, \quad (3.25)$$

$$\bar{u}_2 = \frac{L}{MRT_2}. \quad (3.26)$$

### 3.2.2 Modeling of transverse segregation in a polydisperse bulk bed

The schematic structure of a polydisperse bulk bed is shown in Figure 3.4. There are  $N$  number of different particle sizes in bulk bed which are named from 1 to  $N$  and has the same physical properties. The cross-section areas of these fractions are  $A_1 \dots A_N$ .

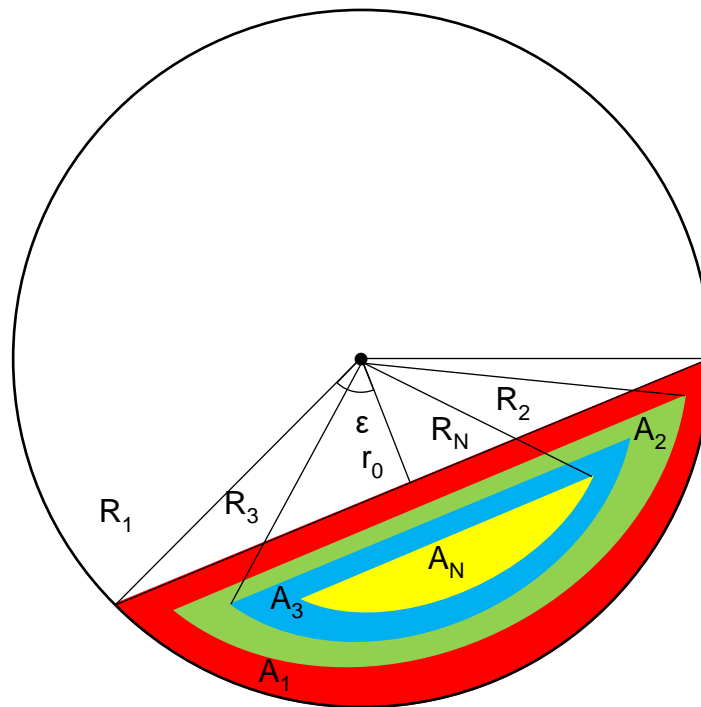


**Figure 3.4** Schematic of transverse segregation in polydisperse system

According to the method in a bidisperse bulk bed, all the particle segments are moved to the upper surface of the particle bed, which is shown in Figure 3.5.

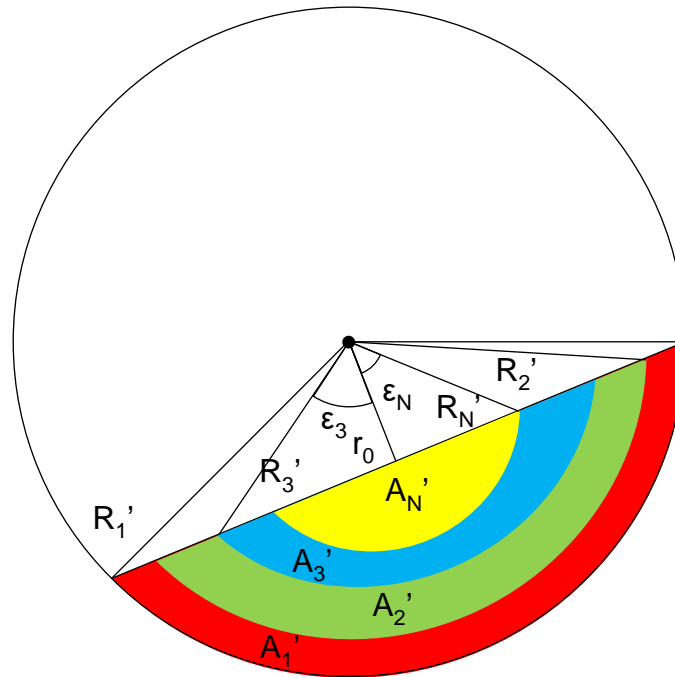


**Figure 3.5** Schematic of adjusted transverse segregation in a polydisperse bulk bed

In this case,  $A_1 = A_1'$ ,  $A_2 = A_2'$ , ...  $A_N = A_N'$  and the total area is equals to

$$\sum_{i=1}^N A_i = A_0 . \quad (3.27)$$

The volume flow rate of each particle size fraction is

$$\dot{V}_i = \dot{M} X_i / \rho_{bi} , \quad (3.28)$$

where  $X_i$  is the initial mass fraction of total mass flow rate and

$$\sum_{i=1}^N X_i = 1 . \quad (3.29)$$

Hence, the volume flow rate could be derived as

$$\dot{V}_i = \frac{4\pi n}{3} \left( \frac{\beta + \psi \cos \theta}{\sin \theta} \right) \left[ (R_i^2 - r_0^2)^{3/2} - (R_{i+1}^2 - r_0^2)^{3/2} \right]. \quad (3.30)$$

It is important that for the first layer of biggest particle  $R_1' = R$  and for the finest particle,  $R_{N+1} = r_0$ .

After combing equation 3.30 and 3.11, the  $R_i$  could be calculated and the filling angle of each one is

$$\varepsilon_i = \cos^{-1} \frac{r_0}{R_i'}. \quad (3.31)$$

The transverse area of each size of particle is written as

$$A_i = \left( \varepsilon_i R_i'^2 - r_0 \sqrt{R_i'^2 - r_0^2} \right) - \left( \varepsilon_{i+1} R_{i+1}'^2 - r_0 \sqrt{R_{i+1}'^2 - r_0^2} \right), \quad (3.32)$$

where for the smallest particle, there is no N+1 component and can be expressed as

$$A_i = \varepsilon_N R_N'^2 - r_0 \sqrt{R_N'^2 - r_0^2}. \quad (3.33)$$

Therefore, the axial velocity a particle size fraction in a polydisperse bulk bed is derived as

$$u_i = \frac{\dot{V}_i}{A_i}, \quad (3.34)$$

and the mean residence time of each particle size is

$$MRT_i = \sum_{j=1}^Z \frac{\delta x}{u_{i,j}}. \quad (3.35)$$

And the mean axial velocity is

$$\bar{u}_i = \frac{L}{MRT_i}. \quad (3.36)$$

It should be mentioned that, for bi- and polydisperse mixing particles, the sauter mean diameter is selected as characteristic diameter  $d_0$  to describe the mixing particles as

$$d_0 = \left( \sum_{i=1}^Z X_i/d_i \right)^{-1}. \quad (3.37)$$

### **3.2.3 Assumptions for modeling the transverse segregation in a bi- and polydisperse bulk bed**

As the model described for transverse segregation in a bi- and polydisperse bulk bed, some assumptions should be mentioned as following parts

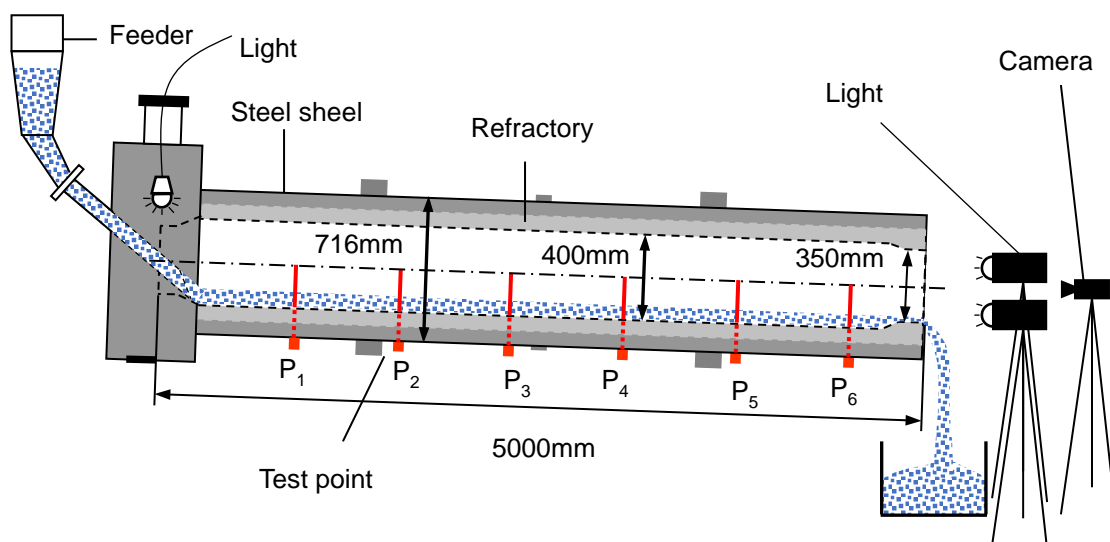
- 1) In bi- and polydisperse system, each particle should have same physical properties and just be different in particle size and bulk bed density.
- 2) The main body of the granular bed for each kind of particle is considered as a rigid body when rotating around the axis.
- 3) There is no slip between particle bed and kiln wall, and also no slip between each particle size fraction which means all the rigid body rotates with the angular velocity of the kiln.
- 4) The finest particle should always be in the core of particle bed and the biggest particles are in the outermost layer. Other particle size fractions are arranged from outside to the core with particle size decreasing.

- 5) All the segments of particle size fractions have the same center of circle with total particle bed.
- 6) There is a thin active layer for each segments of particle size fractions. All the active layers are on the upper surface of particle bed.
- 7) The trajectory of a particle in the active layer is similar to monodisperse system and shown in Figure 2.1. One part of path vector is parallel to the axis and another perpendicular to axis. Each kind of particle has its own path and has no disturbance between each other.
- 8) There is no particle mixing between each segment.
- 9) The value of bulk density and dynamic angle of repose of each particle size fraction is constant in any position.

### 3.3 Experiment of residence time distribution

#### 3.3.1 Experimental apparatus and materials

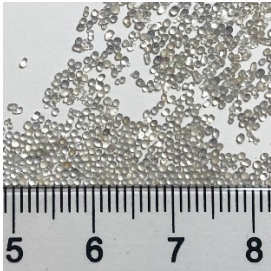
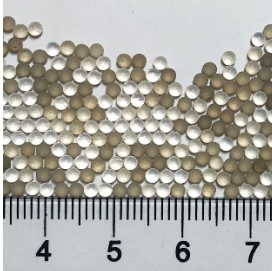
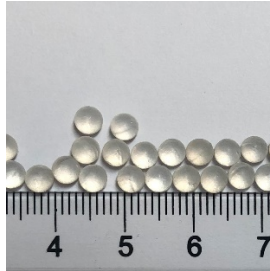
Figure 3.6 describes the schematic of the residence time distribution analysis. All the experiments are operated in the same rotary kiln as introduced in chapter 2.3.1.



**Figure 3.6** Schematic diagram of experimental apparatus for the RTD test

Transparent glass beads are used as test materials with particle sizes of  $0.7 \pm 0.2$  mm,  $2 \pm 0.2$  mm and  $4 \pm 0.3$  mm. The physical properties are listed in Table 3.1.

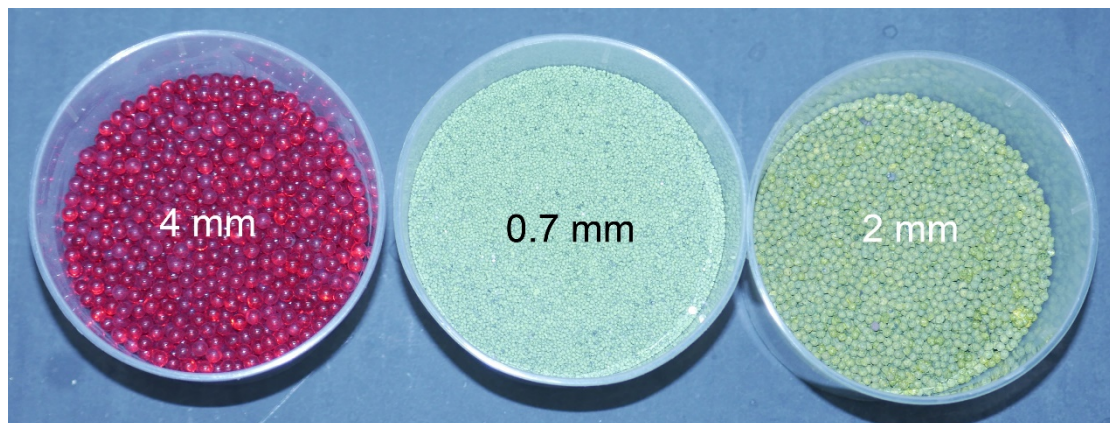
**Table 3.1** Physical properties of glass beads

Figure of particles			
Particle size $d_p$ in mm	$0.7 \text{ mm} \pm 0.2 \text{ mm}$	$2 \pm 0.2 \text{ mm}$	$4 \pm 0.3 \text{ mm}$
Particle density $\rho$ in $\text{kg/m}^3$	2500	2500	2500
Bulk density $\rho_b$ in $\text{kg/m}^3$	1560	1560	1560
Dynamic angle of repose $\Theta$ in $^\circ$	32	32	32

The tracer of 4 mm particles are colored glass beads in ruby red, which has the same physical properties as transparent one. In contrast, for 2 mm and 0.7 mm particles, a magnetic primer is finally implemented to coat the particle and gives a magnetic cover which could be picked up by strong magnet. Due to the smoothness of the particle surface a binder was used for a coating with magnetic cover. A solution of sodium benzoate is used as first coating layer of 2 mm and 0.7 mm particles. Lightly amount of HPMC (hydroxypropyl methylcellulose) is added into the solution to improve the stickiness between the particle and sodium benzoate. The coating process runs in the

fluidized bed and will get particles with white and roughness surface after drying. This white surface is around 0.1 mm and has less influence in particle diameter. Furthermore, all the raw materials of tracer particle are sieved under 0.7 mm and 2 mm which will give more allowance for magnetic cover.

The magnetic primer is pure black. Due to the high density and stickiness, only 5% of total tracer weight pigment is homogeneously coated on the surface and all the coated particle are all around 0.8 mm and 2.1 mm diameter and can be strongly attracted by magnet. In the end, to give clear visual contrast in the video, the 0.7 mm particle tracer will finally be colored in white with spray paint and 2 mm tracer will be colored in green. This third layer of color is extremely thin and has no influence on the particle physical properties. The figure of tracers is shown in Figure 3.7.



**Figure 3.7** Sample of tracers in different sizes

### **3.3.2 Experimental details and measuring method**

The particle mixing and operational conditions of test experiments are shown in Table 3.2. In this case, the bidisperse system is developed by mixing any two sizes of glass beads with 1:1, 1:2 and 2:1 mass ratio and the dynamic angles of repose of each mixing particles are changed with different particle mixing status and operational conditions.



**Table 3.2** Operational test conditions

Particle diameter	0.7 & 2 mm	0.7 & 4 mm	2 & 4 mm
Mixing mass ratio	1:1, 1:2, 2:1	1:1, 1:2, 2:1	1:1, 1:2, 2:1
Dynamic angle of repose in °	27 - 30	25 - 30	25 - 30
Kiln length in m	5		
Temperature in °C	20		
Kiln rotational speed n in rpm	1, 2, 3		
Feed mass flow rate $\dot{M}_s$ in kg/h	50, 100, 150		
Kiln inclination $\beta$ in °	1, 2, 3		

In preparation period, it is important to realize a constant mixing ratio. Therefore, the particles are mixed in small container around 20 l at first and then fed into the feeder.

The experiment starts from the empty kiln with set operational conditions. After reaching steady state condition, the kiln and the feeder should be stopped at the same time. The tracer particles are well mixed with the same mixing ratio as test materials. They have a total amount of 2% of feed mass flow rate. For example, for 0.7 & 2 mm, 1:1 ratio material, 100 kg/h feed mass flow rate condition, the tracers are 1 kg 0.7 mm in white with 1 kg 2 mm in green. All the operational conditions and tracer's weight are listed in the Appendix B.

The tracers are fed into the rotary kiln at the feed end while the kiln is stopped. Meanwhile, the camera should focus on the feed end where the tracers are and begins to record the video till the end of whole experiment. After setting camera, restart the

rotary kiln and the feeder at the same time. It is important that the camera should keep focus on the tracer particle band of the upper surface of particle bed and record the whole axial transport behavior of tracers without stop.

When the tracer approach to the discharge end of the kiln, the outflow was collected in small cups within appropriate time interval. It depends on the feed mass flow rate and axial dispersion of tracers which lies in a range of 10s to 15s interval to confirm all the tracers could be collected.

The collected particle should be numbered along the timeline. Every cups of particles should be sieved into two parts and measured the total weight respectively. For 0.7 mm and 2 mm particle, the tracers could be picked up by strong magnet and get the weight as  $m_{s,i}$ , whereas for 4 mm particle, the photo pixel analysis method is considered to get the mass of tracers and should be treated as following steps.

- 1) A platform with strong white LED light (Figure 3.8) is built to reduce the influence of ambient light.

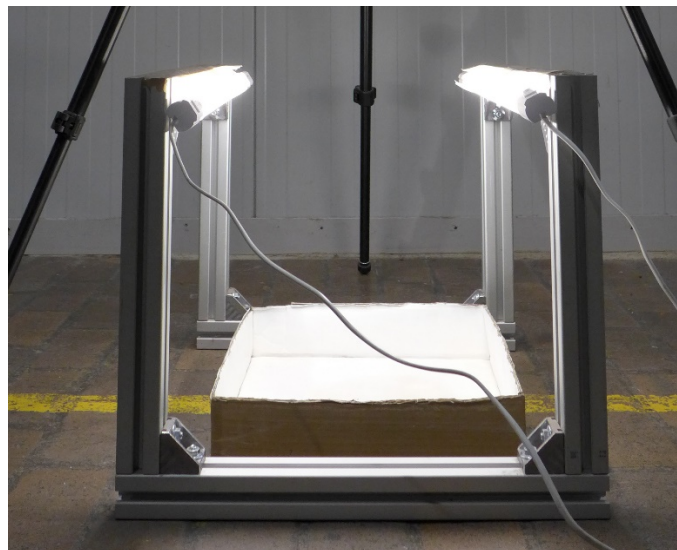


**Figure 3.8** The platform for photograph

- 2) Every sieved 4 mm particle should be evenly spread in a big box which has flat

white surface and enough space to make sure there is just one particle layer on the surface.

- 3) The box with particle is set in the center of the platform and the camera should be located in a fixed position that will take the photo from the center of box. It should be mentioned that the height of tripod, focal length, aperture, shutter and ISO number should be constant for all photos.
- 4) The original photos from camera will be firstly pretreated in photoshop by cutting the useless part (Figure 3.9 a) and increasing the contrast to remove the transparent particles in the figures (see Figure 3.9 b).

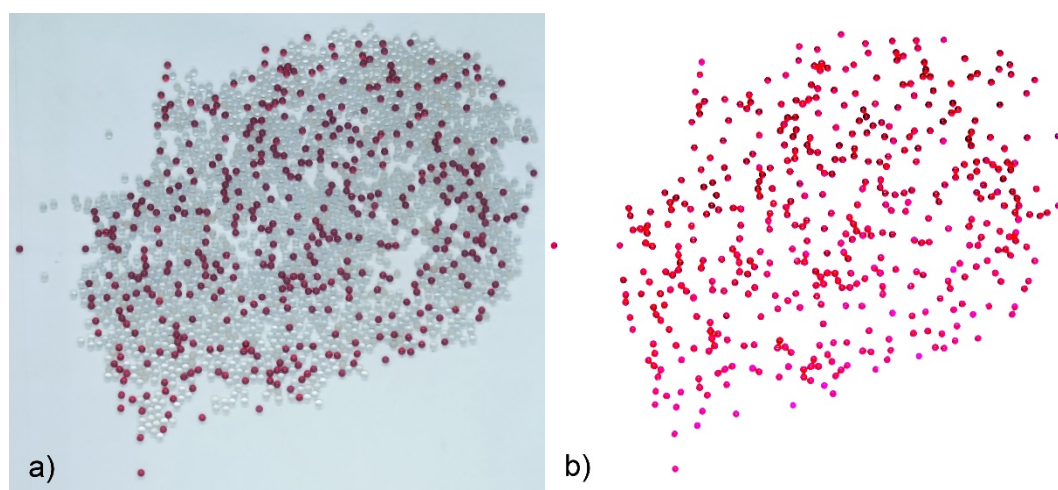


**Figure 3.9** Photoshop pretreatment for digital analysis

- 5) After pretreatment, the photos will be imported and analyzed in Matlab software. In Matlab, the pictures are red as RGB format and in this case, for red particles, the pixel values of green part are smaller than 200 and in contrast, the pixel values of white parts are in the range from 250 to 255. Hence, the pixel number of red particles could be known by count the pixel value under 200. Furthermore, the number of red particles in the photo will be calculated by the ratio between total pixel value and single particle pixel value. Finally, multiplying the number of particles and the weight of single particle gets the mass of tracer particles, where the weight of single particle is 0.8 g

### 3.3.3 Data analysis method

#### 3.3.3.1 Residence time distribution analysis

The axial dispersion model is selected to describe the RTD (Gao et al. 2013) of the experiments. In this model, the residence time distribution  $E(t)$  is calculated based on the concentration of tracers as

$$E(t) = \frac{C(t)}{\int_{t=0}^{\infty} C(t)dt}. \quad (3.38)$$

And to eliminate the noise from the measurements, the RTD measurement is fitted to the Taylor dispersion model as

$$E(\xi, \theta) = \frac{1}{2} \sqrt{\frac{Pe}{\pi\theta}} \exp \left[ -\frac{Pe(\xi - \theta)^2}{4\theta} \right], \quad (3.39)$$

where in this formula,  $\theta = t/\bar{t}$ ,  $\bar{t}$  is the MRT and  $\xi = l/L$ .  $L$  is the total length of the rotary kiln. In our experiments,  $l$  equals to  $L$ ,  $\xi$  equals to 1.

$Pe$  is the Peclet number which describes the evolution of particle distribution in continuous systems, it represents the ratio of the convection rate over the diffusion rate as

$$Pe = \frac{ul}{D_z}, \quad (3.40)$$

where  $u$  is the particle axial transport velocity from feed end to measuring point and  $l$  is the transport distance. If tracers are collected in the discharge end,  $l$  equals to  $L$ .  $u$  is the mean velocity within the transport distance and could be calculated by equation 3.36.  $D_z$  is the axial dispersion coefficient which could be considered as major

parameter to indicate the extent of axial dispersion. Levenspiel (1999) indicated that the dispersion coefficient represents the spreading process in the kiln. Large  $D_z$  means rapid spreading of the tracer curve and small  $D_z$  means slow spreading. If  $D_z$  equals to 0, no spreading happened but just plug flow.

Also,  $(D/uL)$  is the dimensionless number characterizing the spread for the whole kiln and equals to  $1/Pe$  based on equation 3.40. And if  $1/Pe$  approaches 0, that means no dispersion, plug flow. If  $1/Pe$  is infinite, the dispersion is quite large which causes mixed flow.

Therefore, equation 3.39 could be written as

$$E(t) = \frac{1}{2} \sqrt{\frac{Pe \cdot \bar{t}}{\pi t}} \exp \left[ -\frac{Pe(\bar{t} - t)^2}{4\bar{t}t} \right]. \quad (3.41)$$

However, in real case, the measured concentrations  $C(t)_{ov}$  are the overall value in measuring time interval  $\Delta t$ . The mean value of tracer concentration is used as specific value in time interval as

$$C(t_i)_{ov} = \frac{m_{s,i}}{\sum_i^{N_s} m_{s,i}}, \quad (3.42)$$

$$C(t_i) = \frac{C(t_i)_{ov}}{\Delta t}, \quad (3.43)$$

where  $N_s$  is the total number of sample.

Due to the measuring points are discrete, the equation 3.38 can be changed to

$$E(t) = \frac{C(t_i)}{\sum_i^{N_s} C(t_i)\Delta t} = \frac{C(t_i)}{\sum_i^{N_s} C(t_i)_{ov}}. \quad (3.44)$$

In theory,  $\sum_i^{N_s} C(t_i)_{ov} = 1$ , but in real case,  $\sum_i^{N_s} C(t_i)_{ov} \leq 1$ , because of the incomplete collection of simple. Hence, the Taylor dispersion model could be derived based on the concentration of tracers as

$$C(t) = B \frac{1}{2} \sqrt{\frac{Pe \cdot \bar{t}}{\pi t}} \exp\left[-\frac{Pe(\bar{t} - t)^2}{4\bar{t}t}\right]. \quad (3.45)$$

where  $B = \sum_i^{N_s} C(t_i)_{ov}$ .

And the standard deviation for equation 3.45 was describe by Abouzeid et al. (1974) and simplified by Njeng et al. (2015) under low axial mixing in most rotating drums with large Pe ( $Pe > 50$ ) as

$$\sigma^2 = \bar{t}^2 \left( \frac{2}{Pe} - \frac{2}{Pe^2} \right). \quad (3.46)$$

The results of both experiment and fitting curve are shown in Figure 3.10 with the experiment under operational conditions of 150 kg/h, 2 rpm, 2° inclination and 4 mm & 0.7 mm mixing particles. In the figure the experimental values of  $C(t_i)$  are shown as points and the fitting values based on equation 3.45 are as solid lines. The coefficient of determination for 4 mm and 0.7 mm particles are all above 0.97 which shows quite good agreement between experimental values and fitting model. Hence, the MRT for each particle size could be identified. For example, in Figure 3.10, the MRT of 4 mm particles and 0.7 mm particles are 27 min and 29 min separately.

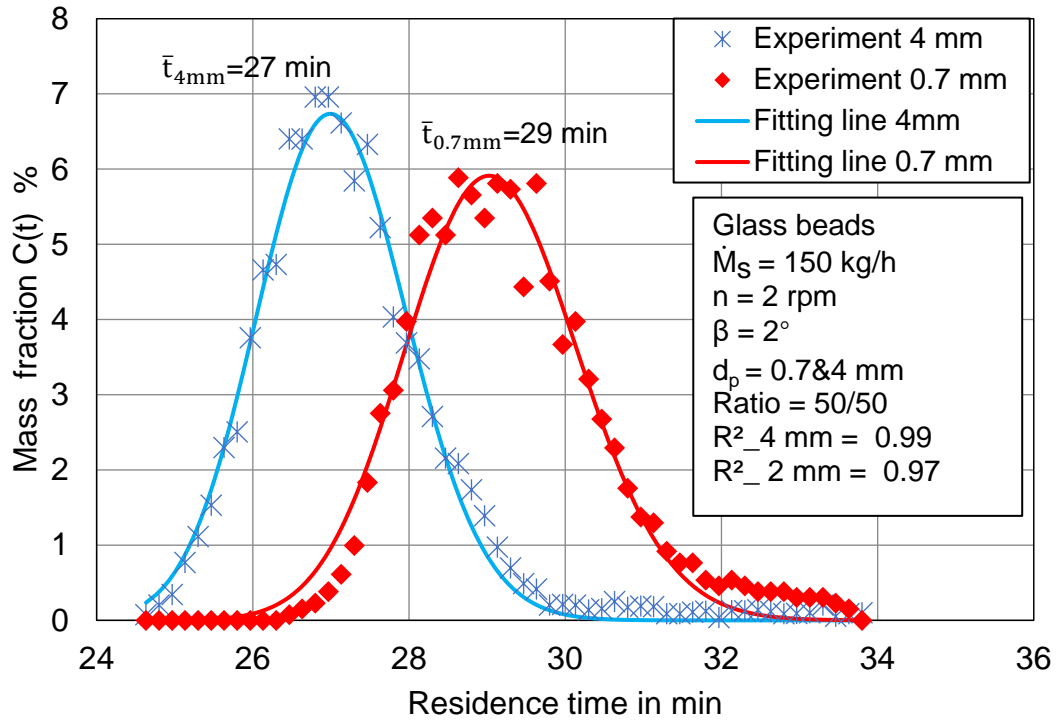


**Figure 3.10** The residence time distribution with fitting lines

The MRT of bi- and polydisperse system could be predicted from the model in chapter 3.2 and the simulation result should be validated by using the MRT from experiments. The comparison results are shown in Figure 3.11.

It is clear to see that, the coefficient of determination of all predicted values are 0.95 which shows quite good performance with experimental results. And when the MRT is under 40 min, the predicted values have less difference to the experimental values. From table 3.2, it shows that three different mixing particles have the same experiment operational conditions. Hence, it could see that for the same operational conditions, all the particle size fraction has the similar MRT and especially for small values under 40 min conditions. However, the difference of MRT will be enlarged with increasing MRT values.

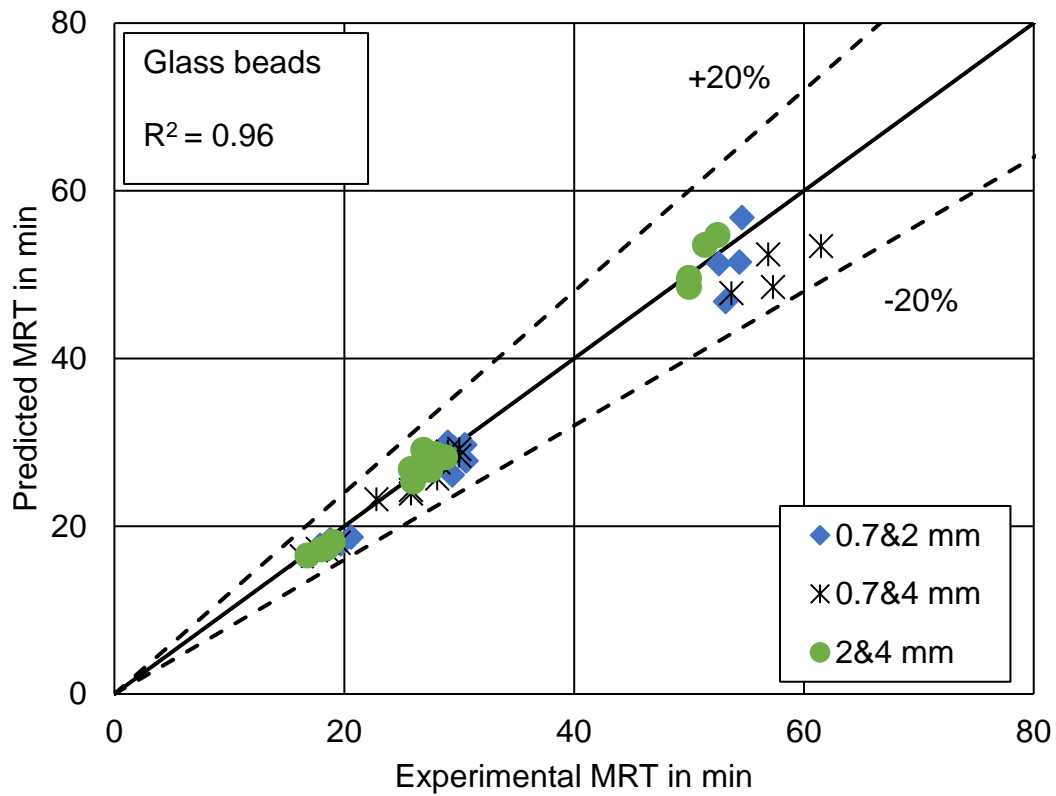


**Figure 3.11** Comparison of predicted and experimental MRT of overall particles

To make the further analysis of the influence of particle size fraction, the  $R^2$  values under particle size mixing conditions are described from Figure 3.12 to 3.14. By comparison of 3 figures, the 2&4 mm mixing particle has the best correlation between predicted values and experimental values with  $R^2$  of both 0.99. That means our model of ring-core structure is good enough to predict the MRT in bidisperse system.



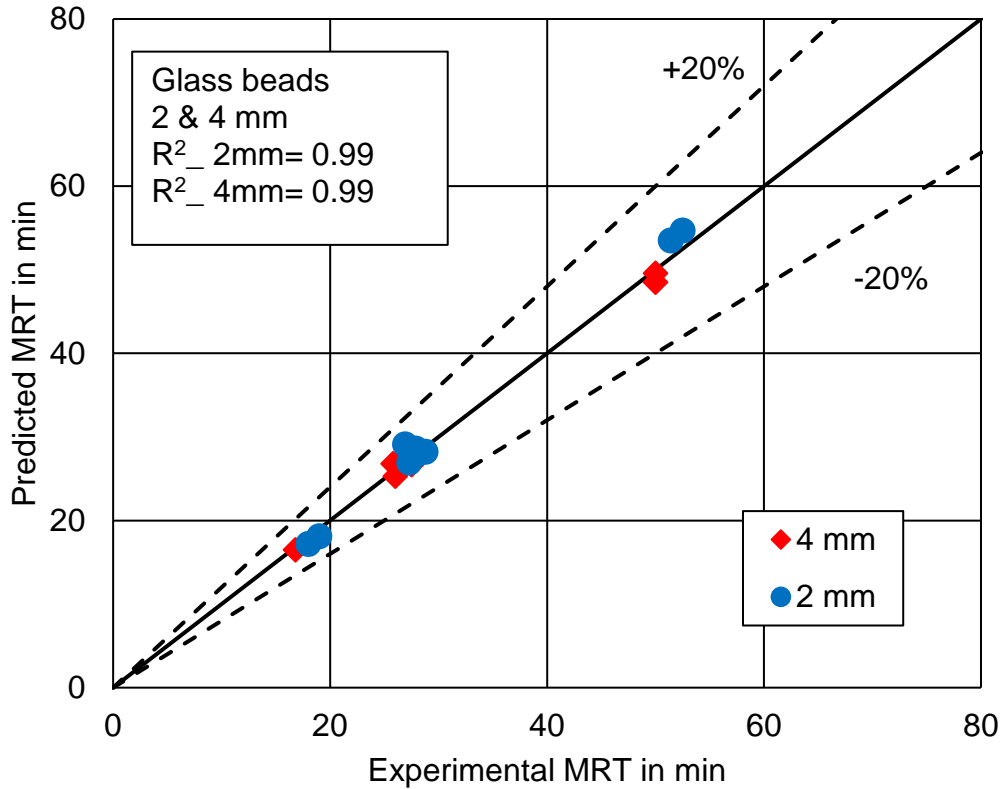


**Figure 3.12** Comparison of predicted and experimental MRT of 2&4 mm bidisperse system

In contrast, for 0.7&2 mm and 0.7&4 mm particles, the  $R^2$  values are relatively small compared to 2&4 mm status. And in most case, the predicted values are smaller than the experimental values. After analyzing the video of whole particle transport behavior, there is an interesting behavior of mixing particle observed. Figure 3.15 shows a specific example of particle bed of 0.7&4 mm, 1:1 mixing rate under 1 rpm,  $2^\circ$  and 100 kg/h feed mass flow rate conditions.

By combining the video of axial transport, it is clear to see that for the free surface of the particle bed, most big particles concentrate in the bottom and the small particles locate in the upper part. For 0.7&2 mm and 0.7&4 mm particles, the deviation of the particle diameter is not only 2 times but also 3 or even above 6 times. With this large particle size difference, the small one will not transport in the active layer as we assumed but easily move through the gaps between big particles and directly distribute

on the inner wall surface of rotary kiln mixing with big particles. This phenomenon will create a smooth surface that could decrease the friction between particle bed and inner wall surface of rotary kiln.

Therefore, with these reasons, in real case, the mixing particles need more time to transport from the feed end to the discharge end of rotary kiln. At the same time, the model described before is with the assumption of rolling model presenting in cross-section view and forming ring-core structure. With these reasons, the predicted values are always smaller than the experimental values especially under small rotational speed and low inclinational angle conditions.

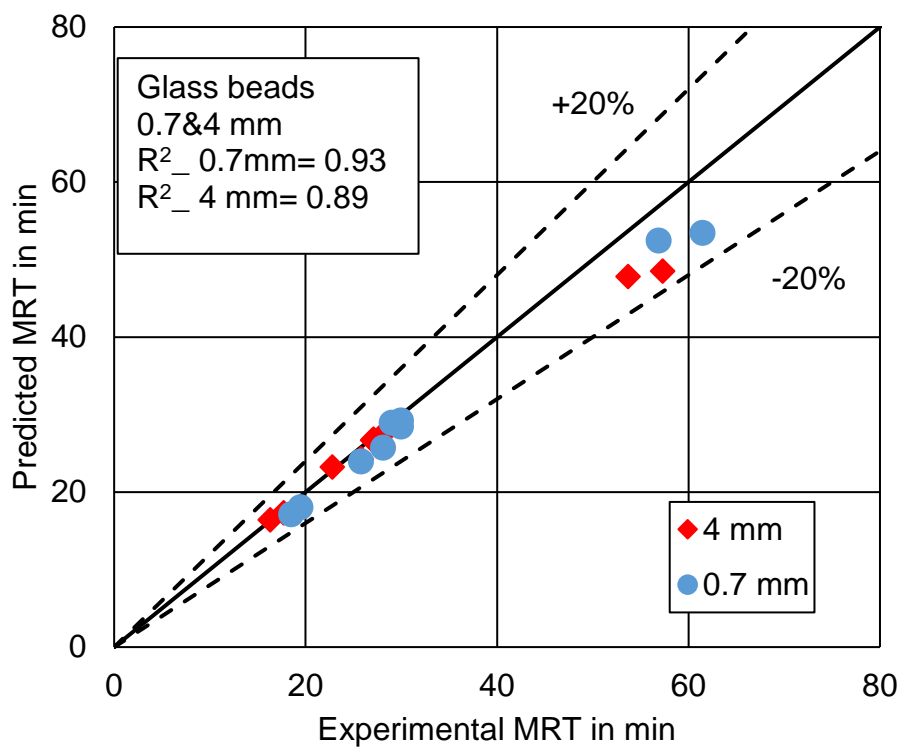


**Figure 3.13** Comparison of predicted and experimental MRT of 0.7&4 mm bidisperse system

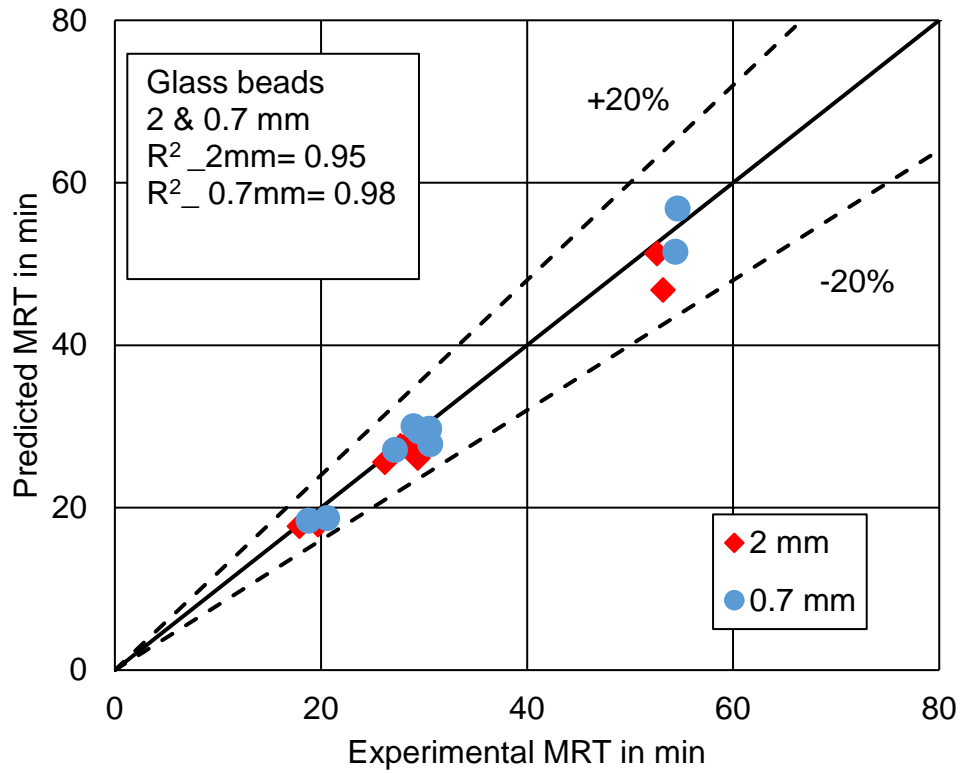


**Figure 3.14** Comparison of predicted and experimental MRT of 0.7&2 mm bidisperse system



**Figure 3.15** Particle bed of 0.7&4 mm mixing particles

### 3.3.3.2 Axial dispersion analysis

Based on the knowledge of statistics, the equation 3.45 could also be implemented to predict the RTD of bi- and polydisperse system. There are 3 unknown variables in this formula which are B,  $\bar{t}$  and Pe. In ideal condition, B equals to 1.  $\bar{t}$  is the MRT of each particle size fraction and could be derived with the model in chapter 3.2. With MRT, the mean velocity of particle transport through the kiln could also be calculated. Hence, for equation 3.45, Pe is only one unknown parameter of axial dispersion coefficient. Based on equation 3.40, the prediction of Pe could be determined through  $D_z$  which is generally estimated by empirical equations. Scherritt et al. (2001) introduced the following equation to predict the axial dispersion coefficient  $D_z$

$$D_z = 0.0011 \left( \frac{n}{n_c} \right)^{0.39} (2R)^{1.15} (d_p)^{0.46} F^{-0.43}, \quad (3.47)$$

$$n_c = \frac{60}{2\pi} \sqrt{\frac{g}{R}}, \quad (3.48)$$

and had good agreement with his experimental data, where n is the kiln rotational speed with unit rpm,  $n_c$  is the critical speed, R is the kiln inner radius in m,  $d_p$  is the particle diameter in m and F is the filling degree of hold-up.

However, Njeng et al. indicated that the empirical of Scherritt et al. (2001) had bad performance in predicting the axial dispersion coefficient in his experiments. The experiments were done within a kiln with lifters. Hence, a new formula was developed by adding all the operational parameters within experiments. Because of no lifters in our kiln, there is no component for the influence of lifters and the model is simplified as

$$D_z = 1.2 * 10^{-7} \left( \frac{\dot{M}_s}{\rho_b} \right)^{-0.871} (n\beta)^{1.674} (\Theta d_p)^{0.435} 2R, \quad (3.49)$$

where  $\dot{M}_s$  is the feed mass flow rate in kg/h,  $\rho_b$  is the bulk density in kg/m<sup>3</sup>,  $\Theta$  is the dynamic angle of repose in degree.

The two correlations above are utilized here to predict the axial dispersion coefficient in bidisperse at first and the results are shown in Figure 3.16.

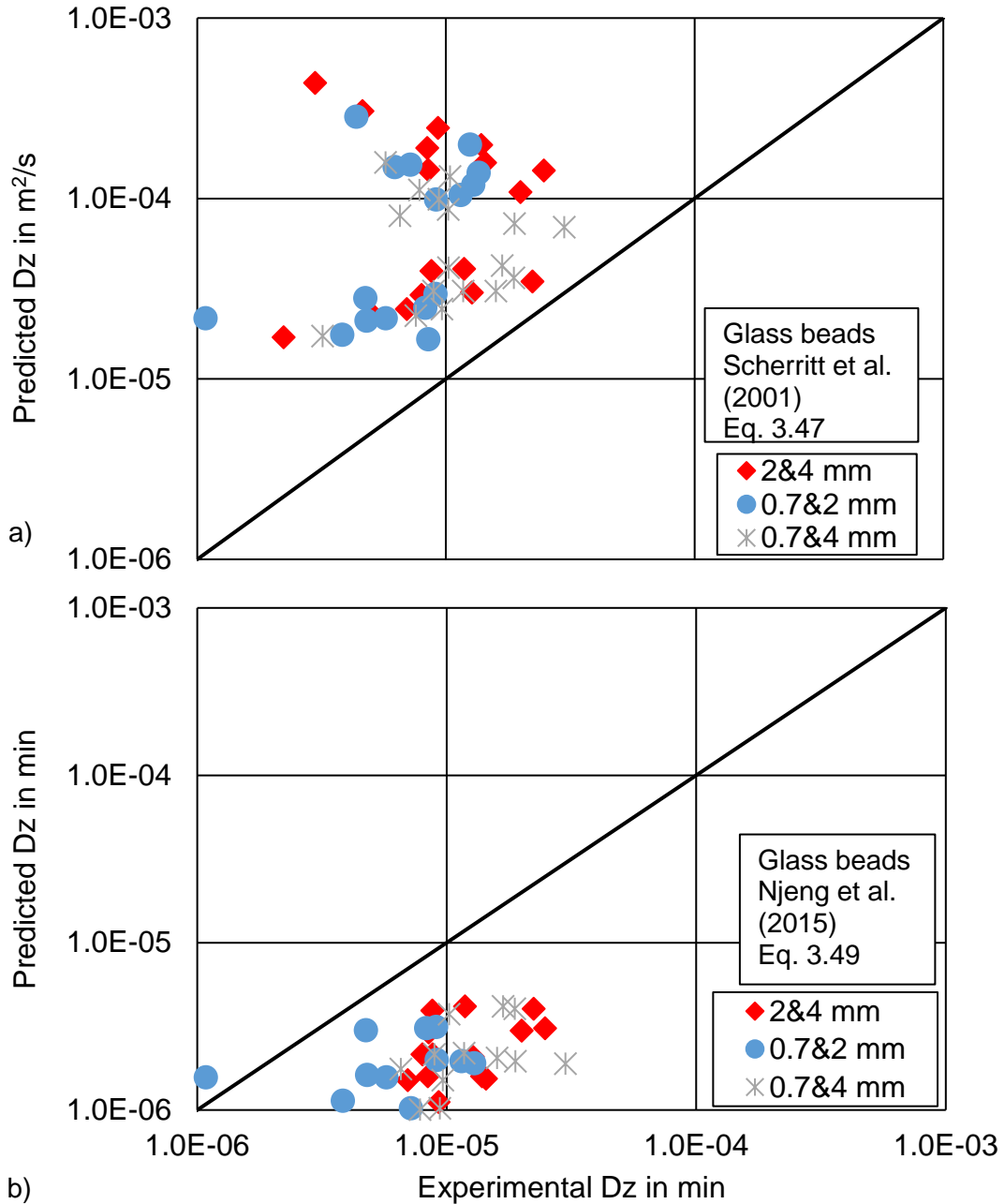


**Figure 3.16** Comparison of axial dispersion coefficient values between predicted and experimental values with models from literatures

It is clear to see that both empirical models from literatures do not match well with experimental values in bidisperse particle system, while the both two models do not contain the components of particle fractions. Hence, a new model based on equation 3.47 is built to describe the axial dispersion coefficient in bidisperse as

$$D_z = 2kR \left( \frac{M}{\rho_b} \right)^a n^b \beta^c \Theta^d d_p^e F^f X^g, \quad (3.50)$$

where F is the total filling degree of particle bed, a, b, c, d, e, f, g and k are all parameters and the values are presented in table 3.3. The comparison between experimental and predicted values are shown in Figure 3.17

**Table 3.3** Parameters for the axial dispersion coefficient in equation 3.50

Parameters	Value	Standard error	Confidence interval	
a	2.1758	1.1951	-0.2297	4.5814
b	-0.4116	1.1413	-2.7089	1.8857
c	-0.5839	0.9834	-2.5633	1.3955
d	-2.9820	1.5624	-6.1269	0.1630
e	-0.0172	0.0690	-0.1561	0.1216
f	-1.8484	1.1393	-4.1417	0.4449
g	0.0081	0.3161	-0.6281	0.6444
k	1.0226	5.2202	-9.4851	11.5303

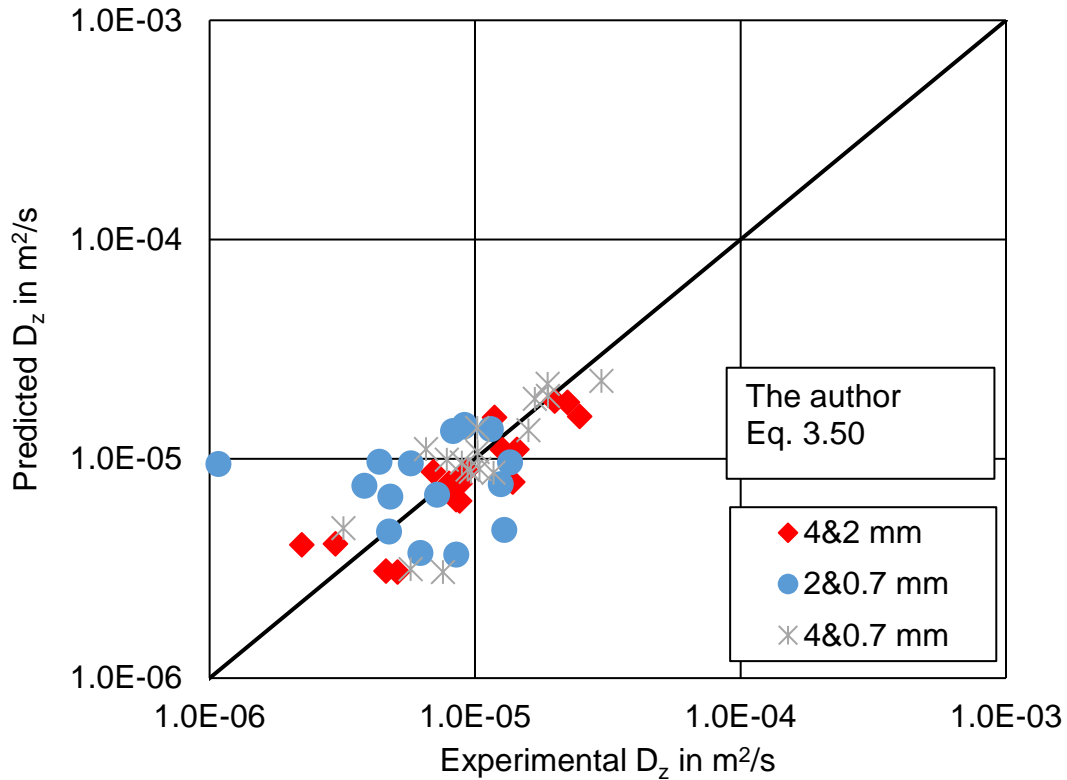


**Figure 3.17** Comparison of axial dispersion coefficient values between predicted and experimental values with equation 3.50

In Figure 3.17, the predicted values show good agreement with experimental data compared to the models from literatures above. That means, as mentioned before, the models of Sherritt et al. and Njeng et al. appeared to be not truly containing the influence of operational conditions and particle size fractions. In contrast, equation 3.50 contains all operational parameters that could influence the axial dispersion in polydisperse system.

Furthermore, it is obviously that some parameters of equation 3.50 in Table 3.3 are extremely small such as  $e$  and  $g$  which means the influence of particle diameter and particle size fraction could be neglected. Therefore, equation 3.50 will be simplified as

$$D_z = 2R \left( \frac{M}{\rho_b} \right)^2 n^{-0.5} \beta^{-0.6} \Theta^{-3} F^{-1.8}, \quad (3.51)$$

where  $k = 1$ ,  $a = 2$ ,  $b = -0.5$ ,  $c = -0.6$ ,  $d = -3$  and  $f = -1.8$ . The comparison between predicted values of  $D_z$  based on equation 3.50 and experimental values are shown in Figure 3.18 which shows also good agreements between each other. That means the dynamic angle of repose and filling degree will also contain the influence of varied particle diameter and particle size fraction and that is also the reason why in equation 3.50 the values of “g” and “e” are quite small.

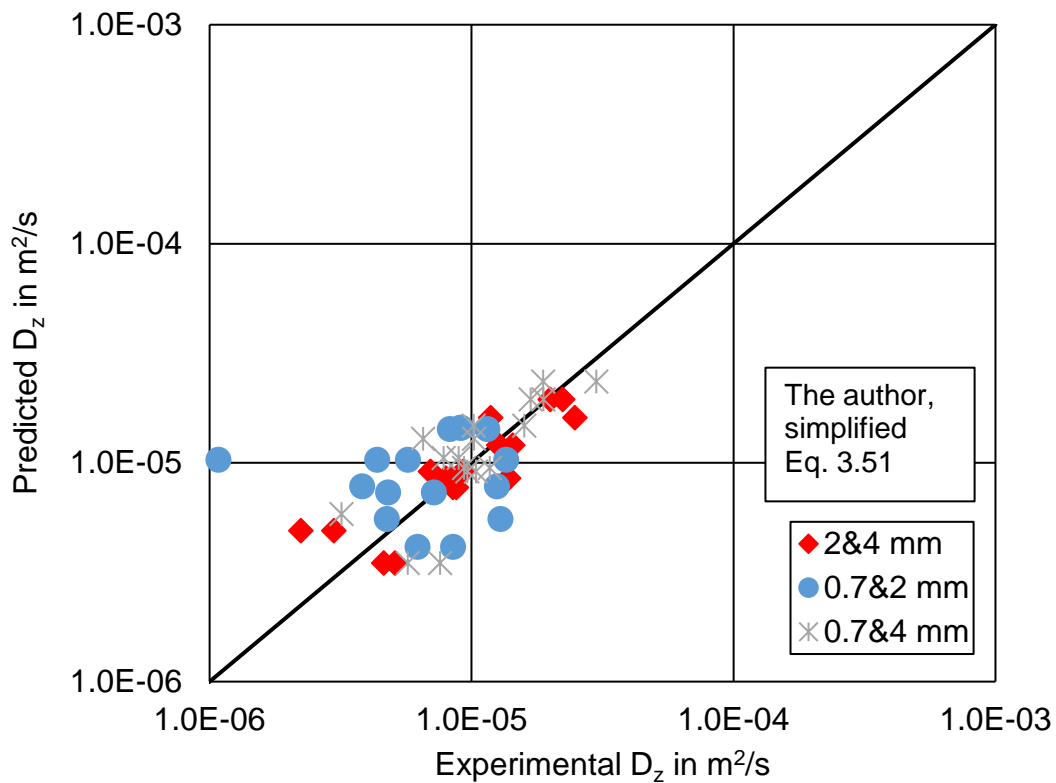


**Figure 3.18** Comparison of axial dispersion coefficient values between predicted and experimental values with equation 3.51



## 3.4 Results and discussion

### 3.4.1 Influence of rotational speed

The influence of rotational speed on the RTD in a bidisperse bulk bed is shown in Figure 3.19 with a constant feed mass flow rate of 100 kg/h and a kiln inclination of 2 °. The experimental values are shown as points and the fitting values are shown as lines. For each kind of mixing fraction, the solid line represents big particles and the dotted line means small particles. It is clear to see that for all three different mixing fractions, the small particles always have larger residence time than big one regardless of varied rotational speed. In the same time, the peak value of the fitting curve which has been introduced previously as MRT of each particle size fraction will decrease with higher rotational speed.

Furthermore, under the same operational conditions, all three kinds of mixing particles have similar residence time behavior especially with high rotational speed. Therefore, the MRT, deviation of fitting curves  $\sigma^2$ , the axial dispersion coefficient  $D_z$  and Peclet number  $Pe$  are selected to make further analysis of the influence of rotational speed and the results are all shown in Figure 3.20.

The connection between MRT and rotational speed is indicated in Figure 3.20 (a). As mentioned before, for all kinds of mixing fractions, big particles will always have shorter MRT than small particles regardless of rotational speed. In the same time, the MRT difference between big and small particles will be decreased with increasing rotational speed. To make the analysis in detail, a predicted MRT equation in monodisperse particle system by Sullivan et al. (1927) is implemented as

$$MRT = 1.77 \cdot \frac{L}{D} \cdot \frac{\sqrt{\Theta}}{n \cdot \beta}. \quad (3.51)$$

It is clear to see that with constant kiln length  $L$ , inner diameter  $D$  and dynamic angle of repose  $\Theta$ , the MRT is inversely proportional to the rotational speed of the kiln as well as inclination angle. In Figure 3.20 (a1), for 2&4 mm mixing particles, with increasing rotational speed from 1 rpm to 2 rpm, the MRT for 4 mm decrease from 50 min to 26 min as well as 2 mm particles from 52 min to 27 min which are both 50% decrement. Similarly, the increased rotational speed from 1 rpm to 3 rpm also leads to approximately 2/3 reducing of MRT for both 4 mm and 2 mm particles. Furthermore, in Figure 3.20 (a2) and (a3), it could also be observed that, this pattern still exists regardless of particle mixing status. Therefore, it could be indicated that in bidisperse particle system, rotational speed has the same influence on MRT as in monodisperse particle system.

The influence of rotational speed on deviation of fitting curves are shown in Figure 3.20 (b). From the knowledge of statistic, the smaller  $\sigma^2$  is, the more concentrated distribution will be. And the shape of the RTD curve will be thinner and higher. In figures, it is clear to see that in most case, the small particle has higher value of  $\sigma^2$  than the big particle especially for rolling model and the differences are almost constant. That means the small particle has wider tracer particle band and more dispersed residence time distributions. In contrast, for slipping and slumping motion, there is no big difference between big and small particles. On the other hand, the value of  $\sigma^2$  will decrease with increasing rotational speed for all large and small particles.

The connections between axial dispersion and rotational speed are described in Figure 3.20 (c). The increment of rotational speed will cause a remarkable raising of axial dispersion coefficient. As mentioned in chapter 3.3.3.1, the large  $D_z$  means rapidly spreading of the tracer curve. However, based on equation 3.39 and 3.45, it shows that the width of the RTD curve is not just only dominated by  $D_z$  but also by the residence time. Therefore, the high rotational speed of kiln just leads to high value of axial dispersion coefficient but finally small width of RTD curve, whereas the residence time

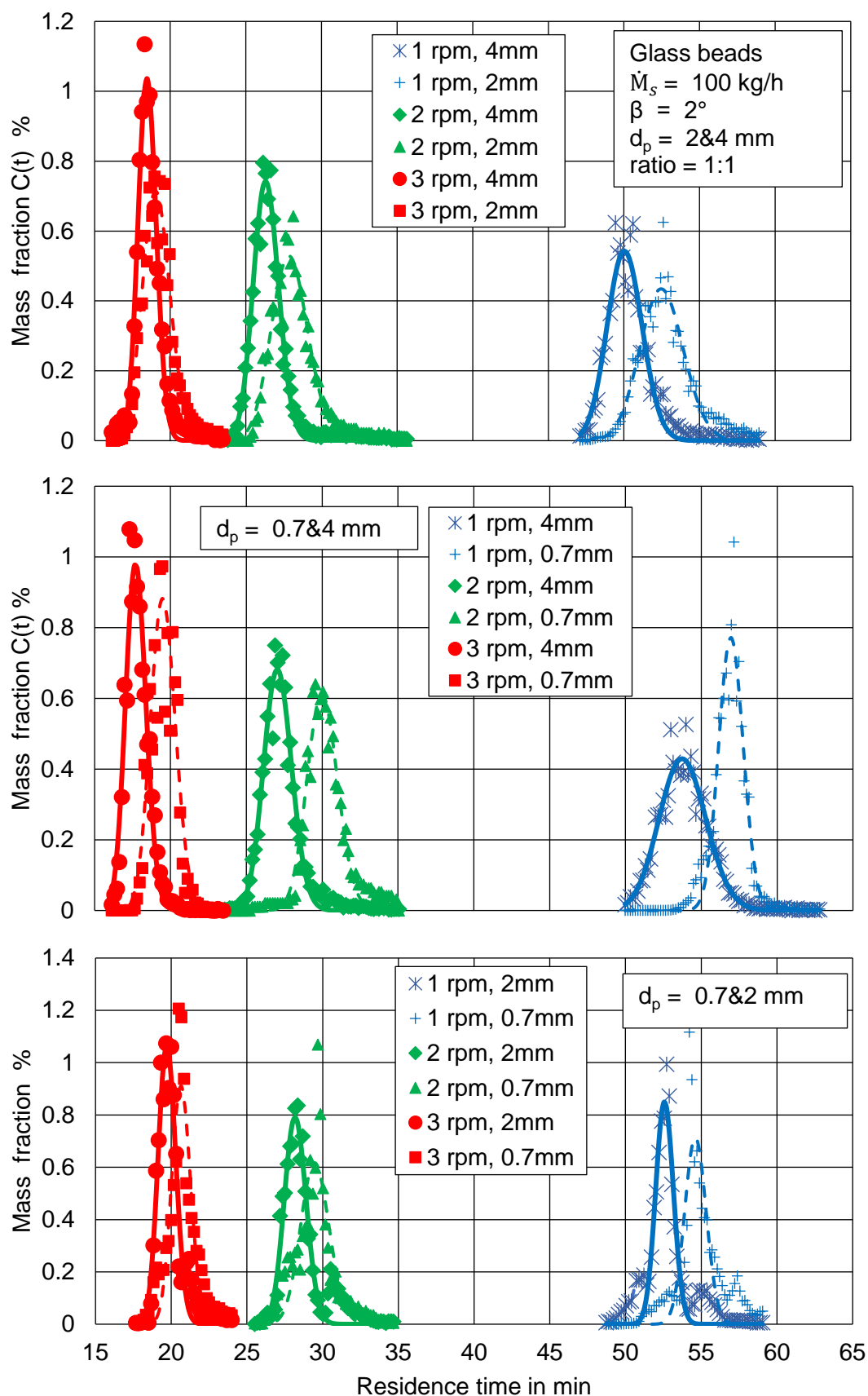


**Figure 3.19.** Effect of the rotational speed on the RTD for different mixing particles

is the dominant factor in forming the RTD comparing to axial dispersion coefficient.

For 2&4 mm mixing particles, the 2 mm particles always have large axial dispersion coefficient than 4 mm particles. The difference between them is quite small with 1 rpm rotational speed and is enlarged rapidly with increasing rotational speed. In contrast, for 0.7&4 mm and 0.7&2 mm particles, although  $D_z$  is enlarged with increasing rotational speed, but there is nearly no difference between big and small particles. The major reason of this tendency is big particle diameter difference. For these two mixing particles, the differences of the diameter are above 5 and 3 times separately. These big particle size difference will cause bad particle transverse motion behavior (the example and explanation has already introduced in chapter 3.3.3.1). Therefore, the 4 mm particle will have large  $D_z$  by mixing with 2 mm particles than with 0.7 mm particles under same operational conditions.

The influence of rotational speed on Peclet number (Pe) is shown in Figure 3.20 (d). Based on the definition of Peclet number, large Pe value means that the particle axial transport is the major motion of whole process and the diffusion could be neglected. Therefore, with low rotational speed, the  $D_z$  is quite small and lead to relatively large Pe which will be reduced with increasing rotational speed. It should be noted that, from equation 3.39, the mean axial velocity  $u$  is another parameter to influence the Pe. And the velocity will raise with increasing rotational speed. Hence, by combining the influence of  $D_z$  and  $u$ , the difference of Pe between big and small particle will become small and the value of every mixing particles is almost the same with equal rotational speed. Moreover, comparing the figure of  $\sigma^2$  it indicates that although high rotational speed leads to strong axial dispersion and small Pe, the variance is small and the RTD curve is narrow. In contrast, the low rotational speed has large Pe but big variance and wide RTD curve. Therefore, this means, the MRT is a more important value of the final axial dispersion than Pe.

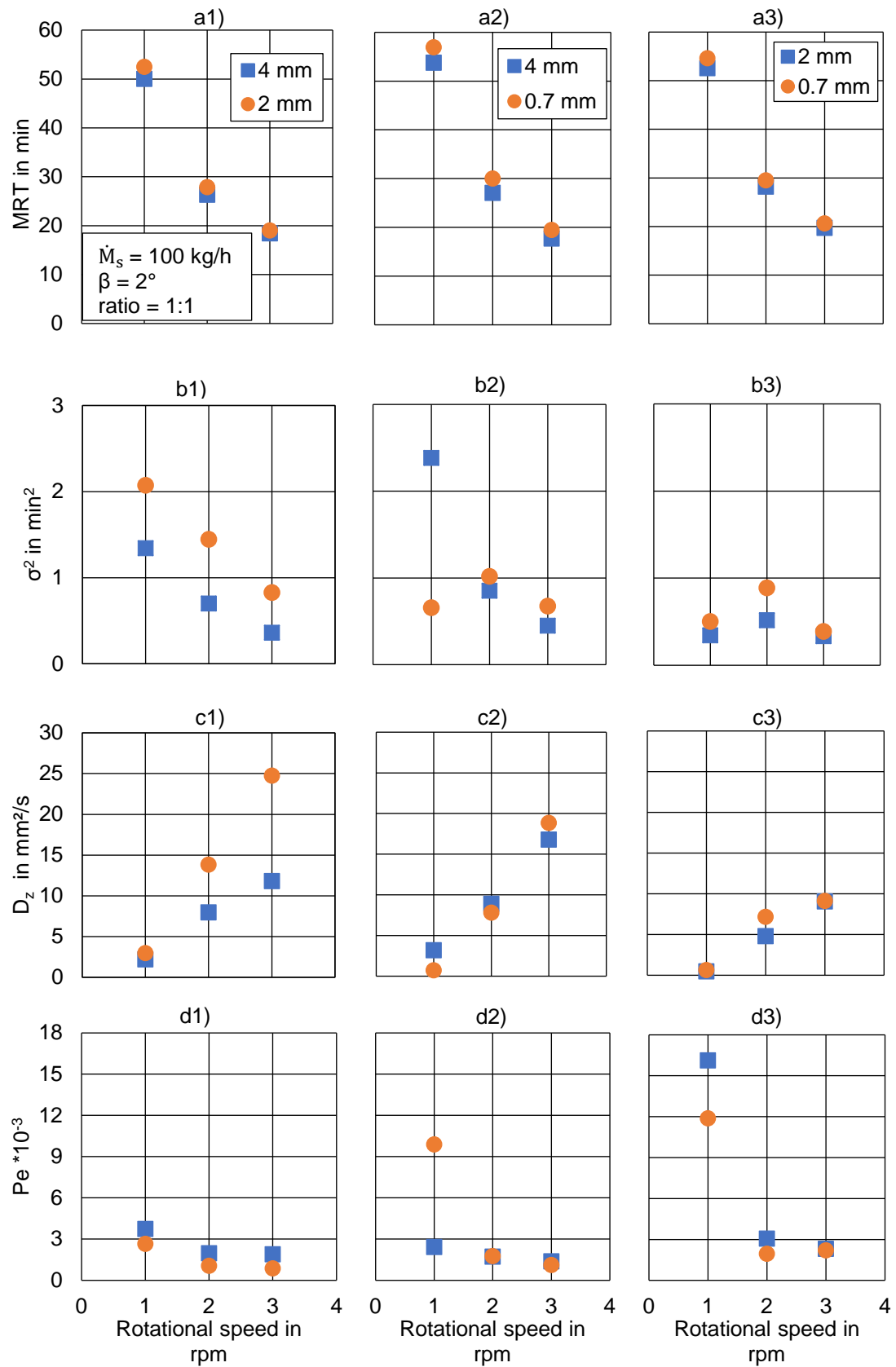


**Figure 3.20** Influence of rotational speed on MRT, variance, axial dispersion coefficient and Peclet number

There are two exceptional cases in the figures which are the  $\sigma^2$  and Pe of 0.7&4 mm and 0.7&2 mm mixing particle under 1 rpm condition (see Figure 3.20 b2, b3, d2, d3). For 0.7&4 mm particles, the  $\sigma^2$  of 0.7 mm is much smaller and Pe is much larger than the value of 4 mm. After comparing with other two particle fractions, it could be concluded that the 0.7 mm particle has quite small axial diffusion by mixing with 4 mm although has a quite large MRT. Similarly, for 0.7&2 mm particles, both big and small particle has quite small variance and huge Pe under 1 rpm. That means, these mixed particles have quite bad axial dispersion with low rotational speed. The explanation of these two cases is already introduced in chapter 3.3.3.1 that if mixing particle has smooth surface and big particle size difference, the small particle will not transport in the active layer and directly drop down towards the bottom of particle bed. This will create a quite smooth surface between particle bed and kiln wall surface which will cause slumping or slipping of transverse motion and quite small axial dispersion.

### 3.4.2 Influence of inclination angle

The RTD curves with varied inclination angles are presented in Figure 3.21. The results are shown under a mass flow of 100 kg/h, a rotational speed of 2 rpm and 1:1 mixing bidisperse bulk bed. The inclination angles are varied from 1 to 3°. All the results are shown with the same format as in Figure 3.19 where the points and the lines are experimental and fitting value separately. The solid lines and dashed lines represent the big and small particles separately. In overall view, the RTD curve will be wide and low with small inclination angle but narrow and high with large angle. That means, the MRT and the axial dispersion will both increase with reducing inclination angle. To make further analysis in detail, MRT, deviation of the fitting curve  $\sigma^2$ , axial dispersion coefficient  $D_z$  and Pe are also selected as specific parameters and all the results are shown in Figure 3.22.

Figure 3.22 (a) shows the relationship between MRT and inclination angles. It is found that with increasing angle, the MRT will decrease rapidly especially from 1° to 2°. The MRT of big particles are always shorter than small one but the difference between big and small particles are not so huge which are all less than 5 min. By combining Figure 3.21, this MRT difference will enlarge with decreasing inclination angles. For all kinds of mixing particles, the MRT with 2 and 3 ° inclination angle are all around 30 and 20 min and only under 1° angle condition has relatively big difference. In this case, 0.7&4 mm particles have longest MRT about 60 min, 0.7&2 mm particles are around 55 min and 2&4 mm are 50 min. That means, for big particles, mixing with small particles will decrease the axial transport velocity and enlarge the MRT. In contrast, for small particles, mixing with big one will decrease the MRT especially under low inclination angle.

From the Figure 3.23 (b) it is clear to see that the variance of the mixing particle decreases with increasing inclination angle which means the RTD curve will be narrow with the increments of inclination angles. Furthermore, there is a huge gap of variance

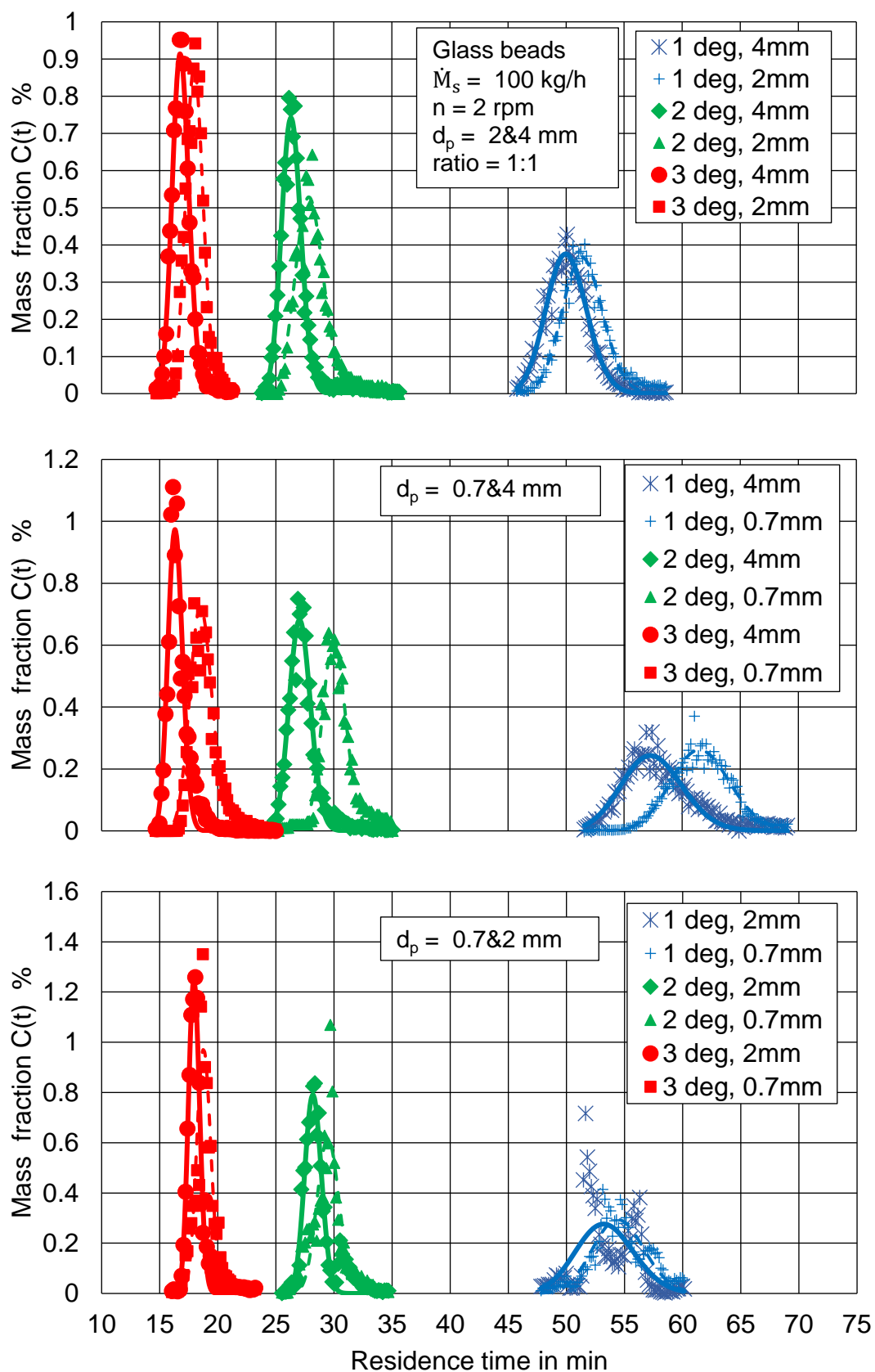


**Figure 3.21** Effect of the inclination angle on the RTD for different mixing particles



between  $1^\circ$  and  $2^\circ$  inclination angle condition especially for 0.7&4 mm and 0.7&2 mm mixing particles. That means, with low inclination angles, the final axial dispersion is much stronger than with large angles. By contrast, the variance difference between  $2^\circ$  and  $3^\circ$  is much smaller which could be easily observed from Figure 3.20. By considering the influence of particle mixing status, for  $1^\circ$  angle condition, the variance of 2&4 mm particles is about 3 which is smaller than 0.7&4 mm with 6.8 and 0.7&2 mm with 5. If only comparing the value of 4 mm and 2 mm separately, the variance will enlarge by mixing with smaller particles, whereas reduce with bigger particles. That is to say, mixing with smaller particle could increase the final axial dispersion especially under low inclination angle condition.

The results of axial dispersion coefficients  $D_z$  are presented in Figure 3.22 (c). For 2&4 mm and 0.7&4 mm, the  $D_z$  will increase with enlarged inclination angle but for 0.7&2 mm particles, slightly increase or almost constant which means increasing inclination angle will have small influence on  $D_z$  especially for small size mixing particles. On the other hand, all the 4 mm particles mostly have the closed  $D_z$  value under same operational conditions especially with low inclinational angles. That means, normally, for big particle diameter the particle mixing status will cause less influence on axial dispersion coefficient than operational parameters.

Furthermore, for all mixing material, the  $D_z$  values of big and small particles have no big differences except  $2^\circ$  angle of 2&4 mm and  $3^\circ$  of 0.7&4 mm. For 0.7&4 mm particles, as mentioned before, large particle size difference leads to no rolling model in cross-section view and no ring-core structure which means large amount of big and small particles are well mixed. Hence, there are high interaction between particles exists due to the high axial velocity. Considering the large size and weight differences of the single particle, small particles will have more influence than big one which leads to the enlarged axial dispersion coefficient obviously. However, for 2&4 mm the deviation difference between big and small particles is not so huge as 0.7&4 mm and the reason

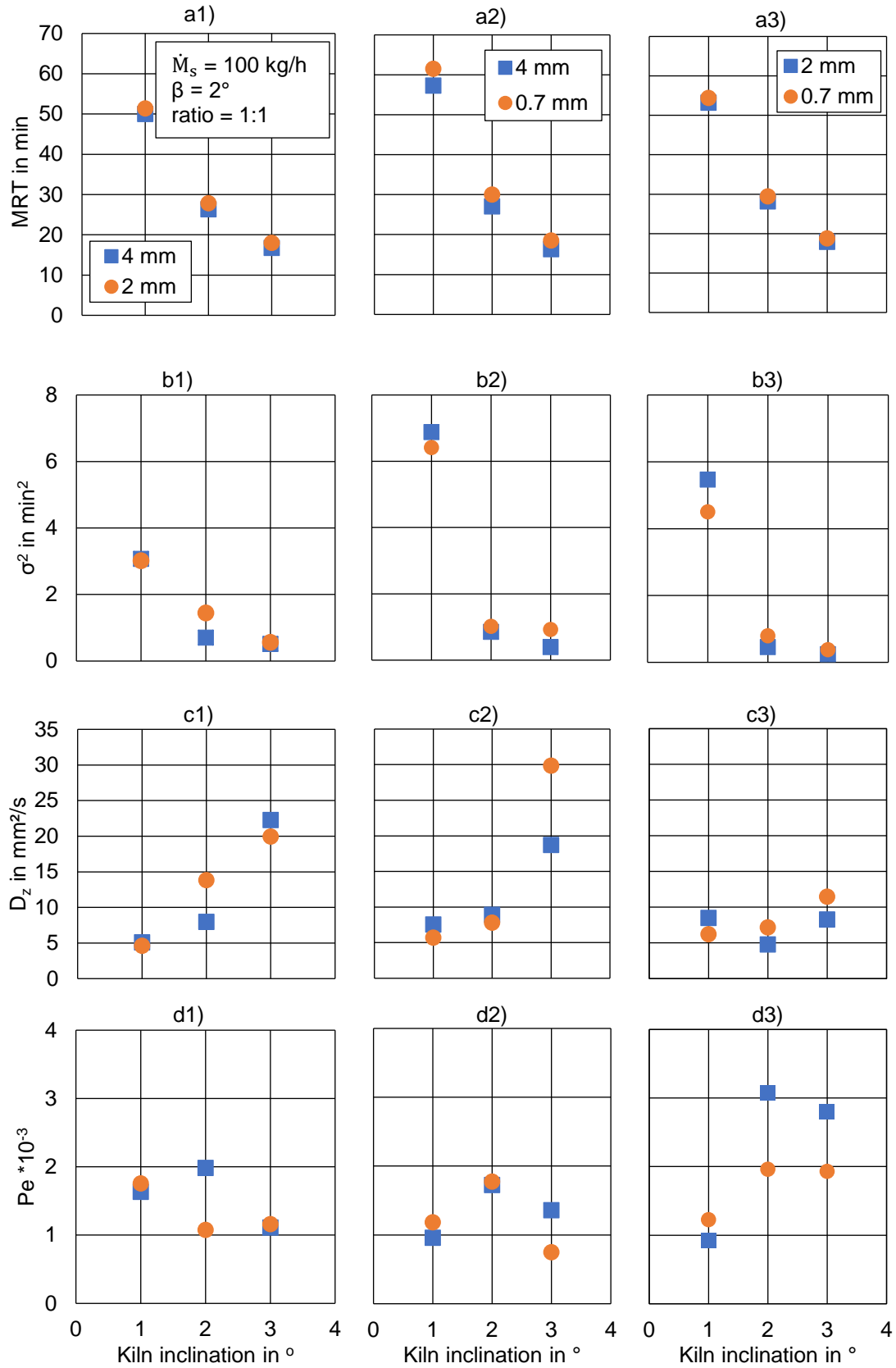


**Figure 3.22.** Influence of inclination angle on MRT, variance, axial dispersion coefficient and Peclet number

is unclear by physical phenomenon.

The influence between the Peclet number and the inclination angle are presented in Figure 3.22 (d). For 2&4 mm and 0.7&4 mm particles, the Pe values are all between 1000 and 2000 regardless of changing inclination angles. That means, although the  $D_z$  will enlarge with increasing inclination angle, the increased axial velocity will counteract the increment at the same time. For 0.7&2 mm particles, this offsetting behavior is more obvious and the axial velocity has more influence than  $D_z$  especially under 2 and 3 ° inclination angles.

### 3.4.3 Influence of feed mass flow rate

The RTD curve with varied feed mass flow rate are introduced in Figure 3.23. All the RTD are under 2 rpm, 2 ° inclination angle and 1:1 mixing bidisperse particle materials conditions. The curves are in the time range from 20 to 40 min and the MRT of each curve are concentrated especially for 2&4 mm and 0.7&2 mm particles. The width of each RTD curve seems also closed by rough estimating which means the feed mass flow rate has almost no influence on RTD for all kinds of mixing particles. Therefore, to make further analysis in detail, MRT, deviation of the fitting curve  $\sigma^2$ , axial dispersion coefficient  $D_z$  and Pe are also selected as specific parameters and all the results are shown in Figure 3.24.

The influence between feed mass flow rate and MRT are introduced in Figure 3.24 (a). With increasing feed mass flow rate, the most MRT are in the range from 25 to 30 min. For 2&4 mm and 0.7&2 mm, the MRT decrease slightly with raising feed mass flow rate. In contrast, the 0.7&4 mm particles have the opposite tendency. Moreover, for one mixing materials, the big and small particles have nearly no time differences except 0.7&4 mm materials. The results from Bensmann et al. (2010) could be utilized to support some evidence. His experiments operated with polydisperse quartz sand which had continuous particle size distributions. The results indicated that the increasing feed mass flow rate could decrease the MRT. In the same time, the larger particle size difference was, the bigger MRT difference would be. Hence, in our experiments, the relatively large MRT difference of 0.7&4 mm mixing particles is correct. On the other hand, the low feed mass flow rate 50 kg/h brings quite small filling degree, about 2% of the kiln. This small filling degree leads to quite thin particle bed in the first half part of the kiln. Due to the large particle size difference, lots of particles are distributed in the kiln inner surface and causes slipping or even worse transverse motion. Therefore, both big and small particles will slowly move towards the discharge end without transverse mixing. However, this phenomenon will not exist in large feed mass flow rate.

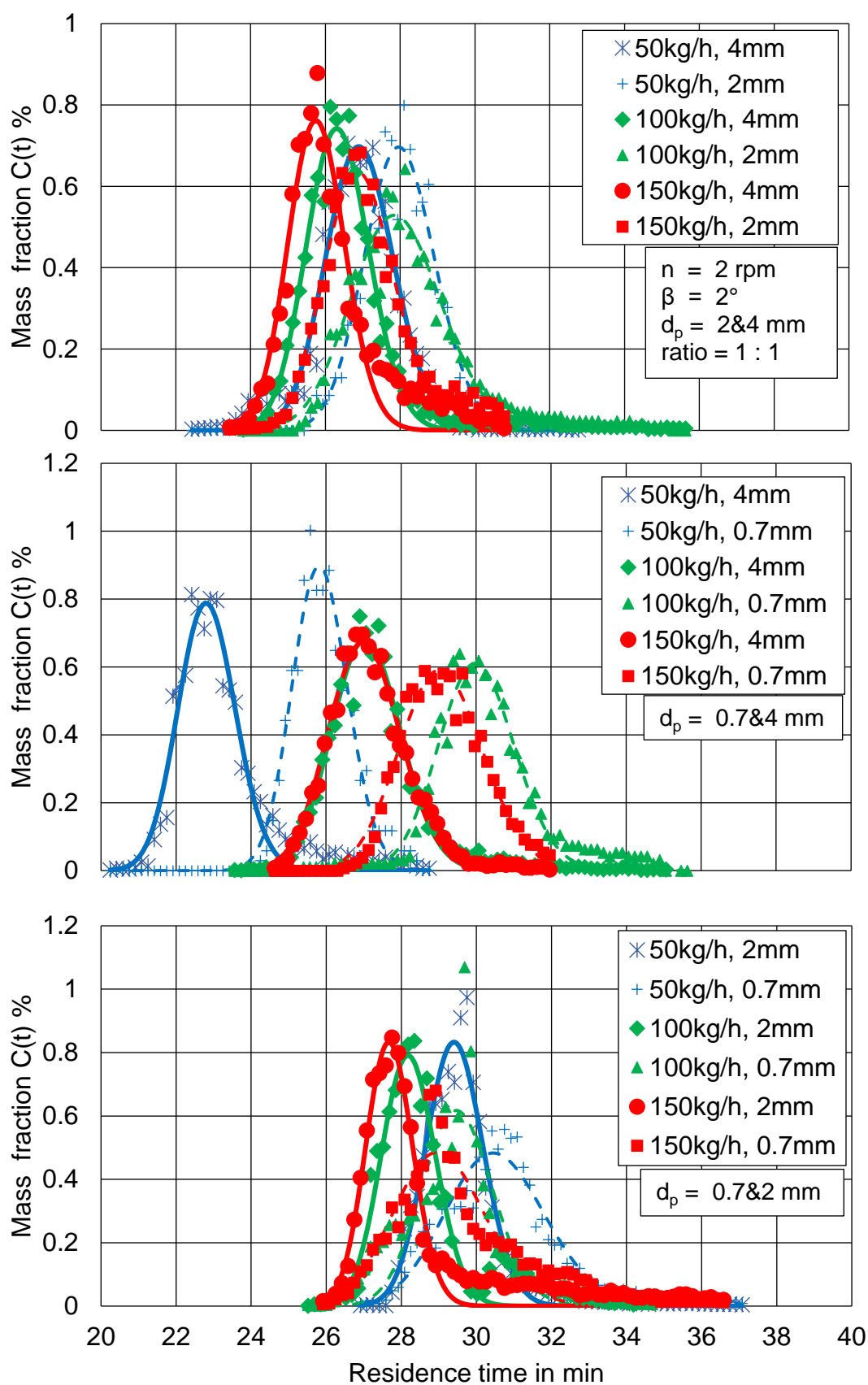


**Figure 3.23** Effect of the feed mass flow rate on the RTD for different mixing particles

The results about variance are shown in Figure 3.24 (b). Based on the results from Njeng et al. (2015), it could be known that the increasing feed mass flow rate will decrease the variance in monodisperse system. Therefore, by comparing with our data, it is found that for 2&4 mm and 0.7&2 mm particles, big particles have the similar pattern as monodisperse system and the degree of decrement is quite small. However, this tendency is not fit well for small particles especially for the case of high mass flow rate with 0.7&2 mm bulk materials. The high number of particles will cause more particle collisions which could lead to large axial dispersion for small particles.

The pattern of variance for 0.7&4 mm particles is opposite to other 2 mixing materials. In this time, as we have described before, the slipping motion and fast axial velocity lead to small variance at first. With increasing feed mass flow rate, the high filling degree brings high potential energy and more particle could have stronger transverse motion. In the same time, the high number of particles lead to more collisions between all particles which causes large variance.

The pattern and explanations could also be used in axial dispersion coefficient  $D_z$  and Peclet number  $Pe$ . For each mixing particles, the MRT is almost constant with changing feed mass flow rate. From equation 3.39 and 3.45, if MRT is constant,  $D_z$  and  $1/Pe$  will follow the tendency of variance which could easily be observed from Figure 3.24 (c) and d). Therefore, the  $D_z$  could also represent the final axial dispersion as variance if only the feed mass flow rate varied.

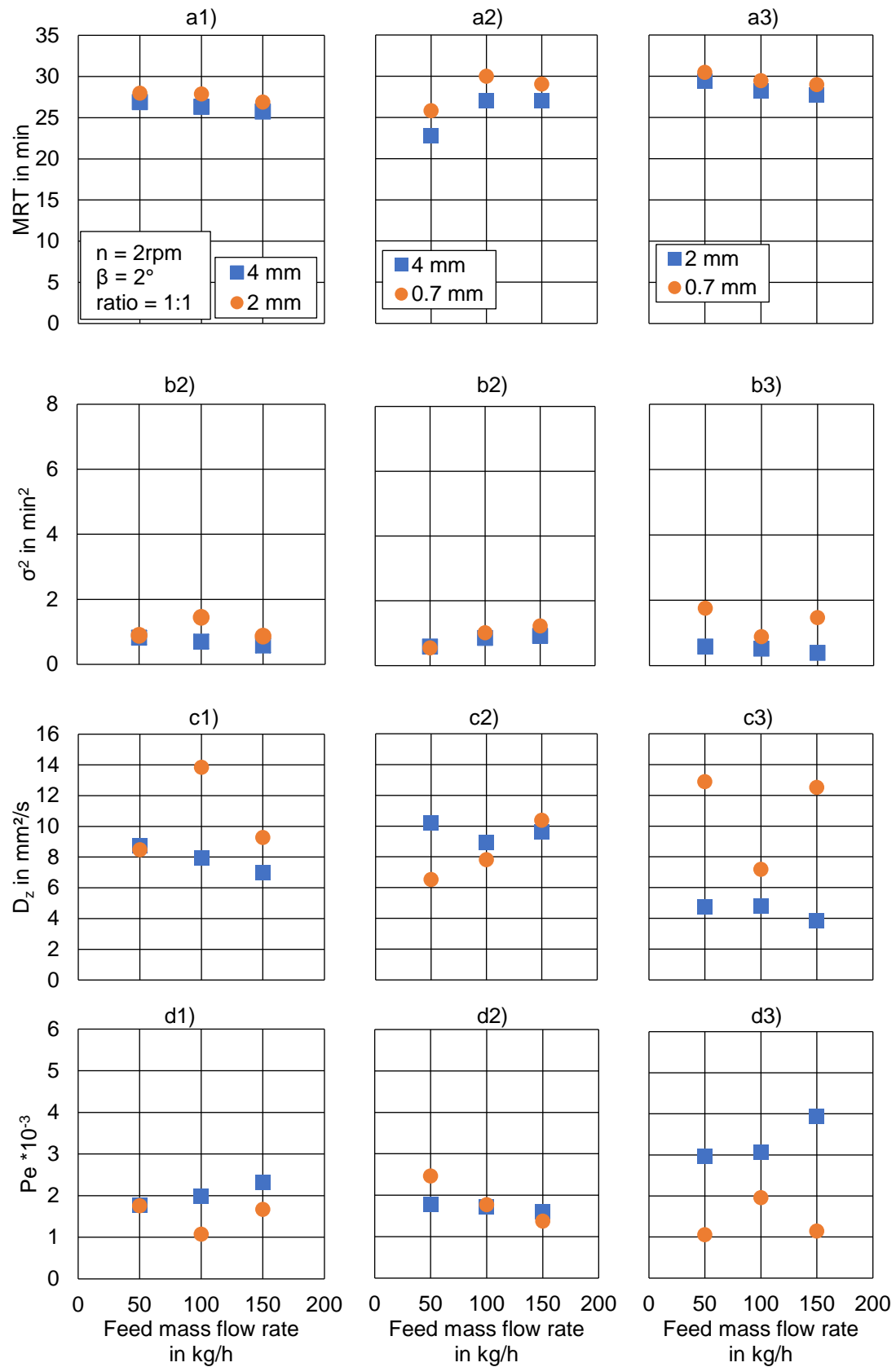


**Figure 3.24** Influence of feed mass flow rate on MRT, variance, axial dispersion coefficient and Peclet number

### 3.4.4 Influence of particle size

For bidisperse particle system, the ratio of big and small particles is also an important parameter effecting RTD. The results of RTD curve with different particle ratio are presented in Figure 3.25. In general, for 2&4 mm and 0.7&4 mm particles, the MRT will decrease with increasing big particle ratio and the width of RTD keeps constant. For 0.7&2 mm particles, it seems a little different with other 2 mixing particles. Therefore, MRT, deviation of the fitting curve  $\sigma^2$ , axial dispersion coefficient  $D_z$  and  $Pe$  are also selected as specific parameters and all the results are shown in Figure 3.26.

For monodisperse materials, based on the study of Liu (2006), the particle diameter will not affect the MRT. However, from Figure 3.26 (a), for 2&4 mm and 0.7&4 mm particles, the MRT decreases with increasing 4 mm particle fraction ratio. By implementing the model in chapter 2, the theoretical MRT of monodisperse under 2 rpm,  $2^\circ$  are all 28.5 min. In Figure 3.26 (a) the x label is the mass ratio between big and small particles in range 0 to 1. If  $x = 0$ , there is no big particle, just small one, whereas with  $x = 1$ , no small particles occurs.

The ideal MRT of monodisperse system could be estimated based on Saeman's model in chapter 2 which is 28.5 min. By comparing with 2&4 mm mixing particles, 28.5 min is equals to the 2 mm particles with 67% of mass ratios. In this case, the particle bed is more closed to pure 2 mm particles and 4 mm particles are just dispersed in the particle bed which has small influence on transverse and axial motion. With increasing 4 mm particles mass ratio, from 0.33 to 0.67, the particle bed will approaching monodisperse system again. However, as it is mentioned before, due to the particle size difference, the small particles located in the gap of big particles will reduce the friction between particle bed and inner wall surface. Hence, the particle bed will have slipping or slumping motion which reduces the dynamic angle of repose.

According to the study of Sullivan et al. (1927) and Chatterjee et al. (1983b), the



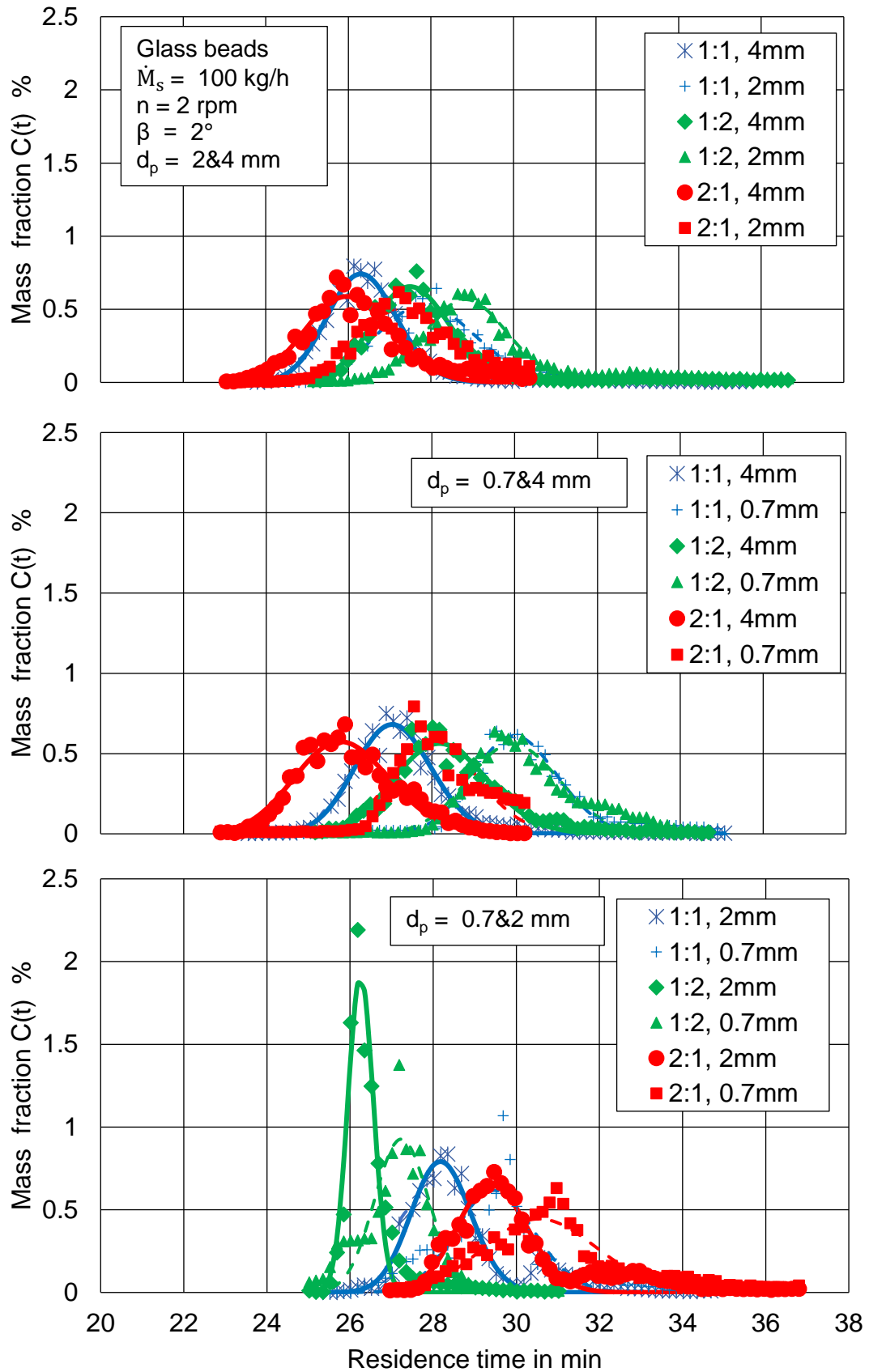


**Figure 3.25** Effect of the particle size fraction on the RTD for different mixing particles

dynamic angle of repose has positive correlation with MRT. That means, reducing dynamic angle of repose will lead to the decrement of residence time and it also appears with 0.7&4 mm mixing particles.

In contrast, for the mixing particle of 0.7&2 mm, the increment of particle mass ratio will enlarge the dynamic angle of repose (see Appendix B). Therefore, the MRT of 0.7&2 mm particles has the opposite pattern to other two mixing status.

The connections between variance and particle size fraction is shown in Figure 3.36 (b). For 2&4 mm and 0.7&4 mm mixing materials, the variance both fluctuate around 1. In these cases, the 4 mm particle will first decrease with increasing mass fraction then increase again which seems as a “V” curve. For 0.33 fraction, the particle bed is considered as mainly structured of small particles. Hence, the big and small particle has similar variance. While the mass fraction is 0.5, the increasing big particles bring more voids and the small particles disperse in the gaps which causes bad transverse motion and low variance especially with 0.7 mm particles. After the fraction increasing to 0.67, the small particle has less influence on transverse motion because of reducing amount. The particle bed approaches to pure big particle bed and the variance could also increase. In this time, the big and small particles also have similar variance of RTD curve. This pattern could also be implemented to explain the axial dispersion coefficient and Peclet number where the results are shown in Figure 3.36 (c) and (d).

In addition, for 0.7&2 mm particles, with increasing of 2 mm particle fraction, the variance will increase especially for 0.7 mm particles. Meanwhile the variance value of 2 mm particles is quite small compared to other two mixing materials. By considering the dynamic angle of repose, it is found that, for 0.33 fraction, the mixing particle has quite bad transverse motion where the whole particle bed is mainly composed as pure 0.7 mm particles and the pure 0.7 mm particles have quite bad slumping motion because of smooth bulk bed surface.

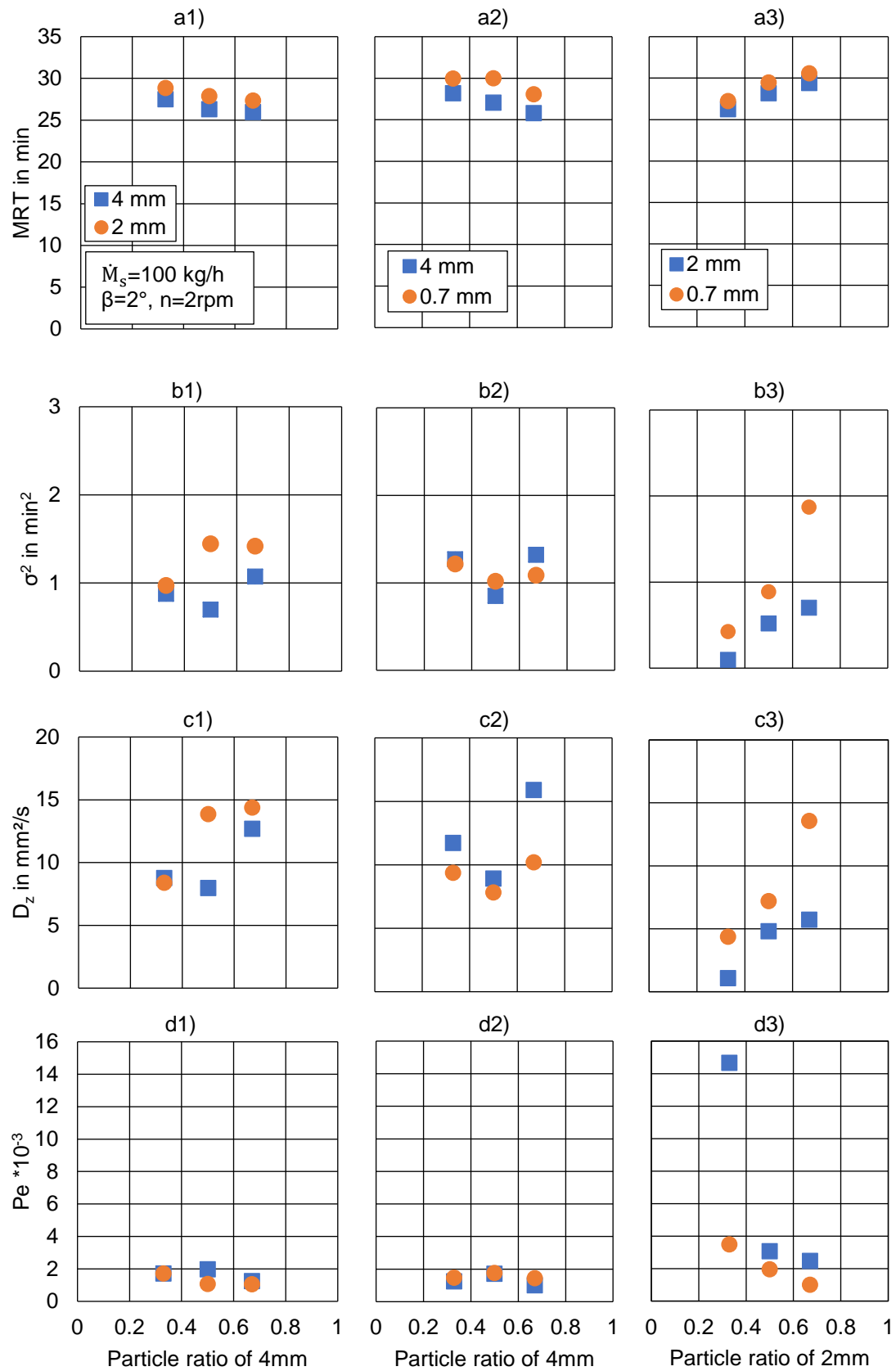


**Figure 3.26** Influence of particle size fraction on MRT, variance, axial dispersion coefficient and Peclet number

On the other hand, the 2 mm particle is smaller and lighter than the 4 mm particle. Hence, the most 2 mm particles will lay on the upper surface of bulk bed without transverse motion and only transport along axis. The Peclet number in Figure 3.36 (d3) is another strong evidence indicates that the axial velocity is much larger than axial dispersion coefficient.

Therefore, with low fraction of 2 mm particles, the variance of 2 mm particles is quite small. Moreover, with increasing of big particle fractions, the bulk bed transverse motion will approach the rolling model and the variance of both 2 mm and 0.7 mm particles will be enlarged.

### 3.5 Conclusion

In this chapter, a new mathematical model based on ring-core structure is developed to estimate the RTD of different particle sizes in bi- and polydisperse bulk bed systems. A series of experiments are done to validate the model with bidisperse system. The raw materials are 0.7, 2 and 4 mm glass beads mixing with different mass fractions. A pilot-scale kiln is utilized as experimental equipment and rotational speed, inclination angle and feed mass flow rate are considered as operational variables within the experiments.

The axial dispersion model is implemented to analyze the experimental data, then MRT, variance of RTD, Peclet number and axial dispersion coefficient could be derived from this model. Furthermore, based on the axial dispersion model, an empirical equation is developed to predict the axial dispersion coefficient which contains all the influencing parameter.

The RTD could be estimated with predicted MRT and  $D_z$  which both have good correlation between predicted and experimental values.

The results are summarized:

- 1) For all mixing particles, the residence time of big size particles is smaller than the MRT of small particles if the other physical properties of the particles are the same. The MRT difference will increase with enlarged particle size difference.
- 2) The rotational speed and inclination angle are two essential parameters which could obviously affect the MRT, variance of RTD curve and  $D_z$ . With increasing of rotational speed or inclination angle, the MRT and the variance will apparently decrease but  $D_z$  will increase. That means, the MRT is a more important weight factor than  $D_z$  which could also be known from equation 3.45.
- 3) The increasing of feed mass flow rate will slightly reduce the MRT and variance which has the similar pattern with monodisperse bulk beds. However, the big particle size difference will lead to opposite pattern compared to small particle size

materials.

- 4) The particle size difference is an essential factor about RTD in bidisperse system. If the particle diameter difference is larger than 2, the small particles will disperse in the gaps between big particles which lead to less friction between bulk bed and kiln inner surface especially for the smooth surface particles. Therefore, the transverse motion of the granular bed will become slipping or slumping which affects the particle mixing and transport significantly.
- 5) The particle size fraction also plays an important role in RTD. However, by varying the mass fraction of big particles from 0 to 1, the MRT will firstly reduce and then increase which presents a “V” curve. That means, the changing of particle size fraction will enlarge the influence of particle size difference and lead to different particle bed motion behavior in rotary kilns. The variance and  $D_z$  will have the similar pattern and fluctuate around a fixed value.

## 4 Process modeling of bi- and polydisperse system

### 4.1 Process model

#### 4.1.1 Basic structure of the process model

Herz (2012) developed a mathematical model which combined complex heat transfer, bulk bed dynamics and chemical reaction inside the kiln together. In this model, the variety of influencing parameters were taken into account and the temperature distribution along the axis of gas ( $T_G$ ), the bulk bed ( $T_S$ ), the inner wall ( $T_W$ ) and the outer shell surface ( $T_{shell}$ ) could be calculated. To describe the model, the infinitesimal volume segment was defined as the control volume which has a discretized axial length  $dz$ . The basic heat transfer mechanism in the transverse view is shown in Figure 4.1 for direct heated rotary kilns.

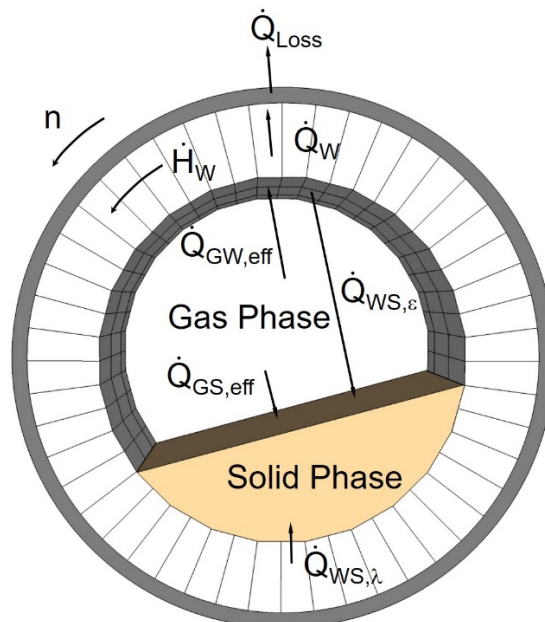


**Figure 4.1** Heat transfer mechanism in the cross section of direct heated rotary kilns

In this segment, the elements of gas phase, bulk bed phase and wall were defined for setting up the conservation equations based on energy balance. For the gas phase the ordinary differential equation

$$d\dot{H}_G = dR_{fuel} + d\dot{Q}_{GS,eff}(h, T_G, T_S) + d\dot{Q}_{GW,eff}(h, T_G, T_S), \quad (4.1)$$

is defined, where  $\dot{H}_G$  is the enthalpy of the gas,  $R_{fuel}$  is the reaction energy term for fuel conversion,  $\dot{Q}_{GS,eff}$  is the effective heat flow (convection and radiation) between gas and the solid bed which is

$$d\dot{Q}_{GS,eff} = d\dot{Q}_{GS,\alpha} + d\dot{Q}_{GS,\varepsilon}, \quad (4.2)$$

and  $\dot{Q}_{GW,eff}$  is the effective heat flow between gas and inner wall which is

$$d\dot{Q}_{GW,eff} = d\dot{Q}_{GW,\alpha} + d\dot{Q}_{GW,\varepsilon}. \quad (4.3)$$

The ordinary differential equation for solid phase is

$$d\dot{H}_S = d\dot{Q}_{GS,eff}(h, T_G, T_S) + d\dot{Q}_{WS,\lambda}(h, T_W, T_S) + d\dot{Q}_{WS,\varepsilon}(h, T_W, T_S) \pm dR_S, \quad (4.4)$$

where  $\dot{H}_S$  is the enthalpy of the solid phase,  $\dot{Q}_{WS,\lambda}$  is the heat flow between covered bed surface and solid phase by conduction,  $\dot{Q}_{WS,\varepsilon}$  is the radiation to the free bed surface. If there are chemical reactions exist in solid bed,  $R_S$  is the reaction energy term for solid component.

To calculate the heat losses through the wall, the surface temperatures of outer shell and



inner wall were determined by combining the differential equations of the gas and solid phase as

$$d\dot{Q}_{GW,eff}(h, T_G, T_W) = d\dot{Q}_{W,amb}(h, T_W, T_{shell}, T_{amb}) + d\dot{Q}_{WS,reg}(h, T_W, T_S) \\ + d\dot{Q}_{WS,\varepsilon}(h, T_W, T_S), \quad (4.5)$$

where  $\dot{Q}_{W,amb}$  is the total heat loss through the kiln wall which consists of the heat conduction through the wall, heat transfer by convection and radiation from the outer shell to the ambient.  $\dot{Q}_{WS,reg}$  is the regenerative heat transfer which is a two-dimensional heat transport combining the circumference enthalpy transport in the wall and the contact heat transfer from wall to solid phase.

By combining the axial transport model in chapter 2, the equation 4.1, 4.4 and 4.5 are coupled with the bulk bed height  $h$  and the temperature of the gas, solid, inner wall and outer shell. The details of the process model system and the solving procedure are shown by Herz (2012).

However, the model was restricted for monodisperse bulk bed systems. Therefore, in the following chapter, the new model for bi- and polydisperse particle systems described in chapter 3 will be taken into account to improve the process model.

### **4.1.2 Heat transfer between the covered wall and bulk bed**

From chapter 3, it is clear to see that in bi- and polydisperse particle system, the overall shape and physical properties of solid bed will not be changed comparing with monodisperse system. In contrast, a ring-core structure will be created inside of particle bed due to different particle size fractions. Therefore, the bulk bed cross section temperature could not be treated as homogeneous, which must be considered within the

process model.

The heat flow of solid bed is from the inner wall and gas phase. For the gas phase, the heat transfer is based on radiation and convection between gas and upper surface of particle bed which has no influence of particle size fractions. As shown in Figure 4.2 the inner wall could be divided into two parts, the covered wall (red curve AB) and uncovered wall (blue curve AB). The heat transfer between uncovered wall and particle bed is through radiation and the particle system will not influence the heat transfer. In contrast, the heat transfer between covered wall and solid bed is defined by the contact heat transfer which could be strongly influenced by the particle size of the bed. Therefore, the model of the contact heat transfer in monodisperse system will be introduced in detail at first.

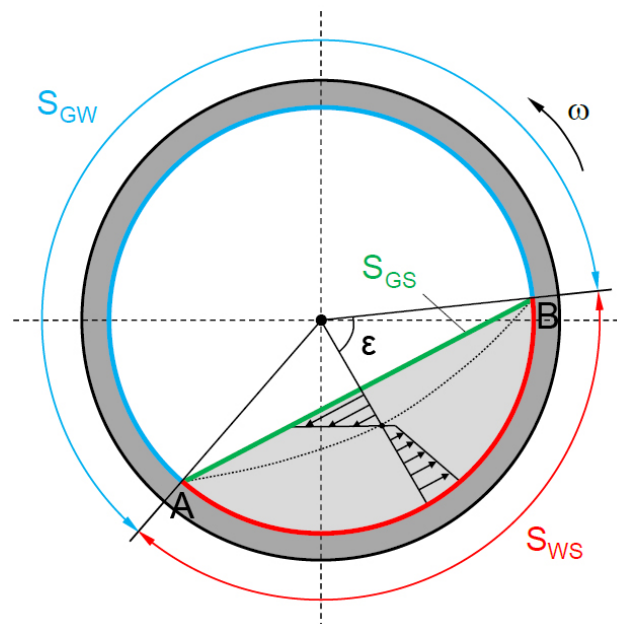


**Figure 4.2.** Geometric surface relation in the cross section of a rotary kiln

The overall heat transfer balance between covered wall and lower region of the bed is described as

$$d\dot{Q}_{WS,\lambda} = \alpha_{WS,\lambda} \cdot dA_{WS} \cdot (T_W - T_S). \quad (4.6)$$

Here  $A_{WS}$  is the contact surface between the covered wall and lower bed region and

$$dA_{WS} = S_{WS} \cdot dz = 2 \cdot R \cdot \varepsilon \cdot dz, \quad (4.7)$$

where  $\varepsilon$  is the half filling angle of the particle bed and  $R$  the inner radius of the kiln.

The overall contact heat transfer coefficient is defined as

$$\alpha_{WS,\lambda} = \frac{1}{\frac{1}{\alpha_{WS,contact}} + \frac{1}{\alpha_{S,penetration}}}, \quad (4.8)$$

where  $\alpha_{WS,contact}$  is the contact heat transfer coefficient between the wall and the particles and  $\alpha_{S,penetration}$  is the penetration coefficient inside the particle bed. The principle of contact heat transfer model was developed by Schlünder (1984) and the schematic is shown in Figure 4.3.

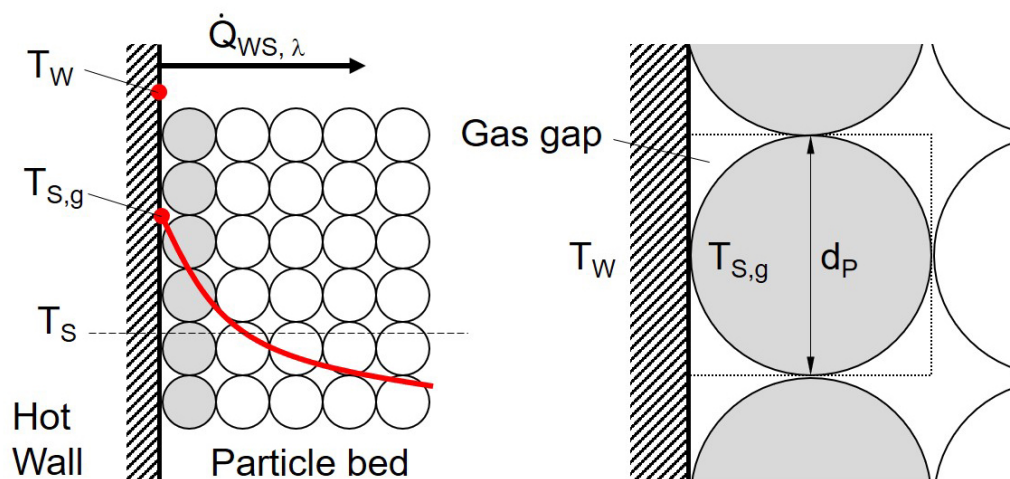


**Figure 4.3.** Schematic of the contact heat transfer between a hot wall and a bulk bed

[Schlünder (1988)]

In this theory,  $T_w$  is the wall temperature and there is a thin layer of gas film which is created by wall and first layer contact particles. This thin layer has the temperature of  $T_{s,g}$  which is much lower than  $T_w$  and the width of the layer is less than particle mean diameter. After that, the second layer is named as penetration layer and the thermal resistance is due to unsteady state heat conduction from the bed surface to the bulk bed. In this case, the temperature  $T_w$  provides the mean temperature of the solid bed. Therefore, the heat transfer coefficient is

$$\alpha_{s,penetration} = 2 \sqrt{\frac{\rho_s c_{p,s} \lambda_s}{\pi t_{contact}}}. \quad (4.9)$$

In this case, the thermo physical properties  $\rho_s, c_{p,s}, \lambda_s$  are the density, specific heat capacity and thermal conduction coefficient of bulk bed. The particle bed could be considered as quasi-continuum. By regarding of the rotation in rotary kilns, the contact time depends on the half filling degree and rotational speed as

$$t_{contact} = \frac{\varepsilon}{\pi n}. \quad (4.10)$$

The contact resistance between inner surface and particle bed surface is based on the theory of Schlünder (1988). A simplified semi-empirical equation by Sullivan and Sabersky (1975) is given as

$$\alpha_{ws,contact} = \frac{1}{\chi} \cdot \frac{\lambda_G}{d_p} \text{ with } \chi = 0.085 \quad (4.11)$$

where  $\lambda_G$  is the thermal conduction coefficient of gas,  $d_p$  is the particle diameter,  $\chi$  is the thickness of gas film. For this thickness, Li (2005) gave a value range from 0.096 to 0.198 with different particles diameter. Further analysis of Nafsun (2015) showed that this value is 0.058 for monodisperse and 0.091 for bi- and polydisperse bed systems

by validated the experimental results of Wes et al. (1976), Lehmberg (1977), Lybaert (1987) and Herz (2012).

Therefore, the total heat transfer coefficient between covered bed surface and particle bed can be expressed as

$$\alpha_{ws,\lambda} = \frac{1}{\frac{\chi d_p}{\lambda_G} + \frac{1}{2} \sqrt{\frac{\pi t_{contact}}{\rho_S c_{p,S} \lambda_S}}}. \quad (4.12)$$

## 4.2 Influence of RTD on thermal process

### 4.2.1 Improvement of transverse segregation model in bidisperse system and application in process model

The transverse segregation model introduced in chapter 3 will be further developed and implemented in the process model. The basic structure of transverse segregation is so called ring-core structure and an example of bidisperse particle bed is shown in Figure 4.4

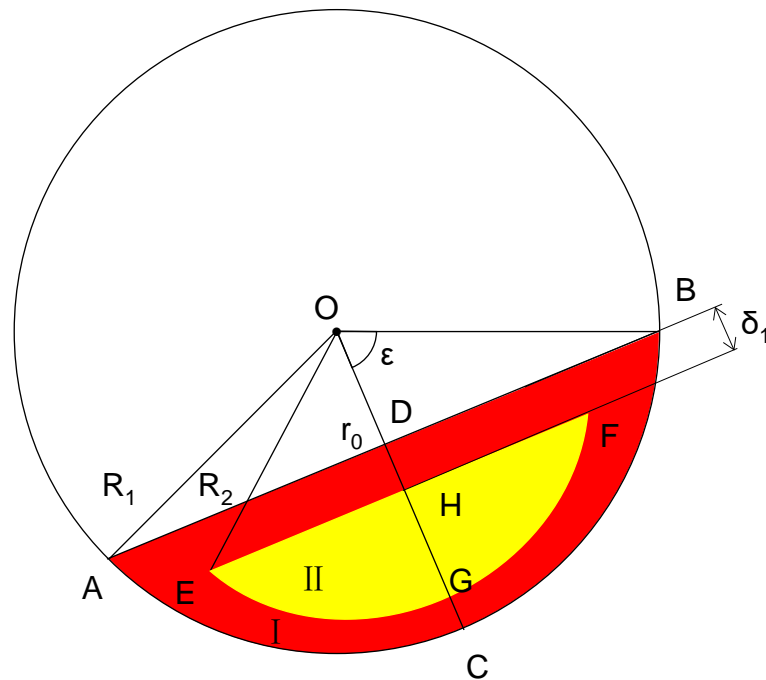


**Figure 4.4.** Schematic of transverse segregation in bidisperse system

The cross-section areas of big size particle I ( $A_1$ ) and small size particle II ( $A_2$ ) could be known by using the mathematical model in chapter 3.2.1. Furthermore, to calculate the heat transfer between particle I and particle II, the location of small particle inside of the particle bed must be known. That means, the distance between upper layer of two particles DH, the small particle bed depth HG and the distance between wall surface and bottom of small particles GC should be determined.

The assumption No. 6 and 7 in chapter 3.2.3 indicate that, the layer of  $\delta_1$  is similar with the definition of the active layer in monodisperse system (see Figure 4.5). Hence, it could be assumed that the layer  $\delta_1$  is the active layer of particle I and the thickness of this layer should be determined.

There are some models to estimate the active layer thickness in monodisperse system and in this time, the model from Liu (2006) was selected as major method to calculate the properties of active layer. Figure 3.5 shows the basic geometric properties of active layer in rolling mode motion.

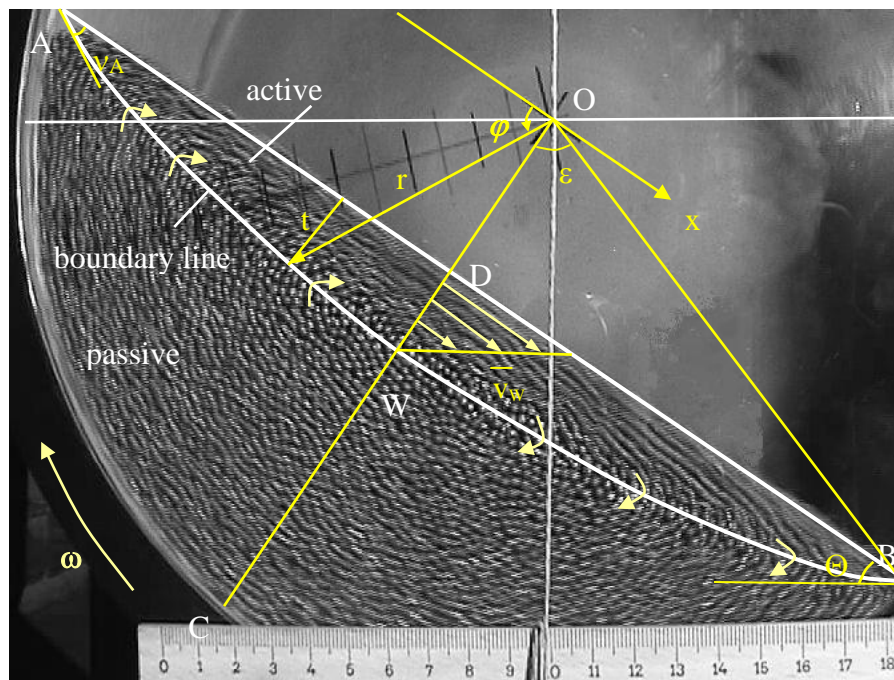


**Figure 4.5.** The rolling-mode granular motion (Liu 2006)

The maximal active layer thickness  $\delta_{max}$  at the vortex point (DW) could be derived as

$$\Delta_{max} = \frac{\delta_{max}}{R} = -\frac{\xi_0}{\tan \Theta} + \frac{1}{k \sin^2 \Theta} \ln \frac{2 + \sin(2\Theta)k\xi_0}{2} + \frac{d}{D}. \quad (4.13)$$

In this equation,  $\Delta$  is the dimensionless thickness of the active layer,  $\Theta$  is the dynamic

angle of repose,  $\xi$  is the dimensionless x-coordinate with

$$\xi = \frac{x}{R}, \quad (4.14)$$

and  $\xi_0$  is

$$\xi_0 = -\sqrt{\sin^2 \varepsilon - 2(1 + \cos \varepsilon) \frac{d_p}{D}}, \quad (4.15)$$

where  $d_p$  is the particle diameter.

Furthermore, the  $k$  in equation 4.13 is a constant value with

$$k = \frac{\tan \Theta - \tan(\nu_A + \Theta)}{\sin \varepsilon}, \quad (4.16)$$

the inclination angle  $\nu_A$  of the boundary line at the top of the particle bed is derived as an empirical equation with dynamic angle of repose in the range from  $25^\circ$  to  $50^\circ$  with

$$\nu_A = 0.32\Theta(1 + F) + 1800Fr \sqrt{\frac{d}{D}}, \quad (4.17)$$

and

$$Fr = \frac{\omega^2 R}{g}. \quad (4.18)$$

In addition, the mean particle velocity in the active layer at the vortex point could be calculated as



$$\bar{v}_W = \omega R \frac{1 - (\Delta_{max} + \cos \varepsilon)^2}{2\Delta_{max}}, \quad (4.19)$$

If this model will be implemented in bidisperse particle system, to the large particle, the particle diameter in equation 4.17 should be considered as  $d_{p,1}$  and the active layer thickness of large particle  $\delta_1$  could be assumed as

$$\delta_1 = \Lambda \cdot \delta_{max,mo}, \quad (4.20)$$

where  $\delta_{max,mo}$  is the maximum active layer thickness of particle I in monodisperse system. In this case, the equations used are from 4.13 to 4.18 and the particle bed is considered as monodisperse system with the operational conditions, dynamic angle of repose, filling angle and filling degree of bidisperse system.

$\Lambda$  is defined as a constant to determine the ratio between  $\delta_1$  and maximum active layer thickness of monodisperse. The value of  $\Lambda$  is varied with different particle size fractions and in the range from 0 to 1. For 1:1 particle size fraction,  $\Lambda$  is assumed as 0.5 and will be reduced with decreasing big particle size fraction and will slightly increase with rising big particle fraction.

After setting the value of  $\delta_1$ , the location of the small particle in mixing bed could be determined as shown in Figure 4.5. The distance from center O to upper surface of small particle bed is OH which is named as  $r_{0,1}$  and written as

$$r_{0,2} = r_0 + \delta_1. \quad (4.21)$$



$$\varepsilon_2 = \arccos\left(\frac{r_{0,2}}{R_2}\right). \quad (4.23)$$

By combining equation 4.22 and 4.23, the unknown variable  $R_2$  could be calculated.

After  $R_2$  is determined, the bed depth of particle bed II HG is

$$h_2 = R_2 - r_{0,2}, \quad (4.24)$$

and  $GC = R_1 - R_2$ .

By the prediction of the layer thickness between particle beds, the transverse segregation model could be considered into the process modeling. Figure 4.6 shows the heat transfer mechanism of a direct heated rotary kiln with bidisperse system. In this case, the ring-core structure is considered within the process model and without chemical reactions. It is clear to see that there is contact heat transfer between particle bed I ( $P_1$ ) and particle bed II ( $P_2$ ) which will influence the energy balance within the particle bed. In contrast, the heat transfer outside of the particle bed will be the same as in monodisperse system. Therefore, the new energy balance for gas phase is

$$d\dot{H}_G = dR_{fuel} + d\dot{Q}_{GS,eff}(h, T_G, T_{S,P_1}) + d\dot{Q}_{GW,eff}(h, T_G, T_{S,P_1}), \quad (4.25)$$

where  $T_{S,P_1}$  is the temperature of particle bed I. In following part, it is assumed that only particle bed I has heat transfer with inner wall and gas phase and the particle bed II could only receive the energy from particle bed I.

The heat loss is derived as

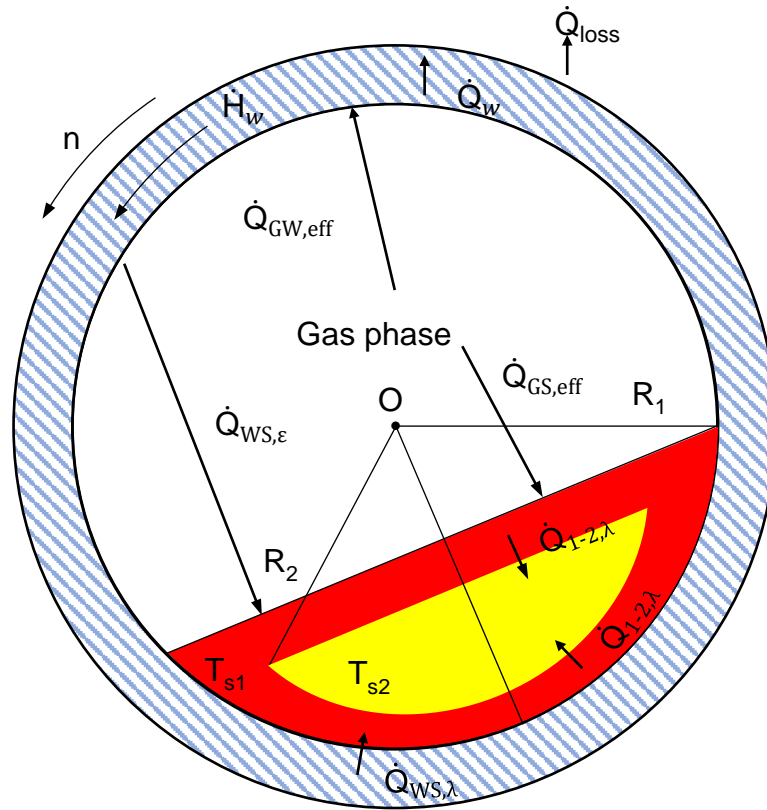


**Figure 4.6.** Heat transfer mechanism in the cross section of a direct heated rotary kilns with bidisperse particle system

$$d\dot{Q}_{GW,eff}(h, T_G, T_W) = d\dot{Q}_{W,amb}(h, T_W, T_{shell}, T_{amb}) + \quad (4.26)$$

$$d\dot{Q}_{WS,reg}(h, T_W, T_{S,P_1}) + d\dot{Q}_{WS,\epsilon}(h, T_W, T_{S,P_1}),$$

which is similar to the case of monodisperse particle bed.

For the particle bed I, the ordinary differential equation of energy balance is written as

$$d\dot{H}_{S,P_1} = d\dot{Q}_{GS,eff}(h, T_G, T_{S,P_1}) + d\dot{Q}_{WS,\epsilon}(h, T_W, T_{S,P_1}) + \quad (4.27)$$

$$d\dot{Q}_{WS,\lambda}(h, T_W, T_{S,P_1}) - d\dot{Q}_{SS,\lambda}(h, T_{S,P_1}, T_{S,P_2}),$$

and for particle bed II, the energy balance could be derived as

$$d\dot{H}_{S,P_2} = d\dot{Q}_{SS,\lambda}(h, T_{S,P_1}, T_{S,P_2}), \quad (4.28)$$

where  $\dot{Q}_{SS,\lambda}(h, T_{S,P_1}, T_{S,P_2})$  is the contact heat transfer between particle bed I and II which could be written as

$$d\dot{Q}_{SS,\lambda}(h, T_{S,P_1}, T_{S,P_2}) = \alpha_{1-2,\lambda} \cdot dA_{1-2} \cdot (T_{S,P_1} - T_{S,P_2}). \quad (4.29)$$

In this equation, the  $A_{1-2}$  is the contact surface between particle bed I and II (see Figure 4.5) which consists of an upper surface EF ( $dA_{1-2,up}$ ) and a bottom arc EGF ( $dA_{1-2,bo}$ ). These two areas could be derived as

$$dA_{1-2,up} = 2R_2 \sin \varepsilon_2 dz, \quad (4.30)$$

$$dA_{1-2,bo} = R_2 \frac{\varepsilon_2}{\pi} dz, \quad (4.31)$$

$$dA_{1-2} = dA_{1-2,up} + dA_{1-2,bo}. \quad (4.32)$$

The heat transfer mechanism between these two particles bed is similar with the mechanism of particle bed and inner wall. Therefore,  $\alpha_{1-2,\lambda}$  is the heat transfer coefficient between big and small particle bed as

$$\alpha_{1-2,\lambda} = \frac{1}{\frac{\chi d_{p,2}}{\lambda_G} + \frac{1}{2} \sqrt{\frac{\pi t_{contact,1-2}}{\rho_{S,2} c_{p,S,2} \lambda_{S,1}}}}. \quad (4.33)$$

In this case, the contact heat transfer time  $t_{contact}$  contains two parts. One is the flowing time through the upper surface EF which is

$$t_{contact,up,1-2} = \frac{2R_2 \sin \varepsilon_2}{\bar{v}_{W,2}}, \quad (4.34)$$

where  $\bar{v}_{W,2}$  is the mean particle velocity within the active layer of small particles based on equation 4.19.

The other one is the transport time in the passive layer of small particles along the bottom surface EGF as

$$t_{contact,bottom,1-2} = \frac{\varepsilon_2}{\pi n}, \quad (4.35)$$

and the total contact time is

$$t_{contact,1-2} = t_{contact,up,1-2} + t_{contact,bottom,1-2}. \quad (4.36)$$

With these equations, the contact heat transfer between big and small particle bed could be clearly derived and easily implemented in process model.

## **4.2.2 Improvement of transverse segregation model in polydisperse system and application in process model**

The major specificity of polydisperse bulk bed is introduced in chapter 3.2.2 and the structure of particle bed is shown in Figure 4.7. Because of the similar ring-core structure with bidisperse particle bed, the distance between each two closed upper surfaces is considered as the active layer and named from  $\delta_1$  to  $\delta_N$  where N is the total number of particle size fractions.

The equation 4.13 to 4.20 are implemented to derive the thickness of each active layer  $\delta_i$ . whereas the radius of each particle bed  $R_i$  could be derived from equation 4.21 to 4.23. To determine each particle bed locations within the bulk bed, the calculation order

is from the outside layer to the core. In this case,  $r_{0,i}$  is the distance from center of circle to the upper surface of bed

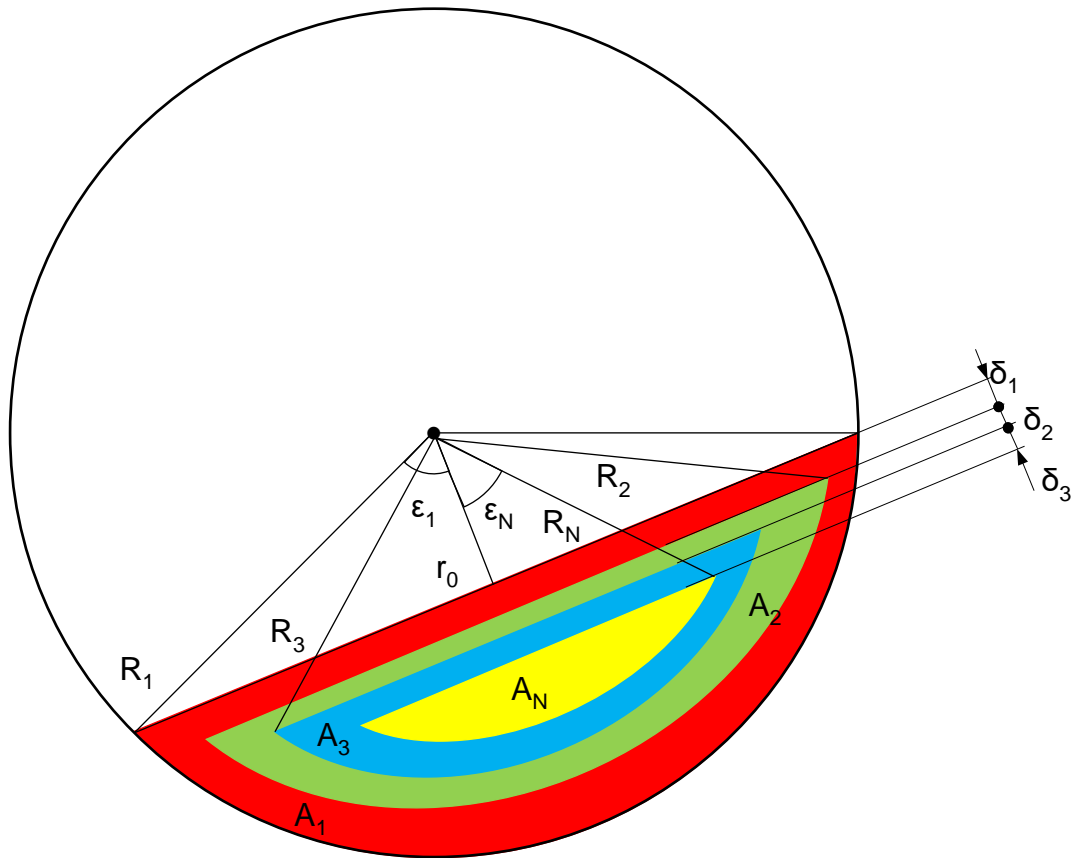


**Figure 4.7** Schematic of transverse segregation in polydisperse bulk bed

$$r_{0,i} = r_{0,i-1} + \delta_{i-1}, \quad (4.37)$$

and  $R_i$  could be solved with following equation

$$\pi R_i^2 \frac{\varepsilon_i}{\pi} - r_{0,i} R_i \sin \varepsilon_i = \sum_{i=1}^N A_i, \quad (4.38)$$

where the half filling angle is defined as

$$\varepsilon_i = \arccos \frac{r_{0,i}}{R_i}. \quad (4.39)$$

After the radius of particle bed  $i$  is determined, the filling degree  $F_i$  which will be used in equation 4.17 for the next particle layer as

$$F_i = \frac{\sum_{i=1}^N A_i}{\pi R_i^2}. \quad (4.40)$$

To the active layer thickness  $\delta_i$

$$\delta_i = \Lambda \cdot \delta_{max,mo,i}. \quad (4.41)$$

In this case, the  $\Lambda$  is assumed as the initial mass fraction of the mixing particles  $X_i$ .

It should be mentioned that for the initial condition of solving process, when  $i=1$ . All the parameters is value of the overall particle bed which are  $r_{0,i} = r_0$ ,  $R_1 = R$ ,  $F_1 = F_0$ ,  $\varepsilon_1 = \varepsilon_0$ , where  $F_0$  and  $\varepsilon_0$  is the filling degree and half filling angel of overall particle bed and determined from the model of Saeman (1952) in chapter 2.

The heat transfer mechanism of polydisperse system is shown in Figure 4.8. The temperature of each particle layer is named from  $T_{S,1}$  to  $T_{S,N}$ . The temperature for each particle size fraction is assumed to be constant. Comparing with the structure of bidisperse particle system before, the energy balance of gas phase and heat loss are the same with equation 4.25 and 4.26. Furthermore, for particle bed, the energy balance for particle 1 is

$$\begin{aligned} d\dot{H}_{S,P_1} = & d\dot{Q}_{GS,eff}(h, T_G, T_{S,P_1}) + d\dot{Q}_{WS,\varepsilon}(h, T_W, T_{S,P_1}) + \\ & d\dot{Q}_{WS,\lambda}(h, T_W, T_{S,P_1}) - d\dot{Q}_{SS,\lambda}(h, T_{S,1}, T_{S,P_2}), \end{aligned} \quad (4.42)$$



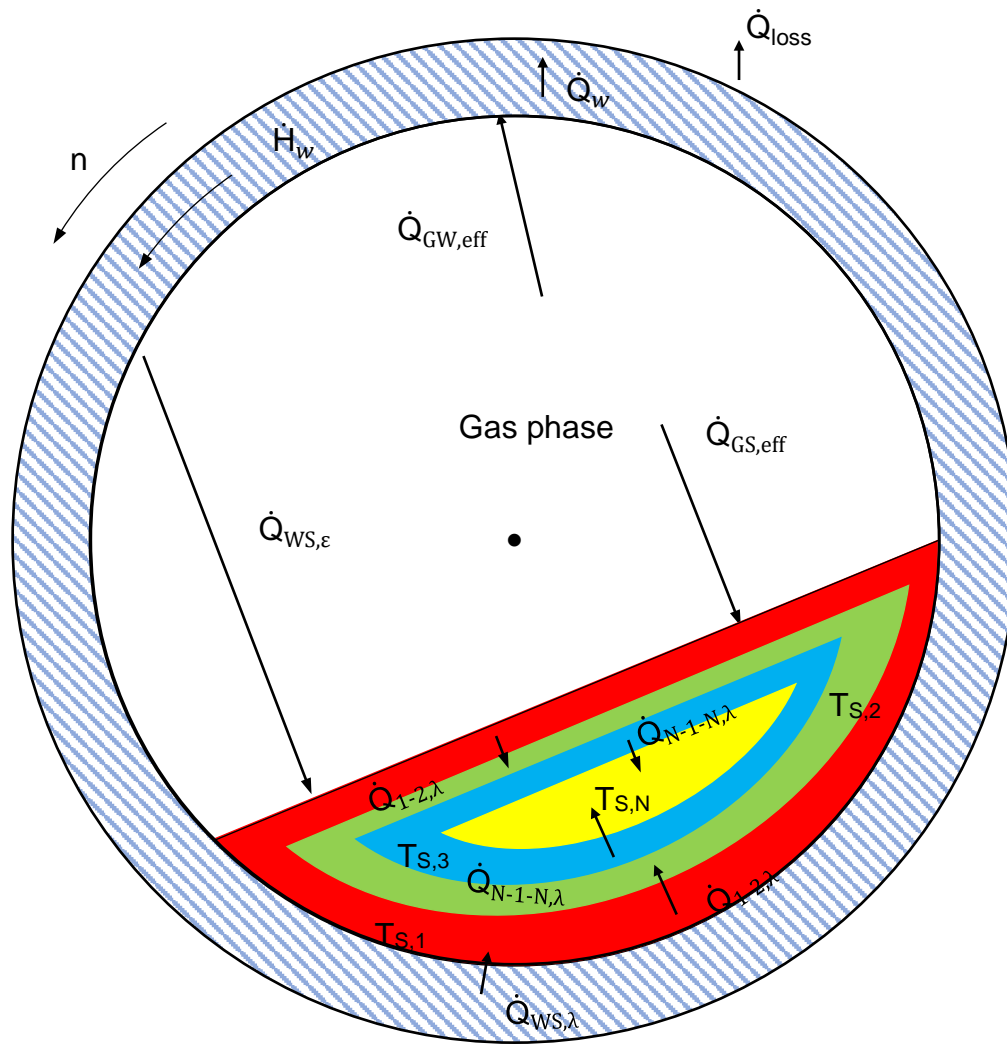


**Figure 4.8.** Heat transfer mechanism in the cross section of a direct heated rotary kilns with polydisperse particle system

and  $d\dot{Q}_{SS,\lambda}(h, T_{S,1}, T_{S,2})$  is defined as

$$d\dot{Q}_{SS,\lambda}(h, T_{S,1}, T_{S,2}) = \alpha_{1-2,\lambda} \cdot dA_{1-2} \cdot (T_{S,P_1} - T_{S,P_2}). \quad (4.43)$$

To particle fraction 2, the ordinary differential equation is derived as

$$d\dot{H}_{S,P_2} = d\dot{Q}_{SS,\lambda}(h, T_{S,P_1}, T_{S,P_2}) - d\dot{Q}_{SS,\lambda}(h, T_{S,P_2}, T_{S,P_3}), \quad (4.44)$$

where in this case, the contact heat transfer between particle fraction 2 and 3 is defined as

$$d\dot{Q}_{SS,\lambda}(h, T_{S,P_2}, T_{S,P_3}) = \alpha_{2-3,\lambda} \cdot dA_{2-3} \cdot (T_{S,P_2} - T_{S,P_3}). \quad (4.45)$$

Therefore, for any two closed particle bed  $i$  and  $i-1$ , the energy balance between these two beds is

$$d\dot{H}_{S,P_i} = d\dot{Q}_{SS,\lambda}(h, T_{S,i-1}, T_{S,i}) - d\dot{Q}_{SS,\lambda}(h, T_{S,P_i}, T_{S,P_{i+1}}), \quad (4.46)$$

with

$$d\dot{Q}_{SS,\lambda}(h, T_{S,P_{i-1}}, T_{S,P_i}) = \alpha_{(i-1)-i,\lambda} \cdot dA_{(i-1)-i} \cdot (T_{S,P_{i-1}} - T_{S,P_i}), \quad (4.47)$$

$$d\dot{Q}_{SS,\lambda}(h, T_{S,P_i}, T_{S,P_{i+1}}) = \alpha_{i-(i+1),\lambda} \cdot dA_{i-(i+1)} \cdot (T_{S,P_i} - T_{S,P_{i+1}}). \quad (4.48)$$

In these equations, the  $A_{(i-1)-i}$  is the contact surface between particle bed  $i-1$  to  $i$  which is defined as

$$dA_{(i-1)-i,up} = 2R_i \sin \varepsilon_i dz, \quad (4.49)$$

$$dA_{(i-1)-i,bottom} = R_i \frac{\varepsilon_i}{\pi} dz, \quad (4.50)$$

$$dA_{(i-1)-i} = dA_{(i-1)-i,up} + dA_{(i-1)-i,bottom}, \quad (4.51)$$

and  $A_{i-(i+1)}$  is the contact surface between particle bed  $i$  to  $i+1$  as

$$dA_{i-(i+1),up} = 2R_{i+1} \sin \varepsilon_{i+1} dz, \quad (4.52)$$

$$dA_{i-(i+1),bottom} = R_{i+1} \frac{\varepsilon_{i+1}}{\pi} dz, \quad (4.53)$$

$$dA_{i-(i+1)} = dA_{i-(i+1),up} + dA_{i-(i+1),bottom}. \quad (4.54)$$

The mechanism of heat transfer between two particle bed is the same as in bidisperse system and the heat transfer coefficient  $\alpha_{(i-1)-i,\lambda}$  is defined as

$$\alpha_{(i-1)-i,\lambda} = \frac{1}{\frac{\chi d_{p,i}}{\lambda_G} + \frac{1}{2} \sqrt{\frac{\pi t_{contact,(i-1)-i}}{\rho_{S,i} c_{p,S,i} \lambda_{S,i}}}}, \quad (4.55)$$

and the contact time for upper and bottom surface are defined separately

$$t_{contact,up,(i-1)-i} = \frac{2R_i \sin \varepsilon_i}{\bar{v}_{W,i}}, \quad (4.56)$$

$$t_{contact,bottom,(i-1)-i} = \frac{\varepsilon_i}{\pi n}. \quad (4.57)$$

whereas the total contact time is

$$t_{contact,(i-1)-i} = t_{contact,up,(i-1)-i} + t_{contact,bottom,(i-1)-i}. \quad (4.58)$$

For the heat transfer coefficient  $\alpha_{i-(i+1),\lambda}$ ,

$$\alpha_{i-(i+1),\lambda} = \frac{1}{\frac{\chi d_{p,i+1}}{\lambda_G} + \frac{1}{2} \sqrt{\frac{\pi t_{contact,i-(i+1)}}{\rho_{S,i+1} c_{p,S,i+1} \lambda_{S,i+1}}}}, \quad (4.59)$$

with contact time

$$t_{contact,up,i-(i+1)} = \frac{2R_{i+1} \sin \varepsilon_{i+1}}{\bar{v}_{W,i+1}}, \quad (4.60)$$

$$t_{contact,bottom,i-(i+1)} = \frac{\varepsilon_{i+1}}{\pi n}, \quad (4.61)$$

$$t_{contact,i-(i+1)} = t_{contact,up,i-(i+1)} + t_{contact,bottom,i-(i+1)}. \quad (4.62)$$

It should be mentioned that, for the last level of particle bed, which is in the core of the total particle bed, there is only heat transfer to the covered bed. Hence, the ordinary differential equation of energy balance is

$$d\dot{Q}_{SS,\lambda}(h, T_{S,P_{N-1}}, T_{S,P_N}) = \alpha_{(N-1)-N,\lambda} \cdot dA_{(N-1)-N} \cdot (T_{S,P_{N-1}} - T_{S,P_N}). \quad (4.63)$$

### 4.2.3 Assumptions of particle bed in process model

Based on the transverse segregation model and the applications in process model, some assumptions should be added following chapter 3.2.3.

- 1) In process model, all the assumptions in chapter 3 are still implemented.
- 2) In process model, there are no interaction between each particle bed.
- 3) The conduction is considered as only heat transfer between each particle bed except the outermost ring of the biggest size particle.
- 4) For one size of particle, the active layer is defined as the space between upper surfaces of itself and adjacent particle bed upper surface. The thickness of this layer is the ratio of largest active layer thickness which based on the model from Liu (2006) and the particle transport velocity in the active layer is considered as the mean velocity.
- 5) The active layer constant  $\Lambda$  depends on particle mass fractions. For a bidisperse system with 1:1 particle mass fraction,  $\Lambda$  is 0.5. This constant will be reduced with decreasing big particle fractions because less particle fraction brings thin active

layer. For polydisperse system, the active layer constant usually equals to the mass fractions of each particle sizes. Moreover, more studies should be done in the future to validate the active layer thickness in transverse motion analysis with bi- and polydisperse bulk bed system.

## 4.3 Results and Discussion

### 4.3.1 Simulation results with monodisperse particle system

The calcination of quartz sand within an industrial scale rotary kiln is selected as reference process for the application of the model mentioned in chapter 4.2. The basic dimension of the rotary kiln is shown in Figure 4.9 which is a direct heated kiln without inner constructions. It has a length of  $L = 40$  m and an inner diameter of  $D = 2$  m which owns the  $L/D$  ratio of 20. The refractory lining has a thickness of  $S_{SW} = 0.4$  m and the diameter of outer steel shell is  $D_{M,o} = 2.8$  m. To maintain a suitable filling degree, a rotational speed of  $n = 1$  rpm and an inclination angle of  $\beta = 1^\circ$  are fixed. The quartz sand under reference conditions is monodisperse with 0.2 mm particle diameter and totally 5 t/h feed mass flow rate.

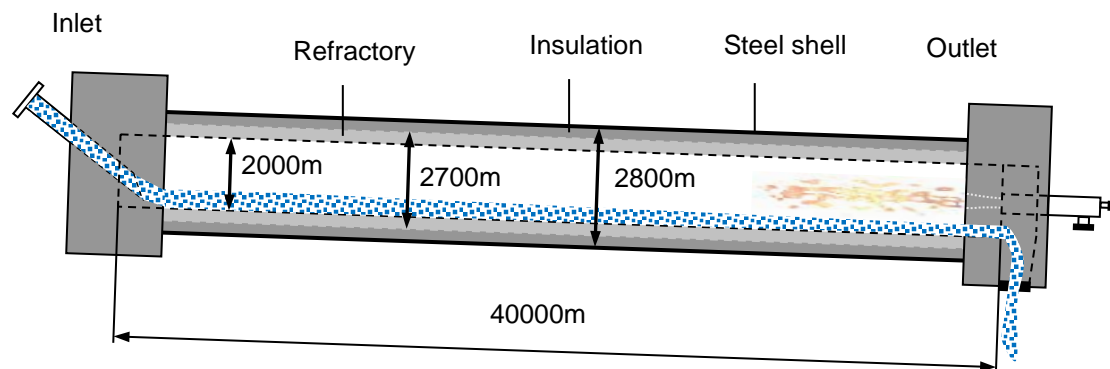


**Figure 4.9** Schematic diagram of the rotary kiln in process modeling

To reach the required product quality, the raw materials should have a minimum residence time of 15 min above the reference temperature of  $T_{S,ref} = 1250^\circ\text{C}$ . The burner is set at the discharge end of the rotary kiln and is adjusted to a power of  $P = 2.3$  MW and a flame length of  $L_{flame} = 10$  m. Further operational and constructive parameter used within simulations are shown in appendix C.

The temperature profiles of the gas, inner wall surface, bulk bed and steel shell are shown in Figure 4.10 (a) as  $T_G$ ,  $T_w$ ,  $T_s$ ,  $T_M$  respectively and the axial profiles of particle

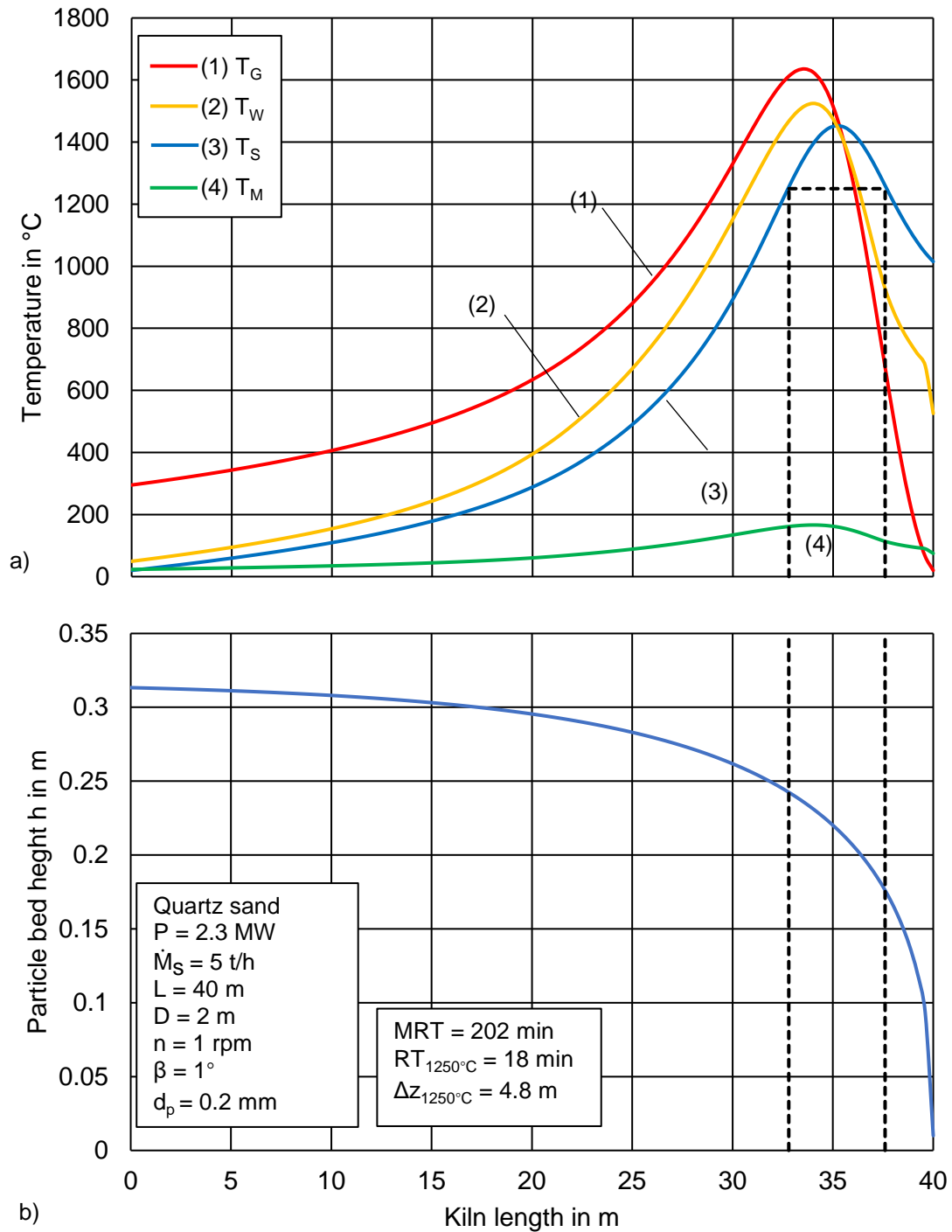


**Figure 4.10** Axial particle bed height and temperature profiles in rotary kiln during calcination

bed height is shown in Figure 4.10 (b). It is clear to see that from the inlet ( $z=0$ ) to the middle of the kiln ( $z = 20$ ) the bed height is around 0.3 m. In contrast, the bulk bed height is reduced towards the outlet ( $z = 40$ ) and has the smallest value of 0.01 m which

is the initial value for the simulation. The slope of the decrement increases significantly till the discharge end of the kiln.

The raw materials of quartz sand are fed into the rotary kiln with ambient temperature of  $T_S = 20^\circ\text{C}$ . The temperature distribution of bulk bed is shown as curve (3) and the maximum temperature is  $T_{S,\text{max}} = 1451^\circ\text{C}$ . The MRT of the particles is 202 min from inlet to the outlet and the axial length of bulk bed temperature above reference temperature is around  $\Delta Z_{1250^\circ\text{C}} = 4.8\text{ m}$  which leads to a residence time of  $RT_{1250^\circ\text{C}} = 18\text{ min}$ . That means the quartz sand of 0.2 mm particles will have enough time and temperature to ensure the product requirement.

It can be seen also from the temperature of gas profile that the maximum temperature of gas  $T_{G,\text{max}} = 1635^\circ\text{C}$  appears at the end of the flame. Due to the heat transfer at the free surface of particle bed and inner surface, the exhaust gas temperature will be reduced to  $T_{G,0} = 295^\circ\text{C}$  at the material inlet of the kiln. Furthermore, the position of the maximum temperature of inner wall surface is almost the same as where the gas is with the maximum temperature of  $T_{W,\text{max}} = 1517^\circ\text{C}$ . However, in the last 5 m distance to the outlet, the particle bed temperature is higher than the gas and inner wall. Hence, in this case, the particle bed will transfer the heat to the gas phase and also to the wall.

The profiles of local heat transfer coefficients are shown in Figure 4.11. The details of heat transfer coefficient definitions are described in Herz (2012). Generally, the radiation dominates the heat transfer in the high temperature range especially in the flame zone. Due to the reason of solid body radiation, the radiative heat transfer coefficient from the inner wall to the free bed surface reaches the highest value about  $\alpha_{WS,\varepsilon} = 354\text{ W/m}^2/\text{K}$  in the area of the flame end. On the other hand, the radiation between gas and inner wall owns the maximum heat transfer coefficient of  $\alpha_{GW,\varepsilon} = 247\text{ W/m}^2/\text{K}$  which is double of the maximum radiative heat transfer coefficient between gas and particle free bed of  $\alpha_{GS,\varepsilon} = 122\text{ W/m}^2/\text{K}$ .



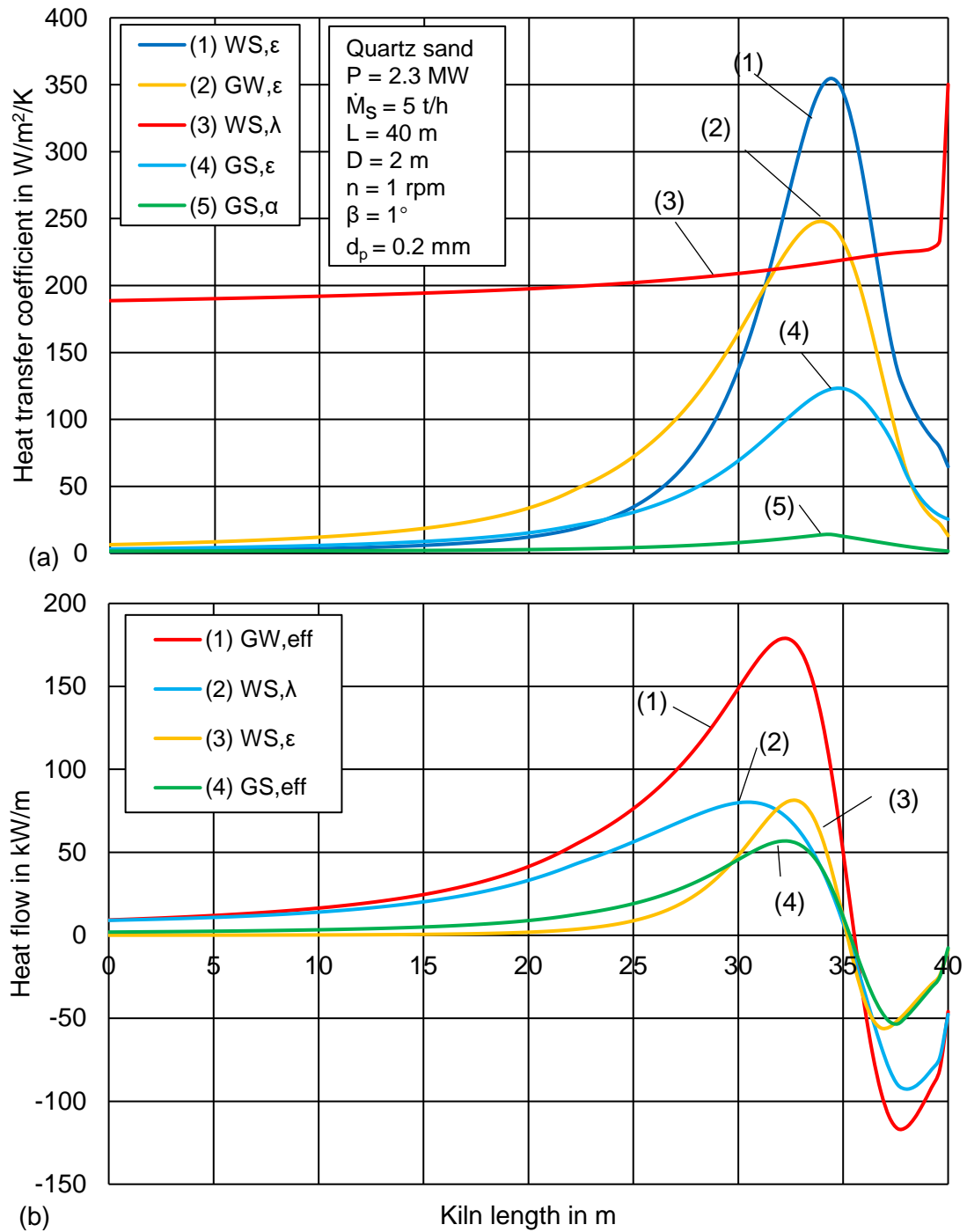


**Figure 4.11** Axial profiles of local heat transfer coefficients and heat flow during calcination

The contact heat transfer coefficient between inner wall and bulk bed increases along the axis and has a huge jump to the highest value of  $\alpha_{WS, \lambda} = 350 \text{ W/m}^2/\text{K}$ . This is due to the reduction of the bed height along the axis which leads to the decreasing of contact

time. From equation 4.12, this reduced time will decrease the contact resistance between inner wall and first layer particles and increase the contact heat transfer coefficient. In addition, the maximum convective heat transfer coefficient is around  $\alpha_{GS,\alpha} = 14 \text{ W/m}^2/\text{K}$  which is quite small compared to other heat transfer coefficients. Hence, the convection plays a subordinate role during the calcination process.

In Figure 4.11(b), the heat flows reach the maximum values in the range of flame end where highest temperature is. After this vertex, all the values decrease to 0 and therefore the region from  $z = 0$  to  $z = 35 \text{ m}$  is named as heating zone of the kiln. Over  $z=35 \text{ m}$  where the bulk bed temperature is larger than the temperature of gas and inner wall, the heat flow are less than 0 which means the bulk bed transfer the heat to the inner wall and gas phase. For this reason, the last 5 m to the outlet can be called cooling zone of the kiln.

It is also obviously observed from the curve (1) and (2) that in the heating zone, the effective heat transfer of gas to the wall and conduction of wall to bulk bed dominate the total process. Based on the heat transfer definitions, only the contact heat transfer can be affected by particle size. Therefore, further analysis of the influence of particle size on the overall process should be described in detail.

In addition, all the simulation results with mono-, bi- and polydisperse particle systems are shown in Appendix C which includes the temperature of exhaust gas, product, maximum bed temperature as well as the heat losses, residence times and product qualities. At the same time, the temperature profiles, heat transfer coefficients and heat flows are shown as figures in Appendix D respectively.

### **4.3.2 Influence of particle diameters in monodisperse systems**

To analyze the influence of particle diameters on process model, in total four different sizes of quartz sand are selected as simulation materials with 0.2 mm, 0.4 mm, 2 mm

and 4 mm particle diameters. All the materials are simulated with the same operational conditions and the comparison results are shown from Figure 4.12 to Figure 4.15. Because of the same initial conditions of bulk bed height and no parameter of particle diameters in the model of Saeman (1952), the particle size has no influence on particle bed profiles and Figure 4.10 (b) presents this pattern with 4 different particle sizes. Therefore, the particle bed profiles as well as the local heat transfer areas are considered as constant in process model if only the particle size is varied.

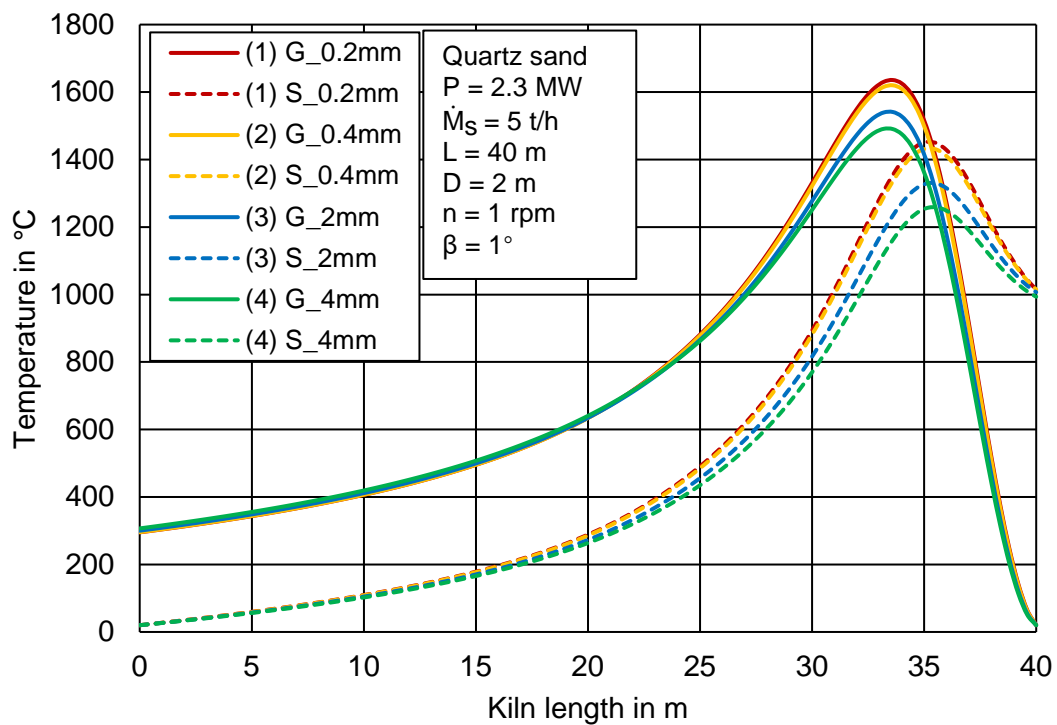


**Figure 4.12** Influence of particle diameters on gas and bulk bed temperature

Figure 4.12 shows the influence of particle diameters on gas and bulk bed temperature. The temperature profiles of gas phase are shown as dotted lines and bulk bed are shown as solid lines. It is clear to see that the highest temperatures of gas phase are always located in the range of flame end regardless of varied particle diameters. The initial temperatures of gas are fixed as 20°C and increase to the maximum values. However, the maximum gas temperature of 0.2 mm particles has the largest value  $T_{G,max,0.2} = 1635^{\circ}\text{C}$  and decreases with increasing particle diameters. The temperature

difference between 0.2 mm and 0.4 mm particles is quite small which is only 15 K. In contrast, the maximum temperature of 2 mm is  $T_{G,max,2} = 1540^{\circ}\text{C}$  and of 4 mm is  $T_{G,max,4} = 1490^{\circ}\text{C}$  which have 95 K and 145 K differences to 0.2 mm respectively. That means, changing of particle diameters has an obvious influence on maximum gas temperatures. Hence, although the 4 mm/2 mm and 0.4 mm/0.2 mm particles own same diameter ratio 2, the larger diameter difference particles have higher gas temperature difference and smaller maximum gas temperatures. In addition, from the peak point to the inlet of rotary kiln, where  $z = 0$ , all the exhaust gas temperatures will be reduced to around  $300^{\circ}\text{C}$  but smaller particles will present lower exhaust gas temperature which means better heat transfer efficiency within the kiln .

At the same time, the bulk bed temperature profiles have a similar pattern with gas. All the maximum bulk bed temperatures are in the position of  $z = 35$  m. The 0.2 mm particle has the largest maximum temperature of  $T_{S,max,0.2} = 1452^{\circ}\text{C}$  and 4 mm particle has the lowest temperature of  $T_{S,max,4} = 1257^{\circ}\text{C}$ . The temperature differences between 0.2 mm quartz sand and other 3 particles are  $\Delta T_{S,0.2\&0.4} = 19$  K,  $\Delta T_{S,0.2\&2} = 122$  K and  $\Delta T_{S,0.2\&4} = 195$  K. These differences have the same tendency with gas phase and relative larger values. If the  $T_{S,ref} = 1250^{\circ}\text{C}$  is selected as reference temperature and 15 min is the minimum residence time as mentioned before. Only 0.2 mm and 0.4 mm particles could realize the requirement of product with residence time of  $RT_{1250^{\circ}\text{C},0.2\text{mm}} = 18$  min and  $RT_{1250^{\circ}\text{C},0.4\text{mm}} = 16$  min. In contrast, this time for 2 mm and 4 mm particles are  $RT_{1250^{\circ}\text{C},2\text{mm}} = 11$  min and  $RT_{1250^{\circ}\text{C},4\text{mm}} = 5$  min respectively which not ensure the required heat-treating time.

Moreover, to study the further impact of particle diameter and process model, the heat transfer coefficient and heat flow profiles are shown in Figure 4.13 to 4.15. In Figure 4.13 (a), the radiative heat transfer coefficient between inner wall and bulk bed are shown as solid lines and contact heat transfer coefficient are as dotted lines. For radiation, the 0.2 mm particle has the largest heat transfer coefficient of

$\alpha_{WS,\varepsilon} = 354 \text{ W/m}^2/\text{K}$  which will be reduced with increasing particle size. That is mainly caused by the larger temperature gradient between inner wall and solid bed than big particles.

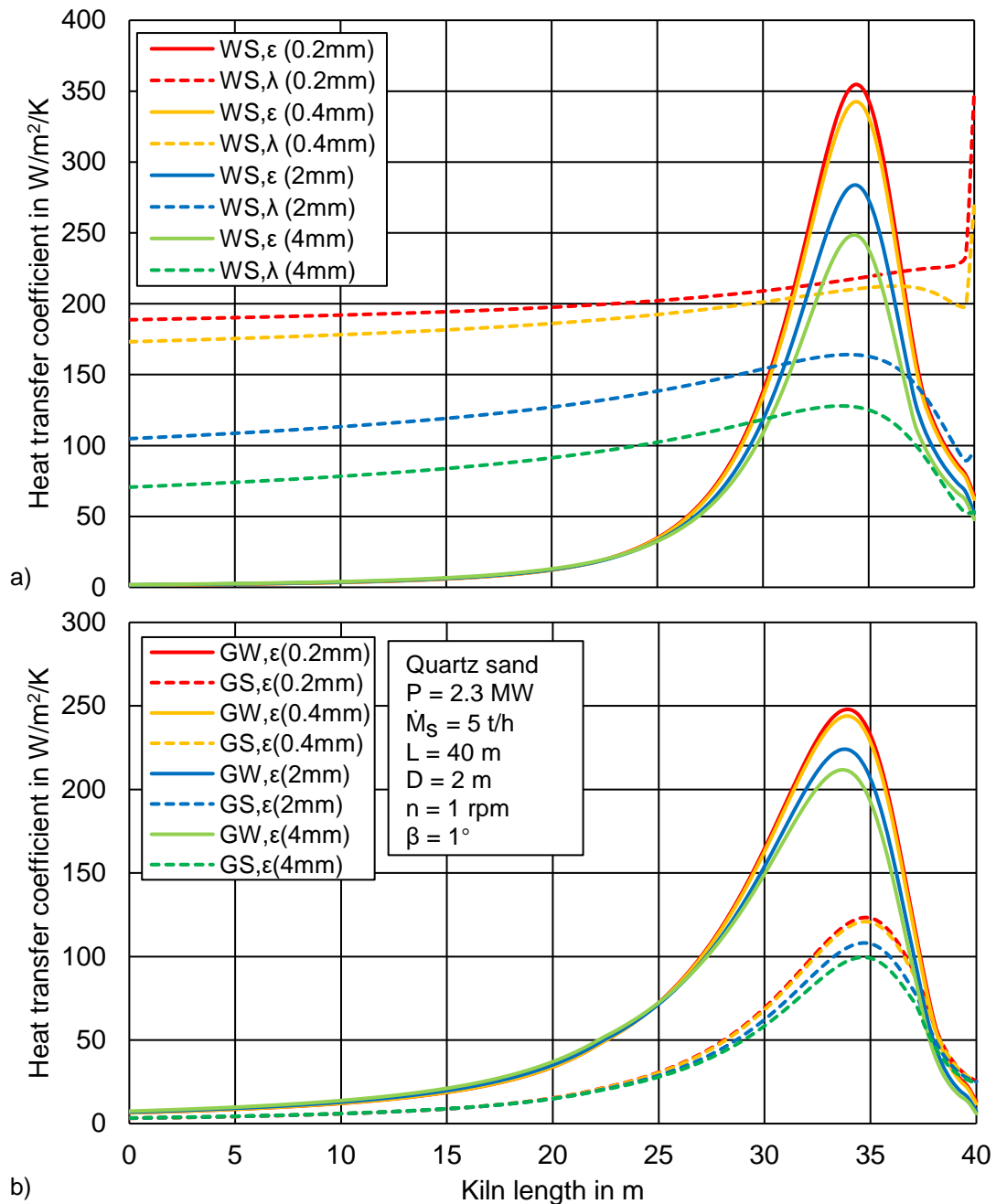


**Figure 4.13** Influence of particle diameters on heat transfer coefficients of a) radiation and conduction between inner wall and bulk bed, b) radiation between gas and inner wall, radiation between gas and bulk bed

On the other hand, the contact heat transfer coefficient profiles between inner wall and particle bed are quite different from other coefficients. For 0.2 mm and 0.4 mm particles, the coefficient values in the inlet ( $z = 0$ ) are in the range of 150 to 200 but reducing to the range between 50 to 100 for 2 mm and 4 mm particles. The contact heat transfer coefficient for all 4 particles increase along axis towards the outlet and the 0.2 mm and 0.4 mm particle reach the highest value in the outlet. In contrast, for 2 mm and 4 mm, the coefficients will decrease after  $z = 35$  m where the bulk bed has the highest temperature is.

To make the further discussion of this tendency, by combining the equation 4.8 and 4.12, the heat resistance of contact and penetration between inner wall and bulk bed are shown in Figure 4.14.

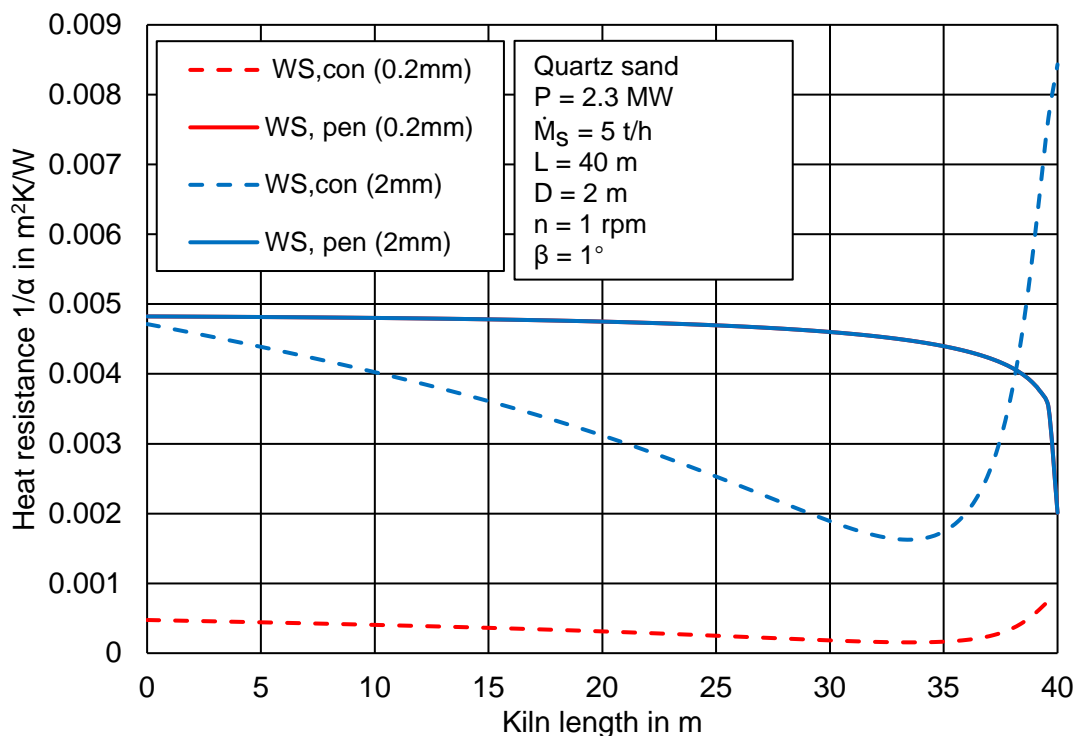


**Figure 4.14** Influence of particle diameters on heat resistance between inner wall surface and bulk bed

In this case, 0.2 mm particles are compared with 2 mm particles which is 10 times

enlarging of particle diameters. It could be observed from the figure that because of the same bulk bed profiles, the heat resistance of penetration will not be influenced by particle diameters. However, this pattern is not fit for the contact heat resistance. For 0.2 mm all the heat resistances are less than  $0.001 \text{ m}^2\text{K/W}$  and it will slightly decrease till the point of maximum gas temperature and increase a little bit in the cooling zone because of the varied gas temperatures. At the same time, based on equation 4.12, the heat resistance of 2 mm should be always 10 times higher than 0.2 mm because of particle diameters. Nevertheless, the thermal conductivity of gas  $\lambda_G$  will be influenced by the gas temperature and the has opposite correlation to heat resistance. Therefore, for 2 mm particles, the heat resistance will be 10 times higher than 0.2 mm particles in inlet and outlet and owns smallest difference in the position of maximum gas temperature where the highest temperature difference is.

With combining of the contact heat transfer model of Schlünder (1988), this phenomenon could also be explained qualitatively. For the contact heat transfer between particle bed and wall, the enlarged particle diameter will lead to larger gas gap between particles as well as particle and wall. Generally, the gas owns much higher heat resistance than solids. Therefore, these two reasons work together to make the 2 mm particles has lower contact heat transfer coefficient than 0.2 mm particles.

In addition, the Figure 4.13 (b) shows the heat transfer coefficient between gas phase and bulk bed as well as the coefficient between gas phase and inner wall. It indicates that these two coefficients have the similar pattern with varied particle diameters. The increased particle diameters will lead to decreasing of maximum heat transfer coefficient and the difference between 2 mm and 4 mm is much larger than the difference between 0.2 mm and 0.4 mm. This is mainly caused by the differences of maximum temperatures of gas phase.

Figure 4.15 (a) shows the particle diameter influence on heat flow. The contact heat

flow profiles between inner wall and bulk bed are shown as solid lines and the radiative heat flow profiles are shown as dotted lines. It is clear to see that the smallest particle has the largest contact and radiative heat flows which will be both reduced with increasing particle diameters. However, the particle diameter has more influence on contact heat flow because of the decreased contact heat transfer coefficient.

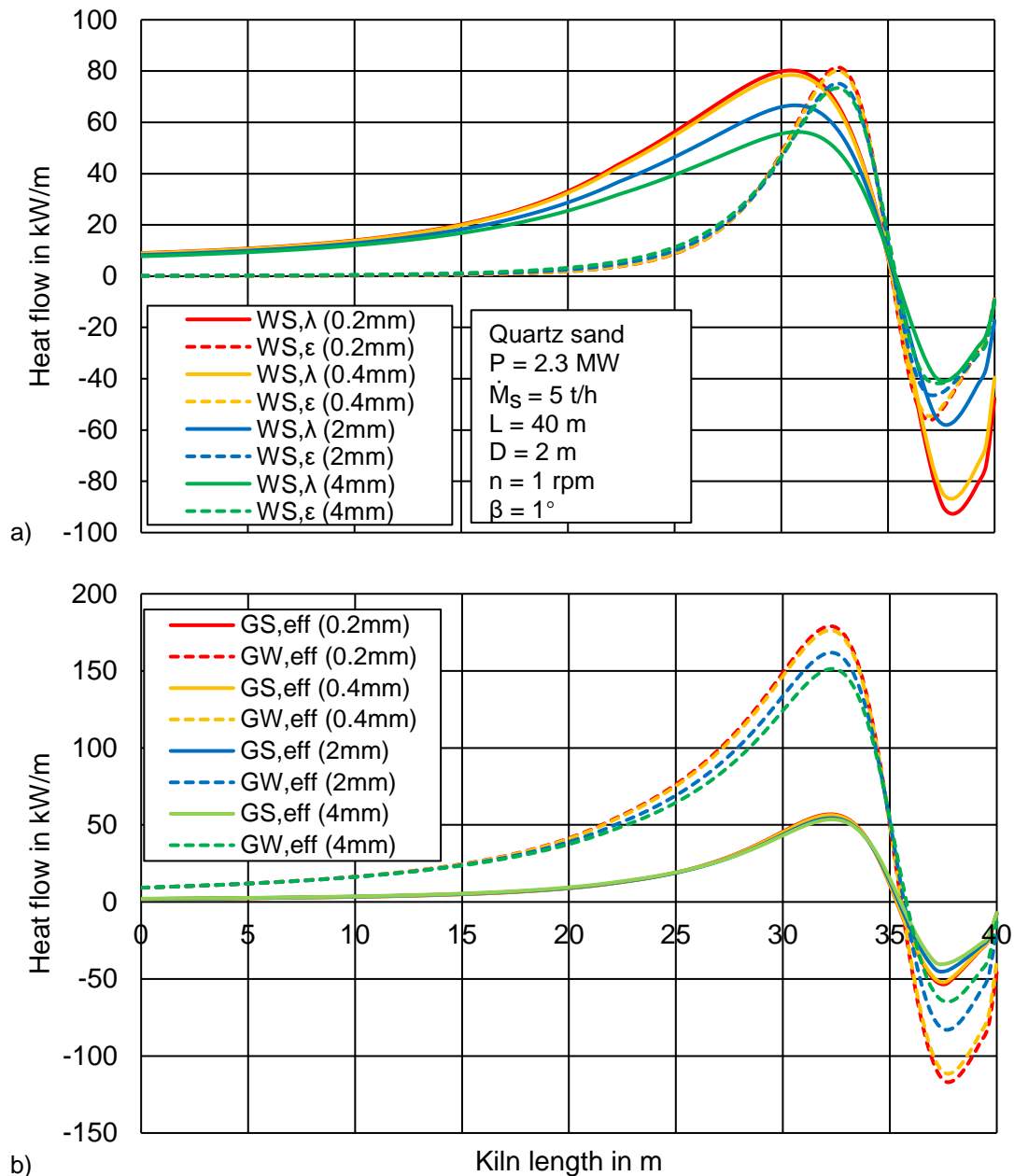


**Figure 4.15** Influence of particle diameters on heat flow of a) radiation and conduction between inner wall and bulk bed, b) effective heat flow between gas and inner wall, gas and bulk bed



The Figure 4.15 (b) shows the influence on effective heat flow. The effective heat flows between gas and bulk bed are shown as solid lines and the effective heat flows between gas and inner wall are shown as dotted lines. It indicates that the absolute value of effective heat flows between gas and inner wall are always larger than the value of gas to bulk bed. The 0.2 mm particle has the largest heat flow value in the flame end region because of the highest gas temperature. Moreover, the 0.2 mm condition has the largest absolute value under zero which mean the largest heat flow from inner wall to gas. This is also due the largest temperature difference between inner wall and gas. With enlarged particle diameter, the maximum heat flow in both positive and negative region will be reduced with decreasing temperature difference between gas phase and inner wall surface. However, the effective heat flow between particle bed and gas phase has no influence with varied particle bed in heating zone.

### 4.3.3 Simulation results with bidisperse particle system

With the combing of the process model and the segregation model in chapter 4.2, the thermal process of quartz sand calcination could be simulated with bidisperse particle system which shows the difference between bi- and monodisperse particle systems with different particle sizes in a same system. Therefore, in this case, the simulated operational conditions are the same with monodisperse particle system before. In contrast, the bulk bed consists of 0.2 mm and 0.4 mm spherical quartz sand particles with mass flow fraction of 50% to 50%. The comparisons of temperature profiles between mono- and bidisperse particle system are shown in Figure 4.16. All the profiles of monodisperse particles are shown as solid lines and the bidisperse systems are as dotted lines. It should be mentioned that the 0.27 mm is the Sauter mean diameter of 0.2&0.4 mm mixing particles with 50% to 50% mass ratio. From Figure 4.16 (a), it is clear to see that the flue gas temperature of monodisperse are almost the same. However, for mixing particles, the peak value of gas temperature is  $T_{G,max,bi-} = 1572^{\circ}\text{C}$  which is around 60 K smaller than the maximum value of monodisperse condition. In Figure 4.16 (b), for the temperature profiles of inner wall surface, the pattern is similar to the

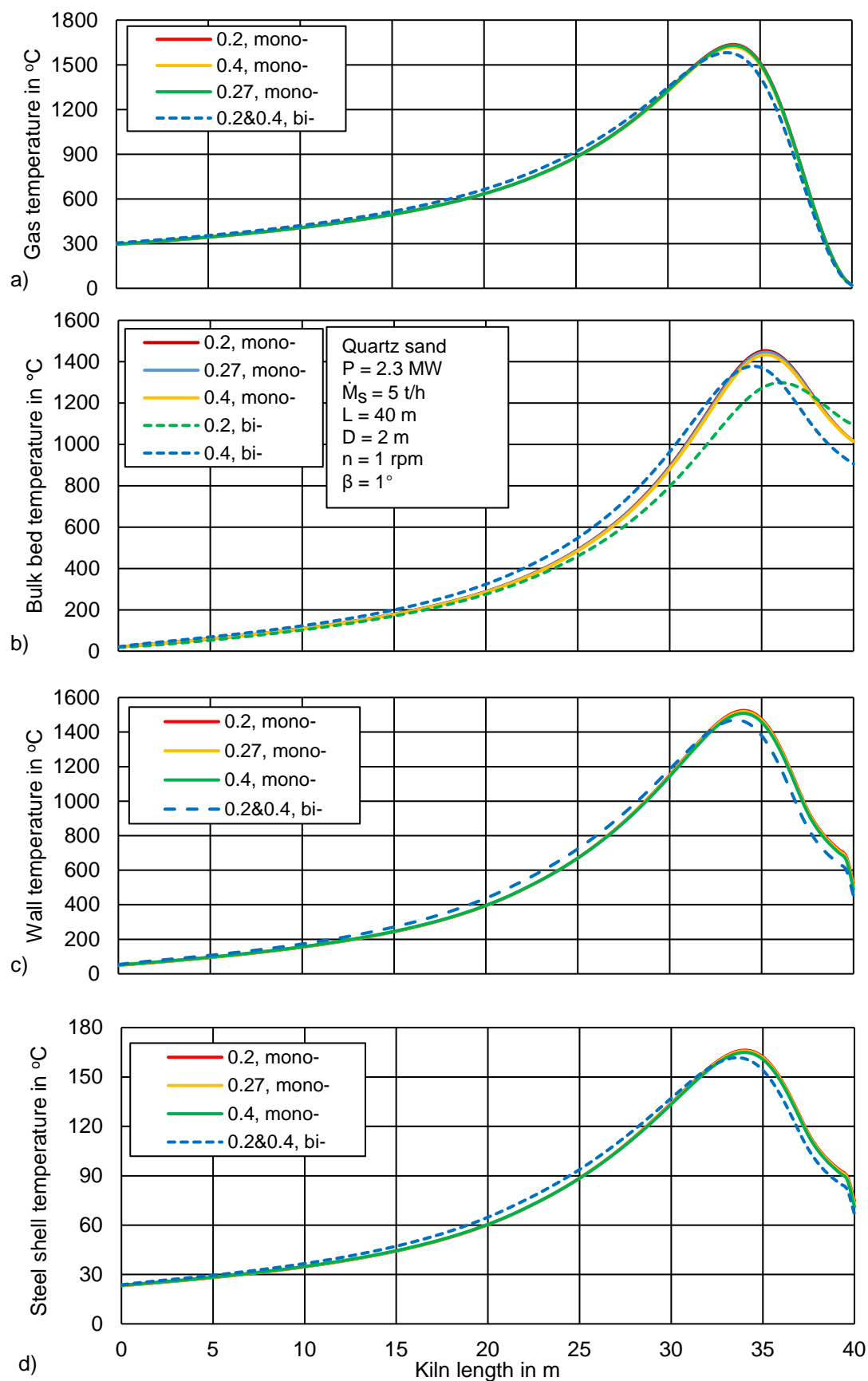


**Figure 4.16** Temperature comparison between mono- and bidisperse particle systems

gas profiles. The maximum inner wall temperature of monodisperse system is larger than of bidisperse system which has the temperature difference of  $\Delta T_w = 40$  K.

The particle bed temperature profiles are shown in Figure 4.16 (c). Because of the ring-core structure, the heat transfer within the particle bed should be considered. Therefore, the 0.2 mm particles in the core could only have contact heat transfer from 4 mm particle bed which is much lower than monodisperse system. On the other hand, for 4 mm particle bed, although it has the similar external heat transfer environment, the heat flow that 0.2 mm particle bed obtained is considered as heat loss for 4 mm. Therefore, both 0.4 mm and 0.2 mm will have lower bed temperatures. For 0.4 mm particle, the maximum temperature is  $T_{S,max,bi-,0.4} = 1375^\circ\text{C}$  and for 0.2 mm particles is  $T_{S,max,bi-,0.2} = 1259^\circ\text{C}$ . However, the temperatures of small particles are not always lower than the big ones. It is clear to see big particles will have higher temperature in the range from the inlet  $z = 0$  to  $z = 36.4$  m and reach highest temperature in the position of  $z = 34.6$  m. After that, the temperature of the small particle bed is always larger than the big one which means the direction of heat transport is from small particles to big ones.

Furthermore, the MRT of the 0.4 mm particles is 192 min from inlet to the outlet and the axial length of bulk bed temperature above reference temperature is around  $\Delta z_{1250^\circ\text{C}, bi-,0.4} = 3.9$  m which leads to a residence time of  $RT_{1250^\circ\text{C}, bi-,0.4} = 15.5$  min. That means the quartz sand of 0.4 mm particles will have enough time and temperature to ensure the product requirement. In contrast, the MRT of the 0.2 mm particles is 212 min and  $\Delta z_{1250^\circ\text{C}, bi-,0.2} = 2.9$  m which owns a residence time of  $RT_{1250^\circ\text{C}, bi-,0.2} = 9$  min. That means the 0.2 mm quartz sand will not ensure the requirement of the product although it has a 100 K higher outlet temperature than 0.4 mm particles. In addition, the temperature profiles of steel shell are presented in Figure 4.16 (d) and have similar patterns regardless of mono- or bidisperse particle bed with a difference of maximum temperature of 3 K.

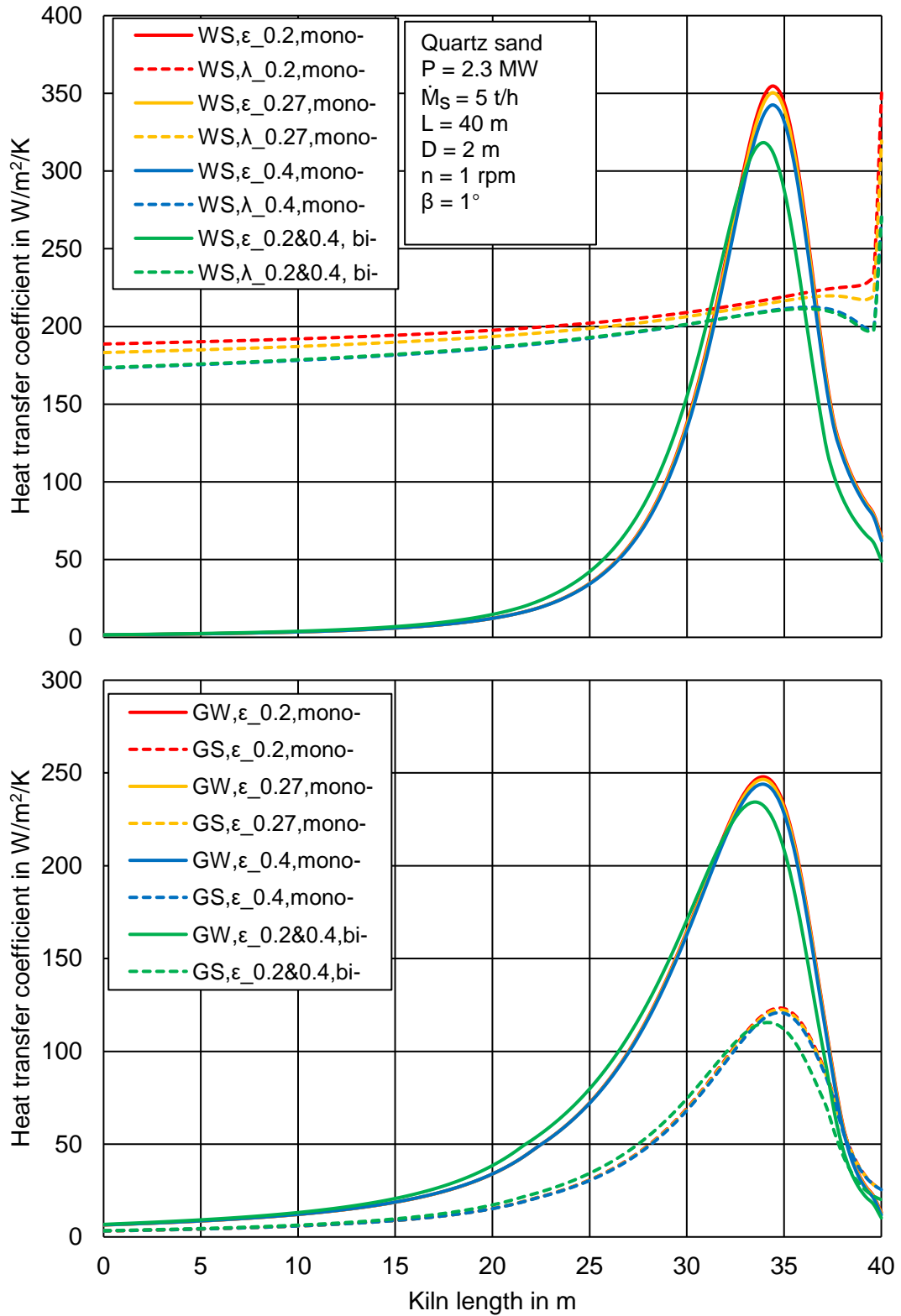


**Figure 4.17** Heat transfer coefficient comparison between mono- and bidisperse particle bed.

The comparisons of the heat transfer coefficient are presented in Figure 4.17. In Figure 4.17 (a) the radiative heat transfer coefficients between wall and particle bed are shown as solid lines and the contact heat transfer are as dotted lines. It indicates that due to the reason of higher inner wall temperature of monodisperse system, the radiative heat transfer coefficients between inner wall and particle bed are always higher than bidisperse particle system which has around  $30 \text{ W/m}^2\text{K}$  difference. In contrast, for the contact heat transfer, the 0.4 mm monodisperse particle bed has the same heat transfer coefficient profiles with bidisperse particle bed because of the same particle composition on the contact surface.

In Figure 4.17 (b) the radiative heat transfer coefficients between gas and inner wall are shown as solid lines and the radiative heat transfer coefficients between gas and bulk bed are as dotted lines. It indicates that for all these two heat transfer coefficients, the maximum values of monodisperse particle system are always larger than bidisperse system which is mainly caused by higher gas temperature of monodisperse system.

The comparisons of heat flow are shown in Figure 4.18. In part (a), the contact heat flow between inner wall and bulk bed are presented as solid lines and the radiative heat flow between inner wall and bulk bed are as dotted lines. Similarly, in part (b), the effective heat flow between gas and particle bed are shown as solid lines and between gas and inner wall as dotted lines. It is clear to see that for these four heat flows, the monodisperse particle bed has higher absolute value of maximum heat flow in both positive and negative region. The critical points of heat flow from positive to negative are all around  $z = 35 \text{ m}$  which means the range of cooling zone are the same regardless of particle bed mixing condition.

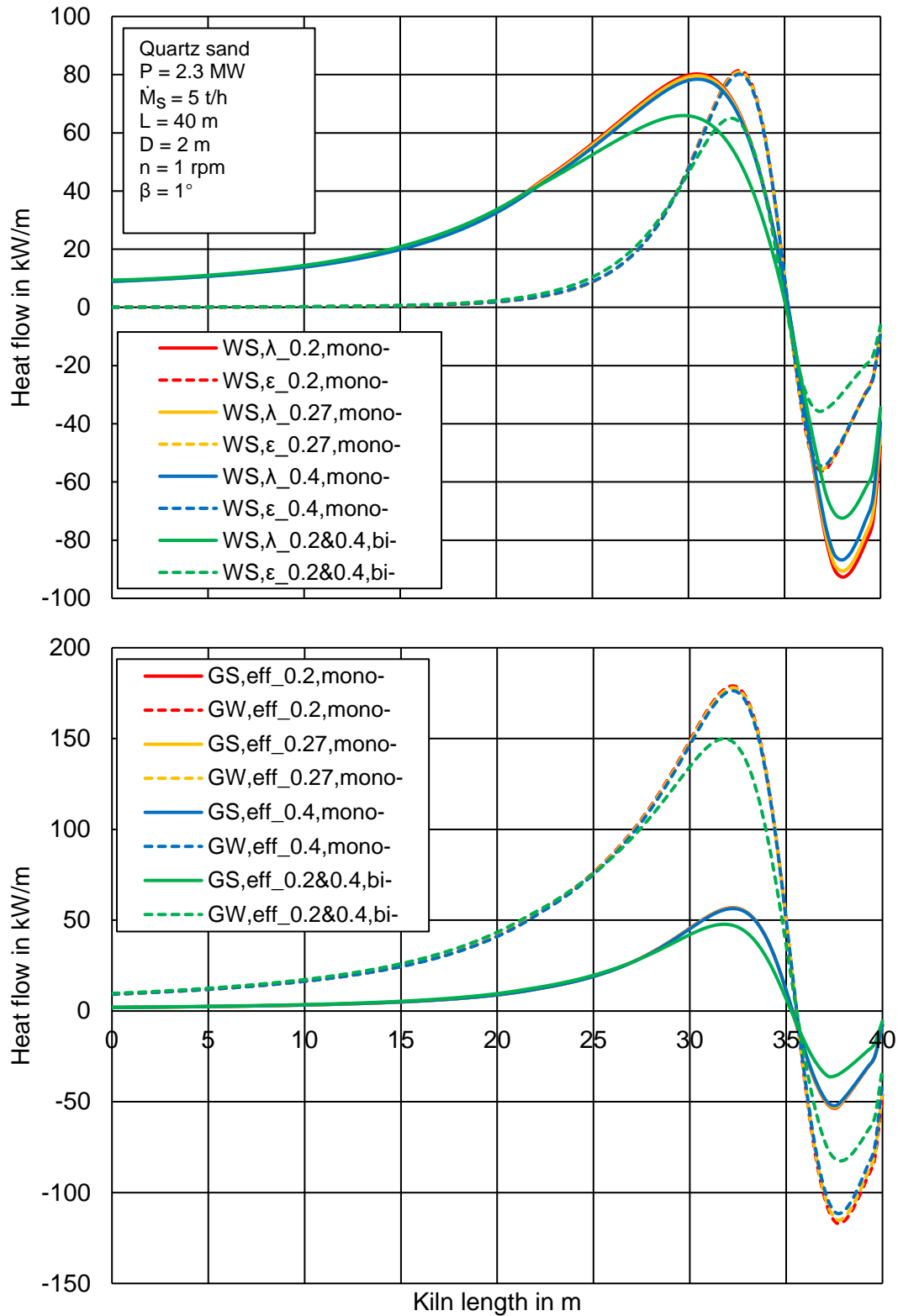


**Figure 4.18** Heat flow comparison between mono- and bidisperse particle bed.

#### 4.3.4 Influence of particle mass ratios in bidisperse particle system

To analyze the influence of the particle mass ratio in bidisperse particle system, 0.2&0.4 mm mixing particles are chosen as test materials with different mass ratios from 70%&30% to 30%&70%. It should be notice that an appropriate mass ratio should be selected to make sure forming an obvious ring-core structure in particle bed. That means, if the mass proportion between big and small particles is approaching 90%&10% or 10%&90%, the particle bed could be easily considered as monodisperse particle system. The operation conditions of process model are the same as before and the temperature profiles of gas and inner wall are presented in Figure 4.19 which shows the gas temperature as solid lines and inner wall temperature as dotted lines. It could be observed that the gas temperature and inner wall temperature have similar tendency. By enlarging the big particle mass ratio, the maximum temperature of gas and inner wall increase to the largest value of  $T_{G,max,30/70} = 1600^{\circ}\text{C}$  and  $T_{W,max,30/70} = 1490^{\circ}\text{C}$  respectively.

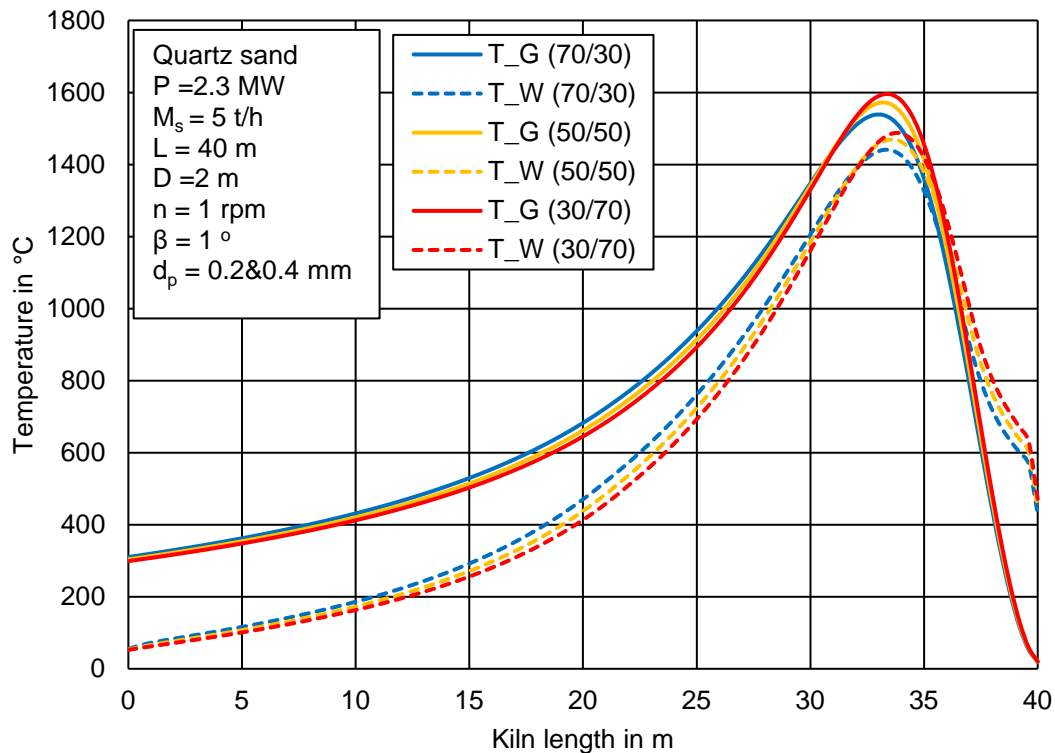


**Figure 4.19** Influence of particle mass ratios on temperature of gas and inner wall

The influence of the particle mass ratio on bulk bed temperatures are shown in Figure 4.20 which presents 0.4 mm particle bed temperature as solid lines and 0.2 mm particles as dotted lines.

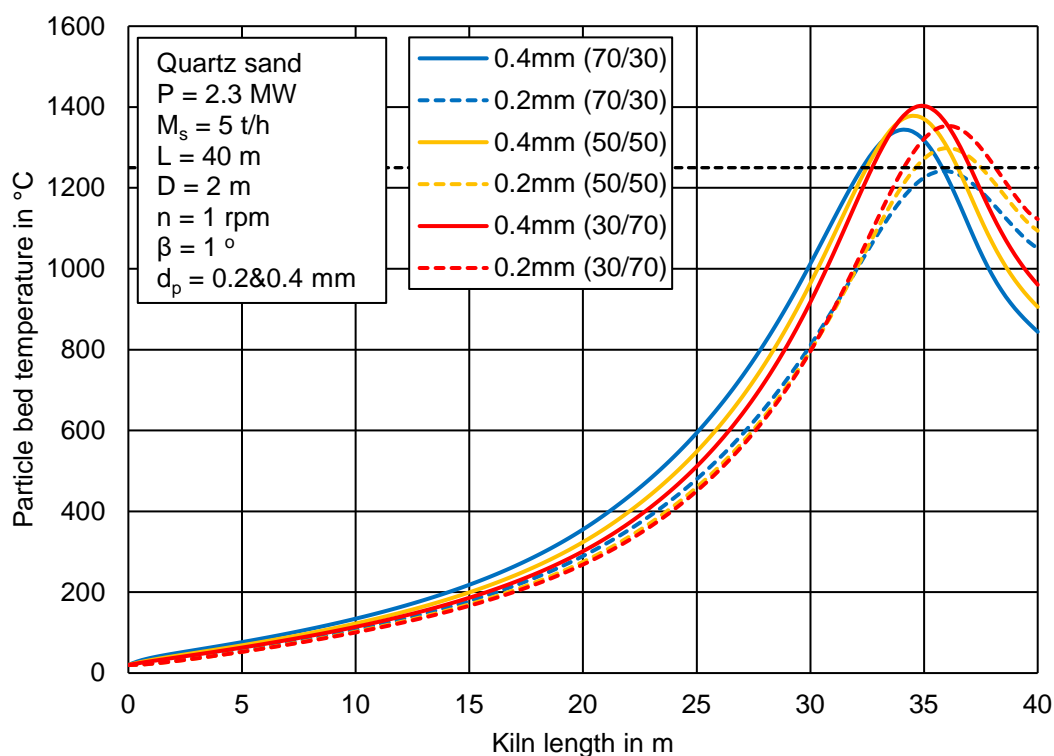


**Figure 4.20** The influence of particle mass ratios on particle bed temperature

It is clear to see that for 0.4 mm particles, with enlarged mass ratio, from 0.3 to 0.7, the maximum bulk bed temperature will also increase. For 30% mass ratio conditions, the 0.4 mm particles have the maximum bed temperature of  $T_{S,max,0.4,30\%} = 1341^{\circ}\text{C}$  which is the lowest compared to other 2 conditions. In the same time, the MRT of 0.4 mm particles is 189 min which is shorter than other particle ratio conditions and the axial length above reference temperature is around  $\Delta z_{1250^{\circ}\text{C},0.4,30\%} = 3.2$  m which leads to a residence time of  $RT_{1250^{\circ}\text{C},0.4,30\%} = 14$  min. Furthermore, with this particle mass ratio, for 0.2 mm particles, the maximum bed temperature is  $T_{S,max,0.2,70\%} = 1241^{\circ}\text{C}$  which is below the reference temperature. Therefore, both 0.2 mm and 0.4 mm particles will not ensure the requirement of the product. With increasing mass ratio of 0.4 mm particles,



the maximum bed temperature will be enlarged to  $T_{S,max,0.4,70\%} = 1400^{\circ}\text{C}$  which is around 150 K larger than 70%&30% condition. Hence, for 0.4 mm particles, the axial length above reference temperature is around  $\Delta Z_{1250^{\circ}\text{C}, 0.4,70\%} = 4.2$  m and the residence time is  $RT_{1250^{\circ}\text{C},0.4,70\%} = 16$  min. Due to the increased temperature of outer ring, the 0.2 mm particle in the core will also have higher bulk bed temperature of  $T_{S,max,0.2,30\%} = 1350^{\circ}\text{C}$  which leads to a wider region  $\Delta Z_{1250^{\circ}\text{C}, 0.2,30\%} = 3.6$  m above reference temperature and larger residence time of  $RT_{1250^{\circ}\text{C},0.4,70\%} = 14$  min. Therefore, the 0.4 mm particles will 100% ensure the product requirement.

The influences of the mass flow ratio on heat transfer coefficient are shown in Figure 4.21. In this figure, the radiative heat transfer coefficient between inner wall to particle bed are shown as solid lines, the contact heat transfer coefficient between inner wall and bulk bed are shown as dotted lines and the conduction between large and small particle bed are as dot dash lines. It is clear to see that the between inner wall and particle bed, the mass ratio has no influence on contact heat transfer because of the constant composition on contact heat transfer surface. In contrast, the radiation between inner wall and solid bed will increase with enlarged mass ratio of 0.4 mm particles which is due to the increased temperature of inner wall. Moreover, the decreased 0.2 mm mass flow rate causes smaller transverse area of 0.2 mm particles which leads to decreased contact time between big and small particle bed. Meanwhile, based on equation 4.12, the smaller contact heat transfer time is, the larger contact heat transfer coefficient will be. Therefore, the increasing mass ratio of big particle will lead to the increment of contact heat transfer between big and small size particle bed.

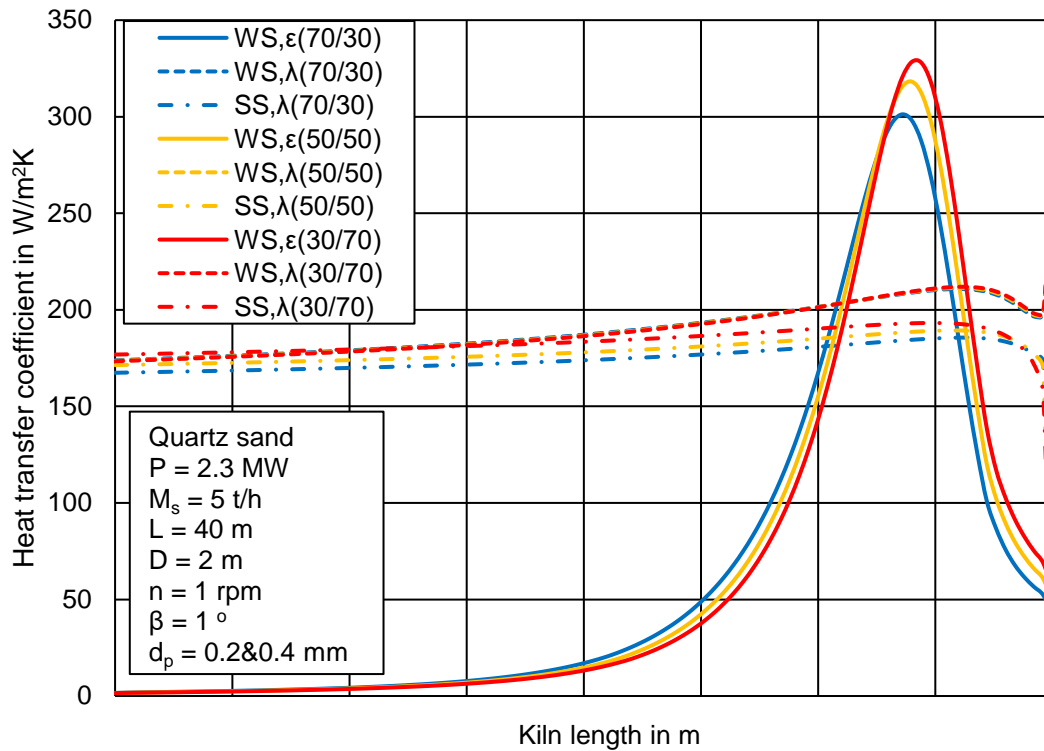


**Figure 4.21** Influence of the particle mass ratio on heat transfer coefficients of radiation between inner wall and bulk bed, conduction between inner wall and bulk bed, conduction between big and small particle bed.

In Figure 4.22, the contact heat flow between inner wall and bulk bed is shown as solid lines and the contact heat flow between big and small size particle bed are shown as dotted lines. It could be observed that although the contact heat transfer coefficient between inner wall and bulk bed is nearly constant with varied particle mass ratios. Due to the increased temperature difference, the heat flow will also be increased with enlarged 0.4 mm mass flow ratios. In contrast, the contact heat flow between particle beds shows the opposite tendency which will be reduced with increasing 0.4 mm particle mass ratios. To explain qualitatively, the 0.2 mm particle bed needs less energy with reduced mass ratio. Furthermore, the contact heat flow between particle beds could be written as

$$d\dot{Q}_{SS,\lambda} = \alpha_{1-2,\lambda} \cdot dA_{1-2} \cdot (T_{S,P_1} - T_{S,P_2}). \quad (4.64)$$

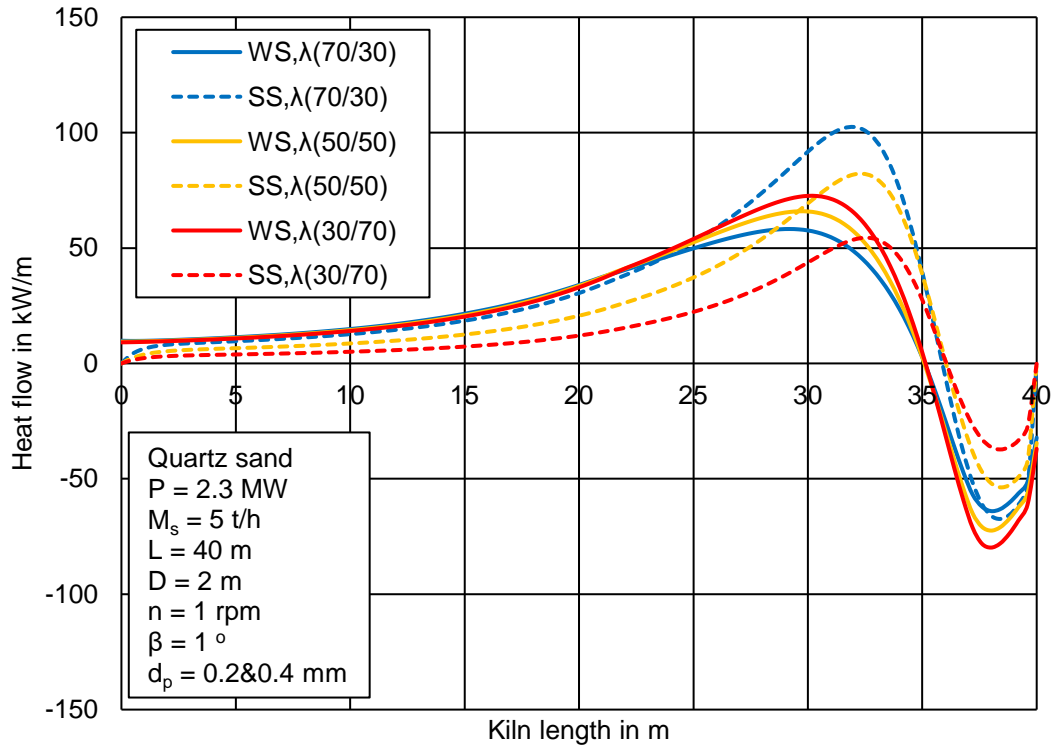


**Figure 4.22** Influence of mass ratio on heat flow of radiation between inner wall and bulk bed, conduction between inner wall and bulk bed

Based on the equation, although there is a slightly increment of contact heat transfer coefficient with increasing 0.4 mm mass ratio, the temperature difference between 0.4 mm and 0.2 mm particle bed is reduced with increasing mass ratio of large particles which could be observed from Figure 4.20. On the other hand, for the contact area, which is the perimeter of the 0.2 mm particle bed in cross-section view, the increased 0.4 mm mass ratio will lead to smaller contact area. Therefore, these two major reasons lead to reduced contact heat flow with increasing large particle mass ratios. In addition, this decreased contact heat flow will also cause higher temperature of 0.4 mm particles.

### 4.3.5 Influence of particle diameters in bidisperse particle system

In this part, 0.2&2 mm and 1&2 mm mixing quartz sand with 50/50 mass ratio are selected as simulated materials and the calcination process are under the same operational conditions as before. The simulated results are compared with 0.2&0.4 mm quartz sand materials and the temperature profiles are introduced in Figure 4.23 and in Figure 4.24.

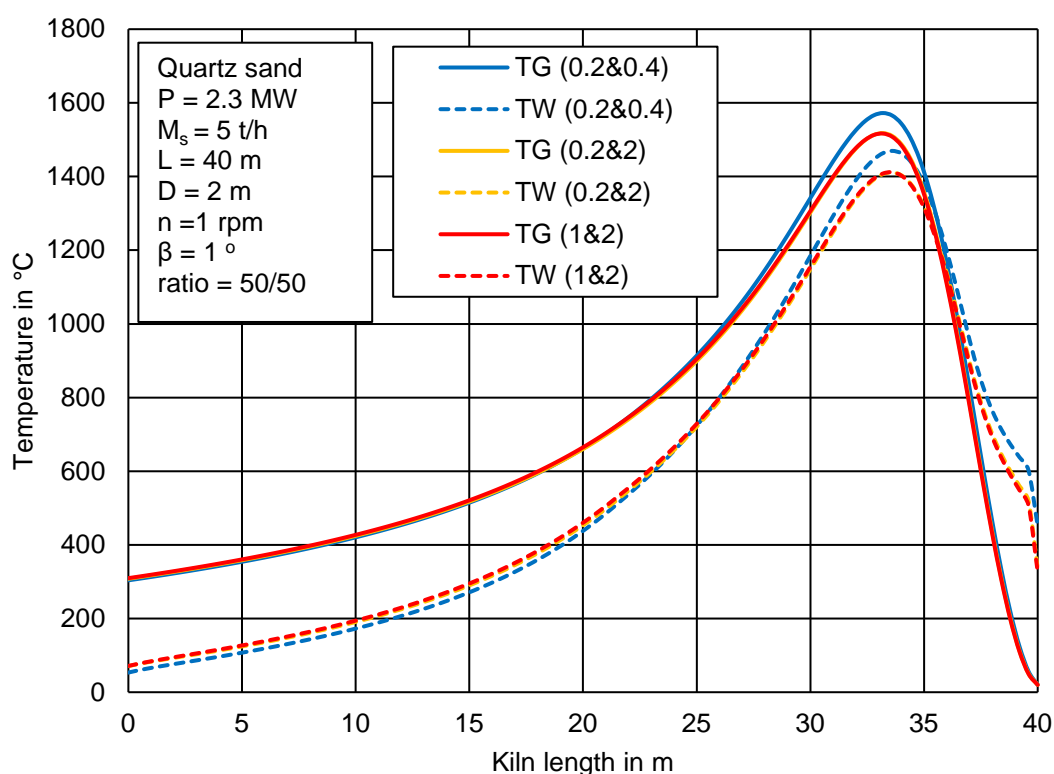


**Figure 4.23.** Influence of particle diameters on temperature of gas and inner wall in bidisperse particle system.

In Figure 4.23, the gas temperatures are shown as solid lines and the inner wall temperature as dotted lines. For both gas and inner wall temperature, the maximum values are all affected by the large particles regardless of the varied size of small particles which could be observed from the temperature profiles of 0.2&2 mm and 1&2 mm mixing particles. In this case, due to the ring-core structure of bidisperse

particle system, the outer rings of the particle bed are all formed with 2 mm particles which leads to the same heat transfers conditions on contact surface as well as to the gas phase. Therefore, the temperature profiles of these two mixing materials are approximately the same. Furthermore, with reduced large particle diameters, the maximum temperature will be increased because of the increased heat transfer coefficient which has been already discussed in chapter 4.3.2.

In Figure 4.24, the solid lines show the temperature profiles of large size particles bed and the dotted lines show the profiles of small ones. As mentioned before, due to the ring-core structure, with increasing of large particle sizes from 0.4 mm to 2 mm, the maximum temperature of big particles will be decreased which leads to the reduced temperature of small particles even if the size of small particles are fixed. Nevertheless,

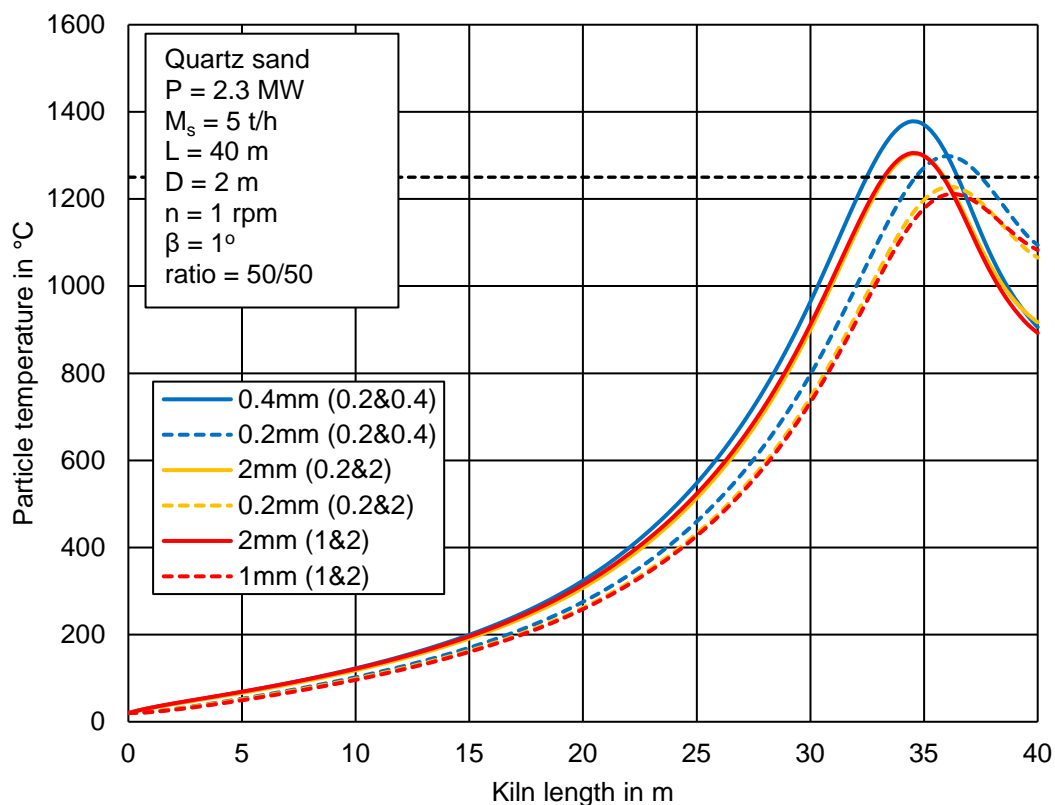


**Figure 4.24** Influence of particle diameters on temperature of particle bed in bidisperse particle system.

if the large particle diameter remains constant and the small one increases, from 0.2&2 mm to 1&2 mm, the maximum bed temperature of large particles are almost the same. At the same time, the temperature of small particle will have a little decrement which is due to the enlarged heat resistance of gas gap between larger particles. In summary, the highest bulk bed temperature will be mainly influenced by the large size particles of the mixing materials. By decreasing the size of large particles leads to higher bulk temperature for the whole mixing particle bed.

To make the further comparisons, the heat transfer coefficient profiles are introduced in Figure 4.25. For the heat transfer between inner wall and particle bed, the radiative

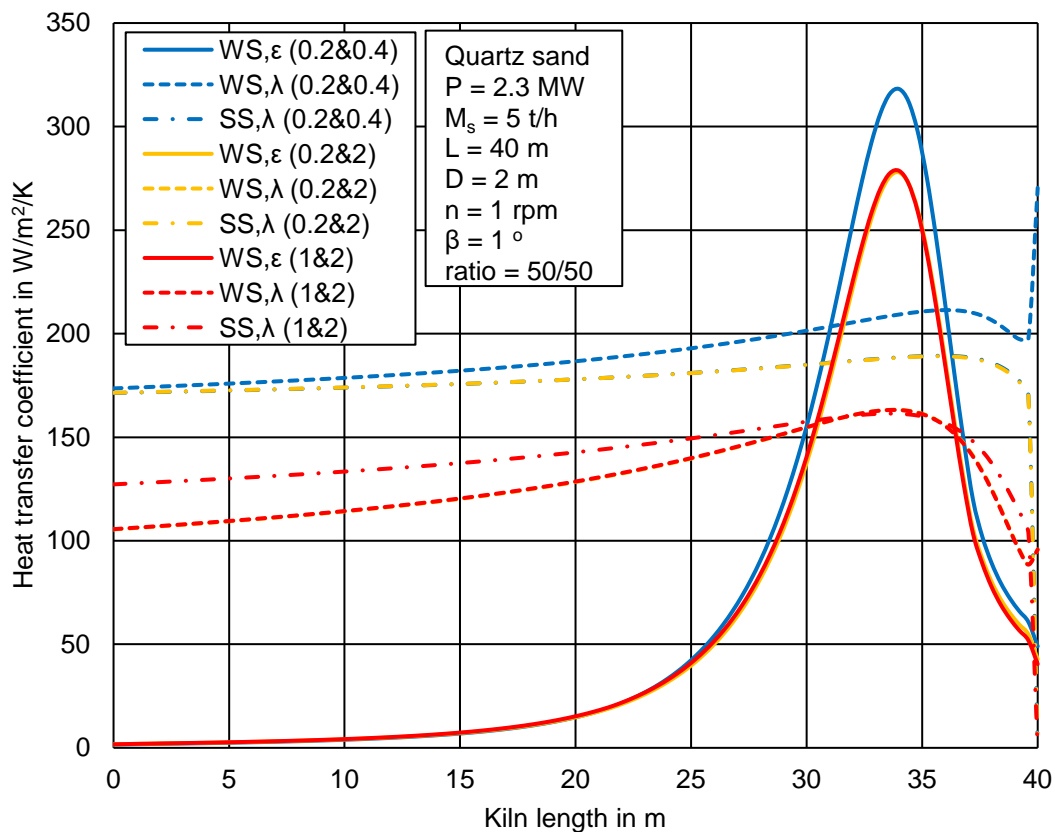


**Figure 4.25** Influence of the particle diameters on heat transfer coefficients.

heat transfer coefficients are shown as solid lines and contact heat transfer coefficients are as dotted lines. Meanwhile, the conductive coefficients between particle beds are

shown as dot dash lines. It is observed that with increasing of large particle sizes, the radiative heat transfer coefficient will be reduced. For 0.2&2 mm and 1&2 mm mixing particles, due to the same heat transfer conditions for outer ring particles, the coefficients are the same which indicates the same pattern for contact heat transfer coefficients between wall and particle bed. On the other hand, for the conduction between big and small particle bed, based on the model in chapter 4.1.2, the coefficients will be dominated by small size particles in the core which will be reduced with increasing diameter of small particles.

In addition, the influence of the particle diameters on heat flow are shown in appendix which has the similar pattern with heat transfer coefficients.

#### **4.3.6 Simulation results with polydisperse particle system**

By implementing the segregation model of polydisperse particle system in process model, the calcination process of quartz sand with polydisperse raw materials could be simulated and the results are shown from Figure 4.26 to 4.28. In this case, 0.2&0.4&1&2 mm mixing particles are selected as simulated materials with 25/25/25/25 homogeneous mass fraction and the other operational conditions are the same as mono- and bidisperse particle systems before. The temperature profiles along the axis of the kiln are presented in Figure 4.26 where the profiles of varied particle sizes are shown from (3) to (6) as dotted lines respectively. It is clear to see that the 2 mm particle bed owns the highest maximum temperature  $T_{S,max,2} = 1319^{\circ}\text{C}$  compared to other three particle beds. This is similar to the bidisperse particle system that the largest size particles located in the outermost ring and has the highest peak value of bed temperature. With reduced particle sizes, the maximum temperature of particle bed will also decrease, and the axial position of this peak value will be shifted from  $Z_{max,2mm} = 34$  m to  $Z_{max,2mm} = 38$  m which is closer to the outlet.

Moreover, the smallest particles located in the core own the highest outlet temperature

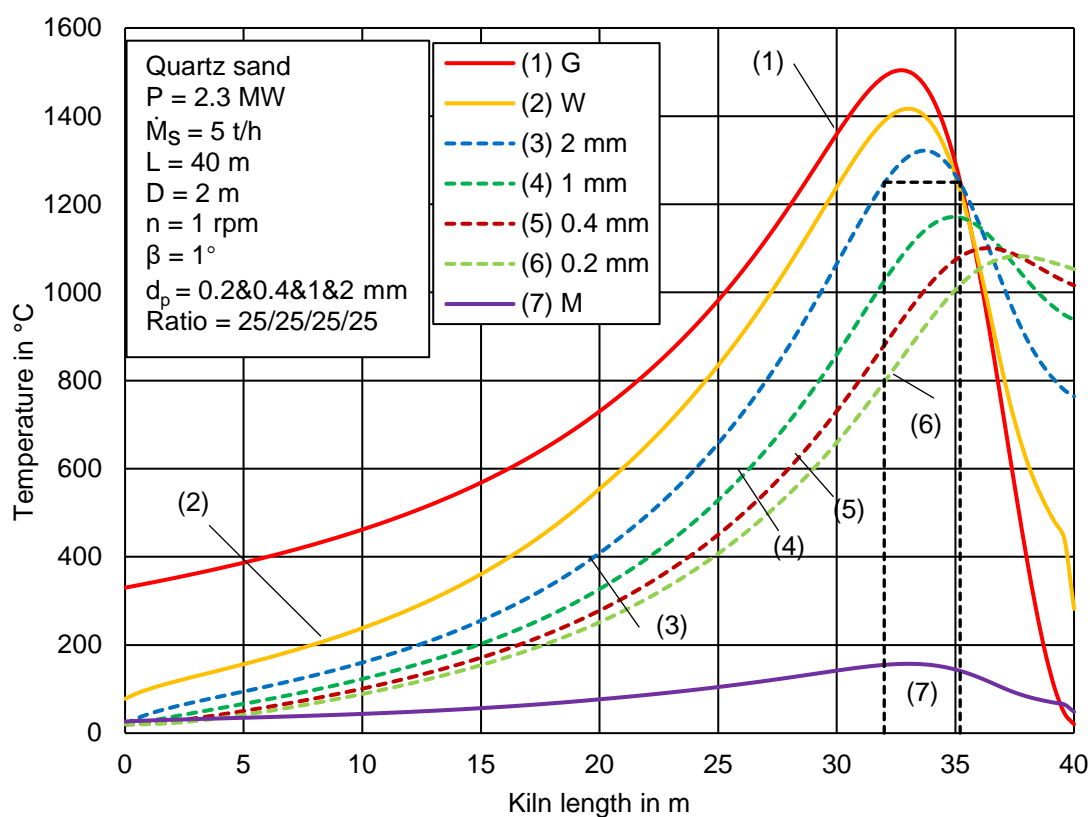


**Figure 4.26** Temperature profiles of polydisperse particle system in rotary kiln during calcination

and it will be reduced with increasing particle diameters which means the largest particles has the lowest outlet temperature. On the other hand, only the 2 mm particle bed owns a region  $\Delta z_{1250^{\circ}\text{C}} = 3.2$  m and the residence time is  $RT_{1250^{\circ}\text{C}} = 13.5$  min which is approaching the required process time. In contrast, the maximum temperature of 1 mm, 0.4 mm and 0.2 mm particle bed are all below reference which means all the product will not ensure the requirement (see Appendix C and D).

The profiles of local contact heat transfer coefficients are introduced in Figure 4.27 which presents the heat transfer between inner wall and particle bed as well as the heat transfer between each size of particle bed. It has already been introduced that based on the ring-core structure, there is only contact heat transfer between each size of particle bed. At the same time, the contact heat transfer coefficient only depends on the particle size of inner layer particle bed and the coefficient will be enlarged by reducing particle



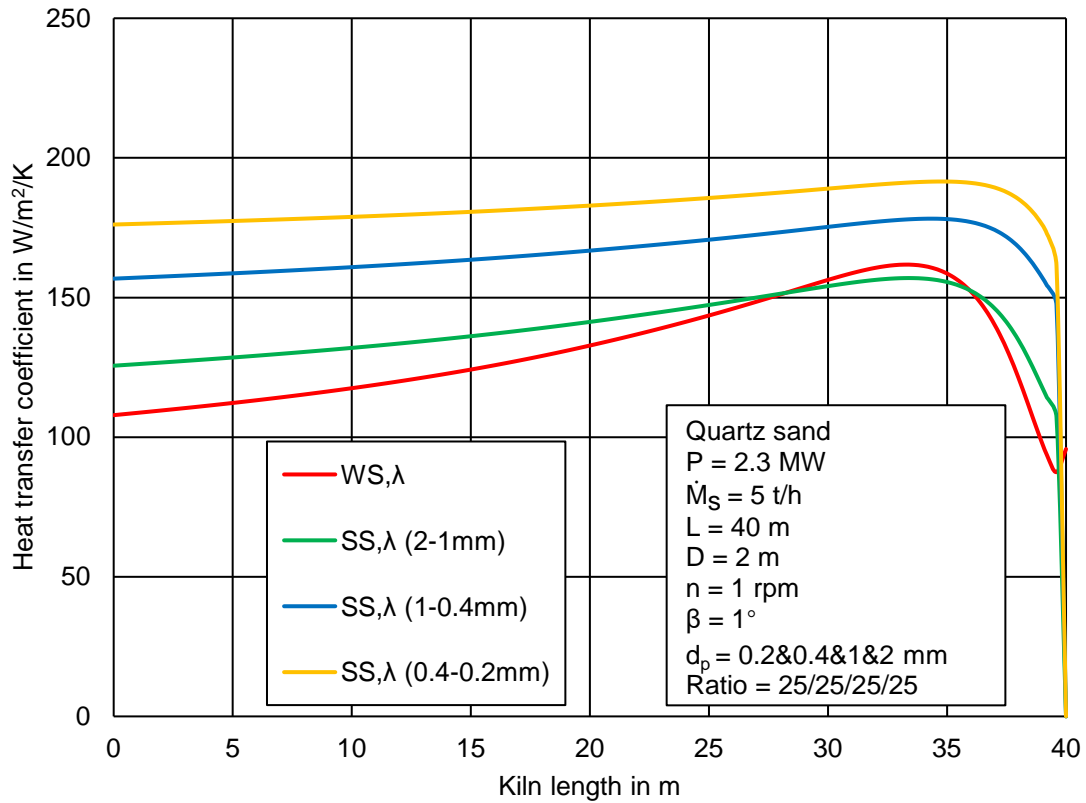


**Figure 4.27** Axial profiles of local heat transfer coefficients with polydisperse particle systems

diameters. Therefore, the heat transfer coefficient between each particle bed will increase from outermost layer to the core. On the other hand, the contact heat transfer coefficients between particle bed will all reduce to 0 in the outlet and there is only contact heat transfer between inner wall and particle bed. That is to say, the low particle bed depth leads to form a no segregation structure and the particles will be considered as a well-mixed particle system which only has heat transfer with inner wall surface.

### 4.3.7 Influence of particle mass ratios in polydisperse system

To analyze the influence of the particle mass ratios in polydisperse particle system, 0.2&0.4&1&2 mm mixing particles are chosen as test materials with different mass ratios from 35/25/25/15 to 15/25/25/35 which means there is no change for 1 mm and 0.4 mm particles. The temperature profiles of each particle bed are shown in Figure 4.28. It should be mentioned that, for some special case such as 45/25/25/5 mass ratio conditions, due to the small fraction of 2 mm particles, the particle bed cannot form the outer ring for 2 mm particles. Therefore, the 2 mm and 1 mm mixing particles are considered as the composition of the outermost ring which own the same particle bed temperature profiles and will not be presented in following content.

It is clear to see that for the 2 mm particles, with increasing mass ratios, the maximum temperature will also be enlarged, and the axial position of this peak value approaches the outlet of rotary kiln which is similar to the bidisperse particle systems. Due to the ring-core structure, the higher 2 mm particle temperature leads to higher inner particle temperatures. That is to say, the reduced 0.2 mm particle mass ratio will cause the increasing of all particle bed maximum temperatures as well as 0.2 mm itself. By comparing the temperature profiles between mono- and polydisperse, it is clear to see that, with the same operational conditions, for 0.2 mm particles, the maximum temperature of monodisperse is  $T_{0.2 \text{ mm,max, mono-}} = 1451^{\circ}\text{C}$  which is much higher than the polydisperse condition  $T_{0.2 \text{ mm,max, poly-}} = 1119^{\circ}\text{C}$  and could not reach the reference temperature of  $1250^{\circ}\text{C}$ . Therefore, the particle size distribution should be homogeneous to bring higher particle bed temperature and less temperature gradient inside of particle bed.

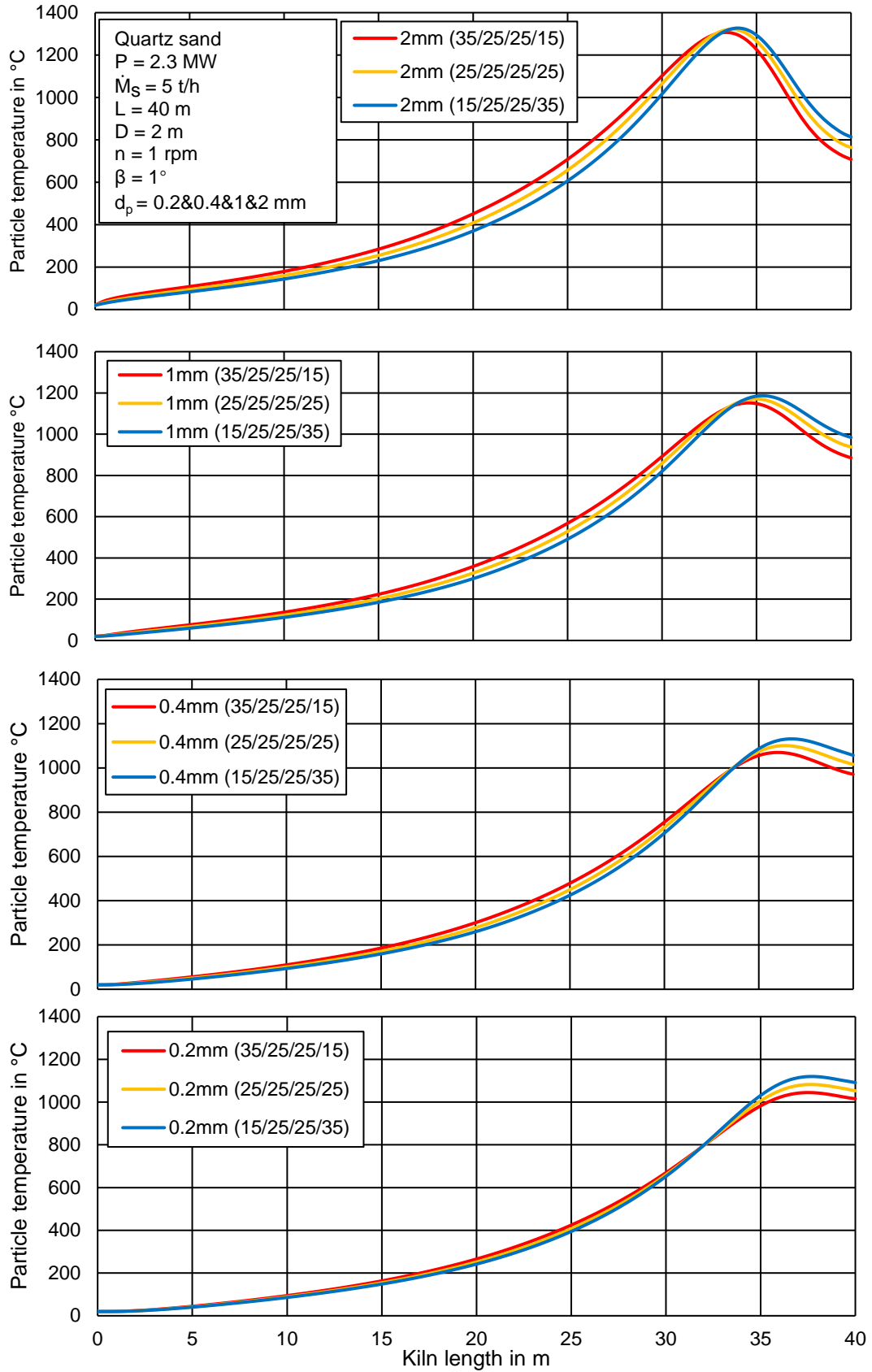


**Figure 4.28** Influence of particle mass ratios on particle bed temperature of polydisperse system

Figure 4.29 shows the profiles of contact heat transfer coefficient with varied mass flow ratios of polydisperse particle systems. In this figure, the contact heat transfer coefficient between 2 mm and 1 mm particle bed are shown as solid lines. The coefficient between 1 mm and 0.4 mm particle bed are shown as dotted lines and the coefficient between 0.4mm and 0.2 mm are as dot dash lines. It is clear to see that for the contact heat transfer coefficients between 2 mm and 1 mm particle bed, the maximum value will be slightly increased with increasing 2 mm particle mass flow ratio which is due to the reason of decreased contact areas based on equation 4.12. Similarly, the reduced mass ratio of 0.2 mm particles also leads to smaller contact area and higher contact heat transfer coefficients. In contrast, between 1 mm and 0.4 mm, the coefficients are nearly the same because there is no change of mass flow ratios which means the contact areas keep constant in this condition.

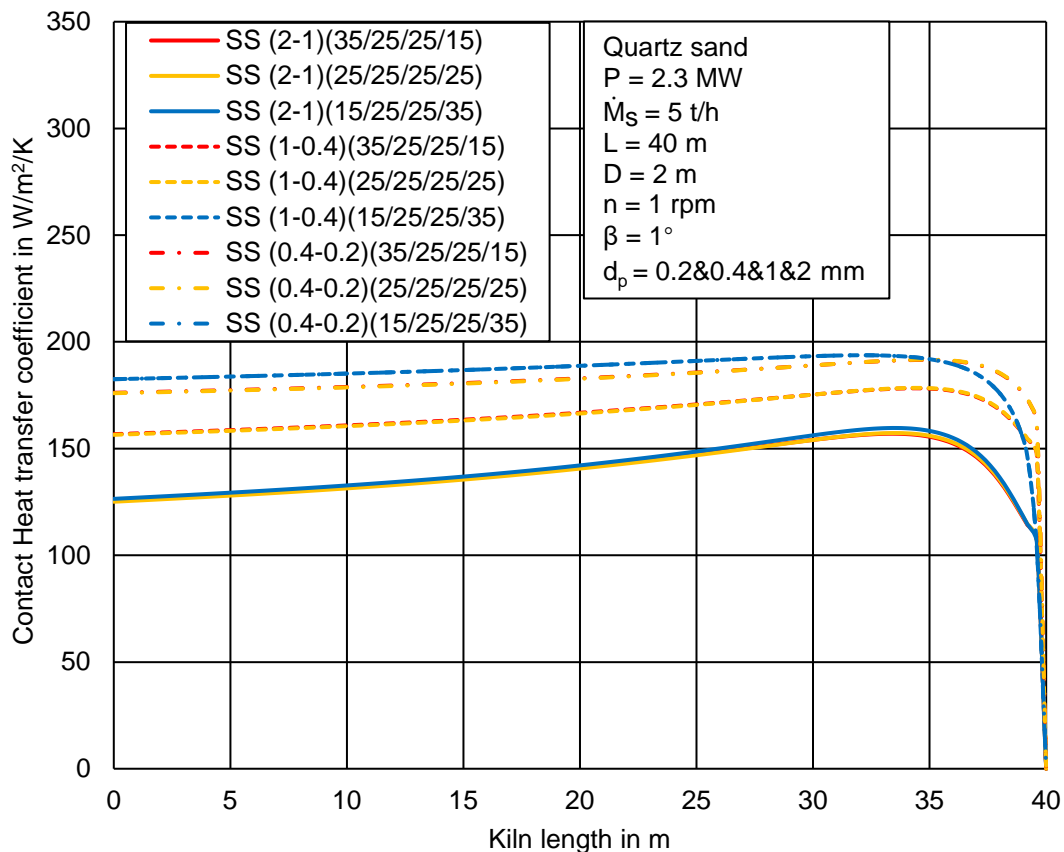


**Figure 4.29** Influence of particle mass ratios on contact heat transfer coefficients of polydisperse system

## 4.4 Conclusion

In this chapter, the segregation model in chapter 3 is improved and implemented in the process model of Herz (2012) to simulate the calcination process of quartz sand in bi- and polydisperse particle systems. Based on this improvement, the particle bed temperature profiles of each particle size could be clear know in detail as well as heat transfer coefficients and heat flow. Mono-, bi- and polydisperse particle system are all considered as simulation materials which give the following patterns and results.

- 1) For calcination, due to the inlet gas temperature of 20°C, there are both heating and cooling zone for the whole process. The axial position of maximum gas temperature is further to the outlet compared to the position of maximum particle temperature.
- 2) For the monodisperse system, the increased particle size brings lower maximum particle bed temperature, shorter reference times and lower contact heat transfer coefficient between wall and particle bed which is caused by the enlarged gas gap between particle bed and inner wall surface.
- 3) For the bidisperse system, due to the existing of heat transfer between big and small particle beds, this heat flow is considered as heat loss of big particle bed. Therefore, the bidisperse particle system will have much lower maximum bed temperature compared to the monodisperse system with the same particle diameter of large particles such as the comparison between 0.2&0.4 mm and 0.4 mm particles.
- 4) For the bidisperse particle system, the particle mass flow ratio is an essential parameter which has a strong influence on particle bed temperature. With enlarging mass flow ratio of big particles, the decreased small particle mass ratio leads to less heat transfer between big and small particles and the particle bed is approaching a monodisperse system. At the same time, the increased mass flow ratio leads to smaller contact areas between big and small particles which also brings higher contact heat transfer coefficients. These two main reasons work together to increase the temperature for both size particles.
- 5) The varied particle diameter is another important parameter on particle bed

temperature. In the bidisperse particle system, the large size particles dominate the maximum value of bed temperatures. If the diameter of the big particle is enlarged, the maximum bed temperature will be reduced which is similar to the monodisperse particle system. In contrast, if the diameter of the large size particle keeps constant, the temperature will have no big difference regardless of the diameter of small particles. At the same time, the reduction of small particle size will bring a slight increment of its bed temperature.

- 6) For the polydisperse system, the energy balance indicates that the heat transfer between every two neighboring layers should be all considered and for the outermost layer, the overall enthalpy will be less than bid- and monodisperse system. Therefore, the polydisperse system has much lower maximum temperature compared to the mono- and bidisperse system which means, in the industrial field, the particle size distribution should be more homogeneous to have higher particle bed temperature and more efficiency of heat treatment.

## 5 Conclusion and recommendation

### 5.1 Conclusion

The particle axial transport inside of the rotary kiln is studied in the present work which contains two parts, the transient process of the monodisperse particle system and the residence time distributions of the polydisperse particle system. For the transient process, the video analysis method is utilized measuring the particle bed depth profiles in a pilot-scale kiln continuously with different kinds of materials. At the same time the mathematical model based on Spurling is implemented to simulate the transient behavior with the same kiln size and operational condition. The simulation results are validated with experiments data that presented good agreements with each other. Rotational speed, feed mass flow rate and inclination angle are varied to see the influence on the stationary time. The results demonstrate that the stationary time will be reduced dramatically with increasing rotational speed or inclination angle at first but finally fluctuate around a fixed value. In contrast, the feed mass flow rate has quite a small impact on stationary time and with increasing feed mass flow rate, there is only a slight increment of stationary time.

The residence time distribution of a polydisperse particle system consists of two parts which are MRT of each kind of particle and variance of the RTD. For the MRT of each particle size, a new mathematical model based on the ring-core structure and segregation model is developed to simulate the axial transport of polydisperse particles. MRT, particle local axial transport velocity and local volume fractions are derived from it. On the other hand, a series of experiments are finished to validate the model with the bidisperse particle system. The raw materials are 0.7, 2 and 4 mm glass beads mixing with different mass fractions. For the variance of the RTD, the axial dispersion model is implemented to analyze the curve of RTD from the experiment where the variance of RTD, Peclet number and axial dispersion coefficient could be derived from it.

Furthermore, an empirical equation is created to predict the axial dispersion coefficient which is quite essential for the estimation on the variance of the RTD.

The results indicate that the new model shows good agreement with experimental data which means the ring-core structure, as well as the mathematical model is appropriate to describe the axial transport of the polydisperse particle system. Furthermore, the rotational speed, inclination angle and feed mass flow rate are also considered as impact factors on RTD which indicated that (i) With the same physical properties, the MRT of big size particles is always smaller than of small particles regardless of mixing status. (ii) The rotational speed and inclination angle have the stronger influence on MRT, the variance of RTD curve and  $D_z$  than feed mass flow rate. (iii) The particle size difference is another essential factor on RTD in the bidisperse system. If the particle diameter difference is big enough, the small size particles transport through big gaps of big particles and concentrate on the bottom of particle bed which will affect the transverse motion of particle bed significantly and lead to fewer correlations with the mathematical model.

The model in chapter 3 is improved and implemented in the process model of Herz (2012) to simulate the calcination process of quartz sand in bi- and polydisperse particle systems. The simulation results could present temperature profiles of each particle size as well as heat transfer coefficients and heat flows. Mono-, bi- and polydisperse particle system were all considered as raw materials which demonstrated that (i) After comparison of the temperature profiles of mono-, bi- and polydisperse particle system, with the same size of largest particles, the more particle dispersity is the lower maximum particle temperature will be. That is mainly caused by the consideration of heat transfer between different size particle beds. (ii) In bi- and polydisperse particle systems, the size of large particles will dominate the temperature of particle bed. However, the varied small particle has slightly influence on the overall temperature profiles. (iii) If the particle categories are fixed, the particle mass fraction is another



essential parameter that has a strong influence on particle bed temperature. With increasing of large particle mass ratio, the maximum particle temperature will also be enlarged. (iv) In the industrial field, it could be recommended that for raw materials, the particle size distributions should be more homogeneous to have higher particle temperature which could own higher efficiency of heat treatment.

## 5.2 Future Work

- 1) For the experiments of RTD, the test materials are different sizes of glass beads that own smooth surface. On the other hand, the rotary kiln utilized has different roughness of the inner surface. These two impact factors will have the influence on the particle transport within rotary kilns such as the diverse dynamic angle of repose or different particle transverse motion behaviors. Therefore, other experiments with different rotary kilns and materials should be done to have more experiments data.
- 2) For the segregation model described in chapter 3 and 4, the transverse location of the core part is based on the assumption which is defined in equation 4.20 and the  $\Lambda$  is varied with particle size mass fractions and in the range from 0 to 1. Therefore, the transverse motion in bi- and polydisperse particle system should be investigated to validate the assumption with experiments and DEM simulations.
- 3) For the simulation results of the process model with bi- and polydisperse particle systems, the calcination process is without chemical reactions and variation of particle diameters. Therefore, the next step is to add both essential factors into the process model with bi- or polydisperse particle system. The results could be validated by a similar process in pilot-scale rotary kilns or the DEM simulation.

## References

- Abouzeid, A. Z. M., & Fuerstenau, D. W. (2010). Flow of non-homogeneous particulates in rotating drums. *KONA Powder and Particle Journal*, 28, 155-166.
- Abouzeid, A. Z., Mika, T. S., Sastry, K. V., & Fuerstenau, D. W. (1974). The influence of operating variables on the residence time distribution for material transport in a continuous rotary drum. *Powder Technology*, 10(6), 273-288.
- Alizadeh, E., Dubé, O., Bertrand, F., & Chaouki, J. (2013). Characterization of mixing and size segregation in a rotating drum by a particle tracking method. *AIChE Journal*, 59(6), 1894-1905.
- Bensmann, S., Subagyo, A., & Walzel, P. (2010). Residence time distribution of segregating sand particles in a rotary drum. *Particulate Science and Technology*, 28(4), 319-331.
- Boateng, A. A., & Barr, P. V. (1996). A thermal model for the rotary kiln including heat transfer within the bed. *International Journal of Heat and Mass Transfer*, 39(10), 2131-2147.
- Boateng, A. A., & Barr, P. V. (1996). Modelling of particle mixing and segregation in the transverse plane of a rotary kiln. *Chemical Engineering Science*, 51(17), 4167-4181.
- Bridgwater, J., Foo, W. S., & Stephens, D. J. (1985). Particle mixing and segregation in failure zones—theory and experiment. *Powder technology*, 41(2), 147-158.
- Britton, P. F., Sheehan, M. E., & Schneider, P. A. (2006). A physical description of solids transport in flighted rotary dryers. *Powder Technology*, 165(3), 153-160.
- Chatterjee, A., Sathe, A. V., & Mukhopadhyay, P. K. (1983). Flow of materials in rotary kilns used for sponge iron manufacture: Part II. Effect of kiln geometry. *Metallurgical Transactions B*, 14(3), 383-392.
- Chatterjee, A., Sathe, A. V., Srivastava, M. P., & Mukhopadhyay, P. K. (1983). Flow of materials in rotary kilns used for sponge iron manufacture: Part I. Effect of some operational variables. *Metallurgical Transactions B*, 14(3), 375-381.

- Dhanjal, S. K., Barr, P. V., & Watkinson, A. P. (2004). The rotary kiln: An investigation of bed heat transfer in the transverse plane. *Metallurgical and Materials Transactions B*, 35(6), 1059-1070.
- Dinesh V, L., & Sai, P. S. T. (2004). A model for residence time distribution of solids in a rotary kiln. *The Canadian Journal of Chemical Engineering*, 82(2), 392-398.
- Duchesne, C., Thibault, J., & Bazin, C. (1996). Modeling of the solids transportation within an industrial rotary dryer: A simple model. *Industrial & engineering chemistry research*, 35(7), 2334-2341.
- Gao, Y., Glasser, B. J., Ierapetritou, M. G., Cuitino, A., Muzzio, F. J., Beeckman, J. W., ... & Borghard, W. G. (2013). Measurement of residence time distribution in a rotary calciner. *AIChE Journal*, 59(11), 4068-4076.
- Gao, Y., Muzzio, F. J., & Ierapetritou, M. G. (2012). A review of the Residence Time Distribution (RTD) applications in solid unit operations. *Powder technology*, 228, 416-423.
- Gao, Y., Vanarase, A., Muzzio, F., & Ierapetritou, M. (2011). Characterizing continuous powder mixing using residence time distribution. *Chemical Engineering Science*, 66(3), 417-425.
- Hallak, B., Specht, E., Herz, F., Gröpler, R., & Warnecke, G. (2017). Influence of Particle Size Distribution on the Limestone Decomposition in Single Shaft Kilns. *Energy Procedia*, 120, 604-611.
- Hatzilyberis, K. S., & Androutopoulos, G. P. (1999). An RTD study for the flow of lignite particles through a pilot rotary dryer part i; bare drum case. *Drying technology*, 17(4-5), 745-757.
- He, Y. R., Chen, H. S., Ding, Y. L., & Lickiss, B. (2007). Solids motion and segregation of binary mixtures in a rotating drum mixer. *Chemical Engineering Research and Design*, 85(7), 963-973.
- Hehl, M., Kröger, H., Helmrich, H., & Schügerl, K. (1978). Longitudinal mixing in horizontal rotary drum reactors. *Powder Technology*, 20(1), 29-37.
- Henein, H., Brimacombe, J. K., & Watkinson, A. P. (1983). Experimental study of transverse bed motion in rotary kilns. *Metallurgical transactions B*, 14(2), 191-205.
- Herz, F., (2012) Entwicklung eines mathematischen Modells zur Simulation thermischer Prozesse in Drehrohröfen. PhD thesis. Otto von Guericke University

- Herz, F., Sonavane, Y., & Specht, E. (2010, August). Analysis of local heat transfer in direct fired rotary kilns. In *2010 14th International Heat Transfer Conference* (pp. 175-182). American Society of Mechanical Engineers Digital Collection.
- Herz, F., Specht, E., & Abdelwahab, A. (2017). Modeling and Validation of the Siderite Decomposition in a Rotary Kiln. *Energy Procedia*, *120*, 524-531.
- Hogg, R., Shoji, K., & Austin, L. G. (1974). Axial transport of dry powders in horizontal rotating cylinders. *Powder Technology*, *9*(2-3), 99-106.
- Hu, Z., Liu, X., & Wu, W. (2018). Study of the critical angles of granular material in rotary drums aimed for fast DEM model calibration. *Powder technology*, *340*, 563-569.
- Huang, A. N., & Kuo, H. P. (2017). CFD simulation of particle segregation in a rotating drum. Part I: Eulerian solid phase kinetic viscosity. *Advanced Powder Technology*, *28*(9), 2094-2101.
- Karra, V. K., & Fuerstenau, D. W. (1977). Material transport in a continuous rotary drum. Effect of discharge plate geometry. *Powder technology*, *16*(1), 23-28.
- Karra, V. K., & Fuerstenau, D. W. (1978). Scale-up of the axial profile of material hold-up in horizontal rotating cylinders. *Powder Technology*, *19*(2), 265-269.
- Lebas, E., Hanrot, F., Ablitzer, D., & Houzelot, J. L. (1995). Experimental study of residence time, particle movement and bed depth profile in rotary kilns. *The Canadian Journal of Chemical Engineering*, *73*(2), 173-180.
- Levenspiel, O. (1998). *Chemical Reaction Engineering*, 3rd Edition, Wiley.
- Li, S. Q., Chi, Y., Li, R. D., Yan, J. H., & Cen, K. F. (2002). Axial transport and residence time of MSW in rotary kilns: Part II. Theoretical and optimal analyses. *Powder Technology*, *126*(3), 228-240.
- Li, S. Q., Ma, L. B., Wan, W., & Yao, Q. (2005). A Mathematical Model of Heat Transfer in a Rotary Kiln Thermo-Reactor. *Chemical Engineering & Technology: Industrial Chemistry-Plant Equipment-Process Engineering-Biotechnology*, *28*(12), 1480-1489.
- Li, S. Q., Yan, J. H., Li, R. D., Chi, Y., & Cen, K. F. (2002). Axial transport and residence time of MSW in rotary kilns: Part I. Experimental. *Powder technology*, *126*(3), 217-227.
- Liu, X. Y., & Specht, E. (2006). Mean residence time and hold-up of solids in rotary kilns. *Chemical engineering science*, *61*(15), 5176-5181.

- Liu, X. Y., Specht, E., Gonzalez, O. G., & Walzel, P. (2006). Analytical solution for the rolling-mode granular motion in rotary kilns. *Chemical Engineering and Processing: Process Intensification*, 45(6), 515-521.
- Liu, X. Y., Zhang, J., Specht, E., Shi, Y. C., & Herz, F. (2009). Analytical solution for the axial solid transport in rotary kilns. *Chemical Engineering Science*, 64(2), 428-431.
- Martin, A. D. (2000). Interpretation of residence time distribution data. *Chemical engineering science*, 55(23), 5907-5917.
- Mellmann, J. (2001). The transverse motion of solids in rotating cylinders—forms of motion and transition behavior. *Powder technology*, 118(3), 251-270.
- Mellmann, J., Specht, E., & Liu, X. (2004). Prediction of rolling bed motion in rotating cylinders. *AIChE journal*, 50(11), 2783-2793.
- Mu, J., & Perlmutter, D. D. (1980). The mixing of granular solids in a rotary cylinder. *AIChE Journal*, 26(6), 928-934.
- Njeng, A. B., Vitu, S., Clause, M., Dirion, J. L., & Debacq, M. (2015). Effect of lifter shape and operating parameters on the flow of materials in a pilot rotary kiln: Part I. Experimental RTD and axial dispersion study. *Powder Technology*, 269, 554-565.
- Njeng, A. B., Vitu, S., Clause, M., Dirion, J. L., & Debacq, M. (2015). Effect of lifter shape and operating parameters on the flow of materials in a pilot rotary kiln: Part II. Experimental hold-up and mean residence time modeling. *Powder Technology*, 269, 566-576.
- Perron, J., & Bui, R. T. (1994). Fours rotatifs: Modele dynamique du mouvement du lit. *The Canadian Journal of Chemical Engineering*, 72(1), 16-25.
- Pollard, B. L., & Henein, H. (1989). Kinetics of radial segregation of different sized irregular particles in rotary cylinders. *Canadian Metallurgical Quarterly*, 28(1), 29-40.
- Rutgers, R. (1965). Longitudinal mixing of granular material flowing through a rotating cylinder: Part II. Experimental. *Chemical Engineering Science*, 20(12), 1089-1100.
- Saeman, W. C. (1951). Passage of solids through rotary kilns: factors affecting time passage. *Chemical Engineering Progress*, 47, 508.

- Sai, P. S. T., Surender, G. D., Damodaran, A. D., Suresh, V., Philip, Z. G., & Sankaran, K. (1990). Residence time distribution and material flow studies in a rotary kiln. *Metallurgical Transactions B*, 21(6), 1005-1011.
- Schlünder, E. U. (1985). Vacuum contact drying of free flowing mechanically agitated particulate material. In *Drying '85* (pp. 75-83). Springer, Berlin, Heidelberg.
- Schlünder, E. U. & Tsotsas, E. (1988) Wärmeübertragung in Festbetten, durchmischten Schüttgütern und Wirbelschichten. Georg Thieme Verlag, Stuttgart, New York.
- Sheehan, M. E., Britton, P. F., & Schneider, P. A. (2005). A model for solids transport in flighted rotary dryers based on physical considerations. *Chemical engineering science*, 60(15), 4171-4182.
- Sherritt, R. G., Chaouki, J., Mehrotra, A. K., & Behie, L. A. (2003). Axial dispersion in the three-dimensional mixing of particles in a rotating drum reactor. *Chemical Engineering Science*, 58(2), 401-415.
- Spurling, R. J., Davidson, J. F., & Scott, D. M. (2001). The transient response of granular flows in an inclined rotating cylinder. *Chemical Engineering Research and Design*, 79(1), 51-61.
- Spurling, R.J. (2000). Granular flow in an inclined rotating cylinder: steady state and transients. PhD thesis. University of Cambridge, UK.
- Sriram, V., & Sai, P. S. T. (1999). Transient response of granular bed motion in rotary kiln. *The Canadian Journal of Chemical Engineering*, 77(3), 597-601.
- Sudah, O. S., Chester, A. W., Kowalski, J. A., Beeckman, J. W., & Muzzio, F. J. (2002). Quantitative characterization of mixing processes in rotary calciners. *Powder technology*, 126(2), 166-173.
- Sullivan, J. D., Maier, C. G., & Ralston, O. C. (1927). Passage of Solid Particles Through Rotary Cylindrical Kilns. U.S. Bureau of Mines Technical Paper, No. 384
- Sunkara, K. R., Herz, F., & Specht, E. (2011, January). Thermal Fluctuations and Heat Transfer Measurements in an Externally Heated Rotary Cylinder. In *ASME/JSME 2011 8th Thermal Engineering Joint Conference*. American Society of Mechanical Engineers Digital Collection.
- Tsotsas, E., & Martin, H. (1987). Thermal conductivity of packed beds: a review. *Chemical Engineering and Processing: Process Intensification*, 22(1), 19-37.

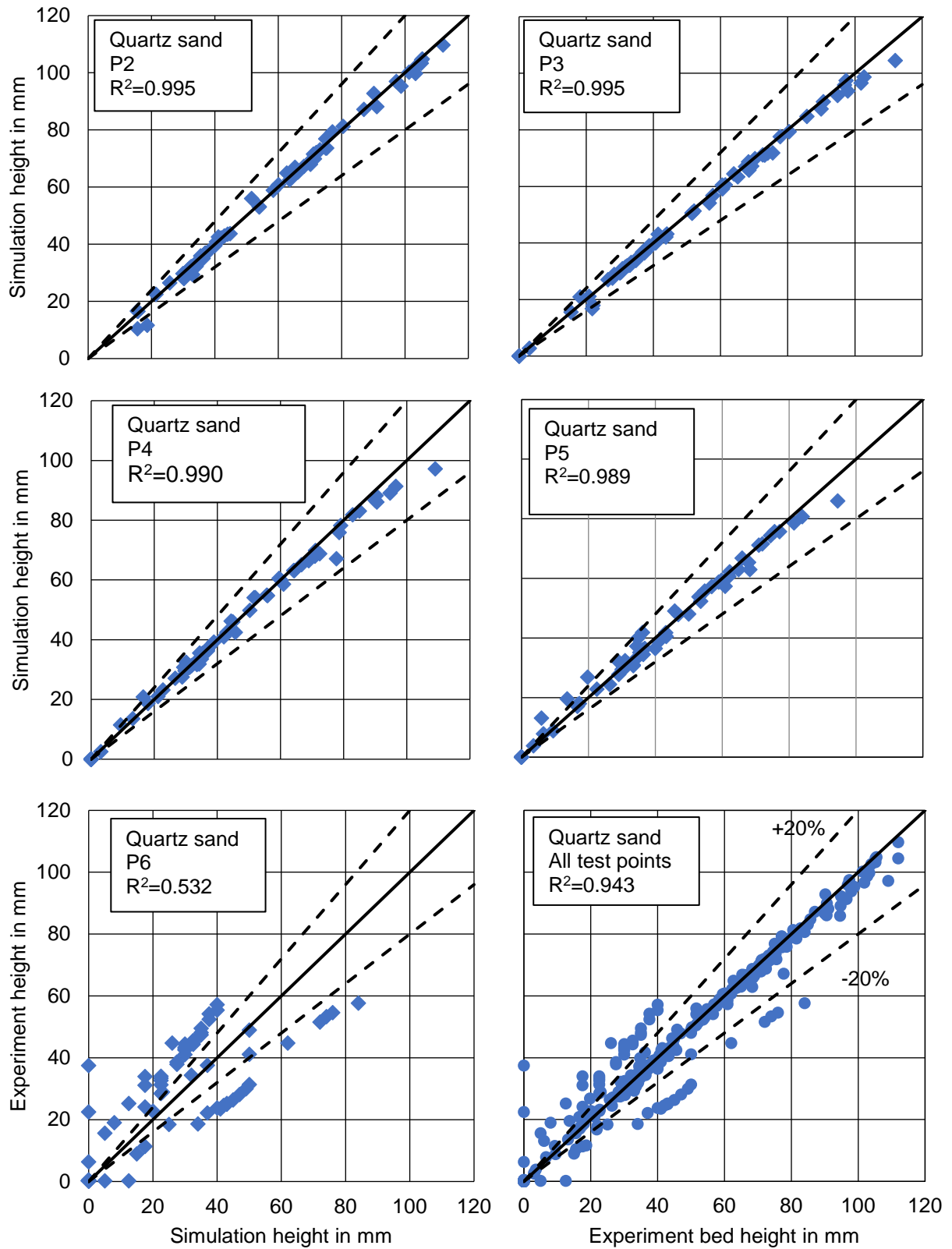
- Tsotsas, E., & Schlünder, E. U. (1990). Numerical calculation of the thermal conductivity of two regular bidispersed beds of spherical particles. *Computers & chemical engineering*, *14*(9), 1031-1038.
- Tsotsas, E., & Schlünder, E. U. (1991). Impact of particle size dispersity on thermal conductivity of packed beds: measurement, numerical simulation, prediction. *Chemical Engineering & Technology: Industrial Chemistry-Plant Equipment-Process Engineering-Biotechnology*, *14*(6), 421-427.
- Vahl, L., & Kingma, W. G. (1952). Transport of solids through horizontal rotary cylinders. *Chemical Engineering Science*, *1*(6), 253-258.
- Van Puyvelde, D. R. (2006). Simulating the mixing and segregation of solids in the transverse section of a rotating kiln. *Powder technology*, *164*(1), 1-12.
- Wes, G. W. J., Drinkenburg, A. A., & Stermerding, S. (1976). Heat transfer in a horizontal rotary drum reactor. *Powder Technology*, *13*(2), 185-192.
- Williams, J. C. (1976). The segregation of particulate materials. A review. *Powder technology*, *15*(2), 245-251.
- Williams, J. C., & Richardson, R. (1982). The continuous mixing of segregating particles. *Powder Technology*, *33*(1), 5-16.
- Yin, H., Zhang, M., & Liu, H. (2014). Numerical simulation of three-dimensional unsteady granular flows in rotary kiln. *Powder technology*, *253*, 138-145.

# Appendix

- Appendix A
- Comparison of transient particle bed depth between simulation and experimental values in different test points.
  - Comparison of stationary time.
- Appendix B
- The list of overall operational conditions with different mixing particle.
- Appendix C
- The simulation data for the calcination process of quartz sand.
  - The temperatures of particle bed and gas of calcination process model with mono-, bi- and polydisperse particle system.
- Appendix D
- The axial profiles of temperature, local heat transfer coefficient profiles and heat flow with mono-, bi- and polydisperse particle system.



## Appendix A

**Figure A.1.** Regression analysis between simulation and experimental bed height of quartz sand

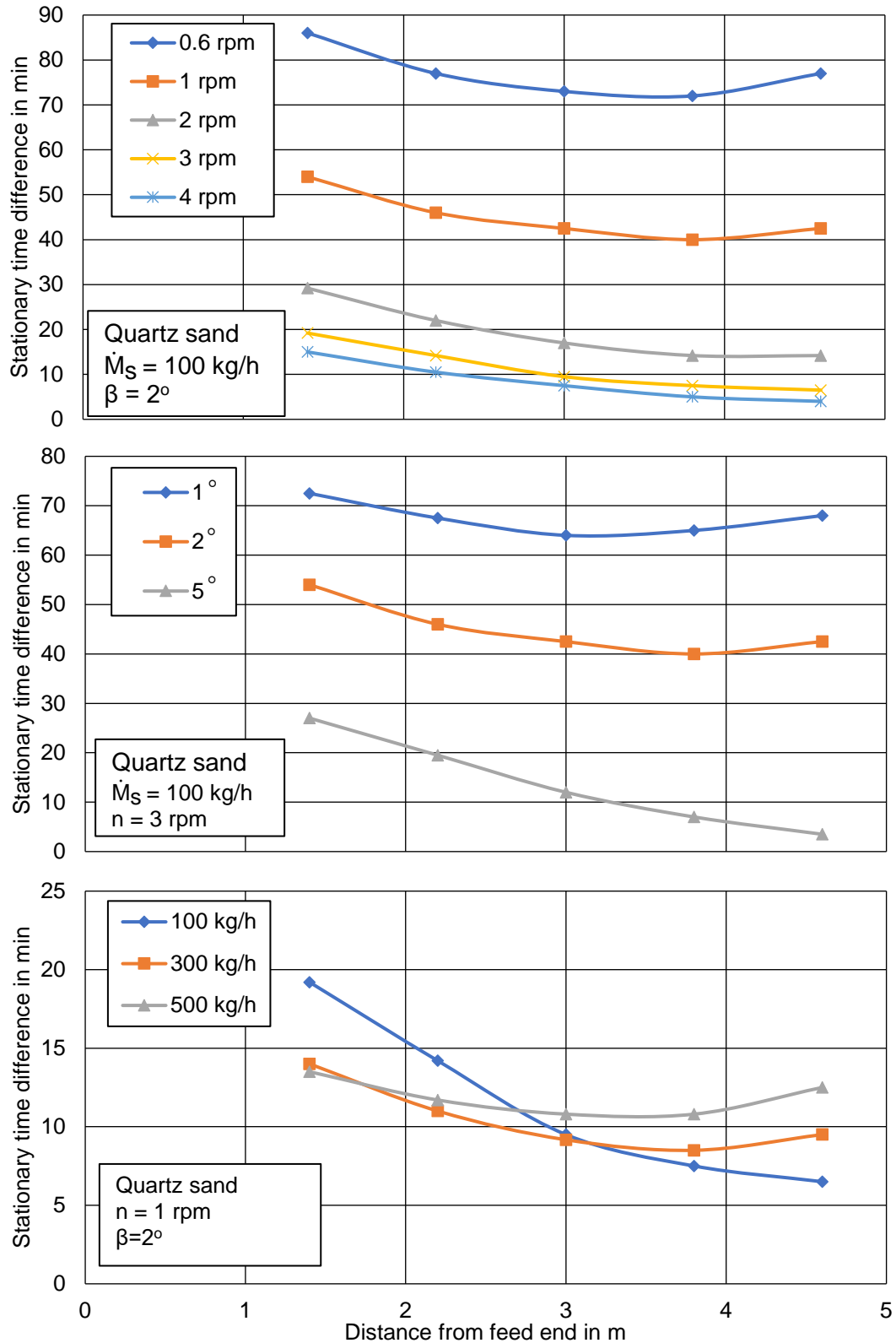


**Figure A.2** Difference between stationary time from discharge and from bed height along kiln axis with varied rotational speed, inclination angle and feed mass flow rate.

## Appendix B

**Table B.1 The list of overall operational conditions of 2&4 mm mixing glass beads which contains particle mixing ratio, weight of tracers, feed mass flow rate, inclination angle, filling degree and dynamic angle of repose**

Particle size in mm	Particle mixing ratio	Weight of tracer particles in kg	Feed mass flow rate in kg/h	Rotational speed in rpm	Inclination angle in °	Filling degree in %	Dynamic angle of repose in°
2&4	1:1	1	50	2	2	2.2	28
	1:1	2	100	2	2	4.5	28
	1:1	3	150	2	2	6.8	28
	1:1	2	100	2	1	8.3	30
	1:1	2	100	2	3	3.0	25
	1:1	2	100	1	2	8.4	26
	1:1	2	100	3	2	3.0	27
	1:2	2	100	2	2	4.5	28
	2:1	2	100	2	2	4.2	26

**Table B.2 The list of overall operational conditions of 0.7&4 mm mixing glass beads which contains particle mixing ratio, weight of tracers, feed mass flow rate, inclination angle, filling degree and dynamic angle of repose**

Particle size in mm	Particle mixing ratio	Weight of tracer particles in kg	Feed mass flow rate in kg/h	Rotational speed in rpm	Inclination angle in °	Filling degree in %	Dynamic angle of repose in°
0.7&4	1:1	1	50	2	2	2.0	25
	1:1	2	100	2	2	4.0	28
	1:1	3	150	2	2	6.8	28
	1:1	2	100	2	1	8.3	30
	1:1	2	100	2	3	2.7	25
	1:1	2	100	1	2	8.1	25
	1:1	2	100	3	2	2.7	27
	1:2	2	100	2	2	4.0	29
	2:1	2	100	2	2	4.0	25

**Table B.3 The list of overall operational conditions of 0.7&4 mm mixing glass beads which contains particle mixing ratio, weight of tracers, feed mass flow rate, inclination angle, filling degree and dynamic angle of repose**

Particle size in mm	Particle mixing ratio	Weight of tracer particles in kg	Feed mass flow rate in kg/h	Rotational speed in rpm	Inclination angle in °	Filling degree in %	Dynamic angle of repose in°
0.7&2	1:1	1	50	2	2	2.4	30
	1:1	2	100	2	2	4.6	29
	1:1	3	150	2	2	7.0	29
	1:1	2	100	2	1	8.0	29
	1:1	2	100	2	3	3.1	27
	1:1	2	100	1	2	9.0	27
	1:1	2	100	3	2	3.0	28
	1:2	2	100	2	2	4.3	27
	2:1	2	100	2	2	4.3	27

**Appendix C****C1 The simulation data of the quartz sand calcination process. (Reference kiln)**

$$L = 40 \text{ m}$$

$$D = 2.0 \text{ m}$$

$$\beta = 1^\circ$$

$$n = 1.0 \text{ rpm}$$

$$\dot{M}_s = 5 \text{ t/h}$$

<b>Parameter</b>	<b>Size</b>	<b>Unit</b>
<b>Particle bed</b>		
Inlet temperature $T_{S,0}$	20	°C
Particle diameter $d_p$	0,2	mm
Dynamic angle of repose $\Theta$	33	°
Specific heat capacity		J/kg/K
Bulk density $\rho_s$	1590	kg/m <sup>3</sup>
Thermal conductivity $\lambda_s$	0.3	W/m/K
Emissivity	0.4	-
<b>Burner</b>		
Fuel	Natural gas	-
Power	2.3	MW
Air-fuel ratio $\lambda$	1.3	-
Combustion air temperature	20	°C
Flame length $L_{\text{Flame}}$	10	m
Burner nozzle length $L_B$	0	m
<b>Steel shell / Wall</b>		
Thickness of refractory $S_{W,1}$	350	mm
Thickness of high temperature insulation $S_{W,2}$	50	mm
Thermal conductivity of layer 1 $\lambda_{W,1}$	1.5	W/m/K
Thermal conductivity of layer 2 $\lambda_{W,2}$	0.7	W/m/K
Density of layer 1 $\rho_{W,1}$	2700	kg/m <sup>3</sup>
Specific heat capacity layer 1 $c_{p,W,1}$	1000	J/kg/K
Emissivity of inner wall	0.7	-
<b>Environment</b>		
Temperature $T_E$	20	°C
Velocity of environment air $w_E$	5	m/s

## C2 Fuel composition of quartz sand calcination process within simulation (Model assumption)

### Natural gas

Component of fuel gas	Proportion [Vol.%]	$\rho_i$ [kg/m <sup>3</sup> ]
CH <sub>4</sub>	93	0.714
C <sub>2</sub> H <sub>6</sub>	3	1.34
C <sub>3</sub> H <sub>8</sub>	1	1.964
C <sub>4</sub> H <sub>10</sub>	0.5	2.59
C <sub>5</sub> H <sub>12</sub>	0.5	3.214
CO	-	1.25
CO <sub>2</sub>	1	1.964
N <sub>2</sub>	1	1.25

Stoichiometric air requirement:

$$L_{req} = 16.4 \text{ kg}_{Air}/\text{kg}_{Fuel}$$

Density of fuel:

$$\rho_{Fuel} = 0.78 \text{ kg}/\text{Nm}^3$$

Heating value of fuel

$$H_{En,Fuel} = 37.4 \text{ MJ}/\text{Nm}^3$$

The composition of air with  $\lambda = 1.3$

Component of air	Proportion [Vol.%]
CO <sub>2</sub>	7.70
H <sub>2</sub> O	14.64
O <sub>2</sub>	4.48
N <sub>2</sub>	73.17

### C3 Influence of particle diameter on calcination process with monodisperse particle system (simulation results)

Particle size [mm]	MRT [min]	RT <sub>T&gt;1250°C</sub> [min] ( $\Delta z$ )	T <sub>S,max</sub> [°C]	T <sub>S,Out</sub> [°C]	T <sub>G,max</sub> [°C]	T <sub>G,0</sub> [°C]
Monodisperse						
0.2	202	18 (4.8m)	1452	1015	1635	295
0.27	202	18 (4.8m)	1446	1015	1630	295
0.4	202	17 (4.6m)	1433	1015	1620	295
2.0	202	12 (3m)	1330	1007	1540	300
4.0	202	5 (1.2m)	1246	993	1491	307

### C4 Influence of particle diameter on calcination process with bidisperse particle system (simulation results)

Mixing ratio	Particle size [mm]	MRT [min]	RT <sub>T&gt;1250°C</sub> [min] ( $\Delta z$ )	T <sub>S,max</sub> [°C]	T <sub>S,Out</sub> [°C]	T <sub>G,max</sub> [°C]	T <sub>G,0</sub> [°C]
Bidisperse 0.2&2 mm							
50/50	0.2	212	0 (0 m)	1227	1065	1517	308
	2.0	192	10 (2.5 m)	1302	916		
Bidisperse 1&2 mm							
50/50	1	215	0 (0 m)	1211	1082	1516	309
	2	192	11 (2.8 m)	1304	892		



**C5 Influence of particle mass flow ratio on calcination process with bidisperse particle system (simulation results)**

Mixing ratio	Particle size [mm]	MRT [min]	RT <sub>T&gt;1250°C</sub> [min] ( $\Delta z$ )	T <sub>S,max</sub> [°C]	T <sub>S,Out</sub> [°C]	T <sub>G,max</sub> [°C]	T <sub>G,0</sub> [°C]
Bidisperse 0.2&0.4 mm							
80/20	0.2	205	0 (0 m)	1211	1024	1518	314
	0.4	188	12 (3 m)	1322	813		
70/30	0.2	207	0 (0 m)	1241	1050	1537	310
	0.4	189	14 (3.4 m)	1343	844		
40/60	0.2	210	7 (2.0 m)	1270	1073	1556	307
	0.4	190	15 (3.8 m)	1362	875		
50/50	0.2	212	10 (2.8 m)	1298	1094	1572	303
	0.4	192	15 (3.8 m)	1377	906		
40/60	0.2	215	13 (3.4 m)	1325	1110	1584	301
	0.4	194	16 (4.0 m)	1391	934		
30/70	0.2	217	14 (3.9 m)	1353	1122	1594	299
	0.4	195	16 (4.2 m)	1402	960		
20/80	0.2	221	16 (4.2 m)	1381	1129	1604	297
	0.4	197	17 (4.3 m)	1413	983		

**C6 Influence of particle mass flow ratio on calcination process with polydisperse particle system (simulation results)**

Particle size [mm]	MRT [min]	RT <sub>T&gt;1250°C</sub> [min] ( $\Delta z$ )	T <sub>S,max</sub> [°C]	T <sub>S,Out</sub> [°C]	T <sub>G,max</sub> [°C]	T <sub>G,0</sub> [°C]
<b>Polydisperse 0.2&amp;0.4&amp;1&amp;2 mm (35/25/25/15)</b>						
0.2	216	0 (0 m)	1044	1015		
0.4	201	0 (0 m)	1070	971	1482	339
1	193	0 (0 m)	1151	885		
2	188	12 (2.8 m)	1306	708		
<b>Polydisperse 0.2&amp;0.4&amp;1&amp;2 mm (30/25/25/20)</b>						
0.2	218	0 (0 m)	1063	1036		
0.4	202	0 (0 m)	1085	994	1494	334
1	194	0 (0 m)	1162	910		
2	188	12 (3 m)	1315	735		
<b>Polydisperse 0.2&amp;0.4&amp;1&amp;2 mm (25/25/25/25)</b>						
0.2	220	0 (0 m)	1081	1052		
0.4	205	0 (0 m)	1100	1016	1504	330
1	196	0 (0 m)	1171	937		
2	188	13 (3.2 m)	1321	764		
<b>Polydisperse 0.2&amp;0.4&amp;1&amp;2 mm (20/25/25/30)</b>						
0.2	222	0 (0 m)	1100	1071		
0.4	207	0 (0 m)	1115	1037	1512	326
1	197	0 (0 m)	1179	961		
2	189	13 (3.2 m)	1325	789		
<b>Polydisperse 0.2&amp;0.4&amp;1&amp;2 mm (15/25/25/35)</b>						
0.2	224	0 (0 m)	1120	1091		
0.4	210	0 (0 m)	1131	1057	1517	322
1	199	0 (0 m)	1186	984		
2	190	13 (3.2 m)	1327	814		
<b>Polydisperse 0.2&amp;0.4&amp;1&amp;2 mm (10/25/25/40)</b>						
0.2	226	0 (0 m)	1139	1112		
0.4	212	0 (0 m)	1146	1076	1521	318
1	201	0 (0 m)	1191	1005		
2	191	13 (3.2 m)	1326	837		

## Appendix D

## D1 Influence of particle diameter with monodisperse particle system

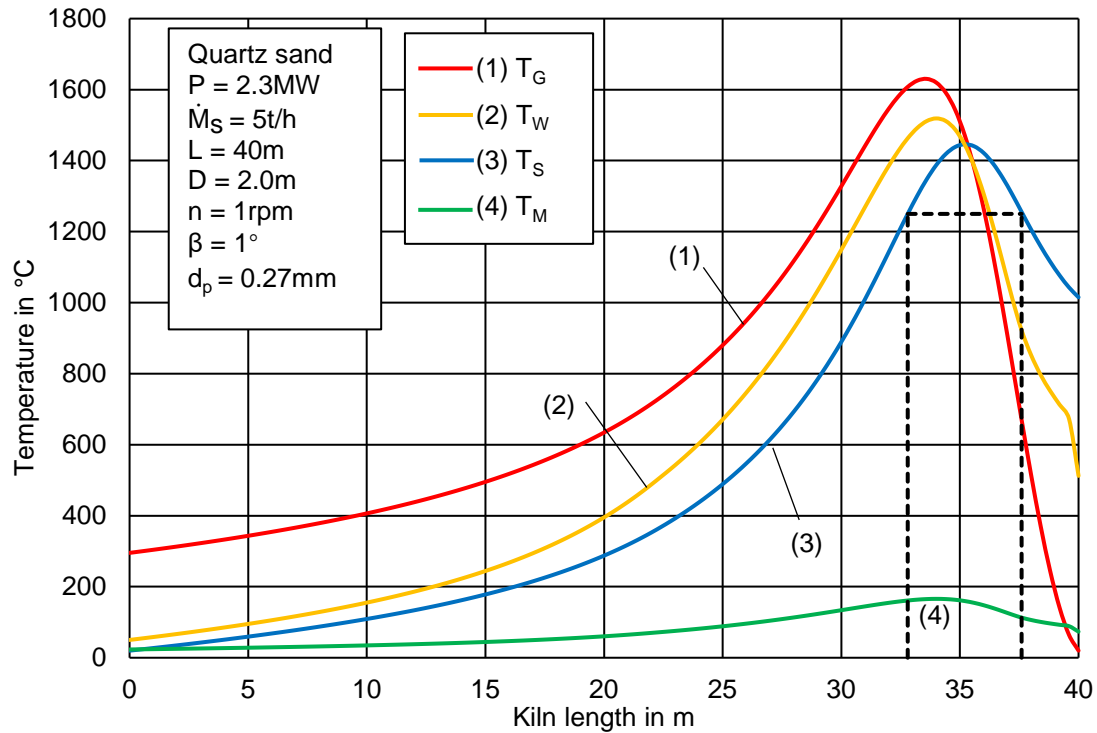


**Figure D.1** Axial temperature profiles of gas, inner wall, solid bed and steel shell. ( $d_p = 0.27\text{ mm}$ )

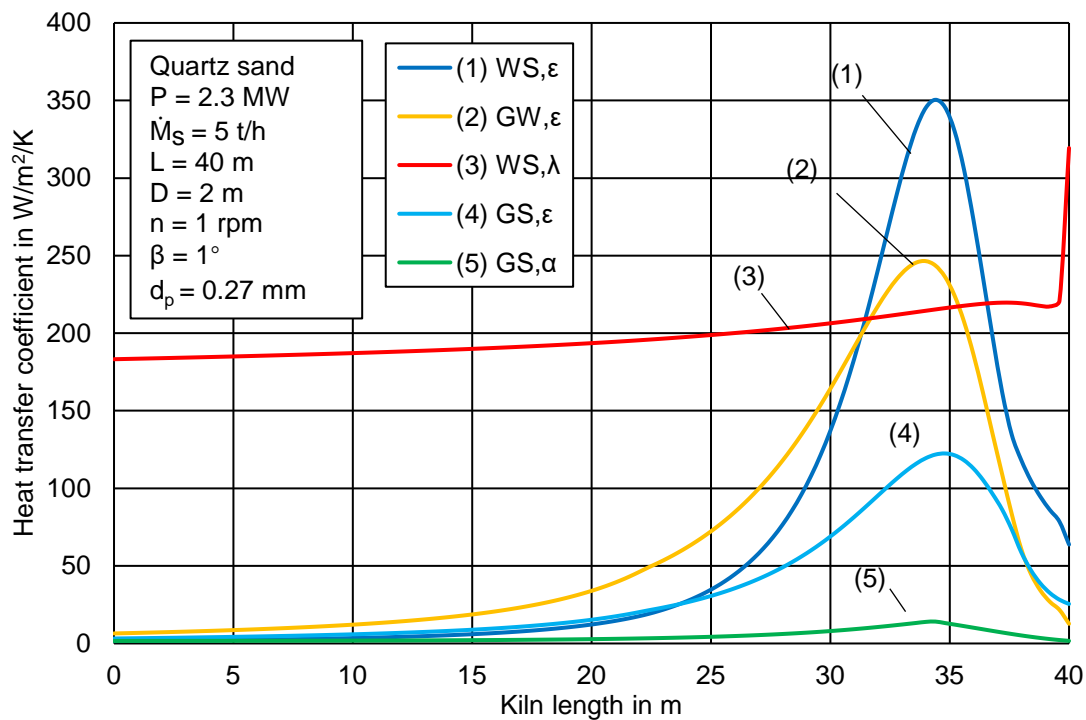


**Figure D.2** Axial radiative heat transfer coefficient between wall and solid bed, gas and wall, gas and solid bed, contact heat transfer coefficient between wall and solid bed and convective heat transfer coefficient between gas and solid bed. ( $d_p = 0.27\text{ mm}$ )

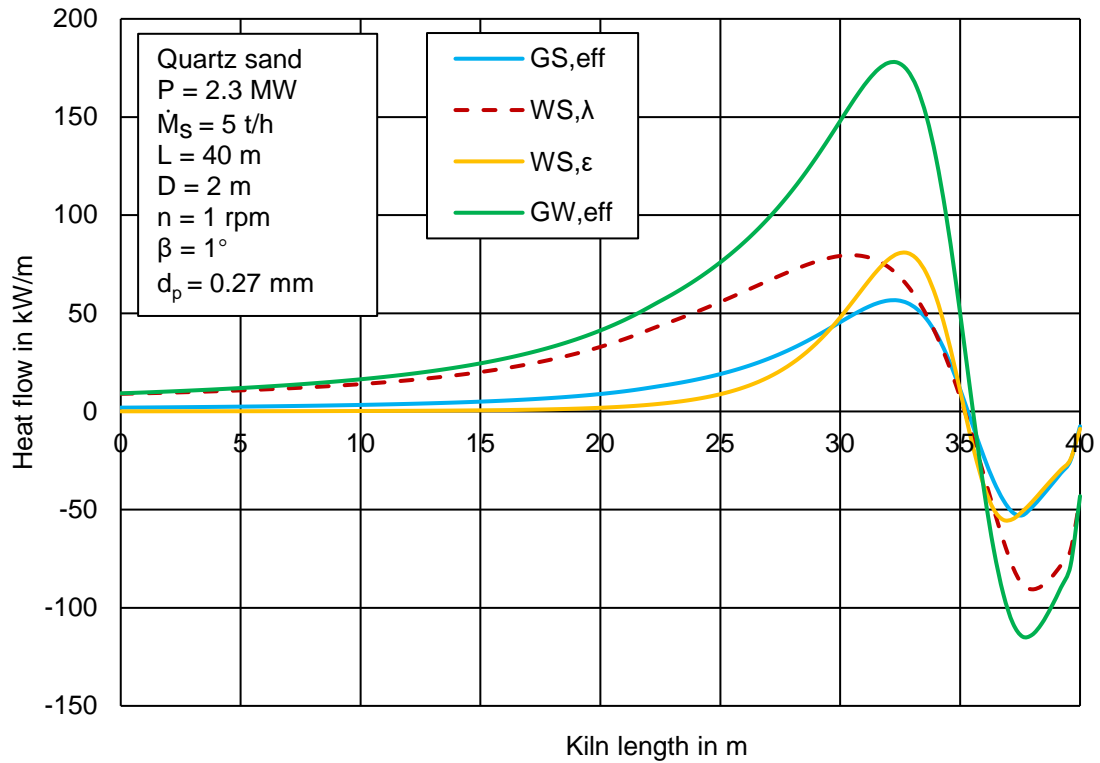


**Figure D.3** Axial effective heat flow between gas and solid bed, gas and inner wall, contact heat flow between wall and solid bed, radiative heat flow between wall and solid bed. ( $d_p = 0.27$  mm)

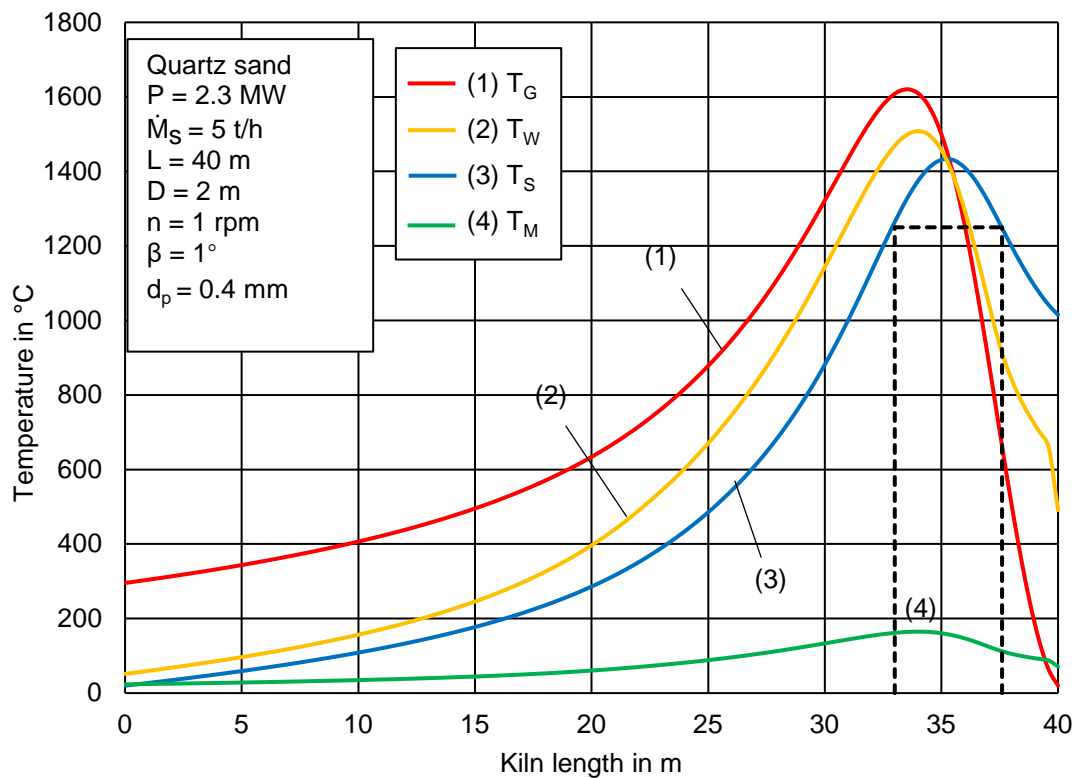


**Figure D.4** Axial temperature profiles of gas, inner wall, solid bed and steel shell. ( $d_p = 0.4$  mm)

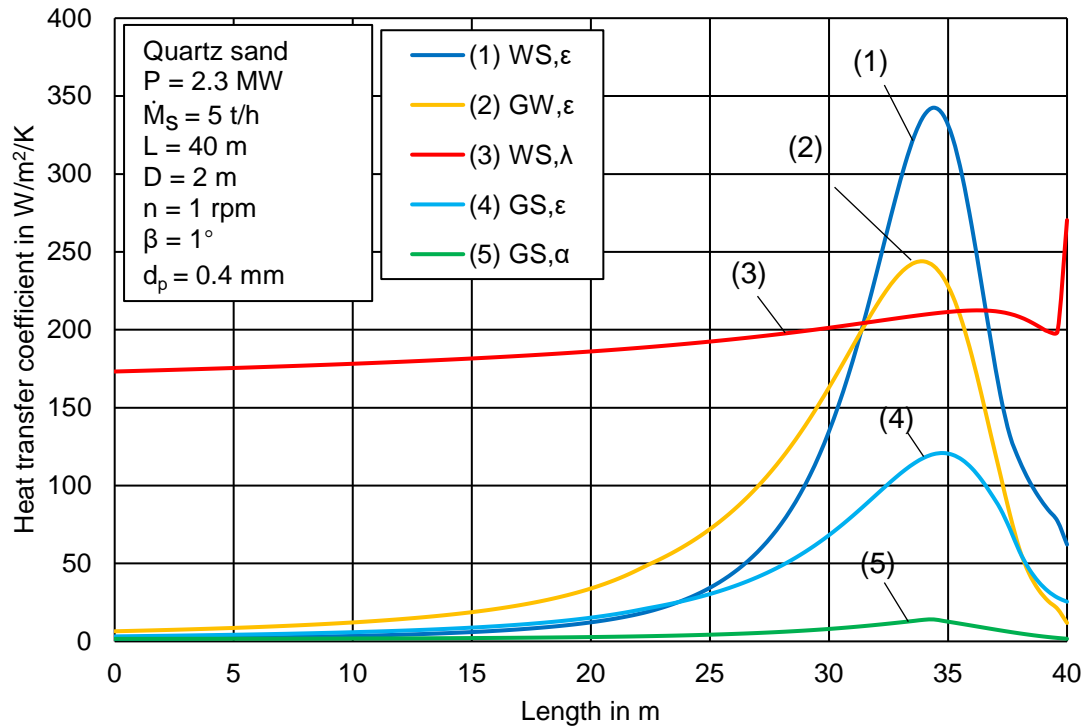


**Figure D.5** Axial radiative heat transfer coefficient between wall and solid bed, gas and wall, gas and solid bed, contact heat transfer coefficient between wall and solid bed and convective heat transfer coefficient between gas and solid bed. ( $d_p = 0.4$  mm)

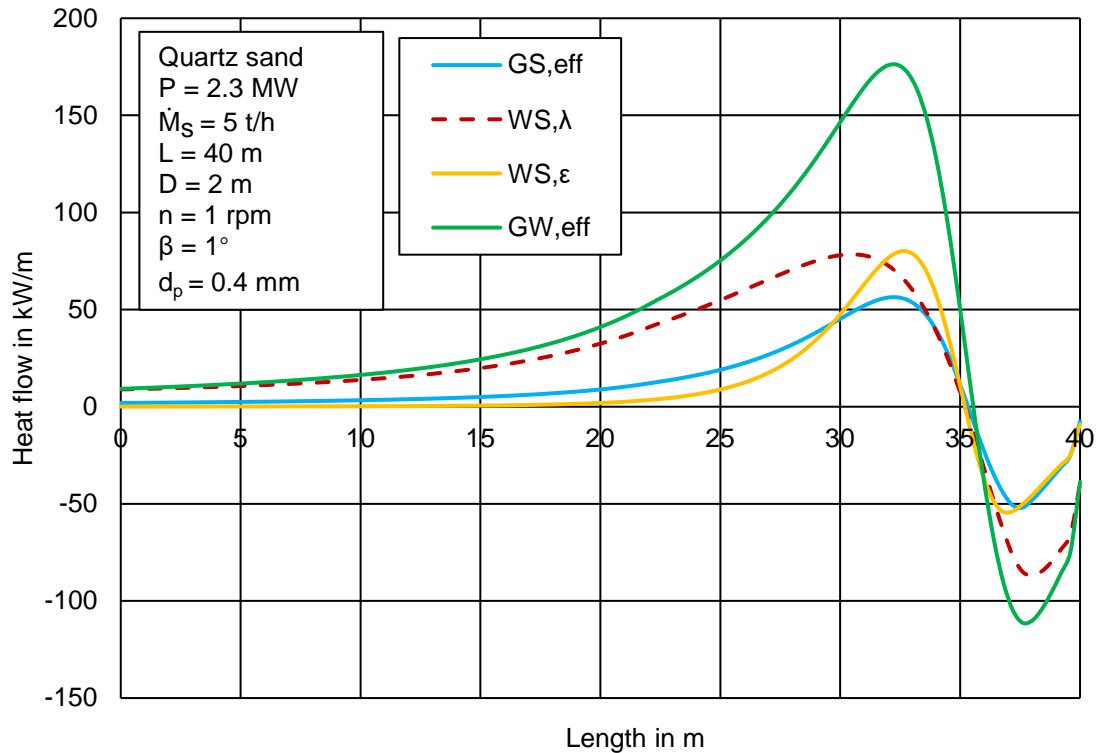


**Figure D.6** Axial effective heat flow between gas and solid bed, gas and inner wall, contact heat flow between wall and solid bed, radiative heat flow between wall and solid bed. ( $d_p = 0.4$  mm)

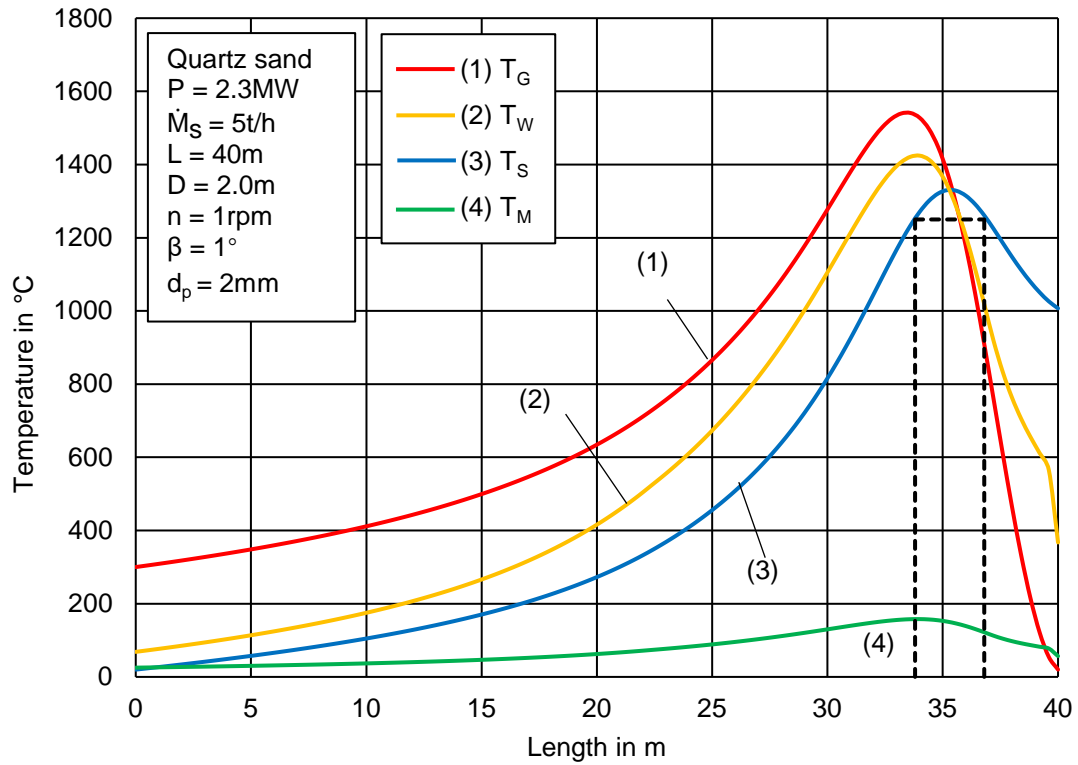


**Figure D.7** Axial temperature profiles of gas, inner wall, solid bed and steel shell. ( $d_p = 2 \text{ mm}$ )

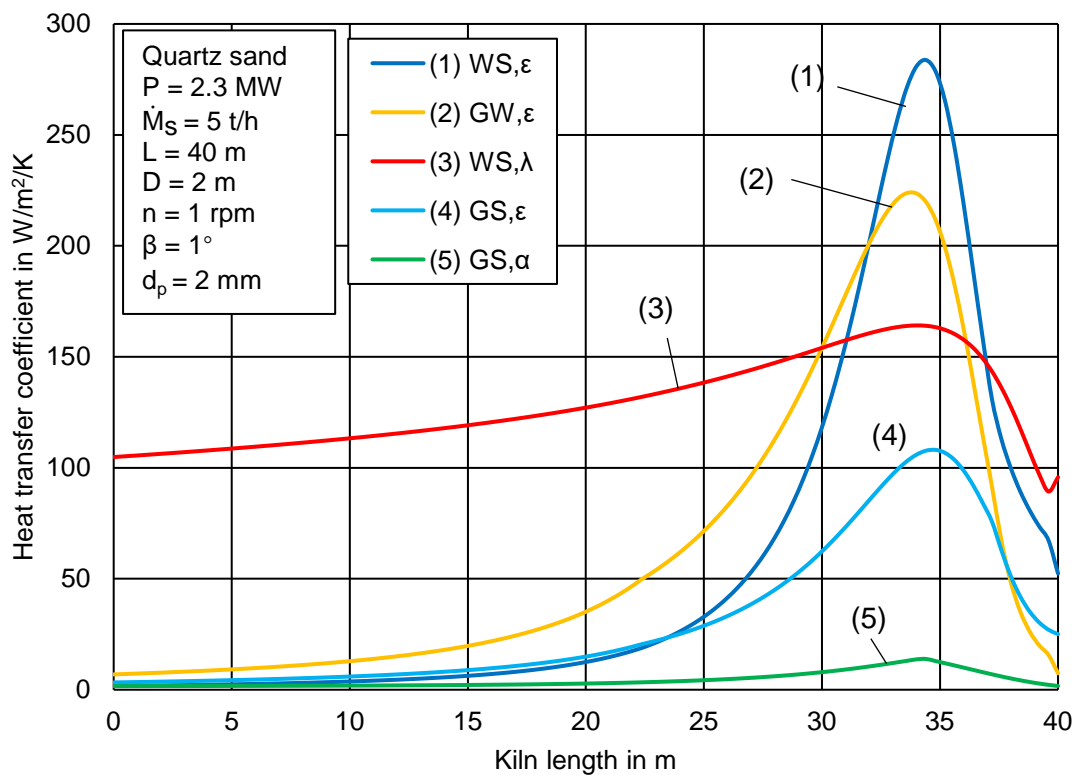


**Figure D.8** Axial radiative heat transfer coefficient between wall and solid bed, gas and wall, gas and solid bed, contact heat transfer coefficient between wall and solid bed and convective heat transfer coefficient between gas and solid bed. ( $d_p = 2 \text{ mm}$ )

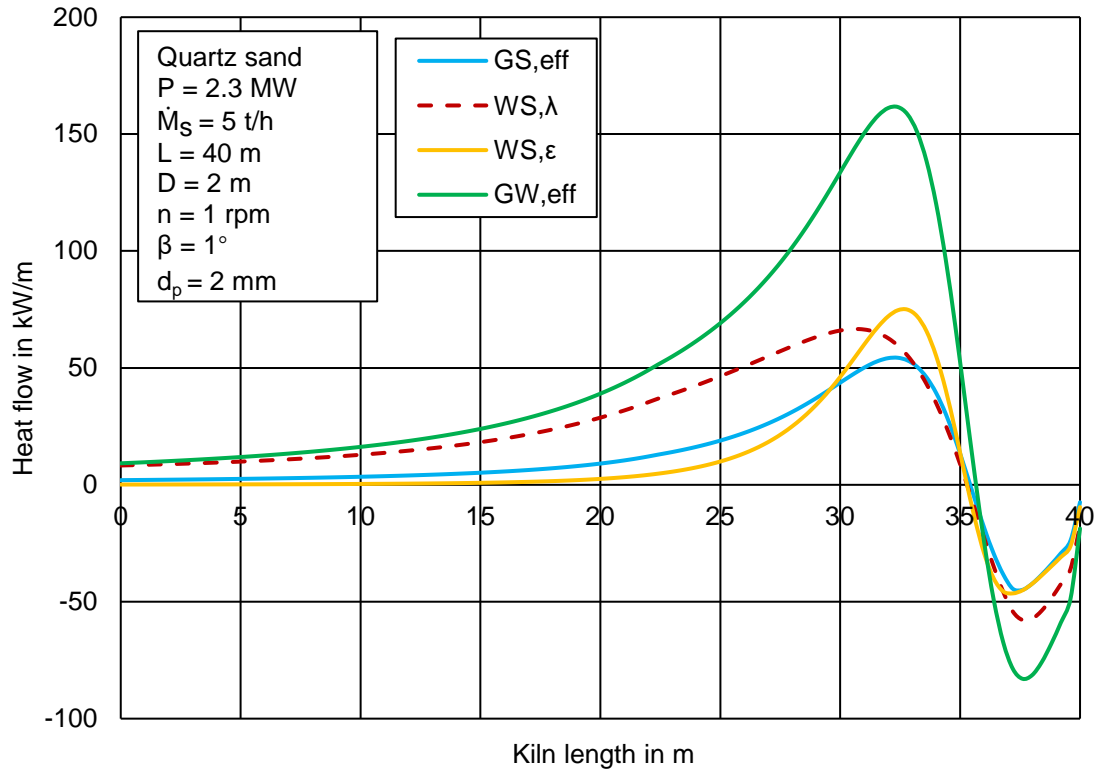


**Figure D.9** Axial effective heat flow between gas and solid bed, gas and inner wall, contact heat flow between wall and solid bed, radiative heat flow between wall and solid bed. ( $d_p = 2 \text{ mm}$ )

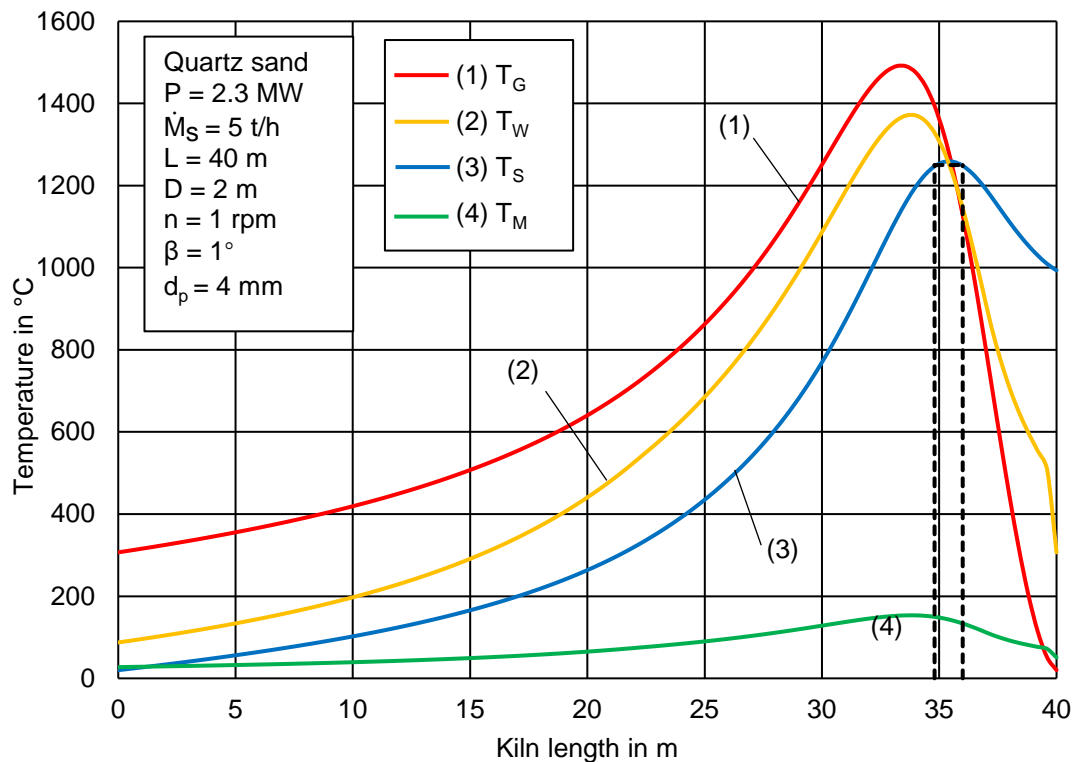


**Figure D.10.** Axial temperature profiles of gas, inner wall, solid bed and steel shell. ( $d_p = 4 \text{ mm}$ )

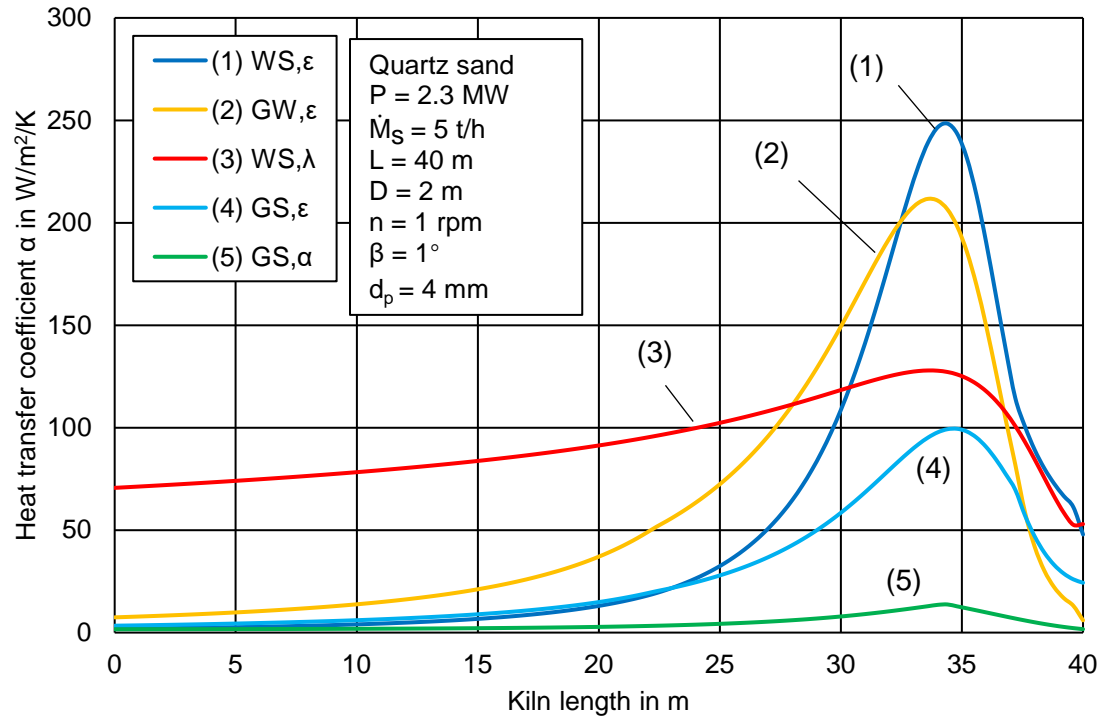


**Figure D.11** Axial radiative heat transfer coefficient between wall and solid bed, gas and wall, gas and solid bed, contact heat transfer coefficient between wall and solid bed and convective heat transfer coefficient between gas and solid bed. ( $d_p = 4 \text{ mm}$ )

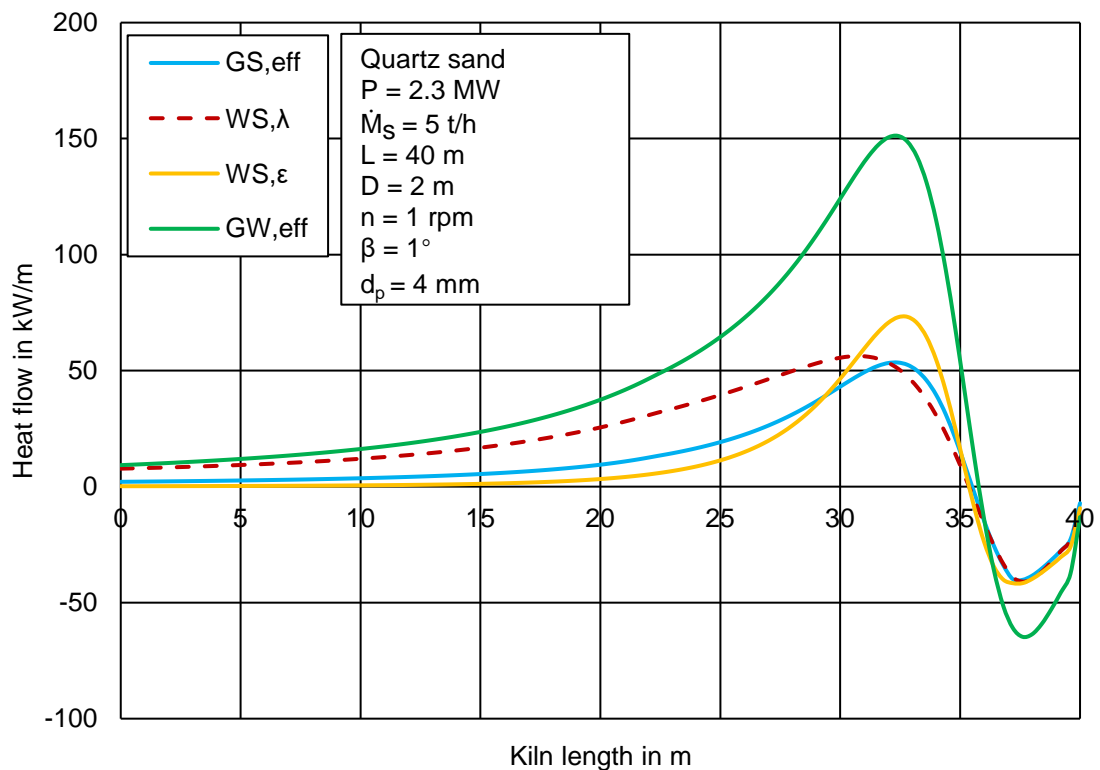


**Figure D.12** Axial effective heat flow between gas and solid bed, gas and inner wall, contact heat flow between wall and solid bed, radiative heat flow between wall and solid bed. ( $d_p = 4 \text{ mm}$ )



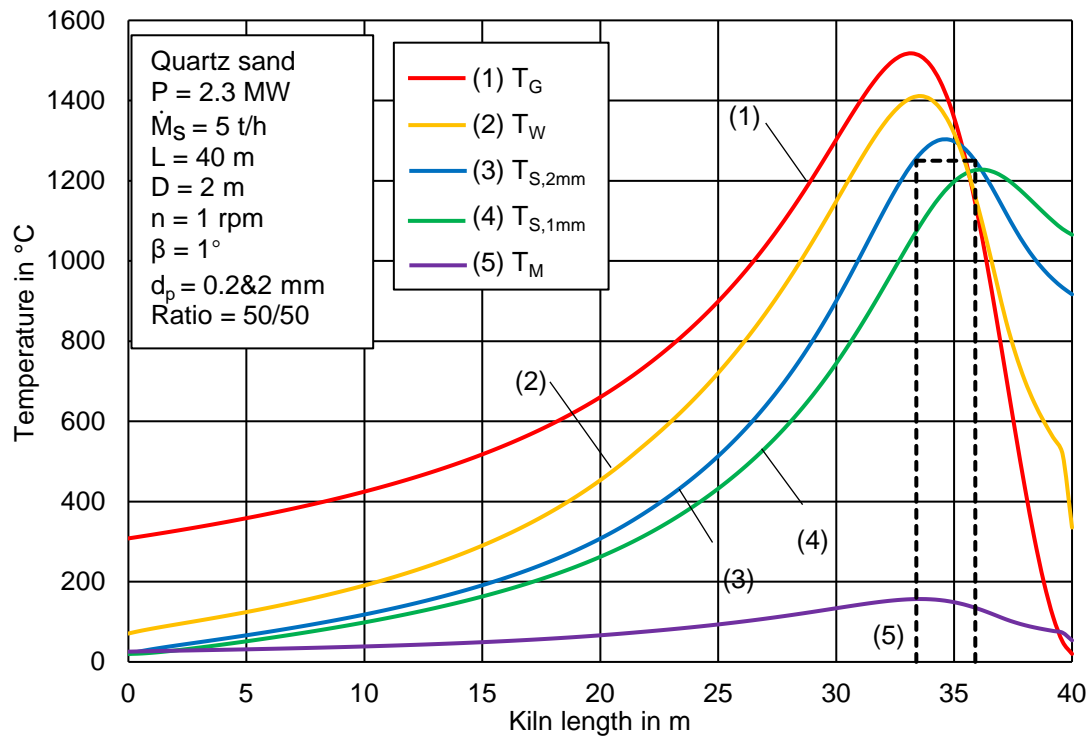


**Figure D.13** Axial temperature profiles of gas, inner wall, solid bed and steel shell. ( $d_p = 0.2\&2 \text{ mm}$ , ratio = 50/50)

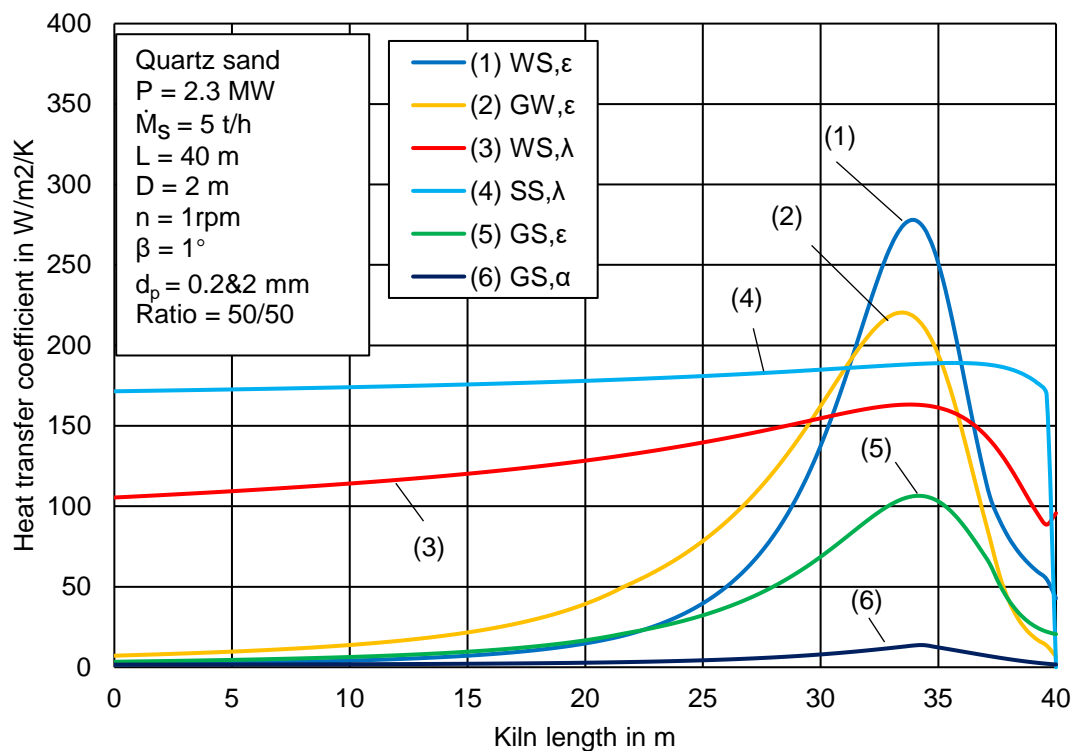


**Figure D.14** Axial radiative heat transfer coefficient between wall and solid bed, gas and wall, gas and solid bed, contact heat transfer coefficient between wall and solid bed, big and small size particle bed and convective heat transfer coefficient between gas and solid bed. ( $d_p = 0.2\&2 \text{ mm}$ , ratio = 50/50)

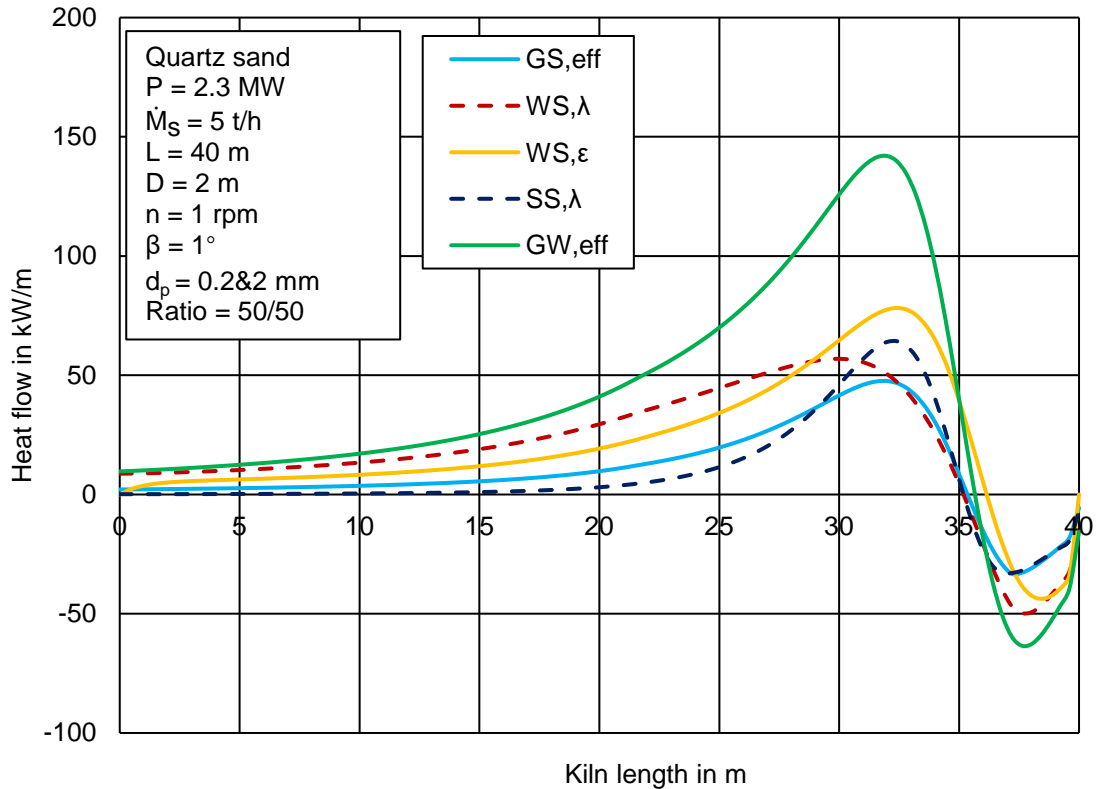


**Figure D.15** Axial effective heat flow between gas and solid bed, gas and inner wall, contact heat flow between wall and solid bed, big and small size particle bed, radiative heat flow between wall and solid bed. ( $d_p = 0.2 \& 2 \text{ mm}$ , ratio = 50/50)

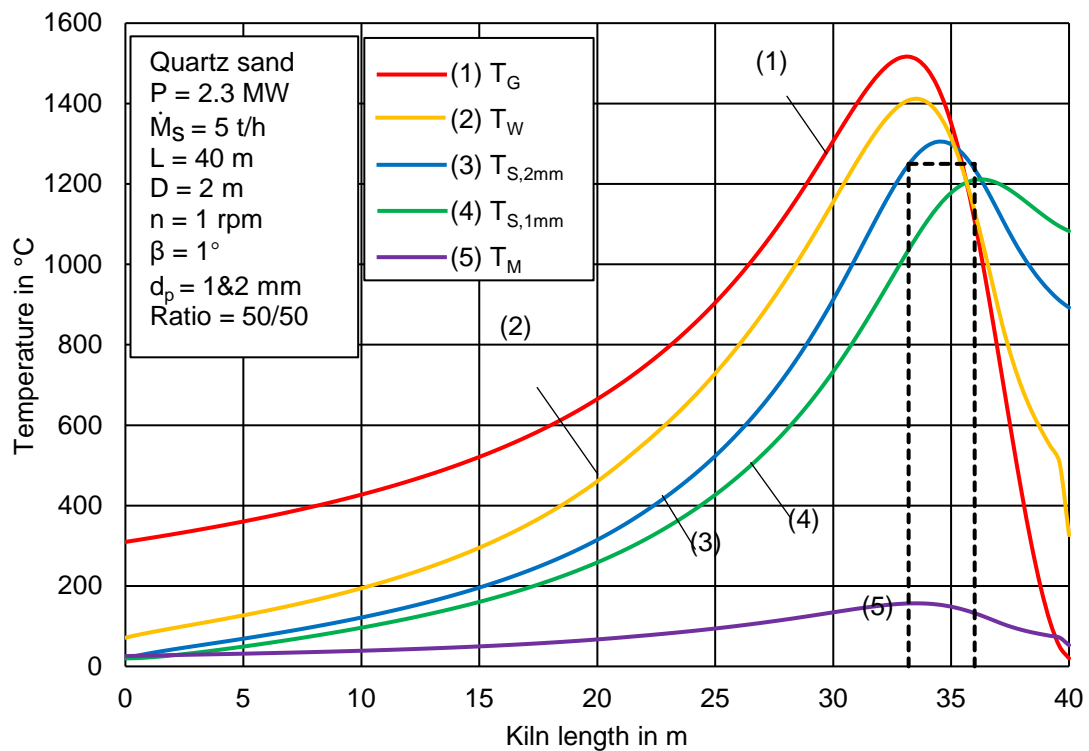


**Figure D.16** Axial temperature profiles of gas, inner wall, solid bed and steel shell. ( $d_p = 1 \& 2 \text{ mm}$ , ratio = 50/50)

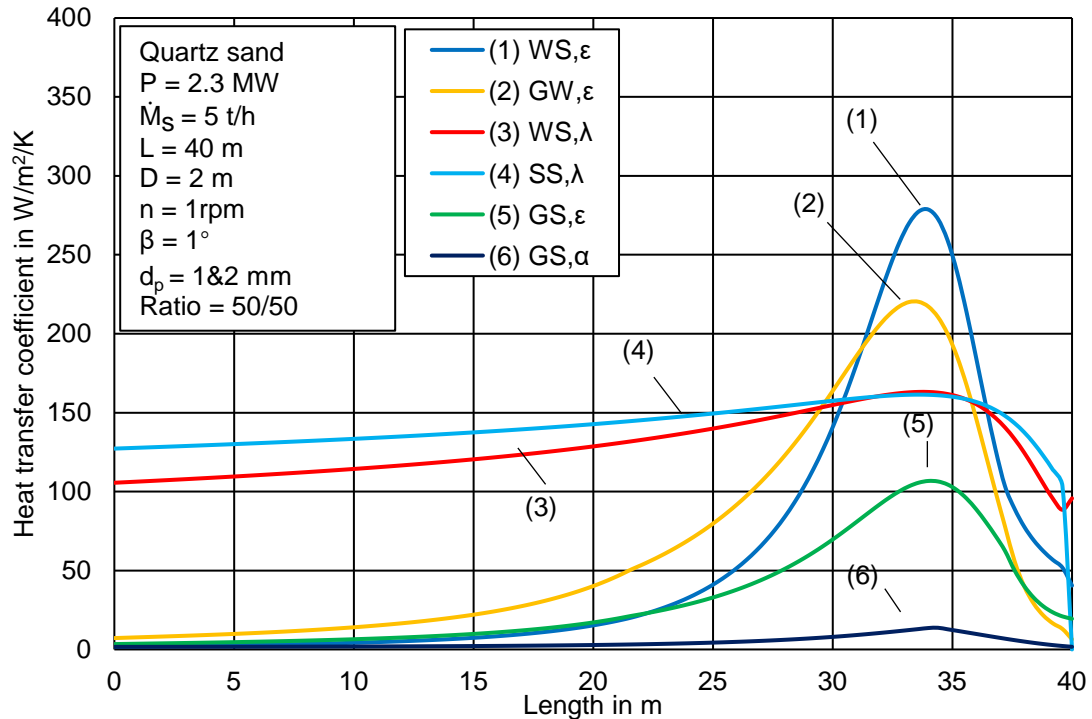


**Figure D.17** Axial radiative heat transfer coefficient between wall and solid bed, gas and wall, gas and solid bed, contact heat transfer coefficient between wall and solid bed, big and small size particle bed and convective heat transfer coefficient between gas and solid bed. ( $d_p = 1\&2$  mm, ratio = 50/50)

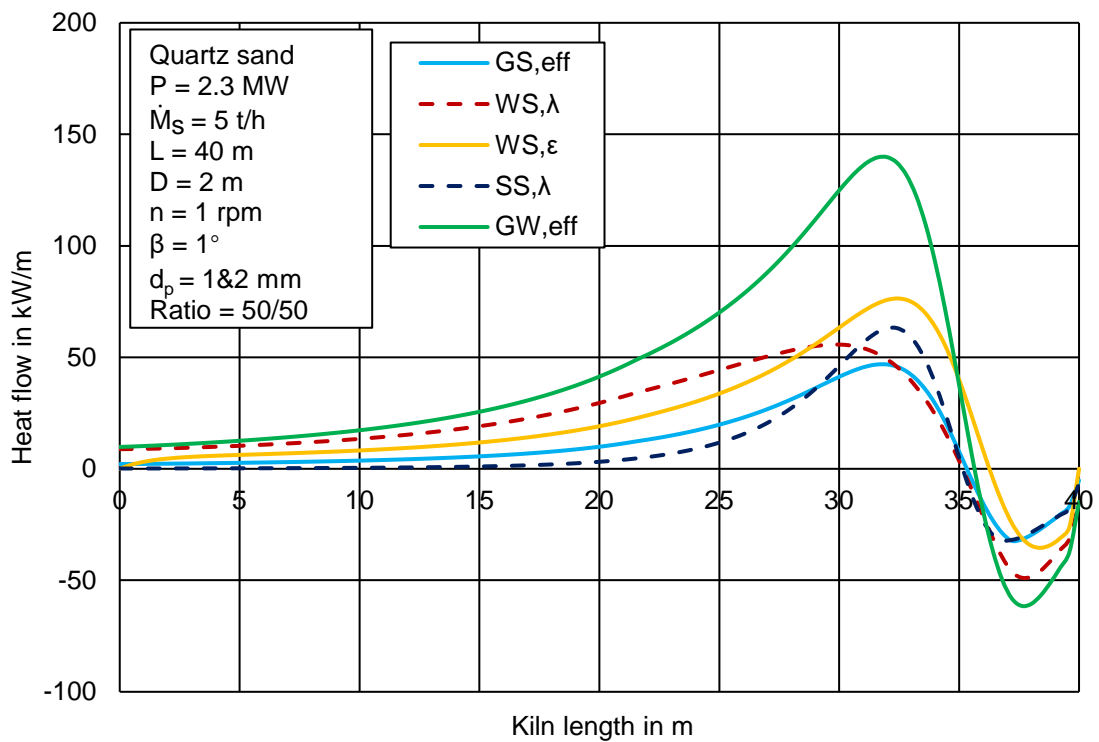


**Figure D.18** Axial effective heat flow between gas and solid bed, gas and inner wall, contact heat flow between wall and solid bed, big and small size particle bed, radiative heat flow between wall and solid bed. ( $d_p = 0.2\&2$  mm, ratio = 50/50)

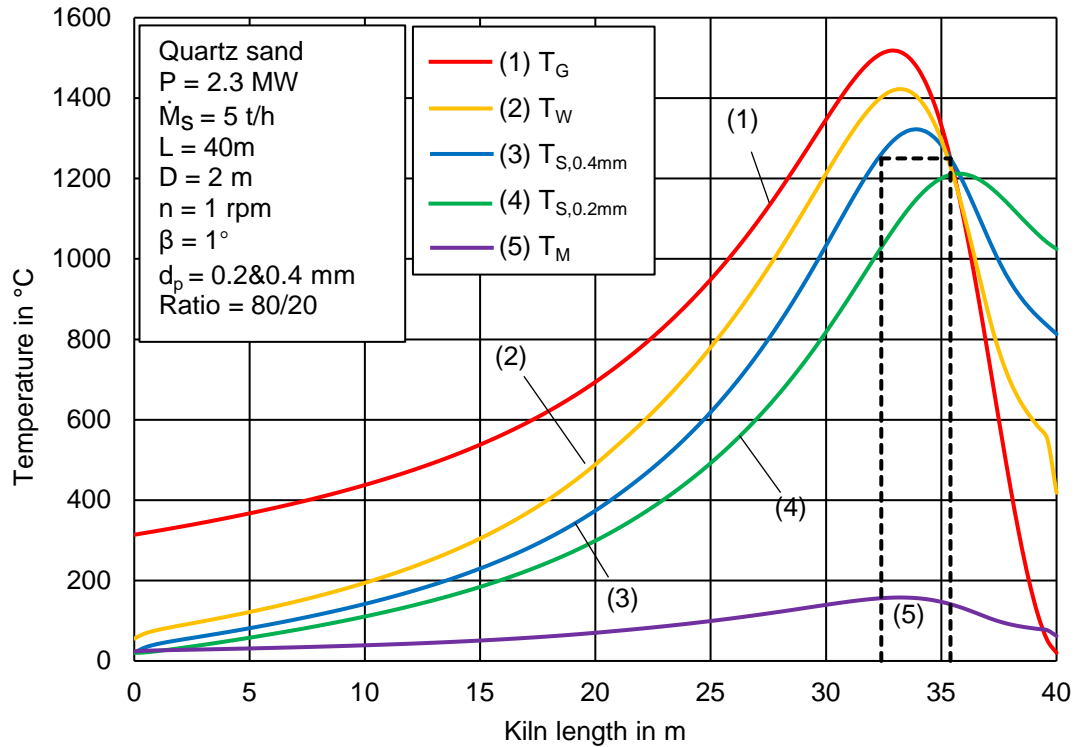


**Figure D.19.** Axial temperature profiles of gas, inner wall, solid bed and steel shell. ( $d_p = 0.2\&0.4$  mm, ratio = 80/20)

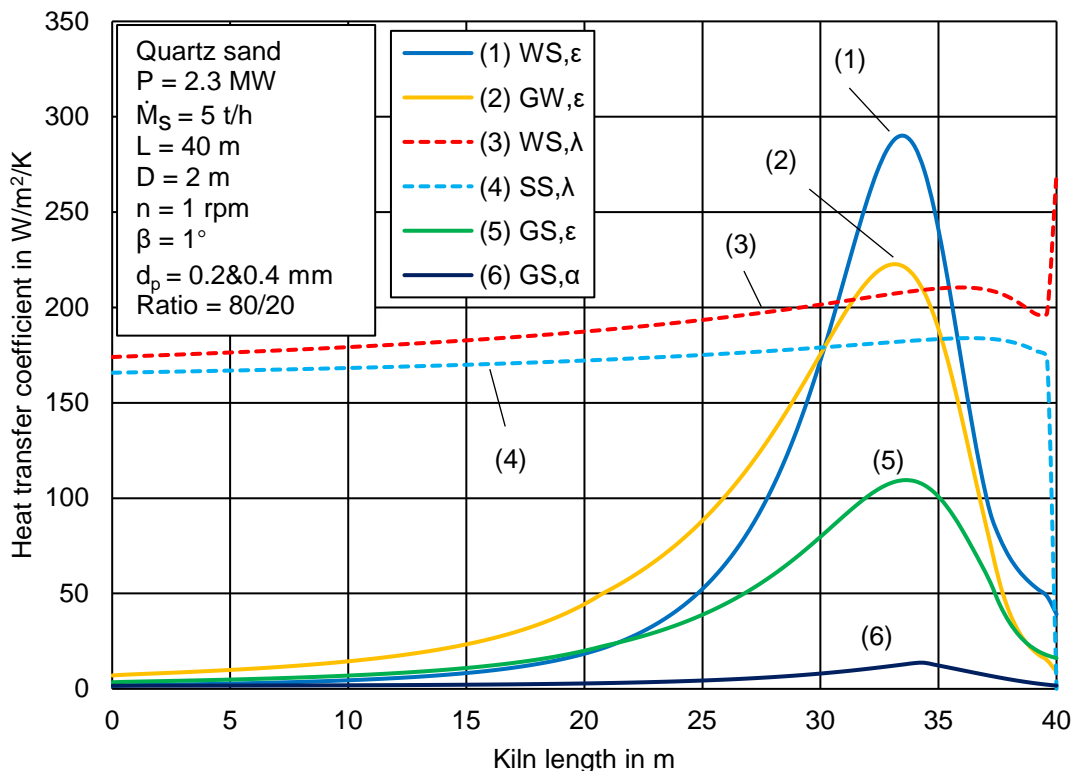


**Figure D.20** Axial radiative heat transfer coefficient between wall and solid bed, gas and wall, gas and solid bed, contact heat transfer coefficient between wall and solid bed, big and small size particle bed and convective heat transfer coefficient between gas and solid bed. ( $d_p = 0.2\&0.4$  mm, ratio = 80/20)

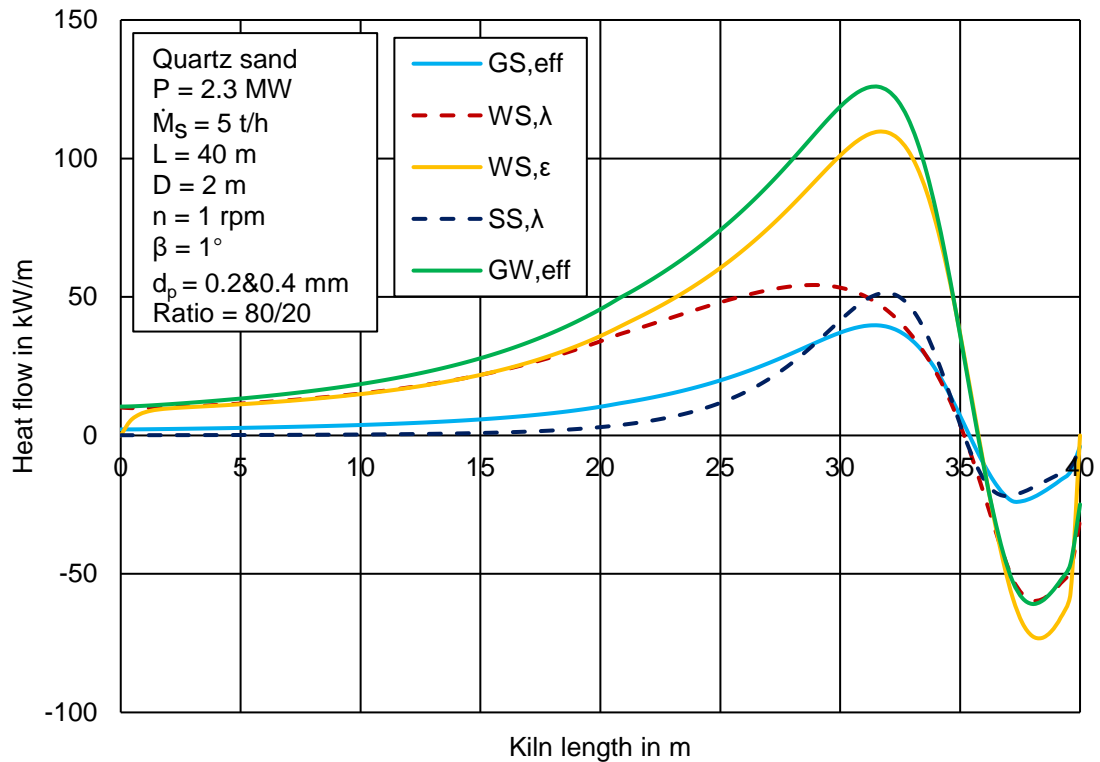


**Figure D.21** Axial effective heat flow between gas and solid bed, gas and inner wall, contact heat flow between wall and solid bed, big and small size particle bed, radiative heat flow between wall and solid bed. ( $d_p = 0.2\&0.4$  mm, ratio = 80/20)

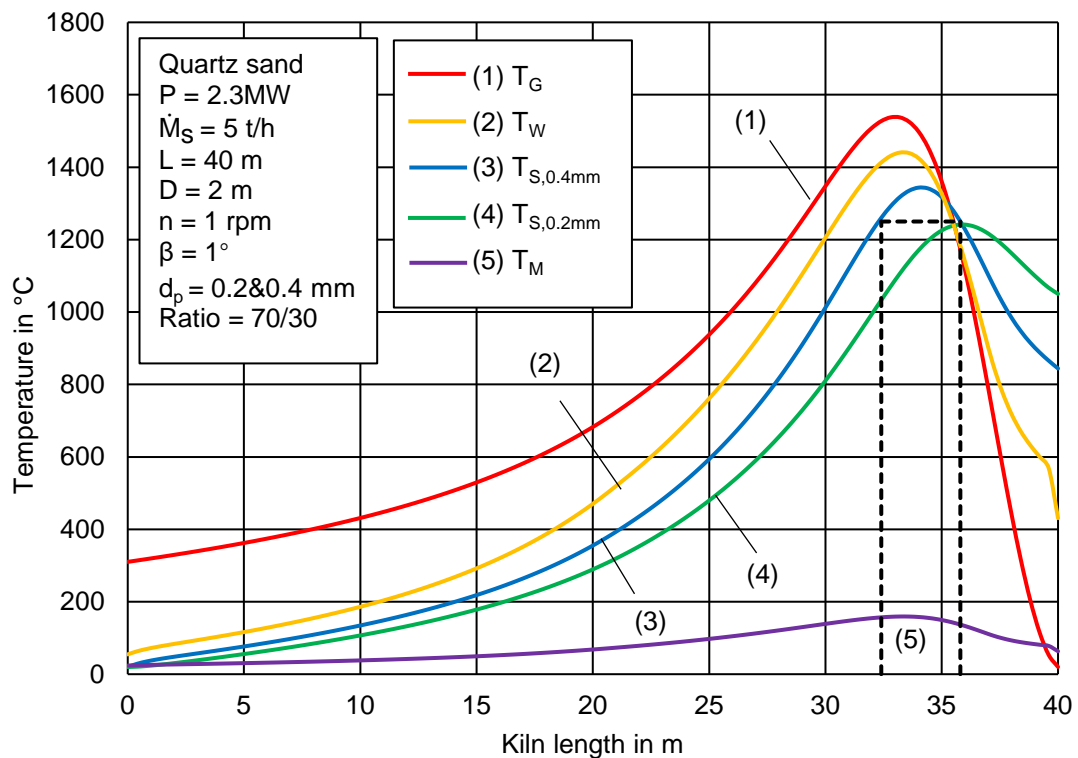


**Figure D.22** Axial temperature profiles of gas, inner wall, solid bed and steel shell. ( $d_p = 0.2\&0.4$  mm, ratio = 70/30)

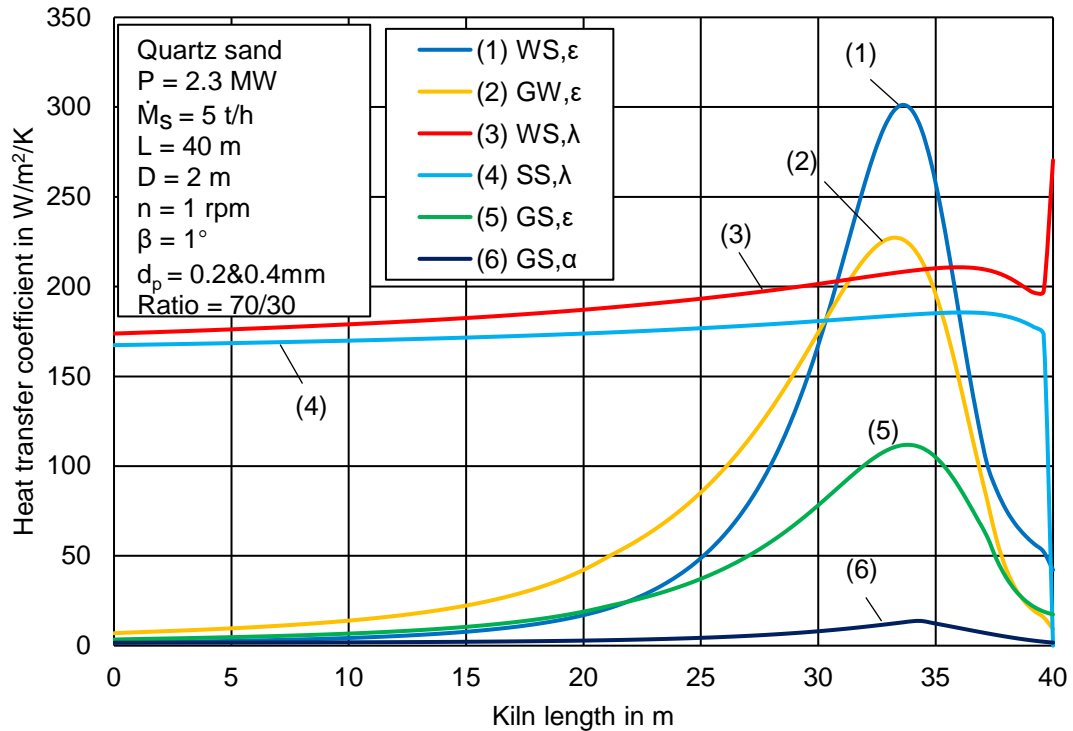


**Figure D.23.** Axial radiative heat transfer coefficient between wall and solid bed, gas and wall, gas and solid bed, contact heat transfer coefficient between wall and solid bed, big and small size particle bed and convective heat transfer coefficient between gas and solid bed. ( $d_p = 0.2 \& 0.4$  mm, ratio = 70/30)

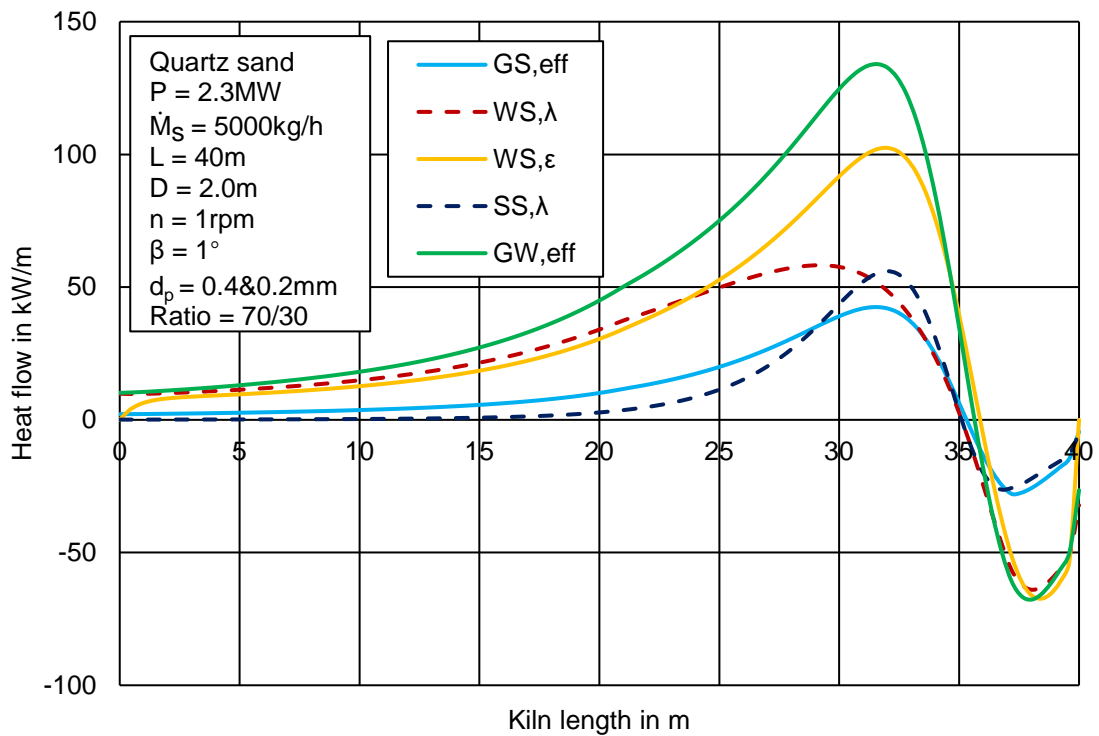


**Figure D.24** Axial effective heat flow between gas and solid bed, gas and inner wall, contact heat flow between wall and solid bed, big and small size particle bed, radiative heat flow between wall and solid bed. ( $d_p = 0.2 \& 0.4$  mm, ratio = 70/30)

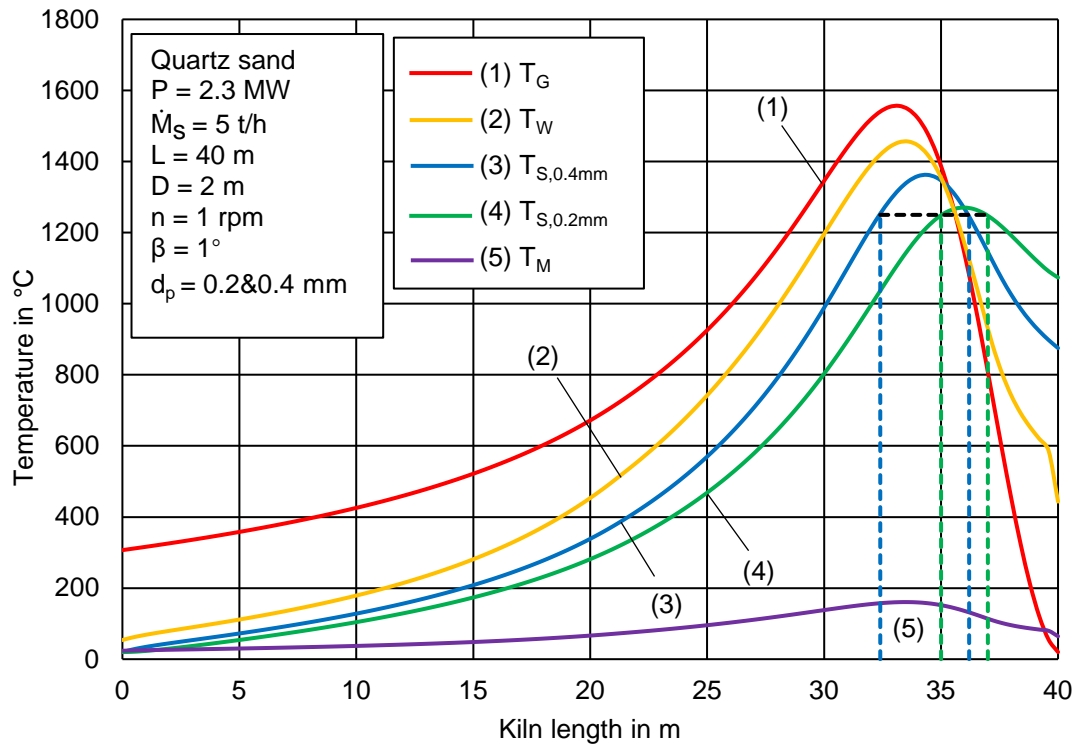


**Figure D.25** Axial temperature profiles of gas, inner wall, solid bed and steel shell. ( $d_p = 0.2\&0.4 \text{ mm}$ , ratio = 60/40)

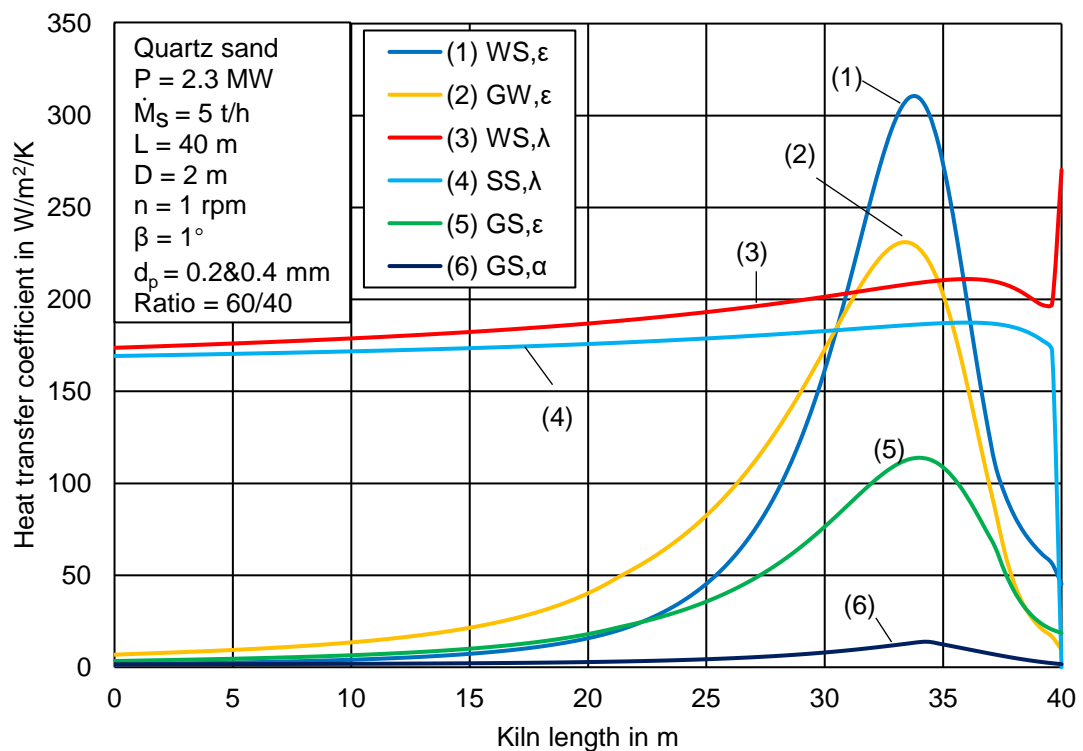


**Figure D.26** Axial radiative heat transfer coefficient between wall and solid bed, gas and wall, gas and solid bed, contact heat transfer coefficient between wall and solid bed, big and small size particle bed and convective heat transfer coefficient between gas and solid bed. ( $d_p = 0.2\&0.4 \text{ mm}$ , ratio = 60/40)

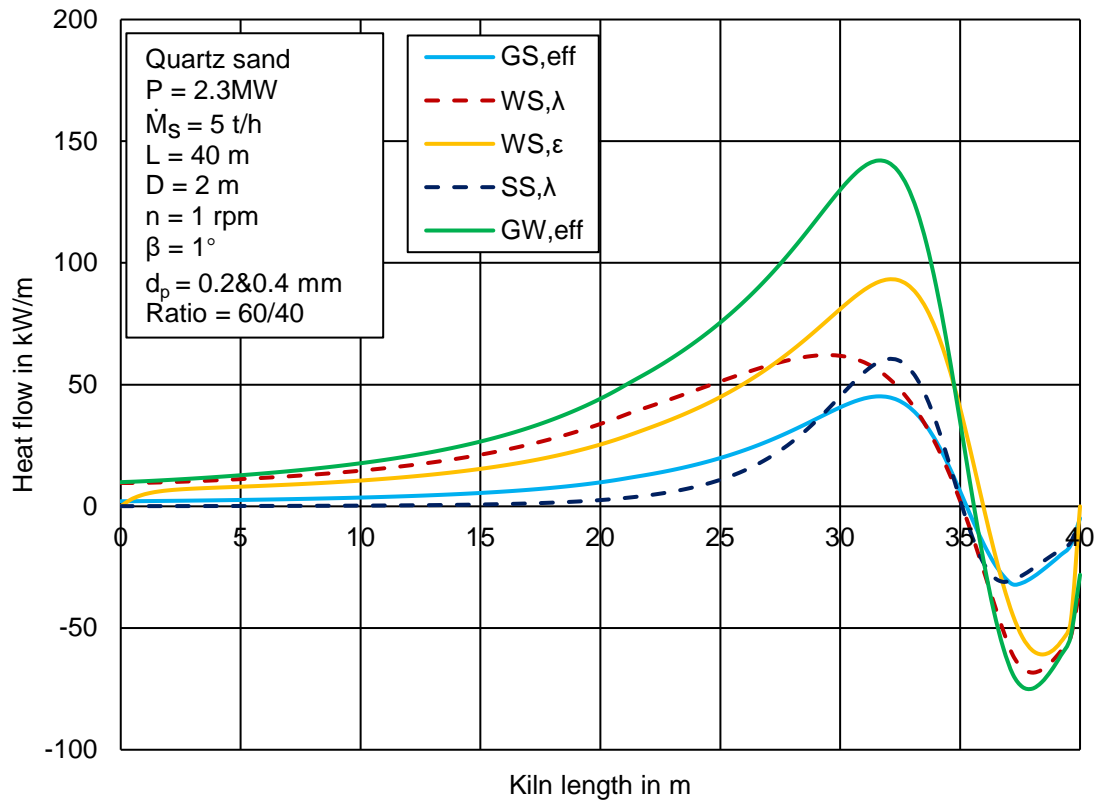


**Figure D.27** Axial effective heat flow between gas and solid bed, gas and inner wall, contact heat flow between wall and solid bed, big and small size particle bed, radiative heat flow between wall and solid bed. ( $d_p = 0.2\&0.4$  mm, ratio = 60/40)

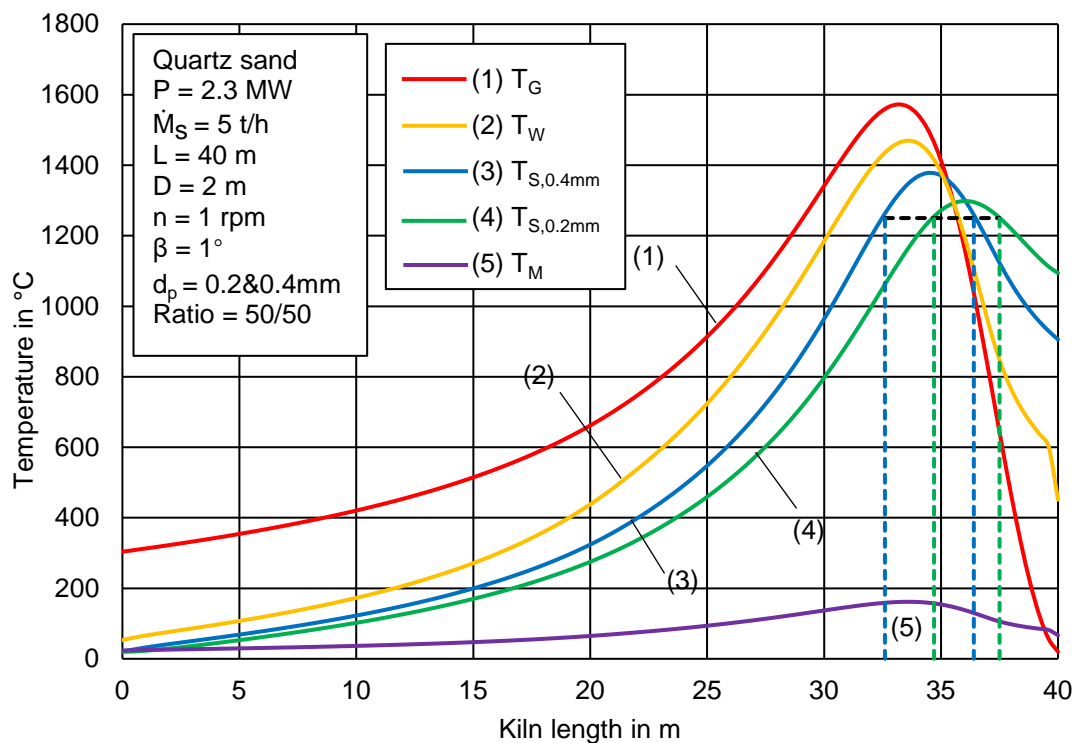


**Figure D.28** Axial temperature profiles of gas, inner wall, solid bed and steel shell. ( $d_p = 0.2\&0.4$  mm, ratio = 50/50)



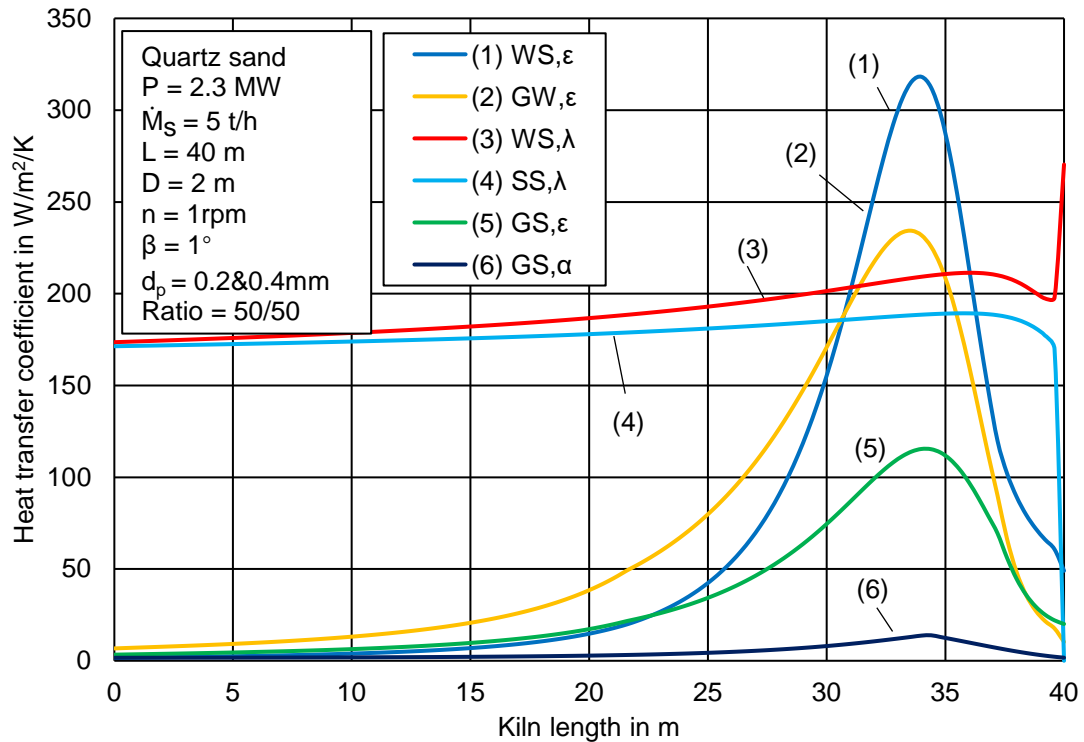


**Figure D.29** Axial radiative heat transfer coefficient between wall and solid bed, gas and wall, gas and solid bed, contact heat transfer coefficient between wall and solid bed, big and small size particle bed and convective heat transfer coefficient between gas and solid bed. ( $d_p = 0.2 \& 0.4$  mm, ratio = 50/50)

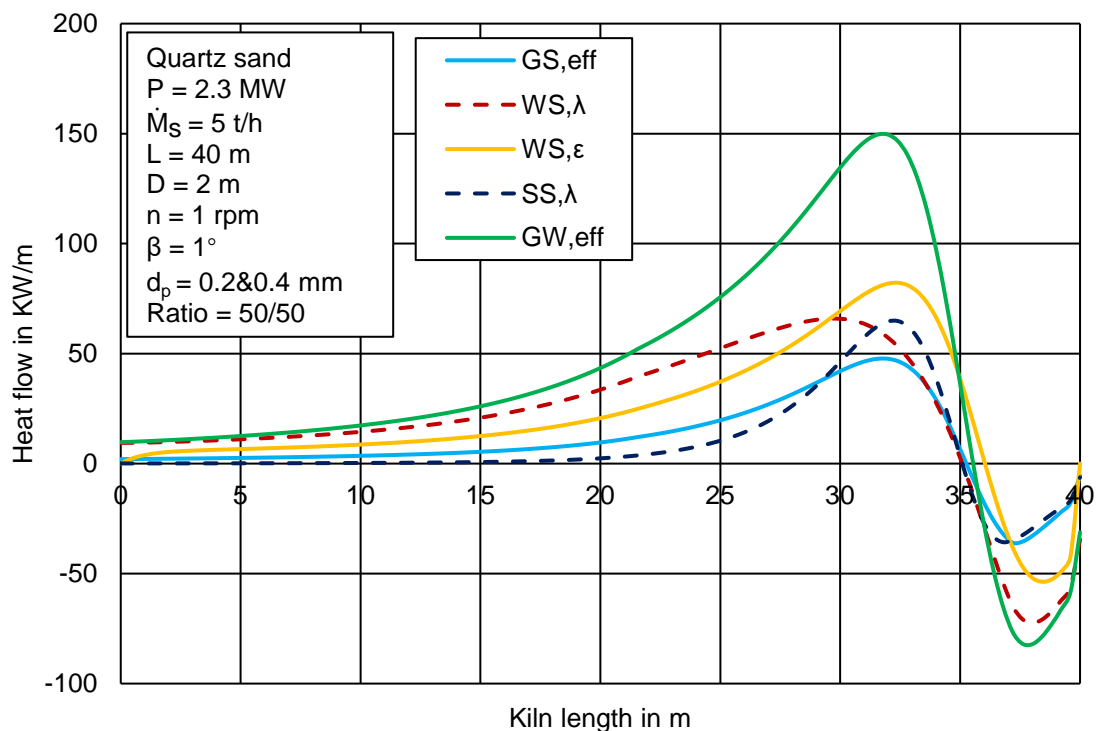


**Figure D.30** Axial effective heat flow between gas and solid bed, gas and inner wall, contact heat flow between wall and solid bed, big and small size particle bed, radiative heat flow between wall and solid bed. ( $d_p = 0.2 \& 0.4$  mm, ratio = 50/50)

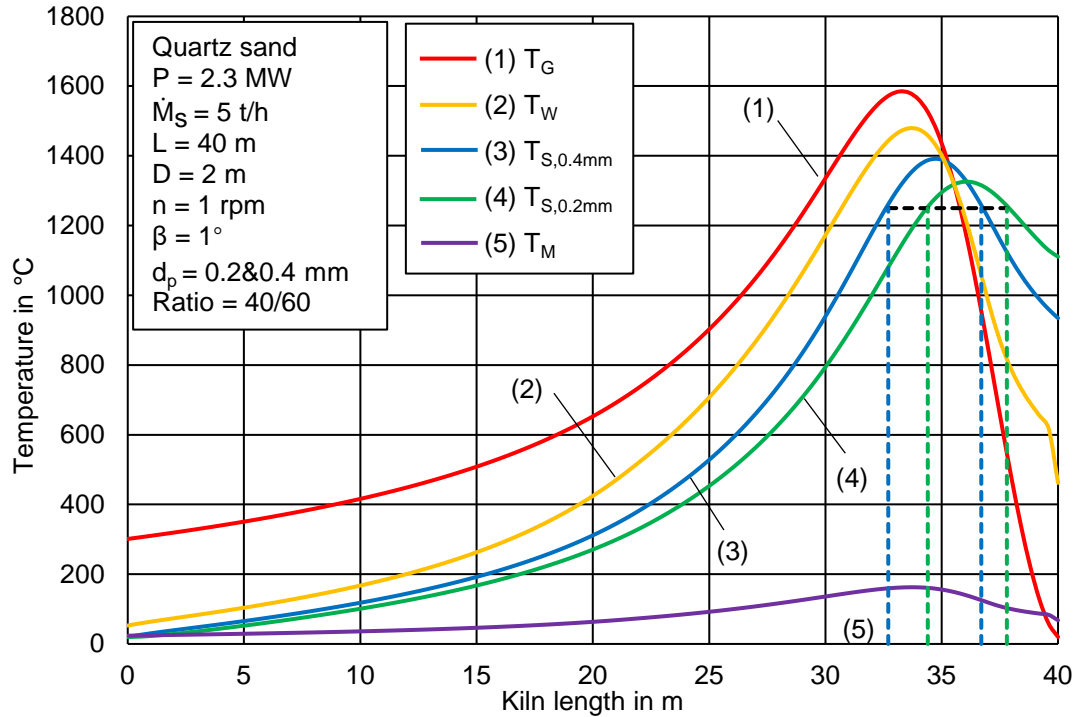


**Figure D.31** Axial temperature profiles of gas, inner wall, solid bed and steel shell. ( $d_p = 0.2 \& 0.4 \text{ mm}$ , ratio = 40/60)

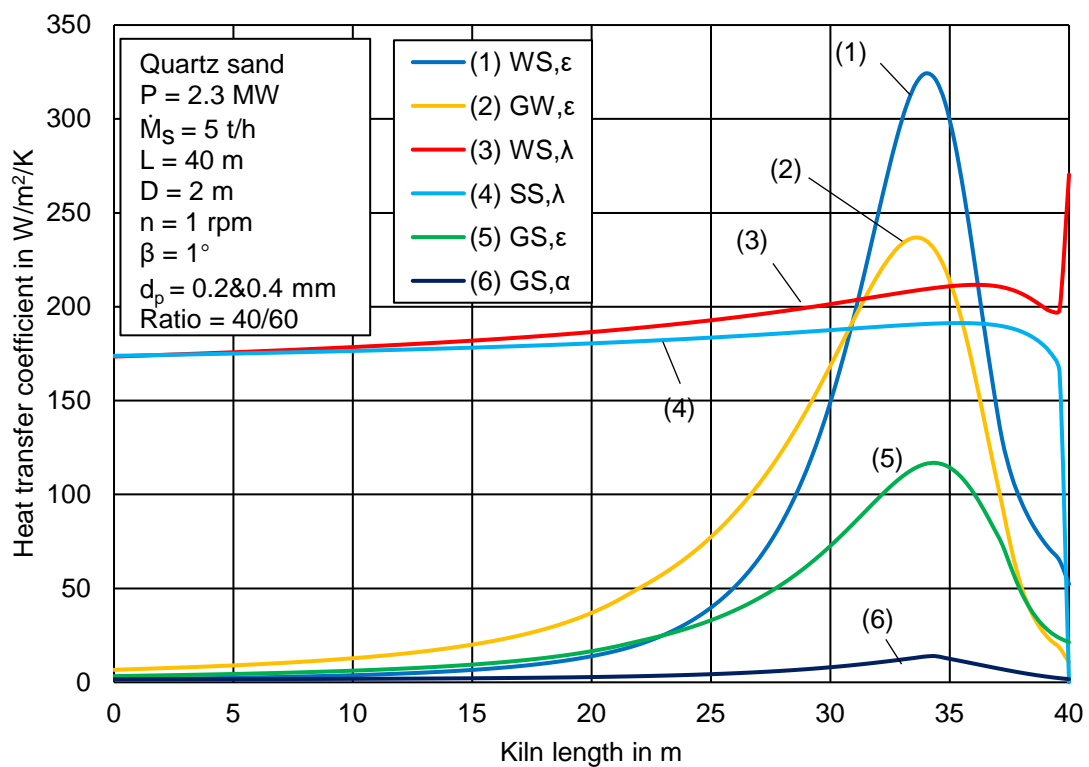


**Figure D.32** Axial radiative heat transfer coefficient between wall and solid bed, gas and wall, gas and solid bed, contact heat transfer coefficient between wall and solid bed, big and small size particle bed and convective heat transfer coefficient between gas and solid bed. ( $d_p = 0.2 \& 0.4 \text{ mm}$ , ratio = 40/60)

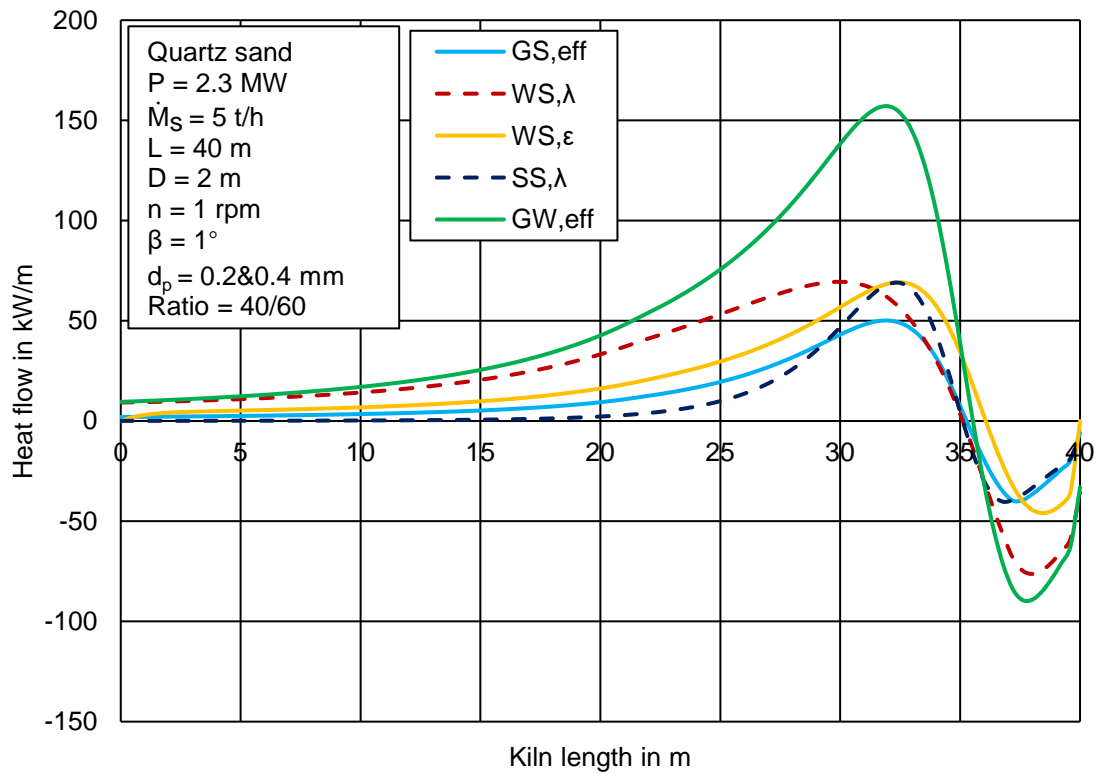


**Figure D.33** Axial effective heat flow between gas and solid bed, gas and inner wall, contact heat flow between wall and solid bed, big and small size particle beds, radiative heat flow between wall and solid bed. ( $d_p = 0.2 \& 0.4$  mm, ratio = 40/60)

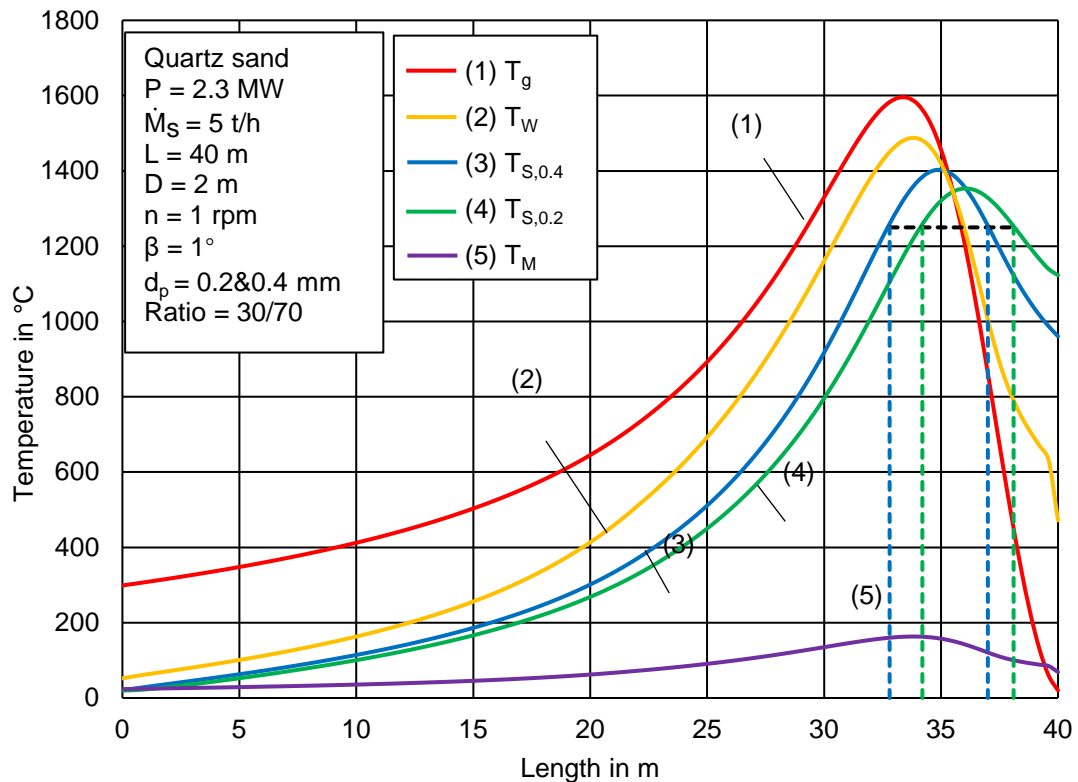


**Figure D.34** Axial temperature profiles of gas, inner wall, solid bed and steel shell. ( $d_p = 0.2 \& 0.4$  mm, ratio = 30/70)

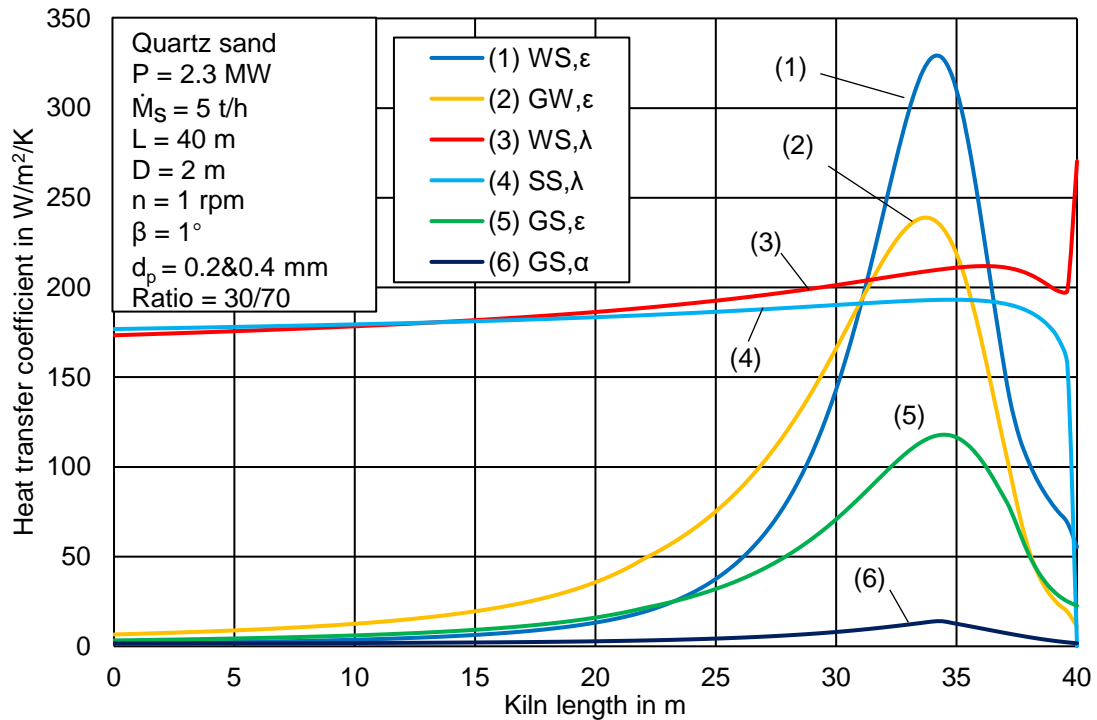


**Figure D.35** Axial radiative heat transfer coefficient between wall and solid bed, gas and wall, gas and solid bed, contact heat transfer coefficient between wall and solid bed, big and small size particle bed and convective heat transfer coefficient between gas and solid bed. ( $d_p = 0.2 \& 0.4 \text{ mm}$ , ratio = 30/70)

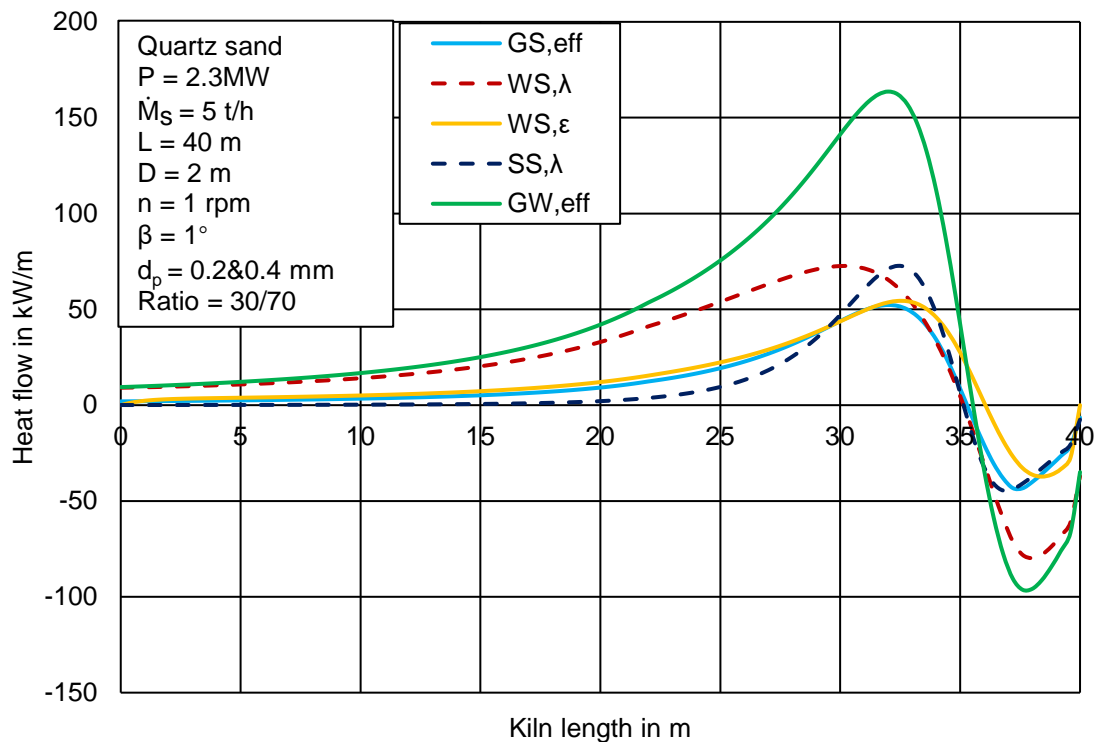


**Figure D.36** Axial effective heat flow between gas and solid bed, gas and inner wall, contact heat flow between wall and solid bed, big and small size particle beds, radiative heat flow between wall and solid bed. ( $d_p = 0.2 \& 0.4 \text{ mm}$ , ratio = 30/70)

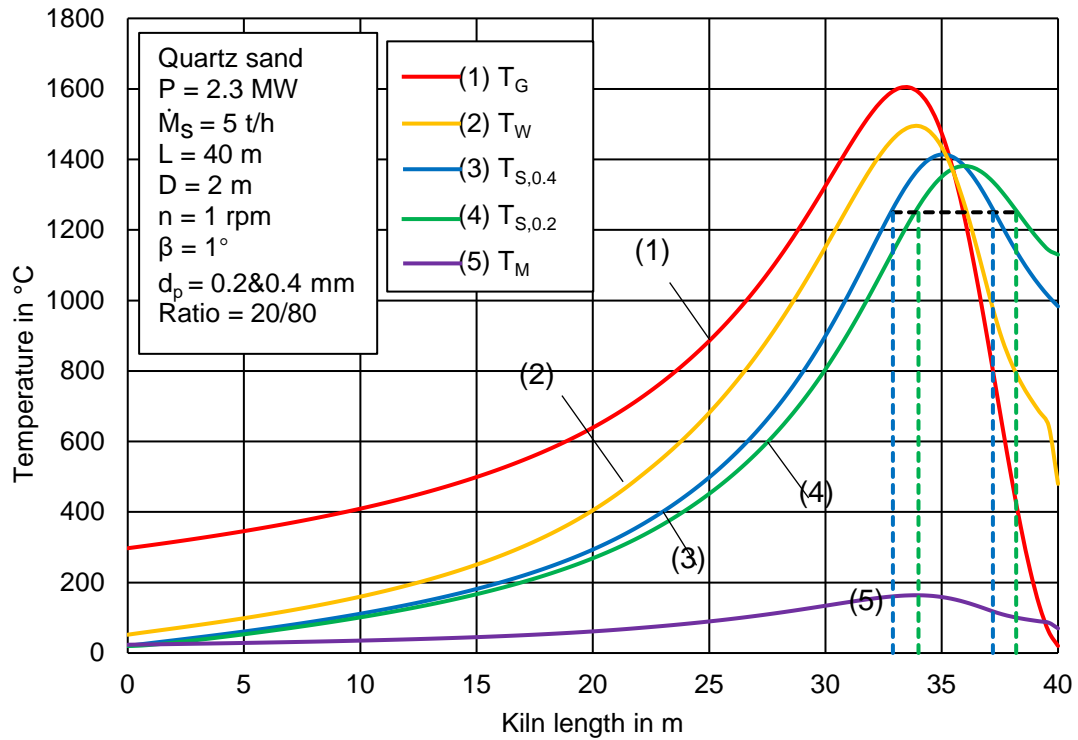


**Figure D.37** Axial temperature profiles of gas, inner wall, solid bed and steel shell. ( $d_p = 0.2 \& 0.4 \text{ mm}$ , ratio = 20/80)

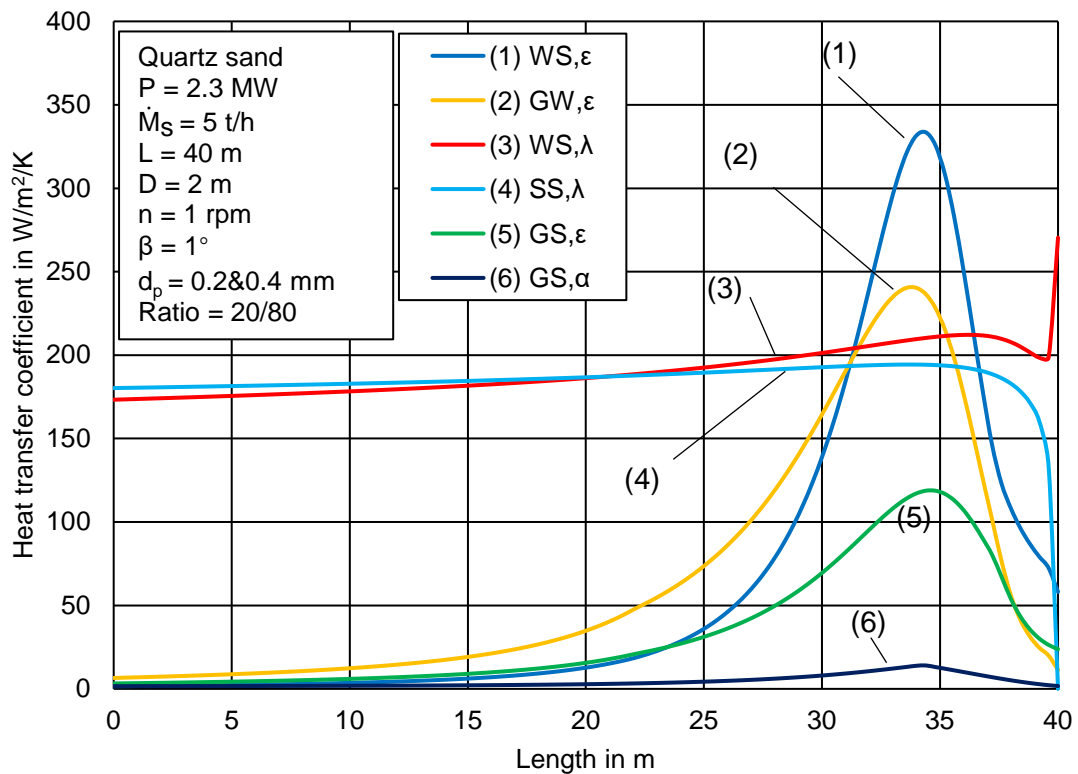


**Figure D.38** Axial radiative heat transfer coefficient between wall and solid bed, gas and wall, gas and solid bed, contact heat transfer coefficient between wall and solid bed, big and small size particle beds and convective heat transfer coefficient between gas and solid bed. ( $d_p = 0.2 \& 0.4 \text{ mm}$ , ratio = 20/80)

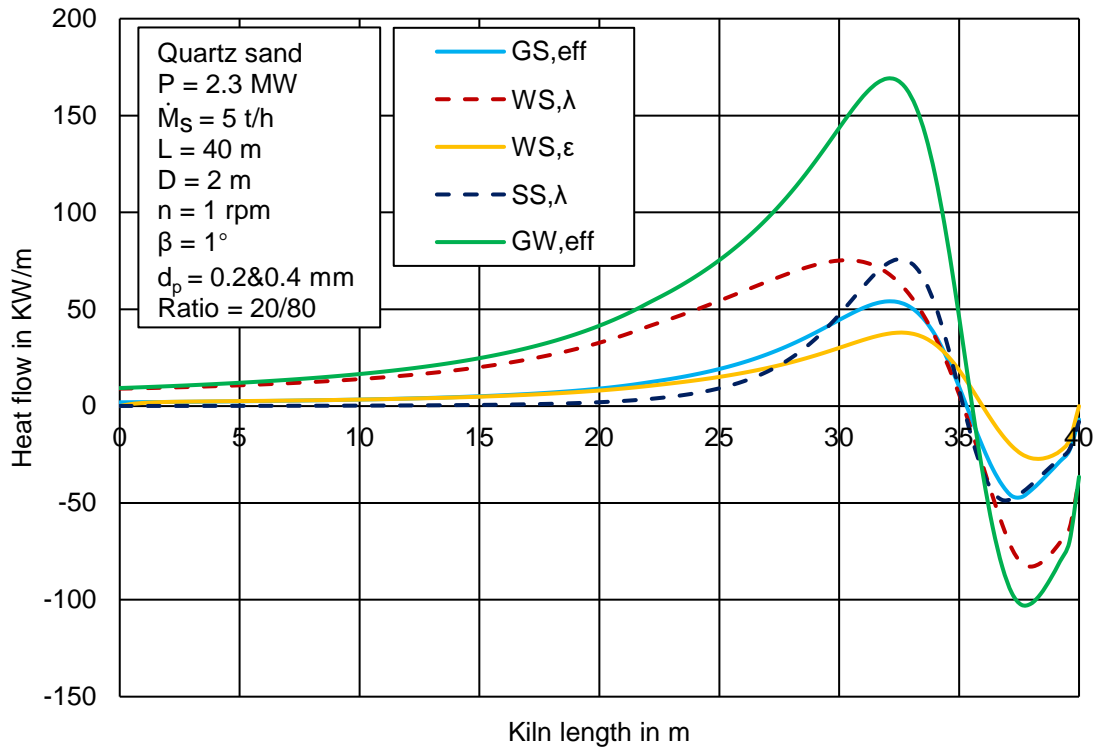


**Figure D.39** Axial effective heat flow between gas and solid bed, gas and inner wall, contact heat flow between wall and solid bed, big and small size particle beds, radiative heat flow between wall and solid bed. ( $d_p = 0.2 \& 0.4$  mm, ratio = 20/80)

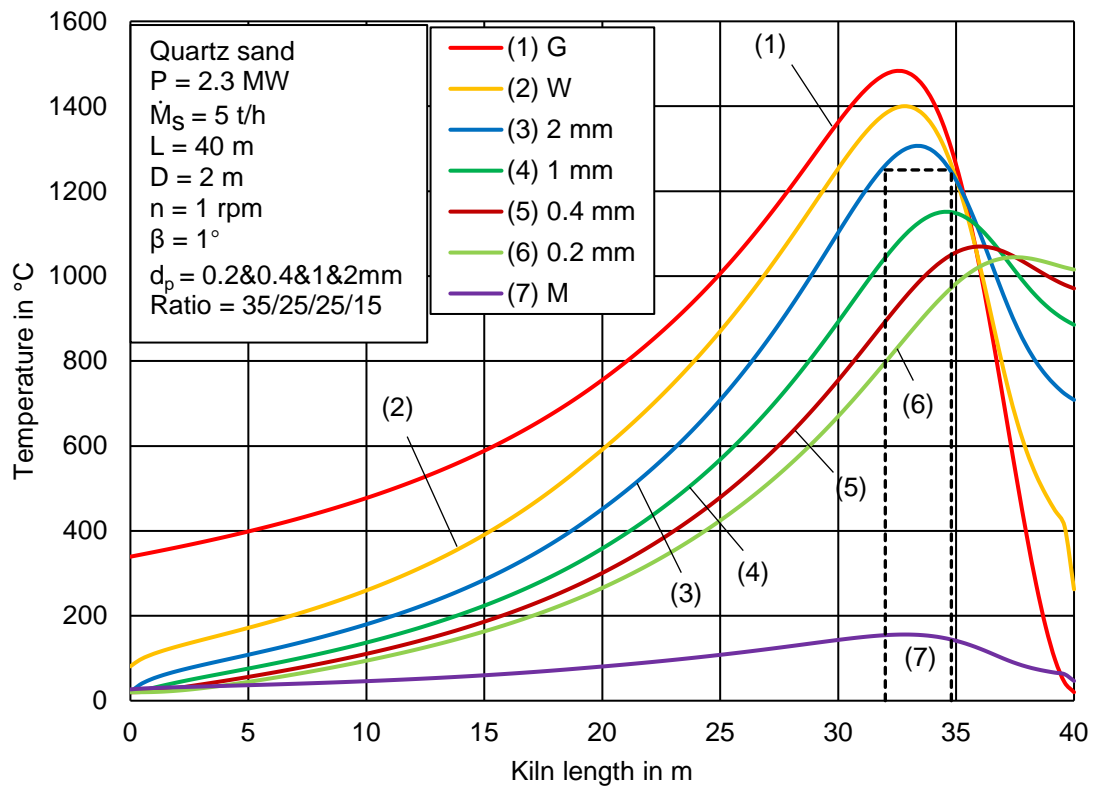


**Figure D.40** Axial temperature profiles of gas, inner wall, solid beds and steel shell. ( $d_p = 0.2 \& 0.4 \& 1 \& 2$  mm, ratio = 35/25/25/15)

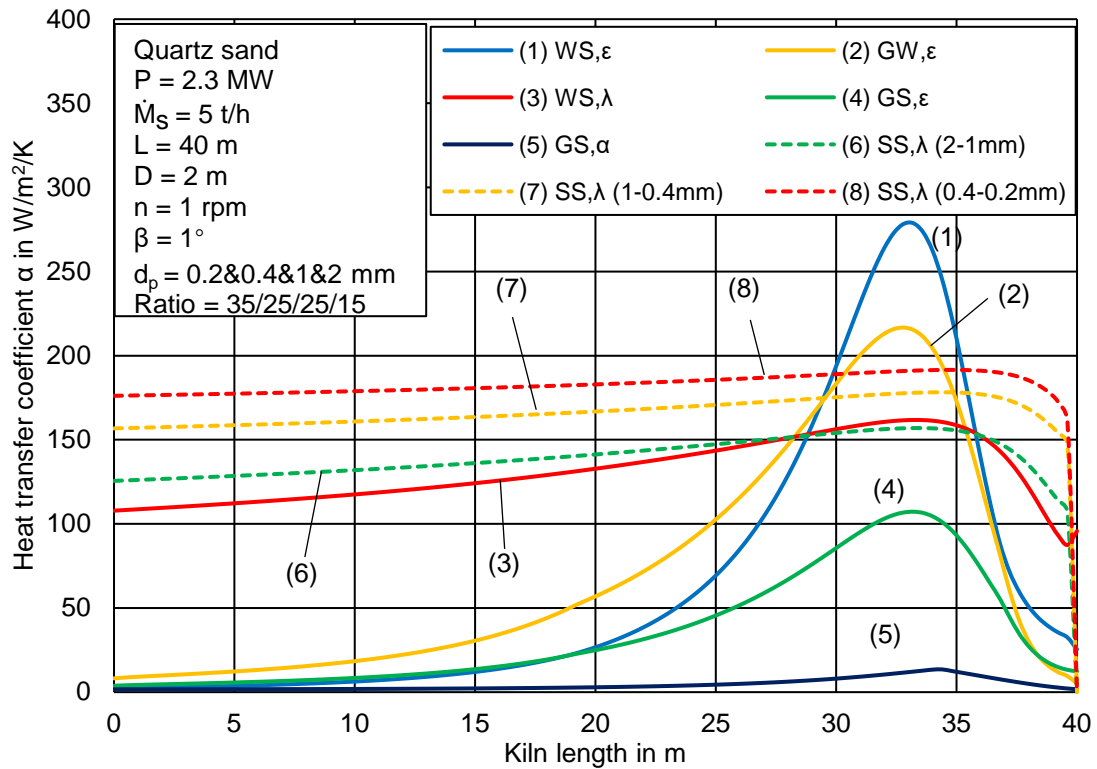


**Figure D.41** Axial radiative heat transfer coefficient between wall and solid bed, gas and wall, gas and solid bed, contact heat transfer coefficient between wall and solid bed, big and small size particle bed and convective heat transfer coefficient between gas and solid bed. ( $d_p = 0.2 \& 0.4 \& 1 \& 2 \text{ mm}$ , ratio = 35/25/25/15)

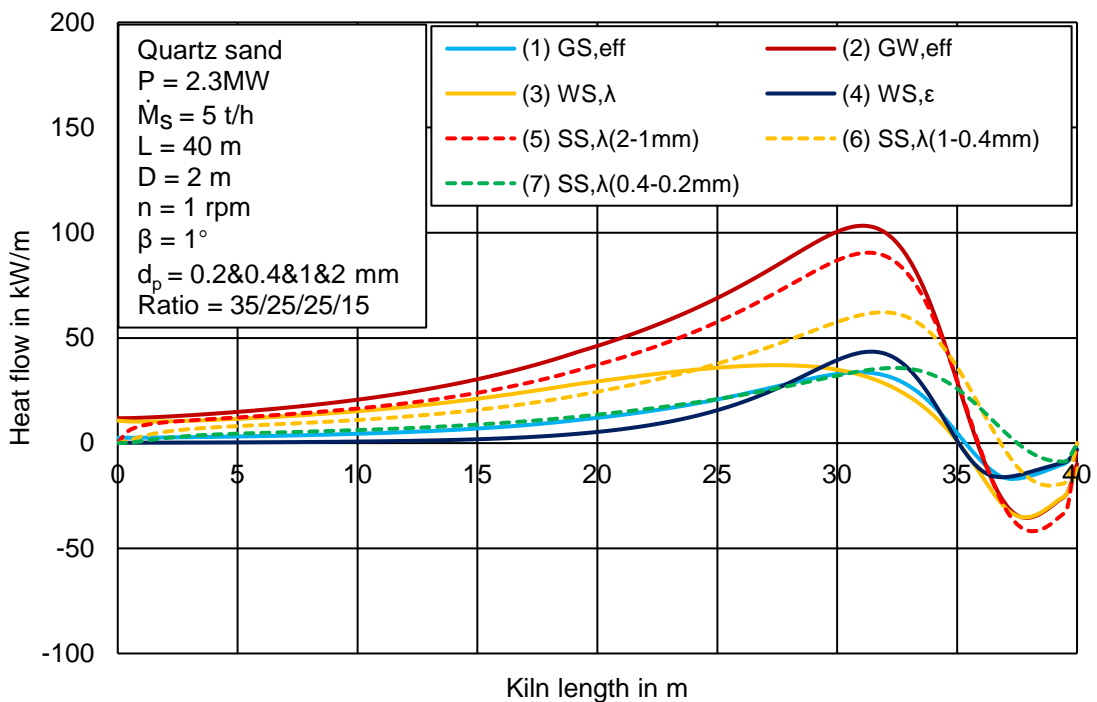


**Figure D.42** Axial effective heat flow between gas and solid bed, gas and inner wall, contact heat flow between wall and solid bed, big and small size particle beds, radiative heat flow between wall and solid bed. ( $d_p = 0.2 \& 0.4 \& 1 \& 2 \text{ mm}$ , ratio = 35/25/25/15)

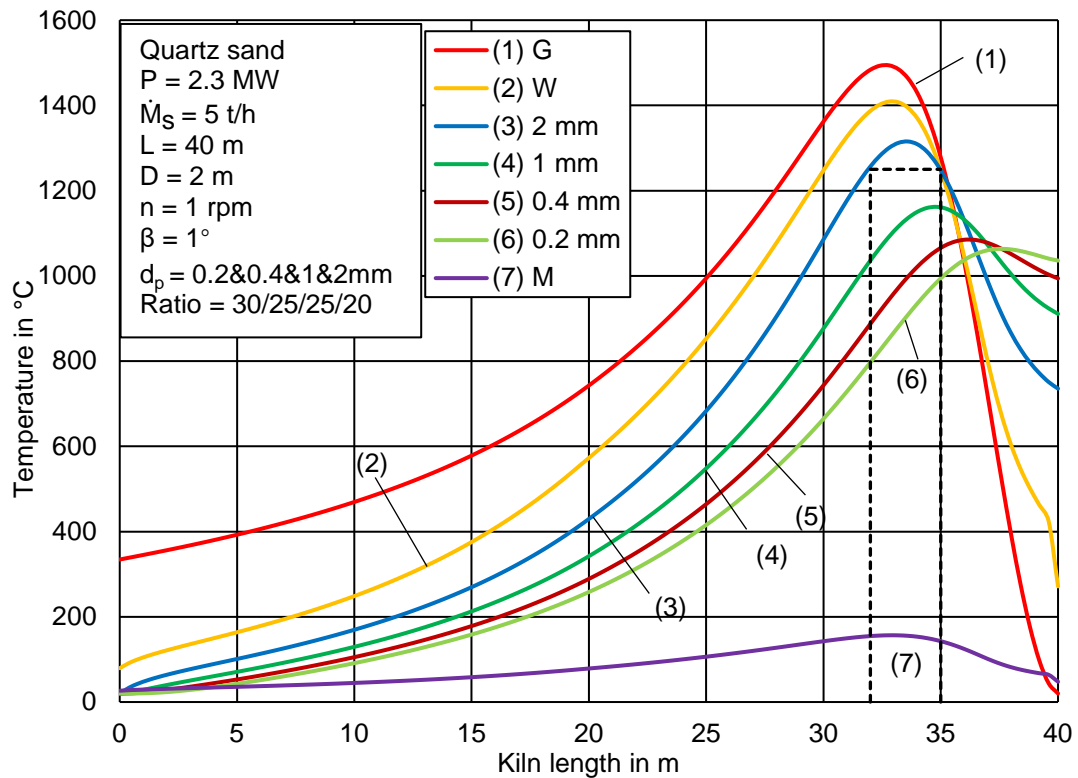


**Figure D.43** Axial temperature profiles of gas, inner wall, solid beds and steel shell. ( $d_p = 0.2 \& 0.4 \& 1 \& 2 \text{ mm}$ , ratio = 30/25/25/20)

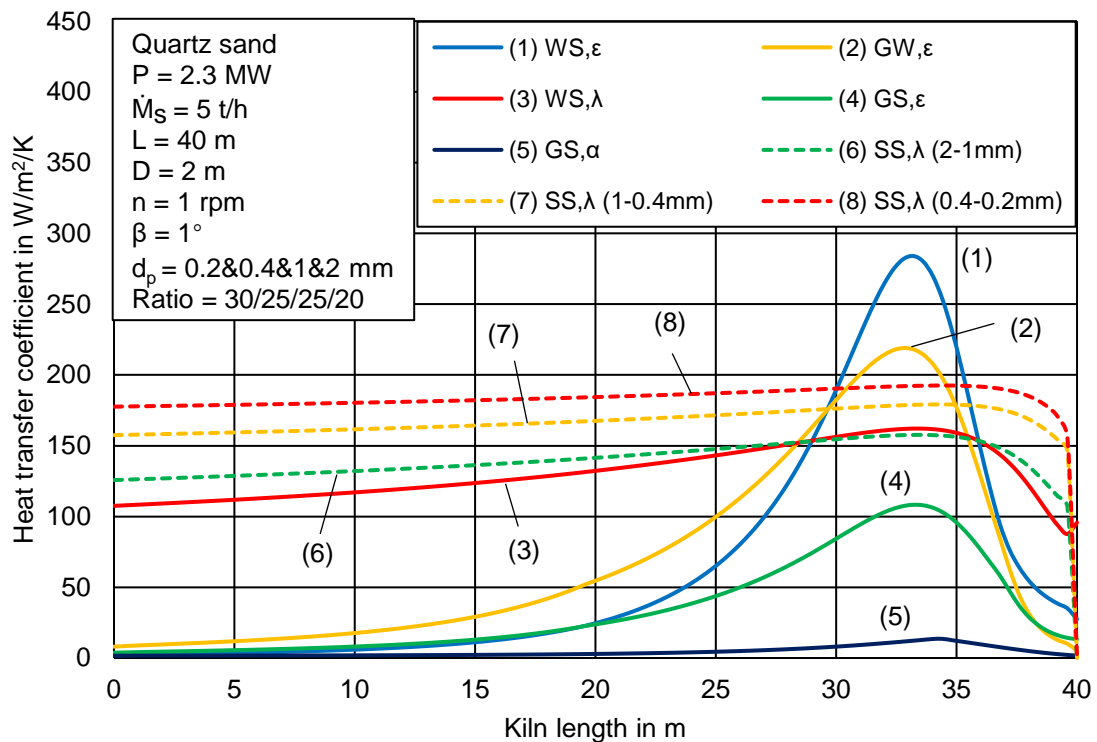


**Figure D.44** Axial radiative heat transfer coefficient between wall and solid bed, gas and wall, gas and solid bed, contact heat transfer coefficient between wall and solid bed, big and small size particle beds and convective heat transfer coefficient between gas and solid bed. ( $d_p = 0.2 \& 0.4 \& 1 \& 2 \text{ mm}$ , ratio = 30/25/25/20)



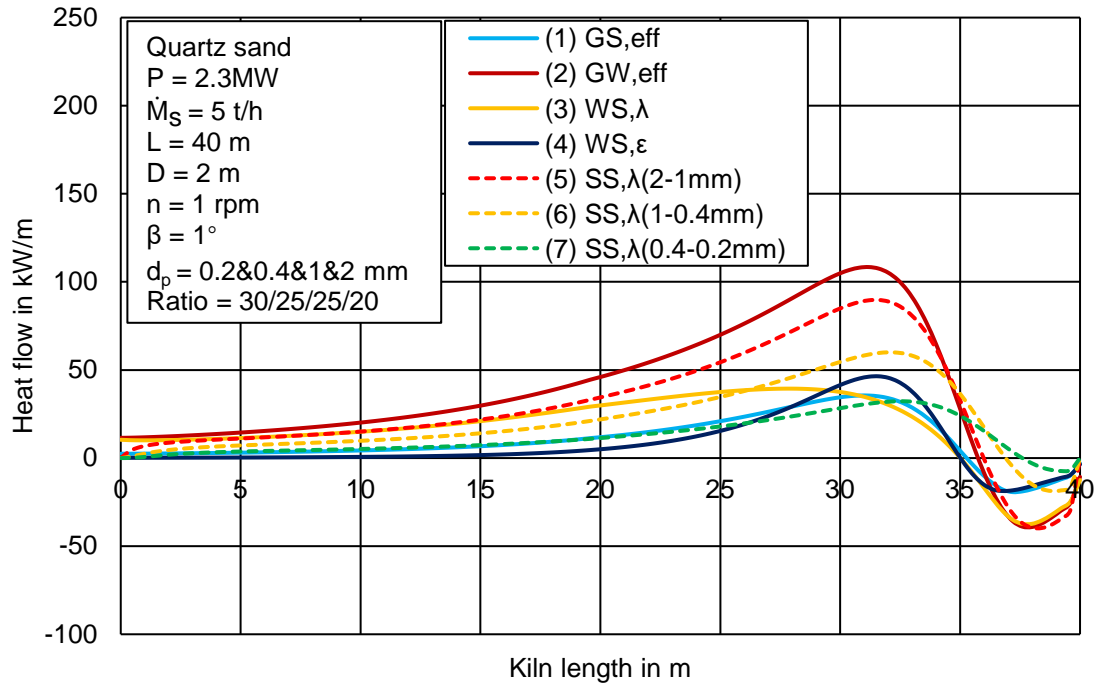


**Figure D.45** Axial effective heat flow between gas and solid bed, gas and inner wall, contact heat flow between wall and solid bed, big and small size particle beds, radiative heat flow between wall and solid bed. ( $d_p = 0.2 \& 0.4 \& 1 \& 2 \text{ mm}$ , ratio = 30/25/25/20)

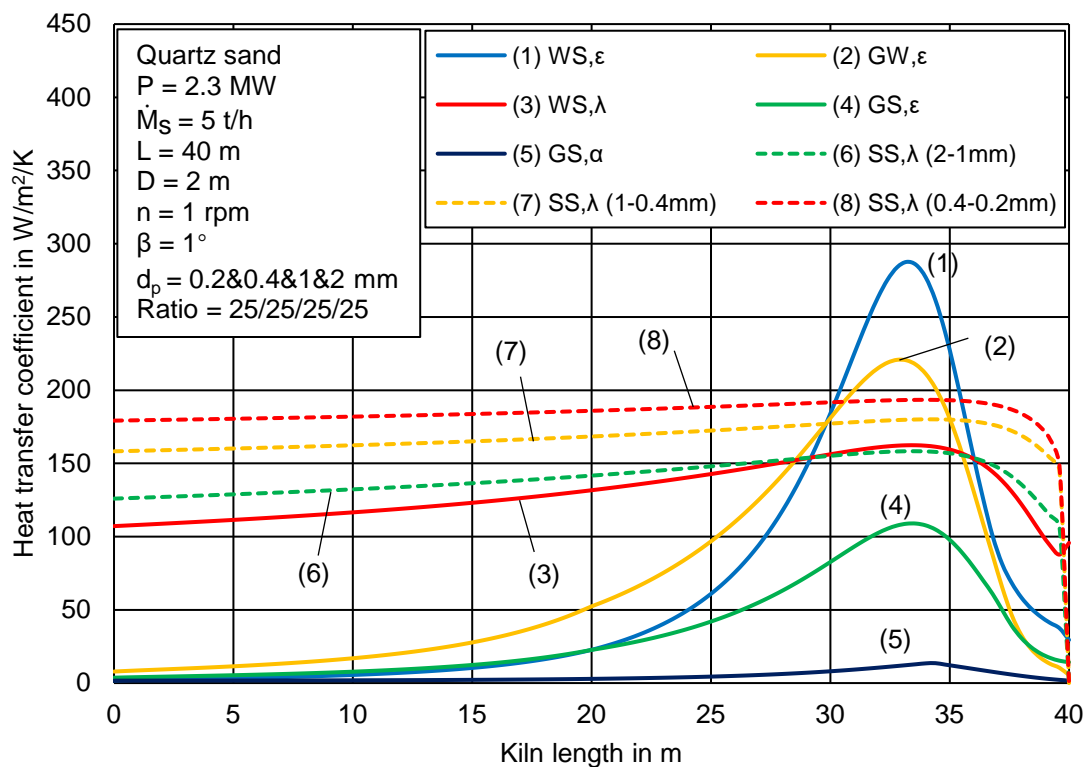


**Figure D.46** Axial radiative heat transfer coefficient between wall and solid bed, gas and wall, gas and solid bed, contact heat transfer coefficient between wall and solid bed, big and small size particle beds and convective heat transfer coefficient between gas and solid bed. ( $d_p = 0.2 \& 0.4 \& 1 \& 2 \text{ mm}$ , ratio = 25/25/25/25)

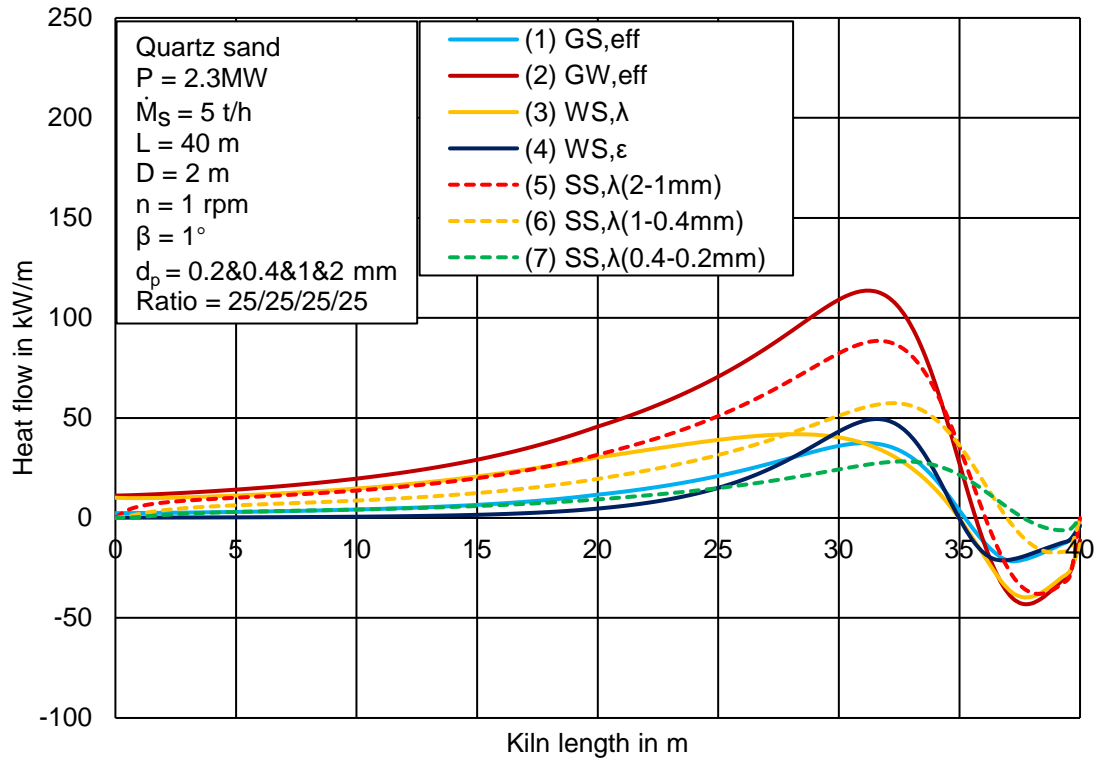


**Figure D.47** Axial effective heat flow between gas and solid bed, gas and inner wall, contact heat flow between wall and solid bed, big and small size particle beds, radiative heat flow between wall and solid bed. ( $d_p = 0.2 \& 0.4 \& 1 \& 2 \text{ mm}$ , ratio = 25/25/25/25)

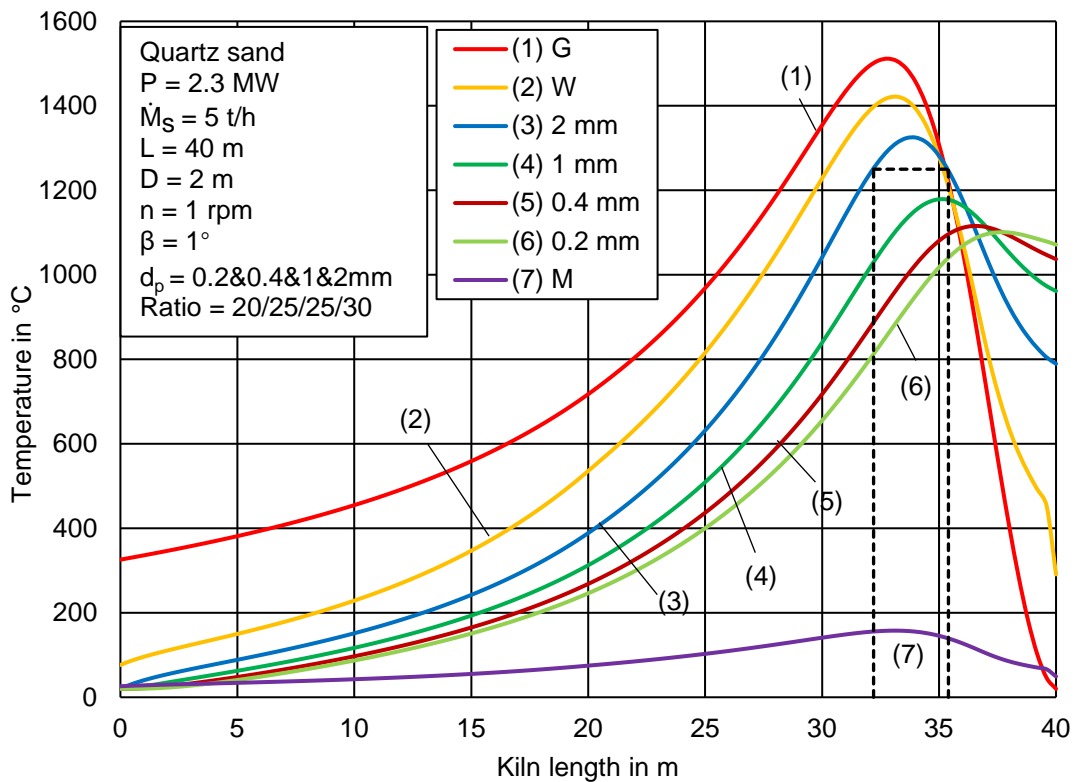


**Figure D.48** Axial temperature profiles of gas, inner wall, solid beds and steel shell. ( $d_p = 0.2 \& 0.4 \& 1 \& 2 \text{ mm}$ , ratio = 20/25/25/30)

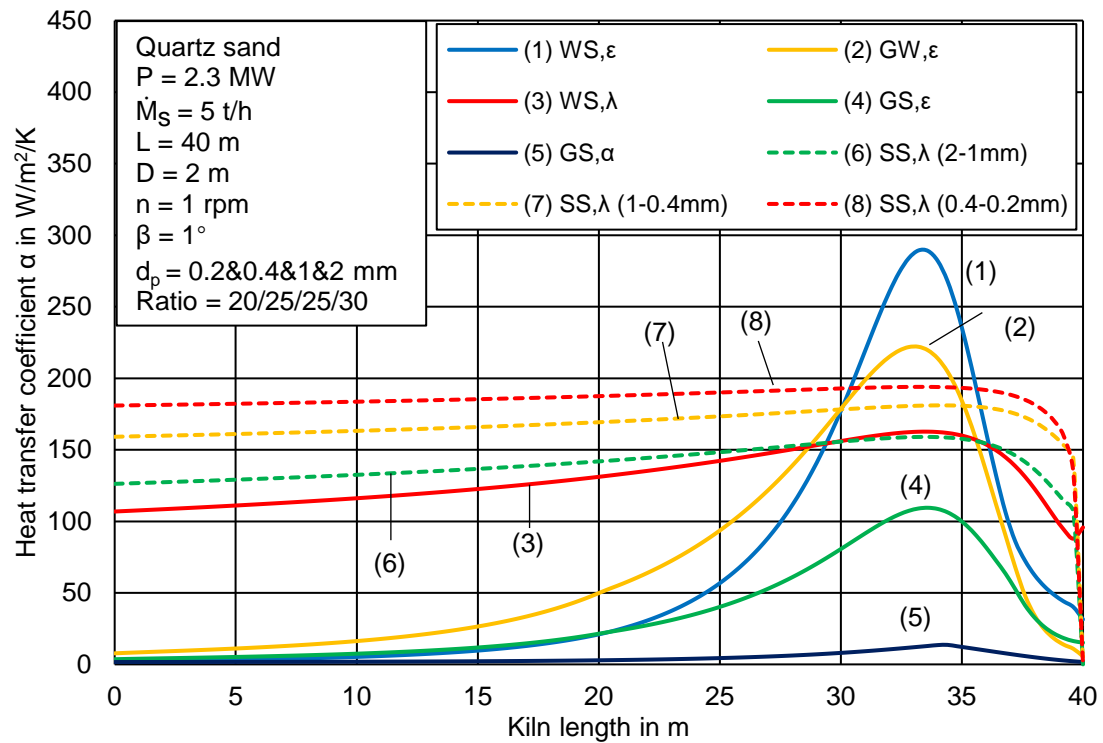


**Figure D.49** Axial radiative heat transfer coefficient between wall and solid bed, gas and wall, gas and solid bed, contact heat transfer coefficient between wall and solid bed, big and small size particle beds and convective heat transfer coefficient between gas and solid bed. ( $d_p = 0.2 \& 0.4 \& 1 \& 2 \text{ mm}$ , ratio = 20/25/25/30)

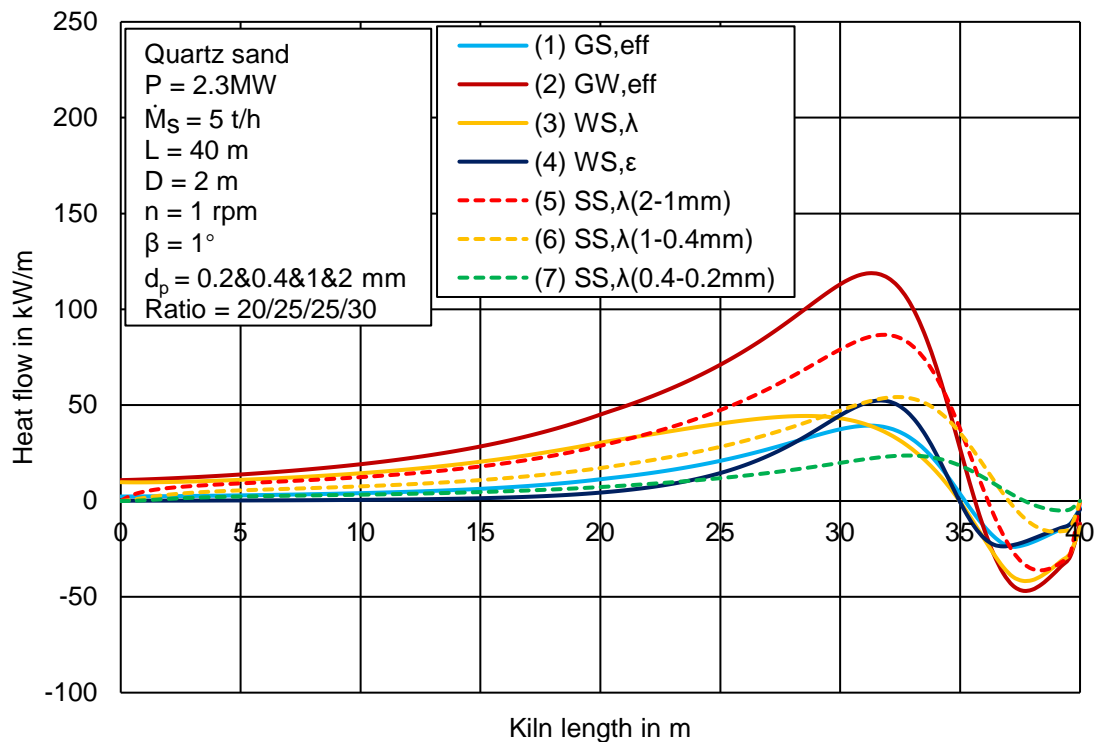


**Figure D.50** Axial effective heat flow between gas and solid bed, gas and inner wall, contact heat flow between wall and solid bed, big and small size particle beds, radiative heat flow between wall and solid bed. ( $d_p = 0.2 \& 0.4 \& 1 \& 2 \text{ mm}$ , ratio = 20/25/25/30)

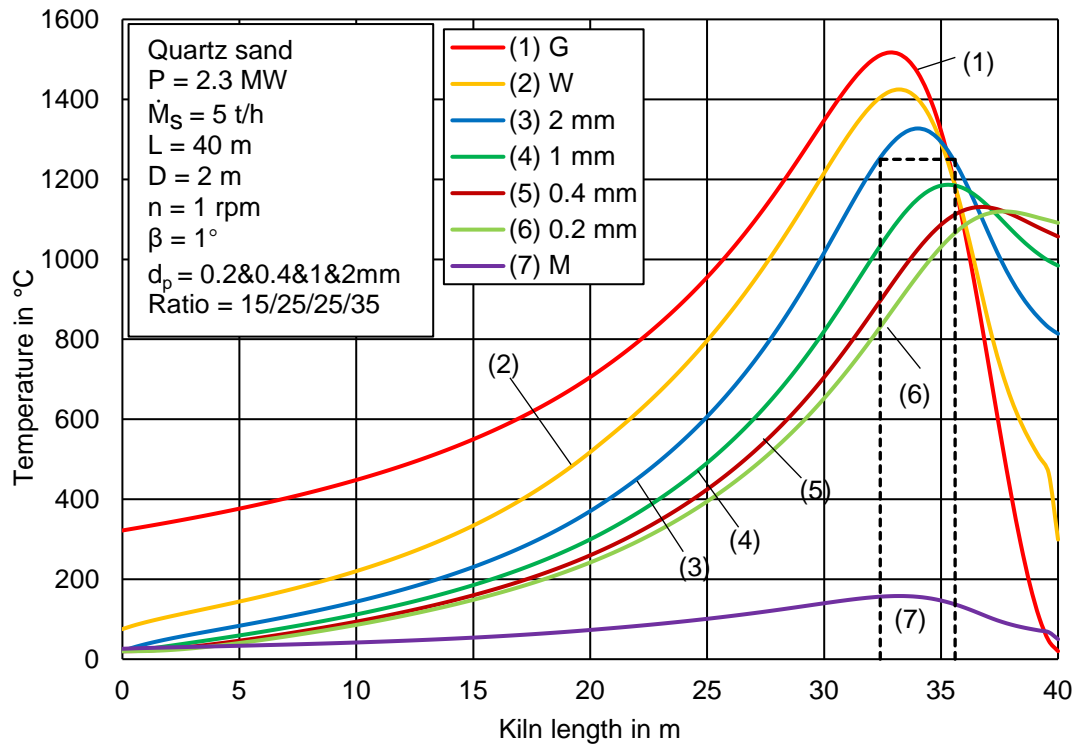


**Figure D.51** Axial temperature profiles of gas, inner wall, solid beds and steel shell. ( $d_p = 0.2, 0.4, 1, 2$  mm, ratio = 15/25/25/35)

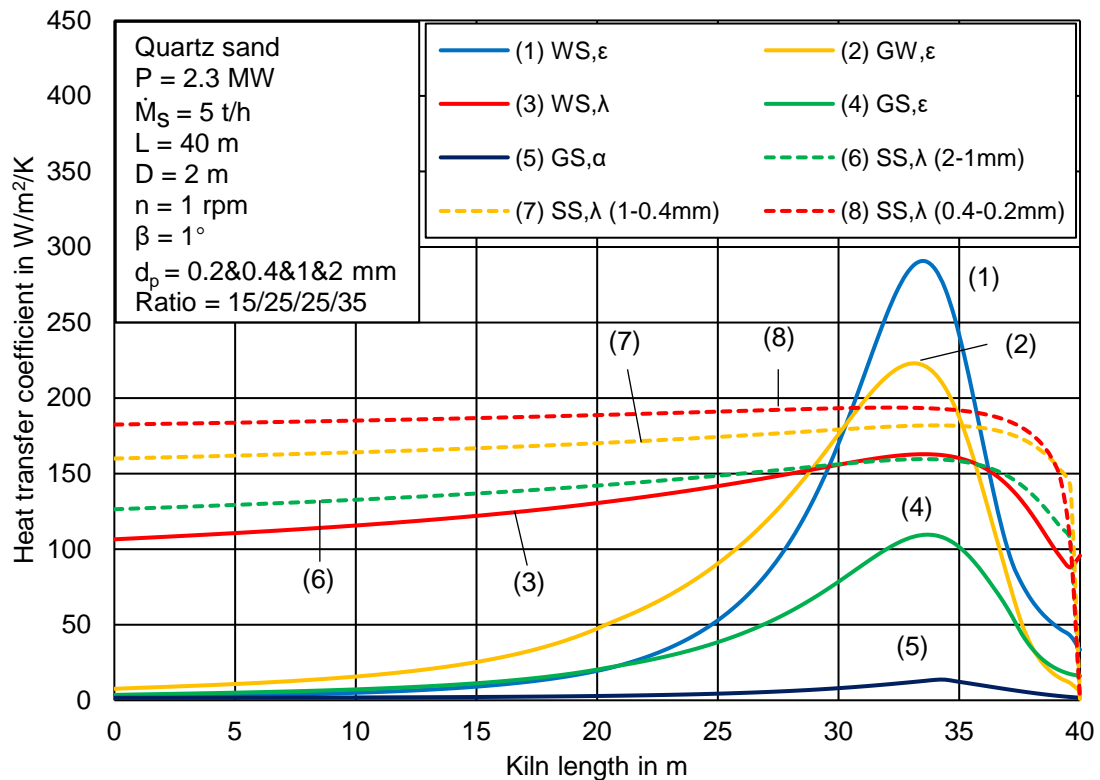


**Figure D.52** Axial radiative heat transfer coefficient between wall and solid bed, gas and wall, gas and solid bed, contact heat transfer coefficient between wall and solid bed, big and small size particle beds and convective heat transfer coefficient between gas and solid bed. ( $d_p = 0.2, 0.4, 1, 2$  mm, ratio = 15/25/25/35)

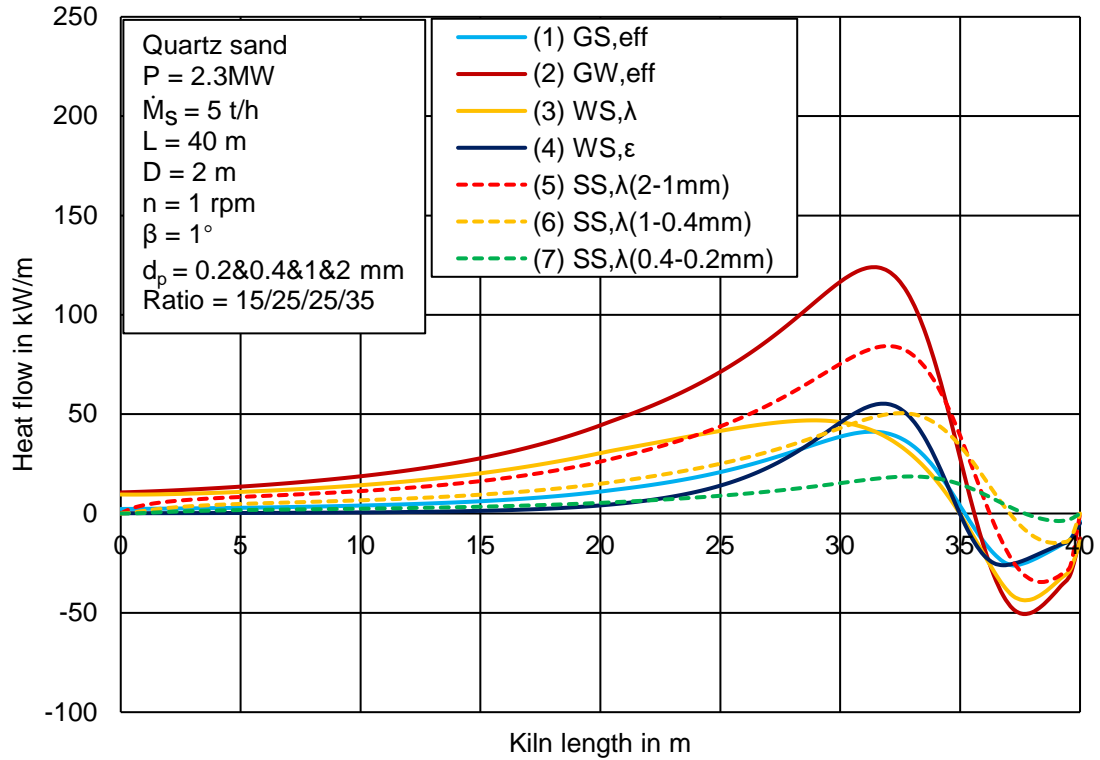


**Figure D.53** Axial effective heat flow between gas and solid bed, gas and inner wall, contact heat flow between wall and solid bed, big and small size particle beds, radiative heat flow between wall and solid bed. ( $d_p = 0.2 \& 0.4 \& 1 \& 2 \text{ mm}$ , ratio = 15/25/25/35)

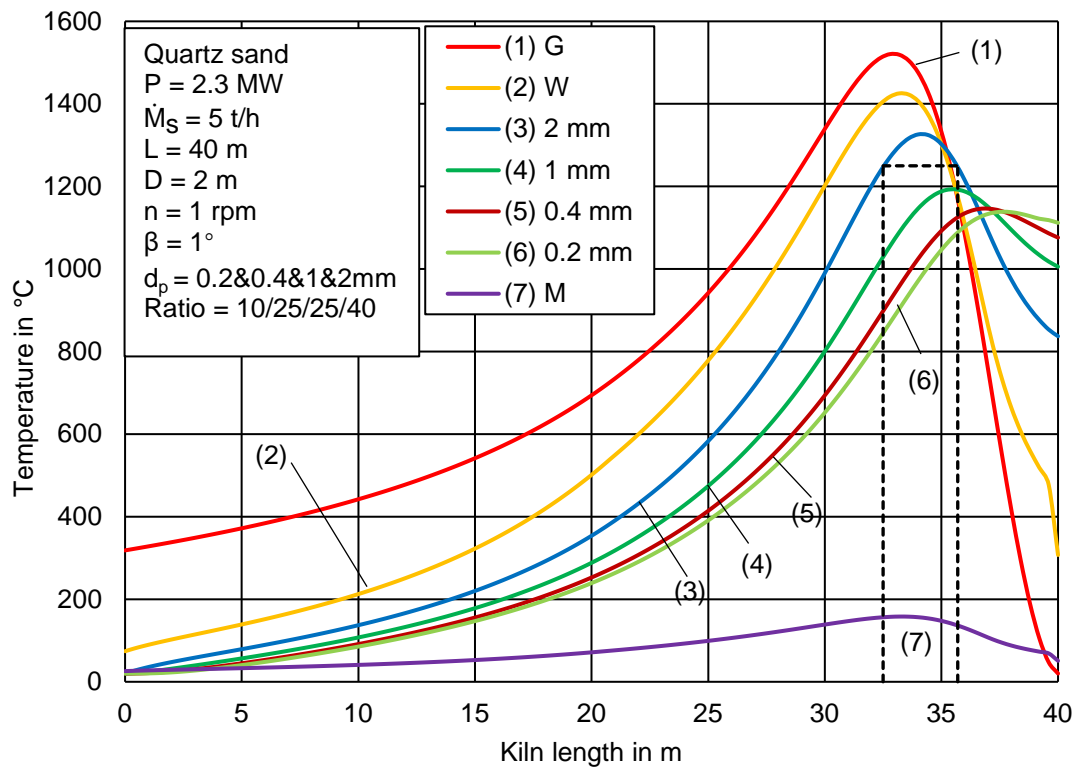


**Figure D.54** Axial temperature profiles of gas, inner wall, solid beds and steel shell. ( $d_p = 0.2 \& 0.4 \& 1 \& 2 \text{ mm}$ , ratio = 10/25/25/40)

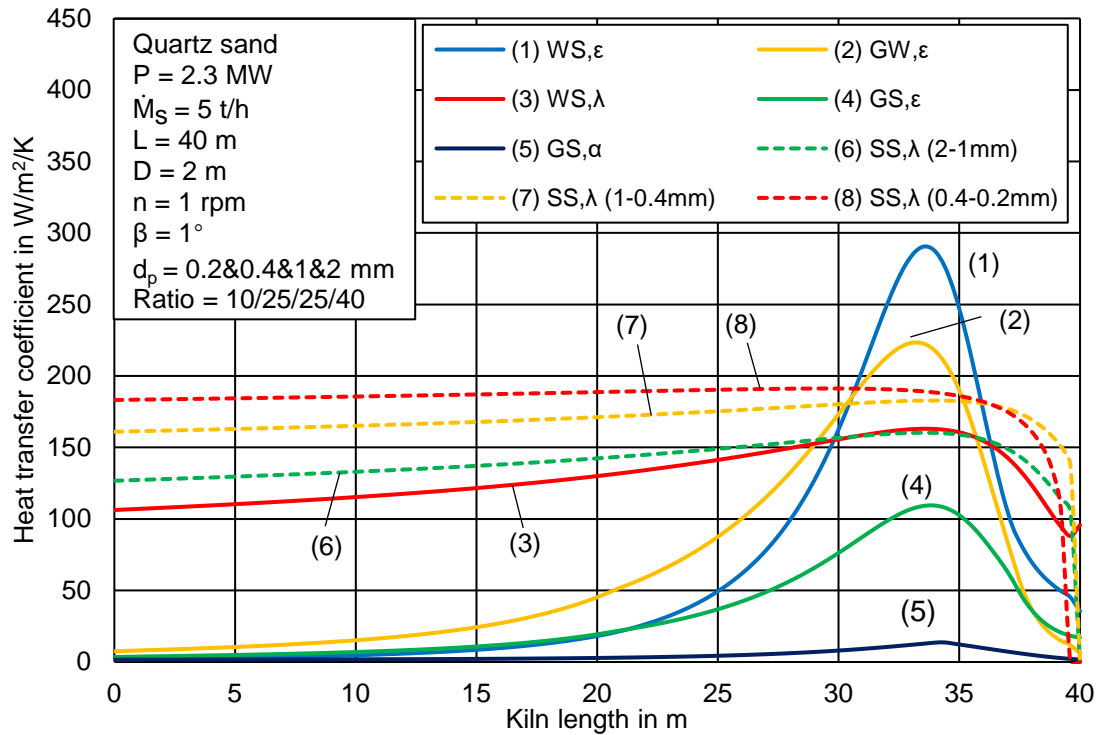


**Figure D.55** Axial radiative heat transfer coefficient between wall and solid bed, gas and wall, gas and solid bed, contact heat transfer coefficient between wall and solid bed, big and small size particle beds and convective heat transfer coefficient between gas and solid bed. ( $d_p = 0.2 \& 0.4 \& 1 \& 2 \text{ mm}$ , ratio = 10/25/25/40)

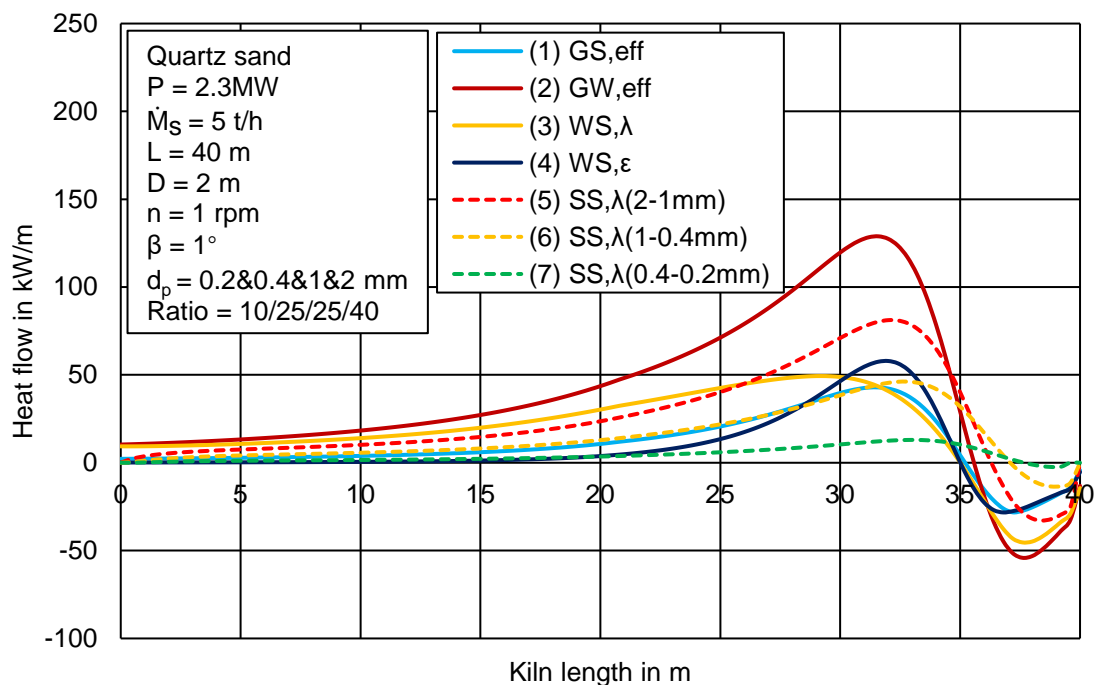


**Figure D.56** Axial effective heat flow between gas and solid bed, gas and inner wall, contact heat flow between wall and solid bed, big and small size particle beds, radiative heat flow between wall and solid bed. ( $d_p = 0.2 \& 0.4 \& 1 \& 2 \text{ mm}$ , ratio = 10/25/25/40)

# Curriculum vitae

## Personal information

Name	Haozhi Jie
Address	J.-G.-Nathusius-Ring 2, WNr.503, 39106 Magdeburg
Nationality	Chinese
Marital status	Married
Date of birth	13.08.1990
Place of birth	Nanjing, China

## Education

<b>04.2015 - Present</b>	Doctorate in Engineering (Dr.-Ing.)
University	Otto von Guericke University Magdeburg
PhD Dissertation	Axial transport behavior and thermal treatment of polydisperse materials in direct heated rotary kilns
<b>10.2012 – 01.2015</b>	Master of Science (M.Sc.)
University	Otto von Guericke University Magdeburg
Major	Chemical and Energy Engineering (Grade 1,5)
<b>09.2008 - 06.2012</b>	Bachelor of Science (B.Sc.)
University	Nanjing Institute of Technology
Major	Power and Energy Engineering (GPA 3,66/4,0)